Université Paris-Sud
École Doctorale 517
Institut de Recherche sur les lois Fondamentales de l'univers, CEA Saclay

Thèse de doctorat

Spécialité Physique

Soutenue le 3 juillet 2015 par

Thibault Main de Boissière

Recherches de WIMPs de basse masse et d'axions avec l'expérience EDELWEISS

Composition du jury :

Président du jury :	M. Réza Ansari	Université Paris-Sud
Directeur de thèse:	M. Eric Armengaud	CEA Saclay
Rapporteurs :	Mme Laura Baudis	Université de Zurich
	M. Jacques Dumarchez	LPNHE
Examinateur :	M. Jules Gascon	IPN Lyon

UNIVERSITE PARIS SUD

Abstract

Low mass WIMPs and axion searches with the EDELWEISS experiment

Thibault Main de Boissiere

In spite of the recent successes of observational cosmology, most of the universe remains poorly known. Known particles (which we call baryons) only make up 5% of the total content of the universe. The standard cosmological model contains two other components: Dark Energy and Dark Matter (respectively 70% and 25% of the total content). Dark Matter, which is generally believed to be a non-relativistic, charge neutral and non-baryonic new form of matter, is the central focus of this work. We studied two likely candidates, namely WIMPs and axions. Our analyses were carried out within the EDELWEISS collaboration which operates detectors sensitive to both WIMP and axion signals.

Axions were first introduced to solve the strong CP problem. They can be produced in the Sun through a variety of processes and in some models, they may also contribute to the Dark Matter density. In this work, we used EDELWEISS data to search for axions through four distinct production-detection mechanisms. These mechanisms involve the coupling of axions to nucleons, photons and electrons. No excess over background was found. These null observations allowed us to set stringent constraints on the axion couplings and exclude several orders of magnitude of the axion mass within specific QCD axion models.

On the other hand, WIMPs are the canonical dark matter candidate whose mass lies in the GeV-TeV range. With the motivation of recent theoretical developments and possible signal hints, we focused our effort on so-called low mass WIMPs (3 to 25 GeV). This thesis describes a new multivariate analysis specifically designed for this mass range, which we tuned using an unblinded fraction of the data set (35 kg.d) from a single EDELWEISS detector. No significant signal over background excess was found and we set an upper limit on the spin-independent WIMP-nucleon cross section of 1.48×10^{-6} pb at 10 GeV.

UNIVERSITE PARIS SUD

Résumé

Recherches de WIMPs de basse masse et d'axions avec l'expérience EDELWEISS

Thibault Main de Boissiere

En dépit des récents succès de la cosmologie observationnelle, la majeure partie de l'univers demeure méconnue: la matière usuelle, dite baryonique, ne représente que 5% du contenu total de l'univers. Dans le modèle cosmologique standard, deux autres composantes complètent notre description: l'énergie noire et la matière noire (respectivement 70% et 25% du contenu total). Dans cette thèse, nous nous intéressons à la matière noire, une nouvelle forme de matière qui doit être non-relativiste, non-baryonique et neutre de charge. Nous avons étudié deux candidats : les WIMPs et les axions. Toutes nos analyses ont été menées au sein de la collaboration EDELWEISS, qui opère des détecteurs sensibles à un éventuel signal de WIMP ou d'axion.

Les axions ont d'abord été introduits pour résoudre le problème de la symétrie CP en chromodynamique quantique. Ils peuvent être produits dans le soleil par des processus divers et, dans certains modèles, peuvent contribuer à la densité de matière noire. Nous avons utilisé les données d'EDELWEISS pour la recherche d'axions suivant quatre modes de production-détection distincts. Ces mécanismes font intervenir le couplage des axions aux nucléons, aux photons et aux électrons. Nous n'avons observé aucun excès de signal par rapport au bruit de fond. Ces constatations nous ont permis d'obtenir des contraintes fortes sur la valeur de chaque couplage d'axion et d'exclure plusieurs ordres de grandeur de la masse de l'axion dans le cadre de modèles spécifiques de QCD.

Les WIMPs font partie des candidats à la matière noire les plus étudiés. Ce sont des particules interagissant faiblement avec une masse pouvant aller du GeV au TeV. Des modèles théoriques et des résultats expérimentaux récents semblent converger vers des masses faibles (de l'ordre de quelques GeV). A la lumière de ces développements, nous avons donc choisi de privilégier l'étude des WIMPs de basse masse (de 3 à 25 GeV). Nous avons mis en place une analyse multivariée particulièrement adaptée à la recherche de WIMPs de basse masse. Cette analyse a été optimisée sur une fraction de 35 kg.jour du jeu de données EDELWEISS complet. Nous n'avons pas observé d'excès de signal par rapport au bruit de fond attendu. Par conséquent, nous avons calculé une limite supérieure sur la section efficace WIMP-nucléon spin-indépendante de 1.48×10^{-6} pb à 10 GeV.

Contents

List of Figures

List of Tables

To Ponicorne

Chapter 1

In search of Dark Matter

1.1 Dark Matter in the Standard Cosmological model

The Standard Cosmological model, also called ΛCDM model, is a formidable achievement built over a century of observations and theories. The now widely accepted picture is that of a universe dominated by Dark Energy and Dark Matter (see Fig. 1.1, right). Remarkably, this model provides an impressive fit to observational data with only 6 free parameters. A detailed description is beyond the scope of this work. However, it is essential to introduce the foundations of modern cosmology to understand the Dark Matter hypothesis: the introduction of cold, non baryonic matter which interacts weakly accounts for a variety of observations unintelligible with ordinary matter alone. Several theories have come up with interesting Dark Matter candidates which will be briefly reviewed.

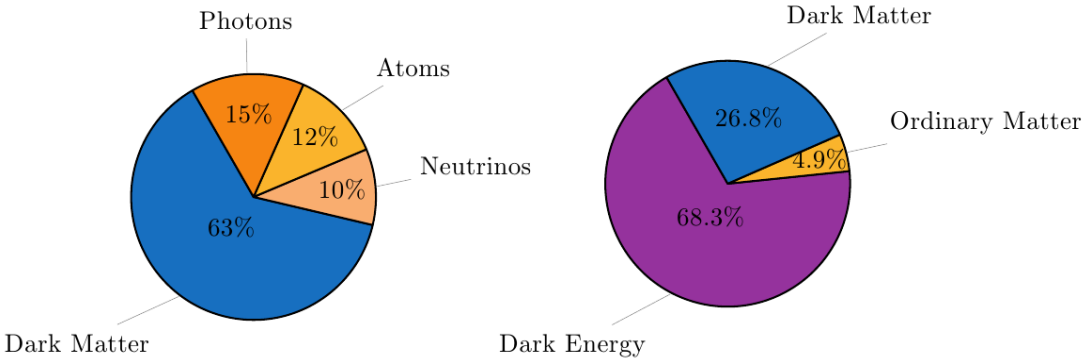

FIGURE 1.1 Left: Energy budget of the universe 380 000 years after Big Bang (recombination epoch). Right: Energy budget today.

1.1.1 Modern cosmology: an introduction

- Geometry and symmetry considerations:

The Cosmological Principle states that the Universe is *homogeneous* and *isotropic*: its properties are independent of both position and direction. There is evidence that this is true *statistically*: The observation of the expansion of the universe [4] shows that it expands at the same rate in all directions. Galaxy surveys [5] show that the universe looks more and more homogeneous and isotropic at large enough scales (see Fig. 1.2).

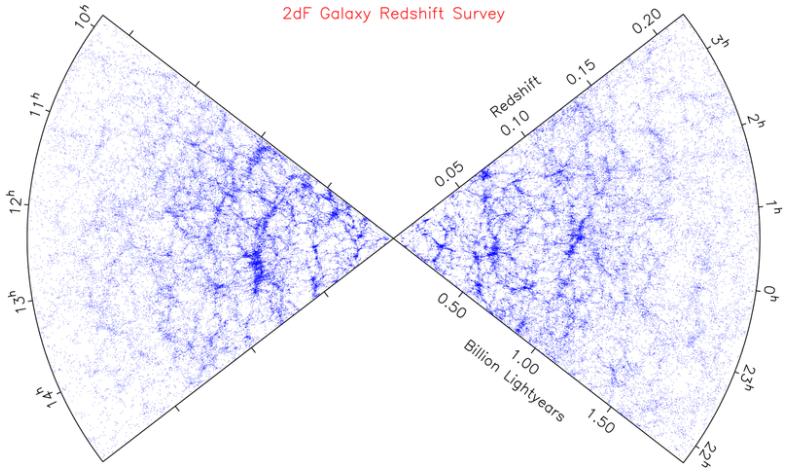

FIGURE 1.2 The 2dF survey galaxy distribution as a function of redshift. At small scales, the distribution is clumpy and structures are clearly visible. However, when averaged over large scales, the distribution looks more homogeneous.

To a first approximation, we can treat the universe as perfectly homogeneous and isotropic. This greatly simplifies our description since space-time can be fully characterized by two parameters: $\boldsymbol{a(t)}$, the scale factor at time t which indicates how the universe is expanding and $\boldsymbol{k}$, which dictates the geometry:

$$k = \begin{cases} -1 & \text{closed} \\ 0 & \text{flat} \\ 1 & \text{open} \end{cases} \tag{1.1}$$

The metric (known as the Friedmann-Robertson-Walker metric or FRW) of such a universe is given by:

$$ds^2 = dt^2 - a(t)^2 \left[\frac{dr^2}{1 - kr^2} + r^2 d\Omega^2 \right] \tag{1.2}$$

- Kinematics:

  How do particles evolve in the FRW spacetime? General relativity tells us that free-falling particles move along geodesics (*i.e.* curves that extremize the proper time between two points). The geodesic equation 1.3 gives us information about the kinematics of the FRW universe.

$$\frac{d^2x^\mu}{d^2\tau} + \Gamma^\mu_{\nu\rho}\frac{dx^\nu}{d\tau}\frac{dx^\rho}{d\tau} = 0 \tag{1.3}$$

  where $\Gamma^\mu_{\nu\rho}$ corresponds to the metric's Christoffel symbols, x^i are the spacetime coordinates and τ is the proper time.

- Dynamics:

  So far, only the symmetries of the FRW spacetime have been invoked. To understand its dynamics, we need to use Einstein's General Relativity equations:

$$G_{\mu\nu} = 8\pi G T_{\mu\nu} - \Lambda g_{\mu\nu} \tag{1.4}$$

  These equations capture the relation between geometry (the Einstein tensor $G_{\mu\nu}$) and the energy content of the universe (the stress-energy tensor $T_{\mu\nu}$). We have also allowed for a cosmological constant Λ. This term can be added to the General Relativity equations without modifying the conservation of the stress-tensor and characterizes the vacuum energy. The first cosmological models discarded such a constant. However, in the 1990's, supernovae surveys [4, 6] showed a non-zero cosmological constant was needed to account for the accelerated expansion of the universe.

  The Einstein tensor can be computed with the metric only. However we need to discuss the contents of the stress-energy tensor. Once again, we can invoke the Cosmological Principle: homogeneity and isotropy force the stress-energy tensor to be that of a perfect fluid:

$$T_{\mu\nu} = (\rho + P)\, U_\mu U_\nu - P g_{\mu\nu} \tag{1.5}$$

  ρ and P are the energy density and pressure of the fluid. U^μ is its four-velocity with respect to the observer. For a comoving observer, $U^\mu \equiv (1, 0, 0, 0)$.

  Combining Eq. 1.2, 1.3, 1.4, 1.5 and using conservation laws we can finally derive the *Friedmann equations*:

$$\begin{aligned} H^2 \equiv \left(\frac{\dot{a}}{a}\right)^2 &= \frac{8\pi G\rho}{3} - \frac{k}{a^2} \\ \dot{H} + H^2 = \left(\frac{\ddot{a}}{a}\right) &= \frac{-4\pi G}{3}\left(\rho + 3P\right) \end{aligned} \tag{1.6}$$

where H is called the Hubble parameter and G is Newton's gravitational constant. Here, ρ and P must be understood as the sum of all contributions to the energy density and pressure in the universe. We write $\rho_{\rm r}$, $\rho_{\rm m}$, ρ_Λ for the radiation, matter and vacuum energy density respectively.

In presence of a perfect fluid with equation of state $P = w \times \rho$, the equations have a simple solution. For a flat ($k = 0$) universe, the solution is:

$$a(t) = a_0 t^{\frac{2}{3(w+1)}} \tag{1.7}$$

- **Matter**: We classify as "matter" particles for which the pressure P is negligible with respect to the energy density ρ. This is the case for a "gas" of non-relativistic particles. Using Eq. 1.7, it is straightforward to see that,

$$\rho_{\rm m} \propto a^{-3} \tag{1.8}$$

- **Radiation**: We classify as "radiation" particles for which the pressure P is a third of the energy density: $P = \frac{1}{3}\rho$. This is the cas for a "gas" of relativistic particles. Eq. 1.7 shows that,

$$\rho_{\rm r} \propto a^{-4} \tag{1.9}$$

- **Vacuum energy**: We have seen that the cosmological constant characterizes the vacuum energy. The vacuum has the following stress energy tensor: $T_{\mu\nu} = \rho_{\rm vac}\, g_{\mu\nu}$. Using Eq. 1.5 we see that it has the same behaviour as a negative pressure fluid with $P_{\rm vac} = -\rho_{\rm vac}$. Eq. 1.7 shows that the vacuum energy density remains constant:

$$\rho_\Lambda \propto a^0 \equiv C^{\rm st} \tag{1.10}$$

Eq. 1.6 can now be recast in a more explicit form:

$$\frac{H^2}{H_0^2} = \Omega_r a^{-4} + \Omega_m a^{-3} + \Omega_k a^{-2} + \Omega_\Lambda \tag{1.11}$$

The Ω are the dimensionless density parameters defined by:

$$\Omega_i = \rho_{\rm i,0} \times \frac{8\pi G}{3H_0^2} = \frac{\rho_{\rm i,0}}{\rho_{\rm crit,0}} \qquad \text{and} \qquad \Omega_k = \frac{-k}{(a_0 H_0)^2} \tag{1.12}$$

In Eq. 1.11 above, we have used the normalisation $a_0 \equiv 1$. The subscript *0* indicates that the quantity is evaluated *today*.

- Thermodynamics:

  At early times, the universe behaves like a plasma. Therefore, we can use thermodynamics and statistical mechanics to track the evolution of particle densities as the universe expands and cools down. This is formalised by Boltzmann's equation,

  $$\frac{1}{a^3}\frac{d\left(na^3\right)}{dt} = C\left[n\right] \tag{1.13}$$

  which relates the rate of change in the abundance (density) of a species given the rates for producing and eliminating the species (merged in the creation/annihilation operator $C\left[n\right]$ above). In the absence of interactions ($C[n] = 0$), we see that the particle density falls as a^{-3}. This is merely a reflection of the expansion of the universe. The volume grows as a^3 but the number of particles is conserved: the particle density must decrease accordingly.

  At equilibrium, the density is given by:

  $$n = \frac{g}{2\pi}\int d^3p\ f(p) \quad \text{where} \quad f(p) = \frac{1}{e^{(E(p)-\mu)/T} \pm 1} \tag{1.14}$$

  where the $+$ (resp. $-$) sign is for fermions (resp. bosons), g is the number of degrees of freedom, T is the temperature, μ is the chemical potential and p is the particle's momentum.

We have now introduced the general framework of the Standard Cosmological model. We motivated the Cosmological principle and used it to simplify the equations of General Relativity. A single equation (Eq. 1.11) can then be used to describe the history of the whole universe while the evolution of a particular species can be tracked with Boltzmann's equation. We introduced four important ingredients: the matter content, the radiation content, curvature and a cosmological constant which can be determined by observational data.

The Planck collaboration [7] recently released some of the most stringent constraints to date: $\Omega_m = 0.308 \pm 0.012$, $|\Omega_K| < 0.005$, $\mathrm{H}_0 = (67.8 \pm 0.9)$ km s^{-1} Mpc^{-1} and $\Omega_\Lambda = 0.692 \pm 0.012$. As advertised above, this corresponds to a universe dominated by matter and dark energy.

1.1.2 Cosmological probes

This section is a brief review of some of the most important cosmological probes, which give precious information on the nature of the universe.

- The Cosmic Microwave Background (CMB):

  The CMB is one of the most powerful tools of observational cosmology. It is made of high energy photons, whose wavelength was stretched to the microwave range by the expansion of the universe. We believe these photons are robust evidence for the Big Bang model. At early times, the universe was hot and dense. As it grew in size, it started to cool until the so-called recombination era, when baryons and photons started to decouple and atoms started to form. At that time, the universe became transparent to the CMB radiation. The CMB photons therefore carry information from the time of last scattering (just before decoupling). The CMB spectrum is that of an almost perfect black body with a mean temperature of 2.725 K. However, small anisotropies of the order of 10^{-5} have been observed [8, 9]: the CMB temperature is not uniform in all directions. The CMB fluctuations can be understood in the framework highlighted in Sec. 1.1 by linearising the Einstein equations around small perturbations. More details on CMB physics can be found in [10]. The parameters of the Standard Cosmological Model can be fitted to the CMB data to high accuracy, providing strong constraints.

- Baryon Acoustic Oscillations (BAO):

  At early times, when the universe was a hot and dense plasma, baryons were heavily coupled to photons. The competing influence of gravity and radiation pressure generated waves in the plasma. At recombination, baryons and photons decouple. The pressure of photons on baryons disappears: photons freely stream away while the baryon oscillation is stalled. This imprints a density excess on the baryon distribution. The presence of additional matter, such as Cold Dark Matter acts as a gravitational wall: there is a tight interplay between the matter densities. This should be apparent when looking at observables like the 2-point correlation function as matter will tend to clump preferentially in the overdense region of the acoustic peak. BAO detection (see [11] for instance) therefore provides constraints on cosmological parameters. Fig. 1.3 below illustrates the evolution of a schematic density perturbation.

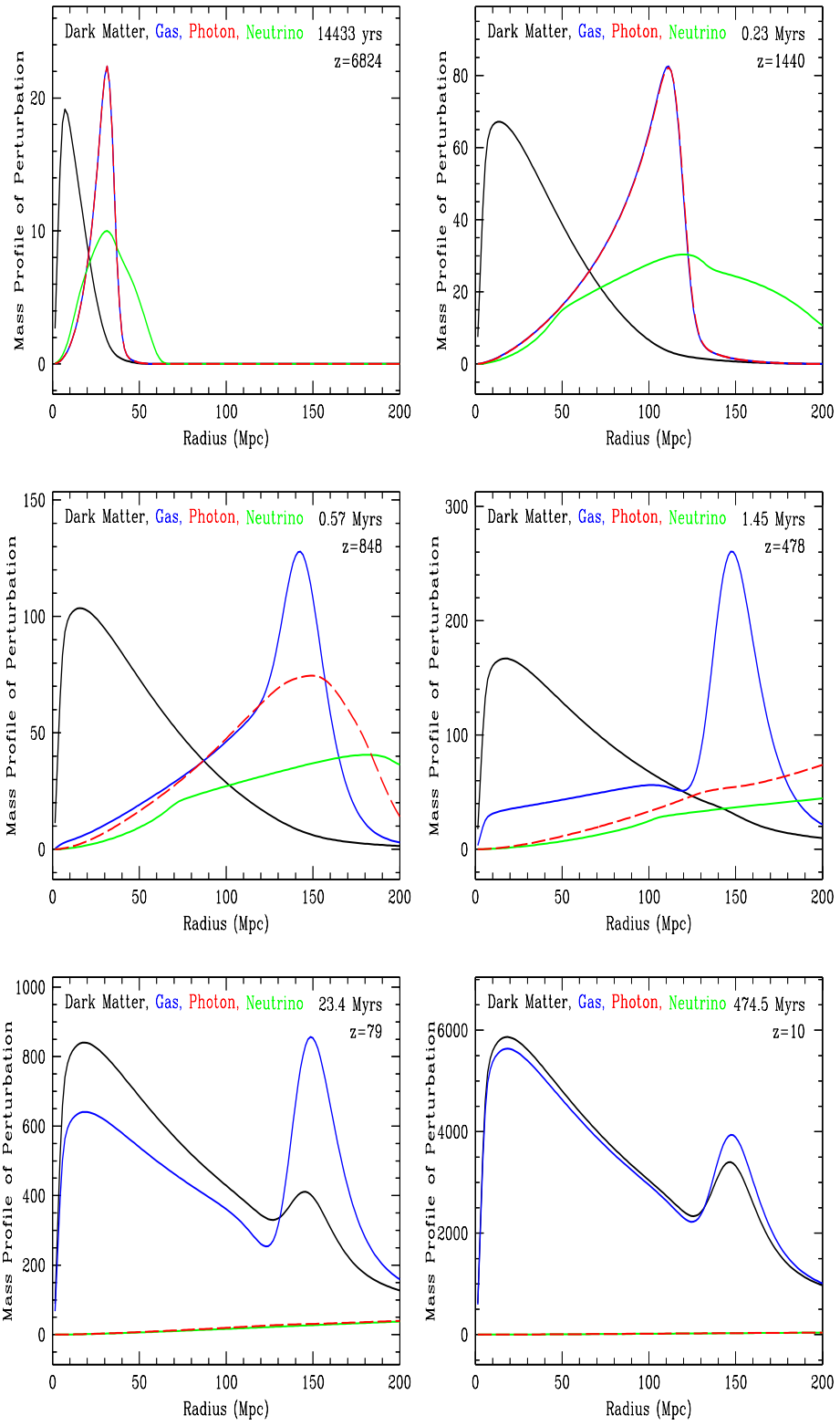

FIGURE 1.3 Schematic evolution of a density perturbation. At first, photon and baryons (gas) are tightly coupled. Since dark matter is only gravitationally coupled to baryons and photons, the dark matter perturbation lags behind (top right hand). At recombination, photons and baryons decouple, the baryon oscillation stalls while photons stream away (middle). At late time, the dark matter pulls baryons near the origin while the baryon oscillation continues to drag dark matter towards the 150 Mpc peak. Figure from [12]

- Supernovae (SNe):

  Supernovae Ia (SNe Ia) are believed to be the result of the explosion of carbon-oxygen white dwarfs. They are limited to a particular mass sometimes known as the Chandrasekhar mass (1.38 solar masses). Beyond this mass, white dwarfs can re-ignite and cause a supernova explosion. Because of this mechanism, the luminosity of SNe Ia is very uniform: they can be used as "standard candles". The observed flux can therefore allow us to infer distances reliably. The measured distances depend on the growth rate of the universe, which itself depends on cosmological parameters such as the matter and dark energy densities. This is how SNe Ia can be used to constrain the standard cosmological model. In practice, model testing is done by comparing the distance vs. redshift relation against predictions.

- Big Bang Nucleosythesis (BBN):

  BBN is a deep and reliable probe of the early universe, as it is based on well-known physics. It combines the Boltzmann equation we saw in Section 1.1.1 and nuclear physics in an exhaustive set of equations which describes, among other things, how light nuclei like He , Li or H could form. The abundances are fixed at $t \approx 180s$ when the universe has expanded and cooled down to a point where the species can no longer maintain thermal equilibrium. The Boltzmann equation then implies that the density dilutes as a^3 while the relative abundances are unchanged. This is the so-called "freeze-out". These abundances can be measured today, providing insight into the early history of the universe. Stellar nucleosynthesis, which occurs at later times, can pollute the primordial abundances through the production of heavier elements. This is why in practice, one looks for regions with low heavy element abundances. The light element abundances can be shown to depend on parameters of cosmological interest, especially the baryon to photon ratio. Using the CMB data (which allows us to measure the photon density precisely) it is therefore possible to access the baryon density Ω_b. This is of particular interest for the validation of the dark matter hypothesis: we have seen that the total matter density can be computed thanks to other cosmological observables. By comparing this density to the baryon density, it is possible to infer whether baryons are the sole matter constituent of the universe.

Using these probes, we are now going to focus our attention on the matter content of the universe, with one question in mind: can we account for all observations with known, baryonic matter alone?

1.1.3 The matter content: evidence for Cold Dark Matter

Cosmologists refer to known matter (nuclei and electrons) as baryons. In this section, we will see that there are a variety of observations which baryons alone cannot explain, making a compelling case for the existence of cold, non baryonic dark matter.

The first tentative evidence for dark matter came from Zwicky and Smith in the 1930's. They measured the velocities of galaxies in the Coma and Virgo clusters. They estimated the total mass needed to gravitationally bind the galaxies at the observed speed and found them to be two orders of magnitude above Hubble's estimation of the galaxy mass. This led Zwicky to postulate the existence of invisible matter that interacts gravitationally which he dubbed *Dunkle Materie* i.e. Dark Matter. The idea gained ground in the 1970's with the measurement of the *rotation curves* of galaxies (see Fig. 1.4).

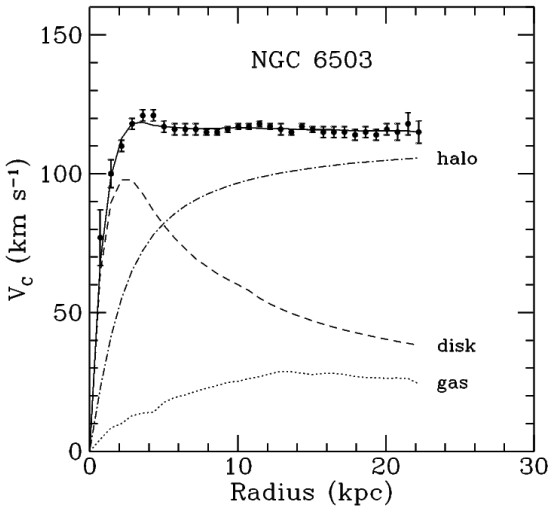

FIGURE 1.4 Rotation curve of NGC 6503. The dotted, dashed and dash-dotted lines are the contributions of gas, disk (stars) and dark matter, respectively. Figure from Ref. [13]

The contribution of stars and gas alone cannot explain the distinctive flat behaviour of the velocity distribution as the distance to the galactic center increases.

By the 1980's, most astronomers were convinced that this "missing mass anomaly" was not going away. So what was this new matter made of? A purely baryonic solution was ruled out because of improving upper limits on the CMB anisotropies (see [14] for instance). Neutrinos were then suggested as potential candidates. However, their mass is so low that they remain relativistic at the time of structure formation (which is why neutrino theories were called "Hot" Dark Matter theories). This has far-reaching consequences on the formation of galaxies: the fluctuations on small scales are damped by the neutrinos' relativistic motion. This predicts a galaxy distribution much more

inhomogeneous than observed [15]. In the face of these difficulties, Cold (non-relativistic) Dark Matter (CDM) gradually emerged as the preferred explanation. Indeed, it was found to be compatible with structure formation [16] and we will see that the probes highlighted in Sec. 1.1.2 provide further compelling evidence.

CDM can be naturally incorporated into the equations of Section 1.1.1. All that is needed is to separate matter into known, baryonic matter and dark matter, which interacts only gravitationally. In the following, we introduce the CDM density, Ω_c such that $\Omega_m = \Omega_b + \Omega_c$.

- The Cosmic Microwave Background (CMB):

  The CMB alone makes a very convincing case for the CDM hypothesis. As we remarked earlier, the scale (10^{-5}) of the temperature anisotropies is orders of magnitude below that predicted for a universe where all the matter is made of baryons. A careful study of the anisotropy power spectrum gives a much more precise understanding of the components of the universe. Fig. 1.5 below shows how the power spectrum changes with four cosmological parameters of interest. In particular, we remark that the relative amplitudes of the second and third peaks is heavily dependent on the baryon density. The Planck best fit [7] leaves little doubt on the existence of CDM. It finds $\Omega_b h^2 = 0.02227 \pm 0.00020$ and $\Omega_c h^2 = 0.1184 \pm 0.0012$ where h is defined such that $H_0 = h \times 100$ km s^{-1} Mpc^{-1}.

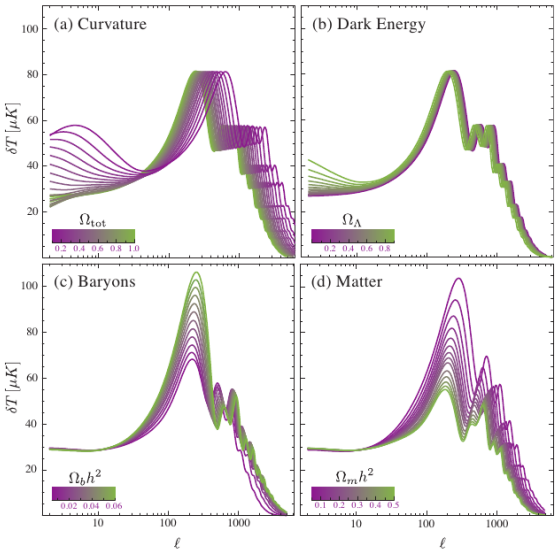

FIGURE 1.5 Temperature anisotropy power spectrum evolution as a function of the cosmological parameters. Top left: influence of curvature (or equivalently, the total density). Top right: influence of the Dark Energy density. Bottom left: influence of the baryon density. Bottom right: influence of the total matter density

- Big Bang Nucleosythesis (BBN):

  As we explained above, it is possible to infer the baryon to photon ratio (denoted by η) from the observed abundance of light elements. With the exception of ^{7}Li (which may be plagued by unknown systematics), the measures essentially converge to $\eta \approx 6 \times 10^{-10}$ which gives [17] $0.021 \leq \Omega_b \leq 0.025$ (95%CL). This is in remarkable agreement with the Planck value. Given that $\Omega_m \approx 0.3$, it provides further evidence for the existence of non baryonic matter.

- BAO and Supernovae:

  BAO and supernovae are observed independently from the CMB and provide sensitivity to parameters of interest such as Ω_m and Ω_Λ. It is therefore possible to combine the measurements to validate and improve the characterisation of the cosmological model. Fig. 1.6 below shows that the probes converge towards $\Omega_m \approx 0.3$ and $\Omega_\Lambda \approx 0.7$. When compared to the CMB and BBN's measure of the baryon density, this provides further evidence for a new type of non-baryonic matter.

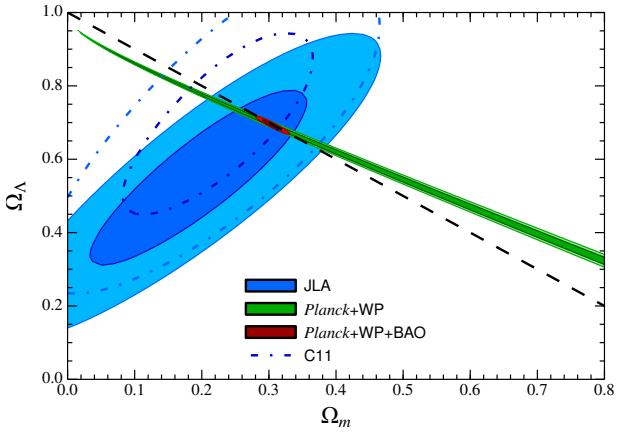

FIGURE 1.6 In blue (JLA), the 68% and 95% confidence contours for the parameters Ω_m and Ω_Λ of the standard cosmological models obtained by the joint SDSS-SNLS supernovae analysis. Also shown in green are the constraints from Planck and WMAP (Planck + WP) and BAO (baryon acoustic oscillations) (in red). The C11 dashed lines correspond to an independent analysis of SNe Ia by Conley *et al.*. The dashed black line corresponds to a flat universe. We see how various cosmological probes can be combined to improve constraints. Figure from [18]

We have seen how a wide range of observations and theoretical motivations pointed to the existence of a new, non-baryonic cold dark matter. The nature of the particle remains unkown. We will now review some of the most popular candidates, postulated by theories Beyond the Standard Model (BSM).

1.1.4 Dark matter candidates

A Dark Matter candidate must typically satisfy four requirements:

- Stable:
  The Dark Matter particle must be stable on the universe's life scale. Otherwise it would have decayed, and we would not see its gravitational effects today.

- Non relativistic:
  The Dark Matter particle must be sufficiently "cold" at the time of structure formation otherwise the initial density perturbations are washed out by relativistic effects, leading to predictions incompatible with observations such as [5]. We can actually derive a lower bound on the dark matter mass by studying small scale structures: the distance that a thermally produced particle streams out of a density perturbation is correlated to its mass. Consequently, the study of the smallest scale at which a clumpy structure can be found provides a lower limit on the dark matter mass. The study of the Ly-α, a probe for small scale structures at $z \approx 3$ gives $m_{\mathrm{DM}} \gtrsim 2$ keV [19]. Dark matter with a mass in the keV range is called Warm Dark Matter (WDM) and leads to the suppression of structure formation at small scales. Some observations actually support the WDM hypothesis [20]: N-body simulations with CDM predict cuspy halos for galaxies and clusters with excessive substructure, in apparent contradiction with observations which find smooth halos with central density cores. This issue is resolved by replacing CDM with WDM. Another issue is that the predicted number of low-mass halos under CDM is much larger than the observed abundance of satellite galaxies in the Local Group [21]. Once again, this can be resolved with a mechanism that suppresses small scale structure formation. This is why we will take some time to discuss the sterile neutrino, an interesting WDM candidate.

- Invisible:
  The Dark Matter particle must be charge neutral. Otherwise it would couple to the photon baryon fluid, leaving an imprint on the CMB..

- Relic density:
  The Dark Matter particle must account for the observed matter density ($\Omega_c h^2 = 0.1184 \pm 0.0012$ and $\Omega_m = 0.308 \pm 0.012$).

With these requirements in mind, we now turn to potential candidates. We will dedicate more space to a specific class of candidates, known as WIMPs (for Weakly Interacting Massive Particles) as they are the main focus of the EDELWEISS experiment.

- MACHO's:
  MACHO stands for MAssive Compact Halo Object. Typically, they are astronomical objects (Black Holes, Brown stars) too dark to be seen. Experiments looking for MACHOs are based on the microlensing effect: when looking at a star, it may happen that a MACHO comes close enough to act as a gravitational lens, which affects the star's luminosity. However, searches for MACHOs [22] and BBN constraints (MACHOs are baryonic objects) have essentially ruled them out as the principal component of dark matter.

- Neutrinos:
  We have already ruled out neutrinos as CDM candidates because of the consequences it would have on structure formation. However there are speculations about a fourth species of neutrino, dubbed the sterile neutrino because it is not charged under the weak interaction. The motivations for introducing a sterile neutrino are two-fold. A favourite explanation of the neutrino mass is the so-called seesaw mechanism which introduces new fermions. In the seesaw mechanism, the mass of this/these new sterile neutrino(s) can be in any range. The other motivation is cosmological: provided that the sterile neutrino has a mass in the keV range, it is a prime candidate for warm dark matter [23]. Since sterile neutrinos are predicted to decay into a neutrino and a photon [24], it should leave a line at an energy half its mass in the X-ray spectrum. Bulbul *et al.* [25] and Boyarsky *et al.* [26] have independently reported an excess a 3.5 keV in the X-ray spectrum of galaxy clusters. However, it is prematurate to give a dark matter interpretation of this signal, because of persistent systematics.

- Axions:
  Axions' properties and motivations will be detailed in another section as they are subject to an independent study in Chap. 3. Here, we restrict the discussion to the case axions can make as a dark matter candidate.

  Axions are generally predicted to have a very small mass:

$$m_a \approx 10^{-6}\,\mathrm{eV}\left(\frac{10^{12}\,\mathrm{GeV}}{f_A}\right) \tag{1.15}$$

  where f_A is the axion decay constant. In spite of this small mass, axions can be Cold Dark Matter because they can be created non thermally. There are two mechanisms by which cold axions may be produced [27]: string/domain wall decay and vacuum realignment. The first one may not contribute at all depending on the interplay of inflation parameters and axion symmetry breaking. Vacuum realignment exists independently from inflation. The general idea is the following: QCD effects cause the axion to oscillate in a temperature dependent potential.

These oscillations do not decay: they contribute to the energy density of the universe. The predicted energy density Ω_a is:

$$\Omega_a \approx \left(\frac{f_A}{10^{12}\ \text{GeV}}\right)^{7/6} \theta_1^2 \tag{1.16}$$

where θ_1 denotes the initial position of the axion field in the QCD potential.

We see that, tuning the axion decay constant f_A or the realignment angle, axions can contribute to the Cold Dark Matter density. Naturalness requirements (Θ is an angle, we expect $\theta \approx \mathcal{O}(1)$) imply that if the QCD axion is dark matter, it must have a decay constant in the 10^{10} GeV - 10^{12} GeV range (or equivalently a mass in the 10^{-6} eV - 10^{-3} eV range).

- WIMPs:
  Weakly Interacting Massive Particles or WIMPs are the most popular Dark Matter candidates. Their mass is usually expected in the GeV - TeV region. Their cross section is dominated by weak processes. Using the Boltzmann equation from Section 1.1.1 we will see why WIMPs have become the most interesting Dark Matter candidates. In the following, WIMPs will be identified by the Greek letter χ, with mass M_χ and density Ω_χ.

  Let us assume that WIMPs annihilate into two massless particles:

$$\chi + \chi \leftrightarrow l + \bar{l} \tag{1.17}$$

  The Boltzmann equation then reads:

$$\frac{1}{a^3}\frac{d\left(n_\chi a^3\right)}{dt} = \langle\sigma v\rangle \left[(n_\chi)^2_{\text{eq}} - n_\chi^2\right] \tag{1.18}$$

  Equation 1.18 can be recast to:

$$\frac{dY}{dx} = -\frac{\lambda}{x^2}\left[Y^2 - Y^2_{\text{eq}}\right] \tag{1.19}$$

  where $Y \equiv \frac{n_\chi}{T^3}$, $x \equiv \frac{M_\chi}{T}$, $\lambda \equiv \frac{M_\chi^3\langle\sigma v\rangle}{H_1}$, $Y = Y_{\text{eq}}$ when WIMPs are in thermal equilibrium and we assumed that Dark Matter production occurred at early times, when radiation dominates and the energy density scales as T^4 so $H = H_1/x^2$ where H_1 is the value of H when $x = 1$.

Equation 1.19 cannot be solved analytically but we can get a good idea of its shape with physics insight. At early times, when the temperature is high and the WIMP interaction rate is greater than the Hubble parameter, WIMPs are at equilibrium. When the temperature decreases ($x \gg 1$) the WIMP density becomes exponentially suppressed: $Y_{\text{eq}} \propto e^{-x}$. Ultimately, the WIMP particles become so rare that they cannot interact enough to maintain the equilibrium density. We say the density "freezes out" and decays as $1/a(t)^3$ because of the expansion of the universe. Without this "freeze out" the WIMPs would have disappeared completely. Well after the freeze out, the equilibrium density has dropped exponentially so Equation 1.19 can be simplified so that we find $Y_\infty = \frac{x_F}{\lambda}$ where Y_∞ is the relic density at late times and $x = x_F$ at freeze out. Fig. 1.7 below shows the numerical solution of Equation 1.19 for various values of λ.

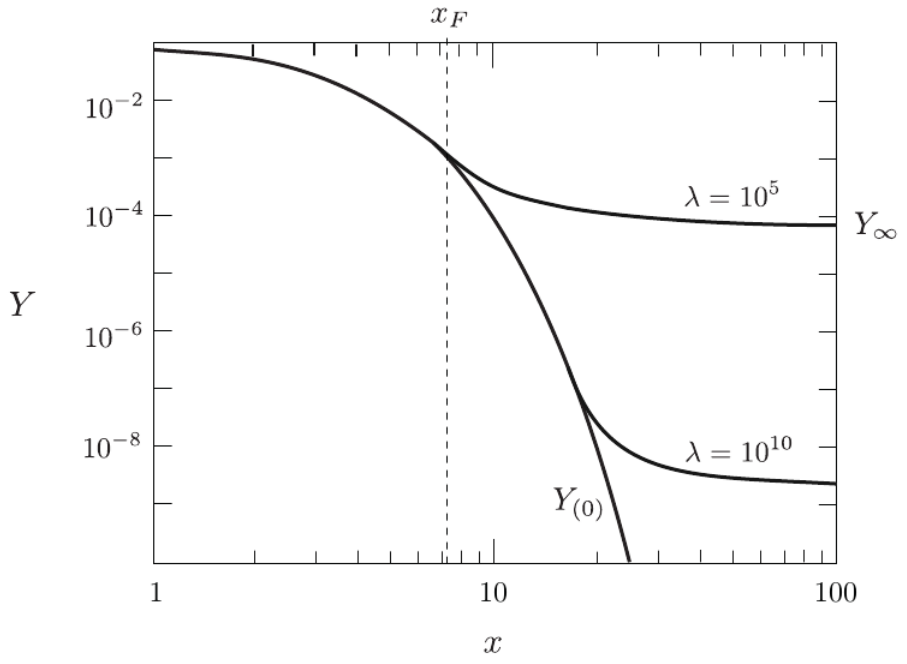

FIGURE 1.7 Abundance of the dark matter particle. There is a distinct change of regime at freeze out.

It is then possible to estimate the contribution of WIMPs to the current energy budget of the universe.

$$\Omega_\chi h^2 = 0.11 \frac{3 \times 10^{-26}\,\text{cm}^3\,\text{s}^{-1}}{\langle \sigma v \rangle} \tag{1.20}$$

where h is the Hubble constant in units of 100 km s^{-1} Mpc^{-1}.

As we saw in Section 1.1.3, Planck constrains the cold dark matter density to $\Omega_c h^2 = 0.1184 \pm 0.0012$. It follows that the expected velocity-weighted annihilation cross-section is in the range of $3 \times 10^{-26}\,\mathrm{cm}^3\,\mathrm{s}^{-1}$. This natural scale for the WIMP annihilation cross-section is often used as a benchmark by Dark Matter detection experiments. Beyond Standard Model theories predict the existence of new particles with weak scale interactions. It so happens that these particles have a typical annilihation cross section $\langle \sigma v \rangle \sim \alpha^2 (100\,\mathrm{GeV})^{-2} \sim 10^{-25}\,\mathrm{cm}^3\,\mathrm{s}^{-1}$ which is remarkably close to that required to account for dark matter. This striking coincidence is often called the WIMP miracle.

Before concluding this section, let us give a few details on one of the most popular BSM theory: Supersymmetry (SUSY).
SUSY is motivated by several observations: the Standard Model makes a distinction between fermions (constituents of matter) and boson (mediators of interactions) so it is natural to ask if there exists a symmetry which unifies the two at a more fundamental level. Further motivation is provided by the hierarchy problem, which seels to answer the enormous difference between the electroweak and Planck scales (or equivalently, between the Higgs mass and the Planck mass). SUSY provides an elegant solution as it introduces new particles (the so-called "superpartners" of known particles) which naturally cancel loop corrections to the Higgs mass and prevent it from diverging.

SUSY is particularly relevant for Dark matter searches because it necessarily introduces a new symmetry (see [28] for more details) which implies the existence of a new stable particle, dubbed the lightest supersymmetric partner. In most SUSY models, this particle is not charged. These two characteristics (stability and charge neutrality) make it a prime candidate for Dark Matter. SUSY predicts various particles with such properties, like the gravitino or the neutralino. The gravitino is the superpartner of the graviton. Since only interacts gravitationnally, it is out of reach of direct detection experiments. This is why most searches are focused on the lightest neutralino which is a superposition of higgsinos, winos and binos (respectively the superpartners of the Higgs boson, the W bosons and the $\mathcal{U}(1)$ gauge field.

1.2 Detection of WIMP Dark Matter

The diagram below (Fig. 1.8) highlights the possible observation windows into dark matter. Colliders try to go back in time when Dark Matter was produced: they look at the scattering products of SM particles, which could include WIMPs. Indirect detection works under the assumption that WIMPs are their own anti-particle. Provided that the WIMP density is high enough, they will annihilate into Standard Model particles, giving rise to a potentially measurable signal. Possible scenarios include the decay into quarks, leptons or gauge bosons, which will in turn decay into observable particles such as protons, photons or neutrinos. Direct detection, which will be the primary focus of this work, relies on Dark Matter scattering with SM model particles, typically nucleons.

This section, will be dedicated to each of these three detection channels, with particular emphasis on direct detection since it is the purpose of the EDELWEISS experiment.

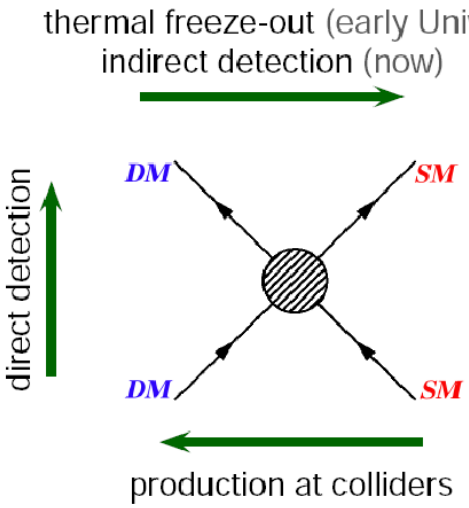

FIGURE 1.8 Basic scheme for dark matter detection. Direct detection looks at the scattering of WIMPs off a target nuclei. Collider experiments seek to produce dark matter by smashing together Standard Model particles while indirect detection looks at possible decay products of WIMPs.

1.2.1 Production at colliders

If colliders reach sufficient energy, Dark Matter can be produced in a reaction of the type:

$$SM + SM \rightarrow DM + DM \tag{1.21}$$

Since WIMPs are very weakly interacting, they do not deposit energy in the detector (in that sense, they are similar to neutrinos). The basic idea to identify Dark Matter is therefore the following: compute the total energy/momentum budget associated to a collision and identify any hint of missing energy. Collider searches have one obvious advantage over direct and indirect detection: they are not subject to astrophysical uncertainties. However, because the eventual new particle spends very little time in the detector, its stability cannot be tested: it is impossible to prove that the detected candidate is the dark matter particle.

There are different ways to look for dark matter at the LHC. One may assume a full theory (like pMSSC or cMSSS) that provides a dark matter candidate which we then seek to constrain [29]. However, we chose to restrict the discussion to so-called model-independent searches for Dark Matter at the LHC: the idea is to use an Effective Field Theory (EFT) to express new physics. This allows easier comparison to direct detection experiments. Even though this approach does not depend on the choice of a BSM scenario, there are important assumptions [30]: WIMPs must be pair-produced at the LHC and possible new particles mediating the interaction between WIMPs and the SM must be too heavy to be produced directly. This justifies that they can be integrated out in an effective field theory approach. Table 1.1 below shows some possible effective interactions:

Name	Initial state	Type	Operator
D1	qq	scalar	$\frac{m_q}{M_\star^3}\bar{\chi}\chi\bar{q}q$
D5	qq	vector	$\frac{1}{M_\star^2}\bar{\chi}\gamma^\mu\chi\bar{q}\gamma_\mu q$
D8	qq	axial-vector	$\frac{1}{M_\star^2}\bar{\chi}\gamma^\mu\gamma^5\chi\bar{q}\gamma_\mu\gamma^5 q$
D9	qq	tensor	$\frac{1}{M_\star^2}\bar{\chi}\sigma^{\mu\nu}\chi\bar{q}\sigma_{\mu\nu}q$
D11	gg	scalar	$\frac{1}{4M_\star^3}\bar{\chi}\chi\alpha_s(G^a_{\mu\nu})^2$

TABLE 1.1 Effective interactions coupling fermionic WIMPs to Standard Model quarks or gluons. $M_\star$ is the suppression scale of the mediator particles which were integrated out. $G_{\mu\nu}$ is the colour field-strength tensor and α_s is the strong coupling constant. Table from [30].

Pair production of WIMPs alone is invisible at the LHC because, as we remarked earlier, the detectors are not sensitive to dark matter. So the simplest search consists in looking for pair production of WIMPs + initial or final radiation (see Fig. 1.9). The event topology of such a reaction is called *monojet* or *monophoton*. They exhibit a single, well-reconstructed jet with high transverse momentum and a large transverse missing energy. Unfortunately, the Standard Model predicts some important backgrounds. The main contribution comes from the production of a Z boson, together with a jet. The Z boson can decay into neutrinos which are undetected (see Fig. 1.10 for the complete list of background events included in the analysis of [30]).

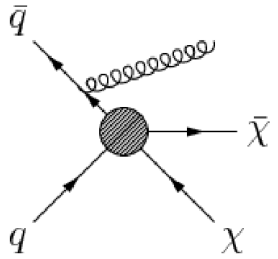

FIGURE 1.9 Example of a monojet search, with pair production of WIMPs and initial state radiation.

No excess of events above background was seen in recent monojet searches at the LHC, so upper limits on the suppression scale $M_\star$ of the effective field theory were set. This limit can be converted to a limit on the WIMP-nucleon scattering cross section [31] in order to allow comparison with direct detection experiments. Fig. 1.11 shows recent results from the ATLAS collaboration. Of course, the eventual limit depends on the choice of the EFT. Scalar coupling to gluons provides very strong limits, while scalar coupling to quarks yields a limit hardly competitive with direct detection constraints.

The constraints are particularly relevant in the low mass region ($\lesssim 10$ GeV) where the sensitivity does not depend on the dark matter mass. This is in contrast with direct detection experiments (more details in Section 1.2.3) which suffer from a kinematic suppression. The sensitivity becomes weaker at higher masses ($\gtrsim 200$ GeV) because of the necessary increase in collision energy. Also, at high masses, the effective field theory approach breaks down because the WIMP mass approaches the suppression scale $M_\star$. What happens beyond the validity region of the EFT depends on the details of the BSM theory.

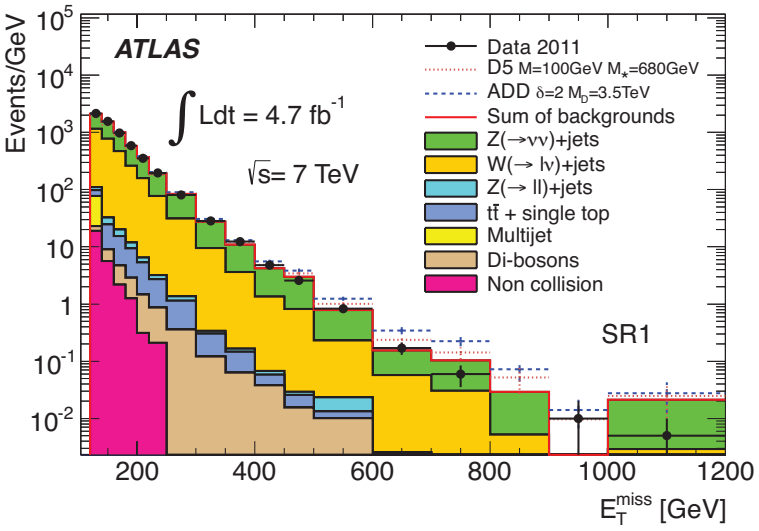

FIGURE 1.10 ATLAS monojet data for Dark Matter searches. The filled color histograms correspond to various background contributions. The dashed red line correspond to the WIMP signal with a cross section equal to the excluded value, assuming vector interactions. The blue line corresponds to a possible Large Extra Dimension (LED) signal, with a cross section equal to the excluded value. No excess above predictions is seen from the data. Figure from [30].

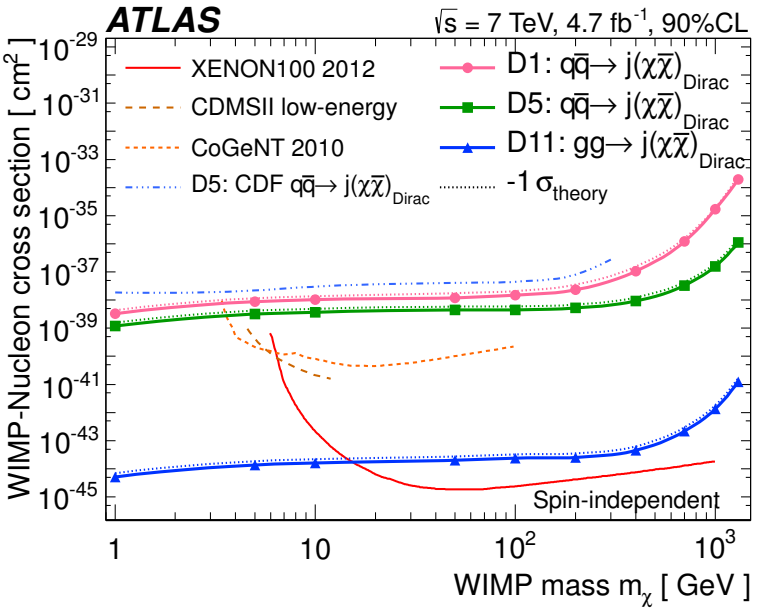

FIGURE 1.11 ATLAS limit on the spin-independent cross section corresponding to different EFT. The limits are compared to direct detection limits (see Section 1.2.3 for more information). The observable recoil energy in the LHC experiment does not depend on the Dark Matter mass for masses below 100 GeV. This is why the limits is flat up to 100 (which can be a Z, a W, a hadronic jet or a γ)GeV. Figure from [30].

1.2.2 Indirect detection

Indirect WIMP searches rely on the detection of the products of WIMP annihilation in astrophysical objects. The flux of WIMP annihilation products is of course proportional to the annihilation rate which is in turn proportional to the square of the WIMP density. That is why it is preferable to look for WIMP annihilation signals in regions of suspected high Dark Matter density, like the galactic center. Other astrophysical objects like the Sun or the Earth can in principle trap Dark Matter: they can turn into sources of DM annihilation products. In this section, we will briefly review the most promising fields of research.

WIMP annihilation in the Sun:

WIMPs can be slowed down and eventually captured in massive objects like the sun where they may eventually annihilate. This process is governed by the following equation:

$$\frac{dN_\chi}{dt} = C_c - C_a N_\chi^2 \tag{1.22}$$

where N_χ is the WIMP density, C_c and $C_a N_\chi^2$ are the WIMP capture and annihilation rate in the sun, respectively. We also neglected the evaporation rate. Then, assuming that the characteristic time of the annihilation/capture process is small compared to the age of the Sun, the WIMP density in the Sun is at equilibrium $\left(\frac{dN_\chi}{dt} = 0\right)$ and we find:

$$\Gamma_a \equiv \frac{1}{2} C_a N_\chi^2 = \frac{1}{2} C_c \tag{1.23}$$

WIMP annihilation products include neutrinos, which may escape from the Sun and reach the Earth where they can be detected by neutrino detectors like IceCube [32] or SuperKamiokande [33]. These detectors can then look for an excess over anticipated background to constrain the WIMP annihilation rate. Through Eq. 1.23, this constraint can be translated to a constraint on the capture rate, which only depends on the scattering cross-section of WIMPs with the relevant nuclei in the sun. This allows an immediate comparison with direct detection experiments (see Fig. 1.12). The abundance of light nuclei in the sun like Hydrogen and Helium allows neutrino observatories to be particularly competitive in the Spin-dependent channel (see Section 1.2.3 for more details).

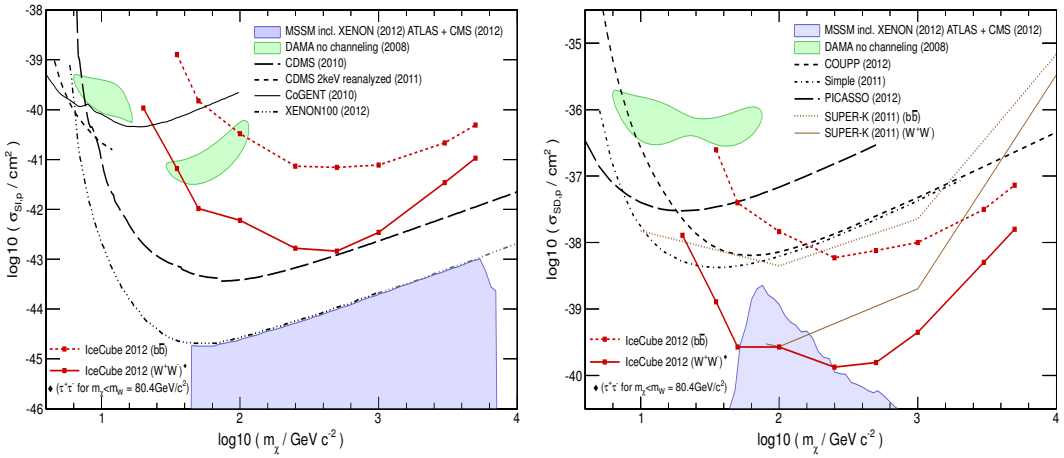

FIGURE 1.12 Left: limits on spin-independent WIMP cross section. Right: limits on spin-dependent WIMP cross section. Icecube results are compared to SuperKamiokande results and direct detection experiments. It provides the most stringent bounds to date in the spin-dependent channel. Figures from [32].

WIMP annihilation in the Galactic Center and Dwarf Galaxies

The Galactic Center (GC) is a prime target for gamma ray searches: it is close to us and is predicted to exhibit large Dark Matter density. Likewise, Dwarf Galaxies are interesting candidates because the gamma signal from standard sources is very much suppressed (undetected as of now). As a result, astrophysical foregrounds which can produce gamma rays are less of an issue. Additionally, the kinematic study of Dwarf Galaxies shows that they exhibit a significant Dark Matter density.

WIMP annihilation can produce gamma rays in two major ways:

1) A continuous spectrum from annihilation into SM particles which eventually produce gamma ray through pion production, Bremsstrahlung or inverse Compton scattering.

2) Mono energetic γ lines through the $\chi\chi \to \gamma X$ channel, where X is another neutral state, like a γ or a Z boson. The latter provides a "smoking gun" signal for WIMP annihilation (a line signal, which should be seen in several locations in the sky is difficult to replicate with astrophysical sources). Unfortunately, it is suppressed by a factor of α^2 with respect to other processes, where α is the electroweak constant, because WIMPs do not couple to photons at tree level.

The expected photon flux from Dark Matter annihilation (obtained for a solid angle $\Delta\Omega$ around the coordinates (ϕ,θ) in the sky) is then given by :

$$\frac{d\Phi_\gamma(E_\gamma, \Delta\Omega(\phi,\theta))}{dE_\gamma} = \frac{1}{4\pi}\frac{\langle\sigma v\rangle}{2m_\chi^2}\sum_f \frac{dN_\gamma^f}{dE_\gamma}B_f \times \int_{\Delta\Omega} d\Omega' \int_{l.o.s.} \rho^2(r(s))\, ds. \qquad (1.24)$$

The first part of the equation plugs in the particle physics information: the WIMP annihilation cross section $\langle \sigma v \rangle$, the primary particles in which WIMPs decay f, with a branching ratio B_f and the corresponding γ spectra $\frac{dN}{dE_\gamma}$. Physicists typically report constraints on $\langle \sigma v \rangle$ as a function of the WIMP mass. This value can then be compared to the "natural" value of Eq. 1.20 needed to account for the correct relic density. The second part describes the distribution of WIMPs in space. It also points to one of the major difficulties of WIMP-induced gamma ray searches: astrophysical uncertainties. Since we want to constrain the particle physics part of the equation (the annihilation cross section), we are forced to make hypotheses on the density profile of dark matter which remains poorly known [34].

Dark Matter signals from the GC and Dwarf Galaxies were recently searched by the FERMI-LAT [35] and H.E.S.S [36] collaborations. FERMI is particularly relevant for low mass WIMPs: owing to a low ($\mathcal{O}(100)$ MeV) energy threshold, it can probe WIMP masses down to a few GeV, depending on the annihilation channel.

Indirect searches remain very challenging as evidenced by conflicting interpretations of the available data: a tentative spectral feature has been found near the GC at ~ 130 GeV using FERMI data [37]. However, the significance of this line has decreased after an updated analaysis [38]. Other analyses [39] favour WIMP masses in the $10 - 50$ GeV interval but urge caution because of background uncertainties.

On the other hand, the FERMI and HESS collaborations found no evidence for a gamma ray excess. Fig. 1.13 shows the upper limits on $\langle \sigma v \rangle$ which the HESS collaboration obtained by pointing at the Galactic Center and several Dwarf Galaxies. FERMI's combined analysis of 15 Dwarf Galaxies (see Fig. 1.14) allowed them to place stringent constraints [35] on thermally produced low mass WIMPs. Depending on the assumed annihilation channel, their analysis can exclude the thermal relic cross section for WIMP masses as high as 100 GeV and begins to constrain the parameter space favoured by a WIMP interpretation of a gamma ray excess at the GC: the exclusion of thermal low mass WIMPs is getting more robust. However, there are significant uncertainties in the detector's response, the expected background and the WIMP density, which respectively lead to shifts of $\pm 9\%, \pm 8\%, \pm 33\%$ in the limit. Nonetheless, this limit remains very relevant to the searches carried out by direct detection experiments as it challenges the recent observation of would-be low mass WIMP signals (see Section 1.2.3 for more details).

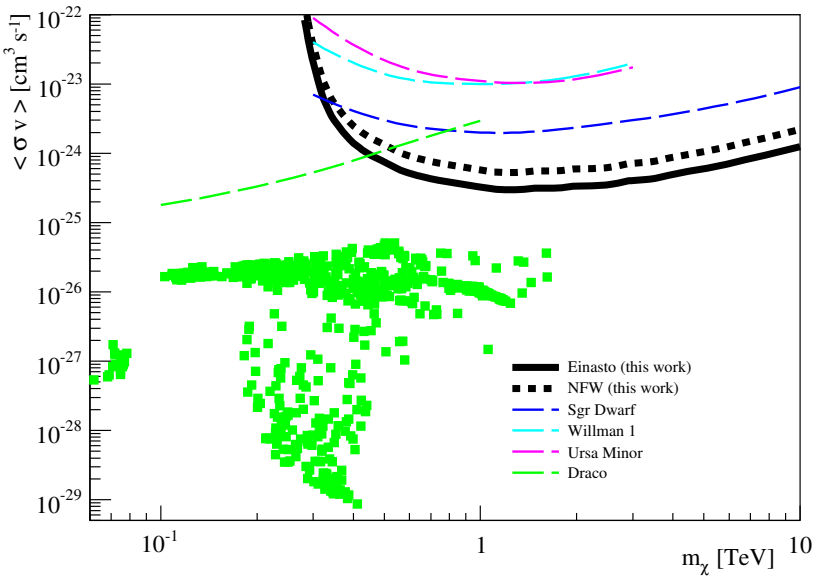

FIGURE 1.13 Upper limit (95% CL) on the WIMP annihilation cross section by the HESS collaboration assuming a 100% branching ration to $b\bar{b}$. Einasto and NFW refer to the WIMP density profiles chosen by the collaboration. Green dots indicate predictions of SUSY models. The black lines show the limits obtained by looking at the Galactic center while the colored lines are limits from Dwarf Galaxies. The Draco line was obtained by the Fermi collaboration Figure from [36].

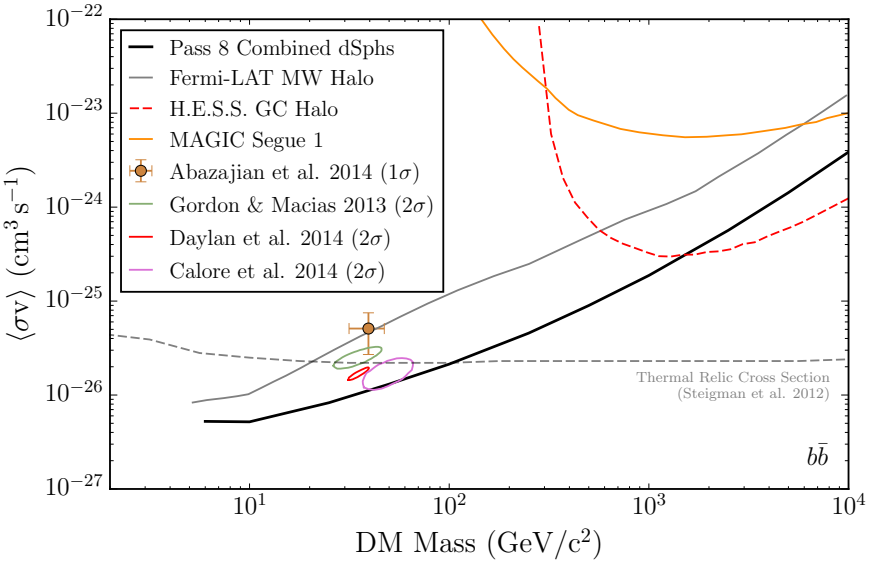

FIGURE 1.14 Upper limit (95% CL) on the WIMP annihilation cross section by the FERMI collaboration, assuming WIMPs decay to a $b\bar{b}$ pair. Closed contours correspond to the regions favoured by the WIMP interpretation of excess observed in the Galactic center. The constraints from the HESS [36] and MAGIC [40] experiments are also shown for comparison. Figure from [35].

1.2.3 Direct Detection

We will now review the motivation and principles of WIMP direct detection in detail. This will help us understand the EDELWEISS experiment, which is based on the direct detection of WIMP scattering over Germanium nuclei. In our derivation, we will closely follow the outline of [41]. We will also use [42] and [43] for the detailed computation of the rate.

Direct detection: elastic scattering off target nuclei

The Milky Way, along with other galaxies, is known to be trapped in a massive Dark Matter halo. If this halo is made of WIMPs, then the expected WIMP flux on earth is $\Phi \approx 10^5 \left(\frac{100\,\mathrm{GeV}}{M_\chi}\right)\ \mathrm{cm}^{-2}\ \mathrm{s}^{-1}$. This flux is sufficiently large that, even though the WIMPs interact only weakly, detection can be envisaged. The mean velocity of WIMPs with respect to the galactic center is expected to be similar to that of stars i.e. a few hundreds of kilometers per second. At these velocities, WIMPs scatter elastically off a given target nuclei. This provides us with the basic idea for Dark Matter direct detection in the laboratory: looking for nuclear recoils in a target detector. We are now going to compute the theoretical event rate, which provides insight for the design of the experiment.

Computation of the event rate

If we assume a local WIMP density ρ_0 and that WIMPs all have velocity $\langle v \rangle$ then the count rate per unit mass in the detector target is given by:

$$R = \sigma_{\chi-N} \langle v \rangle \times \left(\frac{\rho_0}{M_\chi}\right) \times \frac{1}{M_N} \tag{1.25}$$

where $\sigma_{\chi-N}$ is the WIMP-nucleus cross section, M_χ is the WIMP mass and M_N is the target nucleus mass. We need to correct this expression to account for the WIMP velocity dispersion and the energy dependency of the elastic scattering cross section. The following derivations draw heavily from [43].

The elastic scattering occurs in the non-relativistic limit since WIMPs have an average velocity $\langle v \rangle \sim \mathcal{O}(100)$ km/s. It is easy to compute the recoil energy E_R:

$$E_R = \frac{2\mu_N^2 v^2 \cos^2\theta}{M_N} \tag{1.26}$$

v is the WIMP speed relative to the nucleus, μ_N is the reduced mass: $\mu_N = \frac{M_N M_\chi}{M_N + M_\chi}$ and θ is the scattering angle given by:

$$\mathbf{v}_\chi \cdot \mathbf{v_R} = |\mathbf{v}_\chi| \cdot |\mathbf{v_R}| \cdot \cos\theta \tag{1.27}$$

where $\mathbf{v}_\chi$ gives the WIMP initial direction and $\mathbf{v_R}$ gives the outgoing nuclear recoil direction.

Equation 1.26 allows us to define v_{min}: it is the minimum WIMP speed which can cause a recoil of energy E_R: $v_{\min} = \sqrt{(M_N E_R)/(2\mu_N^2)}$

The event rate is then given by:

$$\mathcal{R} \equiv \frac{\mathrm{d}R}{\mathrm{d}E_\mathrm{R}} = \frac{\sigma(q)}{2M_\chi \mu^2}\,\rho_0\,\eta(E_\mathrm{R}, t) \qquad \text{in c/kg.d.keV} \tag{1.28}$$

where $q = \sqrt{2M_N E}$ is the nucleus recoil momentum, $\sigma(q)$ is the WIMP-nucleus cross section and $\eta(E,t)$, is defined by

$$\eta(E,t) = \int_{u>v_{\min}} \frac{f(\mathbf{u},t)}{u}\,\mathrm{d}^3 u\,. \tag{1.29}$$

where $f(\mathbf{u},t)$ is the observed WIMP velocity distribution, which accounts for the movement of the observer with respect to the WIMP rest frame.

In general, we assume that WIMPs are isotropically distributed in an isothermal sphere with density profile $\rho(r) \propto \frac{1}{r^2}$. Since WIMPs are essentially collisionless, their velocities follow a Boltzmann-Maxwell distribution with dispersion σ_v. This is the Standard Halo Model (SHM):

$$\widetilde{f}(\mathbf{v}) = \begin{cases} \frac{1}{N_\mathrm{esc}} \left(\frac{3}{2\pi\sigma_v^2}\right)^{3/2} e^{-3\mathbf{v}^2/2\sigma_v^2}, & \text{for } |\mathbf{v}| < v_\mathrm{esc} \\ 0, & \text{otherwise.} \end{cases} \tag{1.30}$$

Here

$$N_\mathrm{esc} = \mathrm{erf}(z) - 2z\exp(-z^2)/\pi^{1/2}, \tag{1.31}$$

$\overline{v}_0$ is the local circular speed, v_esc is the escape velocity and $z \equiv v_\mathrm{esc}/\overline{v}_0$ is a normalization factor. σ_v is related to $\overline{v}_0$ through:

$$\sigma_v = \sqrt{3/2}\,\overline{v}_0, \tag{1.32}$$

As we remarked earlier, we need to account for the movement of the observer with respect to the WIMP rest frame, characterised by the velocity $\mathbf{v}_\mathrm{obs}$. The equality below

immediately follows:

$$f(\mathbf{u}) = \widetilde{f}(\mathbf{v}_{\rm obs} + \mathbf{u})\,, \tag{1.33}$$

where $\mathbf{v}_{\rm obs}$ is given by:

$$\mathbf{v}_{\rm obs}(t) = \mathbf{v} + \mathbf{v}_{\rm earth} \tag{1.34}$$

where we used the notation $\mathbf{v}_{\rm earth}$ for the earth's velocity with respect to the galactic rest frame and the notation $\mathbf{v}$ for the velocity of the galactic rest frame with respect to the WIMP rest frame. In the following, we will ignore the time dependence of $\mathbf{v}_{\rm obs}$.

For such a velocity distribution, we can compute:

$$\eta(E,t) = \begin{cases} \frac{1}{\overline{v}_0 y}\,, & \text{for } z<y,\ x<|y-z| \\ \frac{1}{2N_{\rm esc}\overline{v}_0 y}\left[\mathrm{erf}(x+y) - \mathrm{erf}(x-y) - \frac{4}{\sqrt{\pi}} y e^{-z^2}\right], & \text{for } z>y,\ x<|y-z| \\ \frac{1}{2N_{\rm esc}\overline{v}_0 y}\left[\mathrm{erf}(z) - \mathrm{erf}(x-y) - \frac{2}{\sqrt{\pi}}(y+z-x) e^{-z^2}\right], & \text{for } |y-z|<x<y+z \\ 0\,, & \text{for } y+z<x \end{cases} \tag{1.35}$$

where

$$x \equiv v_{\rm min}/\overline{v}_0 \quad \text{and} \quad y \equiv v_{\rm obs}/\overline{v}_0, \quad \text{and} \quad z \equiv v_{\rm esc}/\overline{v}_0 \tag{1.36}$$

We are now interested in the cross section. As we saw in Section 1.2.1, it is possible to write an effective Lagrangian, which governs the interaction of WIMPs and quarks. A general Lagrangian can be written as:

$$\mathcal{L} = \left[\alpha_q^A (\bar{\chi}\gamma^\mu\gamma_5\chi)(\bar{q}\gamma_\mu\gamma_5 q)\right] + \left[\alpha_q^S \bar{\chi}\chi\bar{q}q + \alpha_q^V \bar{\chi}\gamma_\mu\chi\bar{q}\gamma^\mu q\right] \tag{1.37}$$

We have separated the Lagrangian into two parts: a spin-dependent part (first term, abbreviated as SD) and a spin-independent part (second term, abbreviated as SI). These two components give distinct contributions to the total cross section, which can be written:

$$\sigma(q) = \sigma_0^{\rm SD} F_{\rm SD}^2(q) + \sigma_0^{\rm SI} F_{\rm SI}^2(q) \tag{1.38}$$

For the spin dependent case, in the limit of zero momentum transfer, the WIMP-nucleus cross section is given by:

$$\sigma_0^{\rm SD} = \frac{32\mu_N^2}{\pi}\left[a_p\langle S_p\rangle + a_n\langle S_n\rangle\right]^2 G_F^2 \frac{J+1}{J} \tag{1.39}$$

where J is the total angular momentum of the nucleus, G_F is Fermi's constant, $\langle S_{p,n} \rangle$ is the proton/neutron spin expectation value and $a_{p,n}$ is the proton/neutron scattering amplitude derived from Eq. 1.37.

For the spin independent case, in the limit of zero momentum transfer, the WIMP-nucleus cross section is given by:

$$\sigma_0 = \frac{4\mu_N^2}{\pi} \left[Z f_p + (A - Z) f_n \right]^2 \tag{1.40}$$

We have introduced A and Z, respectively the mass and atomic number of the target nucleus. f_p (resp. f_n) denotes the WIMP coupling to protons (resp. neutrons). They can be derived from the Lagrangian of Eq. 1.37. Because the SUSY LSP is a Majorana fermion for which the vector term vanishes, we have neglected the vector interactions.

Even though setting $f_p \neq f_n$ has interesting phenomenological consequences [44], standard WIMP analyses consider that the coupling to protons is the same as the one to neutrons ($f_p = f_n$). In that case, Equation 1.40 reduces to:

$$\sigma_0 = \frac{4\mu_N^2}{\pi} A^2 f_p^2 \tag{1.41}$$

When momentum is effectively transferred, the WIMP nucleus cross section must take the nuclear form factor (parameterised with the momentum transfer q) into account: $\sigma(q) = \sigma_0 \times F^2(q)$. Following [45, 46], we have:

$$F_{\mathrm{SD}}^2(q) = \frac{\sin(q r_n)}{q r_n} \tag{1.42}$$

$$F_{\mathrm{SI}}^2(q) = \left(\frac{3 j_1(q R_1)}{q R_1} \right)^2 \exp\left[-q^2 s^2 \right] \tag{1.43}$$

where $r_n \approx 1.0 A^{1/3}$ fm, $s \simeq 1$ fm measures the nuclear skin thickness, R_1 is a function of s and A and j_1 is the spherical Bessel function.

Before continuing the discussion, we will note that direct detection experiments may use different targets (like Germanium, Xenon or Silicium) so that the WIMP-nucleus cross section changes from an experiment to another. This is why the standard practice is to express results in terms of the cross section normalised to a single nucleon and which we will refer to as $\sigma_{\chi-n}$. For the spin-independent case, $\sigma_{\chi-n}$ is given by:

$$\sigma_{\chi-n} = \left(\frac{\mu_n}{\mu_N} \right)^2 A^{-2} \sigma_{\chi-N} \tag{1.44}$$

Designing a dark matter direct detection experiment

Let us analyse the computation of the WIMP event rate. From Equations 1.39, 1.41, we see that the spin-independent contribution scales as A^2, which favours heavy targets, while the spin-dependent contribution scales as $\langle S_{p,n} \rangle^2$ which favours targets with a large nuclear spin factor like ^{19}F. That is why experiments which focus on the spin-independent contribution use heavy targets like Germanium (EDELWEISS[1] and CDMS[47] collaborations) or Xenon (XENON[48] and LUX [49] collaborations). However, there exists experiments which focus on the spin-dependent channels. They use lighter elements with large nuclear nuclear angular momentum like ^{19}F (Picasso [50], COUPP [51]).

We will now focus on the spin-independent channel as it is the primary focus of the EDELWEISS experiment. Combining the equations above, we can plot the expected event rate for a detector with perfect resolution (see Fig. 1.15). Let us look at two important parameters:

- **The WIMP mass:** Sensitivity to low mass WIMPs ($\lesssim$ 10 GeV) is challenging because the bulk of the signal is found at very low energies ($\lesssim$ 5 keV). This means that the detector threshold will play a crucial role in identifying a potential signal. At higher masses, the signal is broader and robust results can be obtained even if the threshold is high.

- **The target nuclei:** We have seen that under a general approximation, the amplitude of the signal is proportional to A^2. This means that high A targets are generally favoured, although other parameters like the threshold, the nuclear form factor and the WIMP mass can affect the sensitivity. This is particularly important for low mass WIMP searches. For instance, a Germanium based experiment like EDELWEISS-III, with a threshold better than 1.5 keV will be sensitive to roughly 20% of the recoil spectrum of a 7 GeV WIMP mass. However, a Xenon based experiment with an 8.4 keV threshold like XENON100 [48], will be able to probe only 0.05% of the recoil spectrum! In this case, the experiment is sensitive to the tail of the recoil distribution only. That is, it can only detect the WIMPs with the largest velocity with respect to the laboratory frame. This tail may change a lot under different halo assumptions: the results become model-dependent. Systematics on the detector response can also lead to severe misinterpretations of the data. These comments urge caution on the interpretation of low mass WIMP searches.

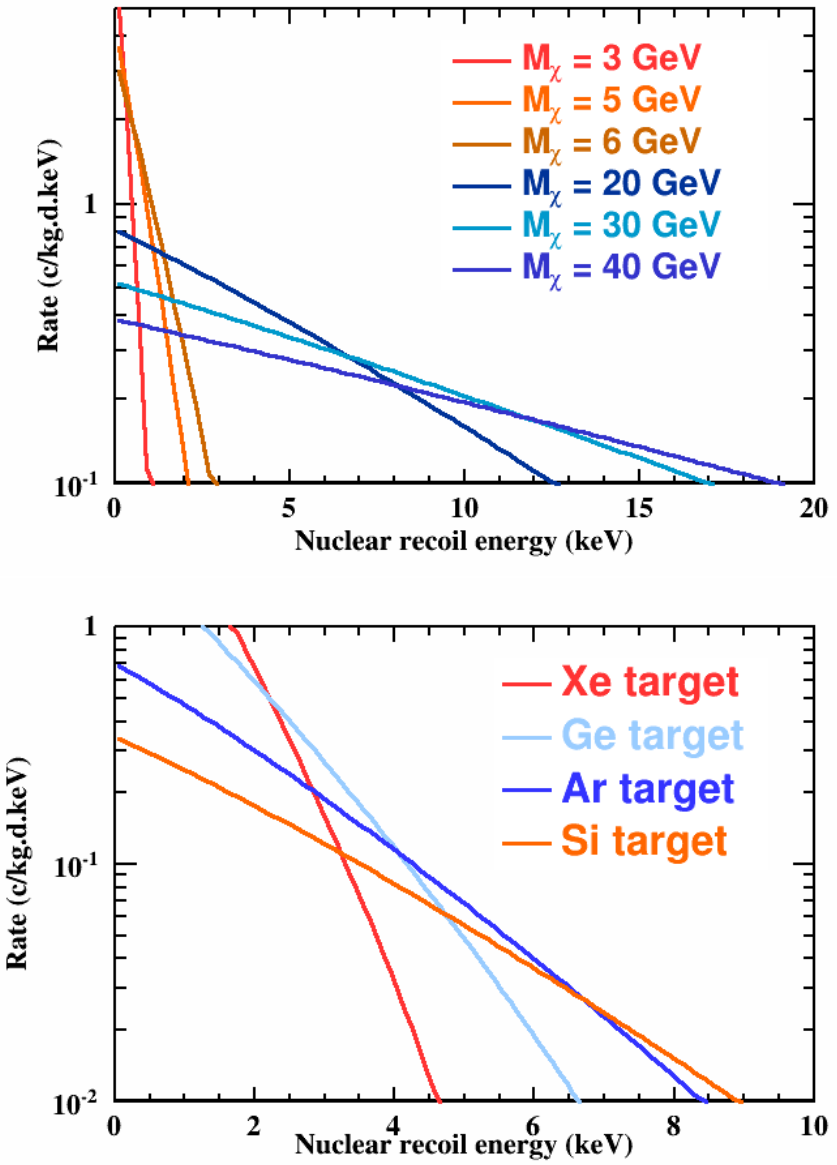

FIGURE 1.15 Top: Event rate for a Germanium target and for different WIMP masses. Bottom: Event rate for various targets for $M_\chi = 8$ GeV. For all curves, the cross section is set to 10^{-5} pb.

Now that we know more about the WIMP event rate, we get a better idea of the experimental difficulties faced by direct detection experiments and the parameters we can tune to overcome them. We saw that the typical nuclear recoil energies are expected between 1 keV and 100 keV. These typically low energies explain why a lot of the research effort is dedicated to lowering the experimental threshold. This is of particular importance for low mass WIMPs ($\lesssim 10$ GeV) as the signal is concentrated at even lower energies. Heavy target nuclei are therefore clearly favoured. Another challenge lies in the total event rate. Ever-improving constraints on the WIMP-nucleon cross section

imply that it is extremely low (less than an event per year of data taking and per kg of detector). This requires large detector masses and exposures. Dark matter identification is further complicated by background events: most materials are contaminated by radioactive elements with rates greater than the expected WIMP rate. Cosmic muons may also contribute as they can induce neutrons which also scatter off the target. Part of the solution consists in going underground (the rock overburden provides shielding from cosmic rays), surrounding the detectors with thick shields and selecting radiopure materials. These observations dictate the general strategy for direct detection: the focus should be on achieving low thresholds, designing methods for background rejection and building massive detectors.

An overview of direct detection experiments

We will now review the various technologies used in direct WIMP searches. In particular, we will be interested in the background rejection methods specific to each technology. For more detailed information about backgrounds in the EDELWEISS experiment, see Chapter 2.

- Noble liquids:

  Experiments based on the use of noble liquids typically involve a dual-phase (liquid and gas) Time Projection Chamber (TPC). These TPCs record the prompt scintillation light, emitted as a particle recoils in the liquid target. Ionization electrons are also produced; they are detected via the proportional scintillation light emitted as they are accelerated in the gas phase. Both signals are detected by an array of photomultipliers. The time difference between the signals provides spatial resolution on the vertical axis. The shape of the signal on the photomultipliers provides spatial resolution on the horizontal plane. The ratio of the two scintillation signals provide discrimination between nuclear recoils (as expected from WIMPs but also neutrons) and electronic recoils (mostly photons and electrons). Neutrons can lead to multiple scatters while WIMPs interact only once. Multiple scatters can be rejected thanks to the position information. The use of noble liquids has several advantages: they have relatively easy cryogenics, high mass numbers and are easily scalable. Notable collaborations include LUX [49], XENON100 [48] and XMASS [52] (which is single phased and only measures the scintillation signal) for Xenon, and Darkside [53] for Argon.

- Bolometric detectors:

  Bolometers convert the recoil energy into phonons and the resulting temperature increase can be measured. As we will see in Chapter 2, it is possible to detect very small energy deposits by lowering the temperature of the crystal. Germanium and Silicium detectors can also be used to detect an ionisation signal. Indeed, crystalline semiconductors possess a region (band) of forbidden electron states between the valence band, in which electrons are bound, and the conduction band in which electrons propagate freely. In pure semiconductors at cryogenic ($T_c \approx 20\,mK$) temperatures, there are effectively zero free charge carriers because the Boltzmann energy ($E = kT_c$) is negligible with respect to the gap energy between the conduction and valence band. The semi-conductor then behaves as an insulator and we are free to apply an electric field (until the breakdown limit) without inducing a current. This is how the ionisation can be measured: an incident particle can deposit enough energy to strip electrons from the valence band. If an electric field is applied, the electron/hole pairs can drift to the surface of the detector where electrodes can collect them. This is the basic mechanism for event detection in crystal based experiments like CDMS [47] and EDELWEISS [1]. As for noble liquids, the combination of the two signals give information on the location of the interaction and its nature, which allows background rejection. These two experiments use Germanium crystals to look for WIMPs (CDMS also operates Silicium detectors). The CRESST experiment [54] which uses $CaWO_4$ crystals measures the scintillation light rather than the ionisation.
  Other experiments like the CoGeNT experiment [55] only look at the ionisation signal. Thus, their background discrimination is not as efficient and they have to rely on background modelisation or the possible detection of a time modulation (due to the Earth's orbit around the sun) for WIMP detection.

- Metastable liquids or gels:

  In these experiments, a liquid is superheated and compressed such that bubbles can form through particle interactions. The phase transition is explosive and bubble formation is accompanied by an acoustic signal, which is tracked by piezoelectric sensors. The liquid generally contains ^{19}F, which enhances the spin-dependent cross section. In addition the mass number of ^{19}F is low. These factors combine to show that the spin-dependent channel is clearly favoured. Background rejection is performed in two ways: the operating conditions render the detector insensitive to usual electromagnetic backgrounds like electrons or photons. This is one of the major advantages of these methods which only need to discriminate against α or

neutron recoils. In addition, the amplitude and frequency content of the detector response is different for α and nuclear recoils. This allows further discrimination. Notable experiments include PICASSO [50], COUPP [51] and SIMPLE [56]. The PICASSO and COUPP groups have recently merged to form the PICO collaboration [57].

- Crystal scintillators:

  Scintillation experiments like DAMA [58] or KIMS [59] rely on the detection of scintillation light by photomultiplier in arrays of crystals. Multiple arrays provide veto for multiple scattering. Partial discrimination can be achieved between electronic and nuclear recoils thanks to the difference in the decay times of the scintillation pulses. The results of the DAMA experiment are essentially based on the search for an annual modulation in the data, which could provide evidence for WIMPs.

WIMP search results

To conclude this section, we will look at the current state of the art dark matter results (see Fig. 1.16, 1.17) and examine current claims and exclusion limits. As we remarked earlier, the detection of low mass WIMPs ($\lesssim 10$ GeV) calls for a specific strategy since most of the signal is found at very low ($\lesssim 5$ keV) energies: the sensitivity is limited by the experimental threshold. At higher masses, the requirements on the threshold are less stringent. The focus is on increasing the exposure while ensuring background rejection. This is why we will split the results in two sections:

- **High mass results:**

  XENON100 [48] and LUX [49] have provided the most stringent constraints on the WIMP-nucleon cross section to date. Indeed, the detector design allows the definition of a large fiducial mass with excellent self shielding. Furthermore, they are favoured by their high mass target (recall that the WIMP rate scales as A^2). This combination of large exposure and background suppression accounts for the success of Xenon based experiments. To this date, no signal hint was found for high mass WIMPs. The resulting exclusion limits are shown on Fig. 1.17.

- **Low mass results:**

  The low mass region continues to stir debate as mixed results have been reported: some experiments have claimed evidence for a signal, while others found no trace of WIMPs. As can be seen from Fig. 1.16, there are tensions between these two conflicting interpretations. Let us review recent experimental results:

  The DAMA collaboration has made perhaps the most well-known claim to Dark Matter detection. They observed a modulation over time of the event rate which can be accounted for by WIMPs. However, as pointed in [60], the claim is weakened by several experiments, based on different technologies, which exclude the DAMA signal region.

  The CoGeNT collaboration has also reported various regions of interests for a potential WIMP signal. As mentioned above, the CoGeNT collaboration relies on background subtraction and modulation detection to look for WIMPs. However, the modulation found by CoGeNT is higher than that required for WIMPs and objections can be made on the surface/volume event separation of the CoGeNT analysis [60].

  The CRESST collaboration has also reported potential signal evidence. However, subsequent analyses with an upgraded setup do not confirm the excess previously seen. [54].

  The CDMS collaboration also reported an anomalous excess in their Silicium detectors [61]. A likelihood analysis argues for a background+WIMP signal at the 3σ confidence level. The CDMS collaboration itself excluded the Silicium signal with a subsequent low threshold analysis of Germanium data [62].

  The EDELWEISS, LUX, CDMS, CRESST and XENON100 collaboration [48, 49, 62–64] have all reported negative results in the search for low mass WIMPs. It is interesting to note that noble gas based experiments do not necessarily have the defining advantage: their energy resolution is lower than that of crystal experiments, there is more uncertainty on the nuclear recoil response of the detector and they are limited in threshold by how much photoelectrons they can detect. Thus, there is an opportunity for bolometric experiments, like EDELWEISS-III, to probe the low mass region with better sensitivity. Indeed, the current experimental threshold is already lower than that of LUX [49] and can be further improved by a change of electronics and electric field boosting techniques. What is clear is that improving the threshold and the discriminating capabilities at low energies is a priority for experiments dedicated to the search of low mass WIMPs. It will shed much needed light on the validation of discovery claims or the confirmation of null results.

Let us close this chapter with a few concluding remarks. The field of Dark Matter detection is more active than ever, with contributions from the LHC, indirect and direct detection experiments. The first two have recently provided important results which challenge the low mass WIMP scenario: the study of Dwarf galaxies by Fermi imposes strong lower bounds on the mass of a possible thermal relic from the Big Bang. SUSY scans at the LHC are pushing the boundaries of the simplest models (cMSSM and pMSSM) to regions with higher mediator mass and very weak cross section. Because of these strong constraints on standard, thermal Dark Matter, direct detection experiments now turn to non-standard scenarios like asymmetric Dark Matter [65] to provide motivation for low mass WIMPs. The conflicting results (signal hints versus exclusion) can be somewhat alleviated by departures from the standard assumptions such as a different velocity profile or isospin violating interactions at the cost of a certain degree of fine-tuning. This issue should be resolved with the next generation of dedicated low mass experiments whose ultimate goal is to reach the neutrino floor: an irreducible background triggered by the scattering of solar neutrinos on the target nuclei.

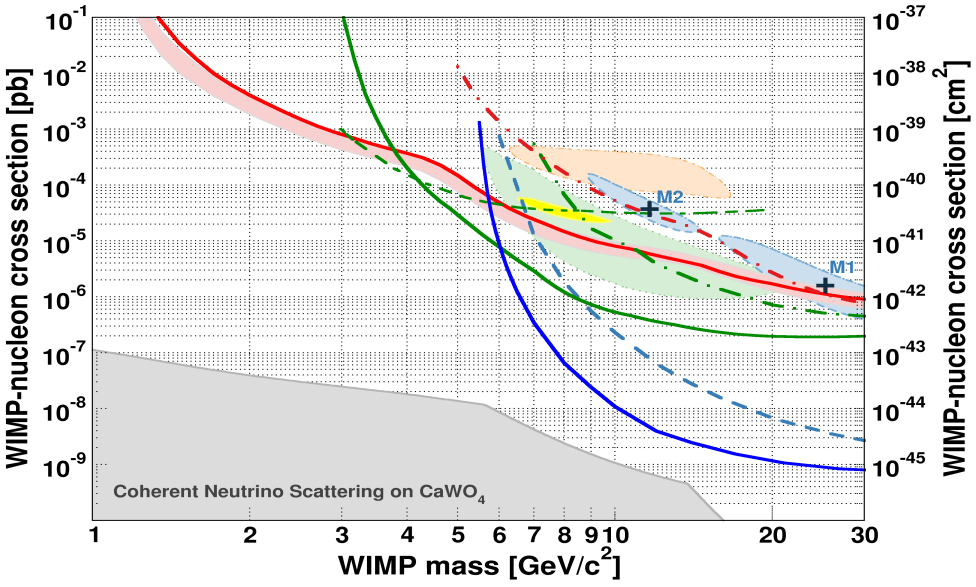

FIGURE 1.16 Current limits on WIMP spin-independent cross section. The limits are given as a function of the WIMP mass. The gray region is the limit for a background-free $CaWO_4$ experiment arising from coherent neutrino scattering, dominantly from solar neutrinos. Shown in green are the limits (90% CL) from Ge-based experiments: SuperCDMS (solid), CDMSlite (dashed) and EDELWEISS (dash-dotted). The parameter space favored by CDMS-Si is shown in light green (90% CL), the one favored by CoGeNT (99% CL) and DAMA/Libra (3σ level) in yellow and orange. The exclusion curves from liquid xenon experiments (90% CL) are drawn in blue, solid for LUX, dashed for XENON100. The CRESST limit (90% CL) is shown in red. CRESST contours are also shown in light blue. Also in grey is the limit for a background-free $CaWO_4$ experiment arising from coherent neutrino scattering, dominantly from solar neutrinos [66]. Figure from [54].

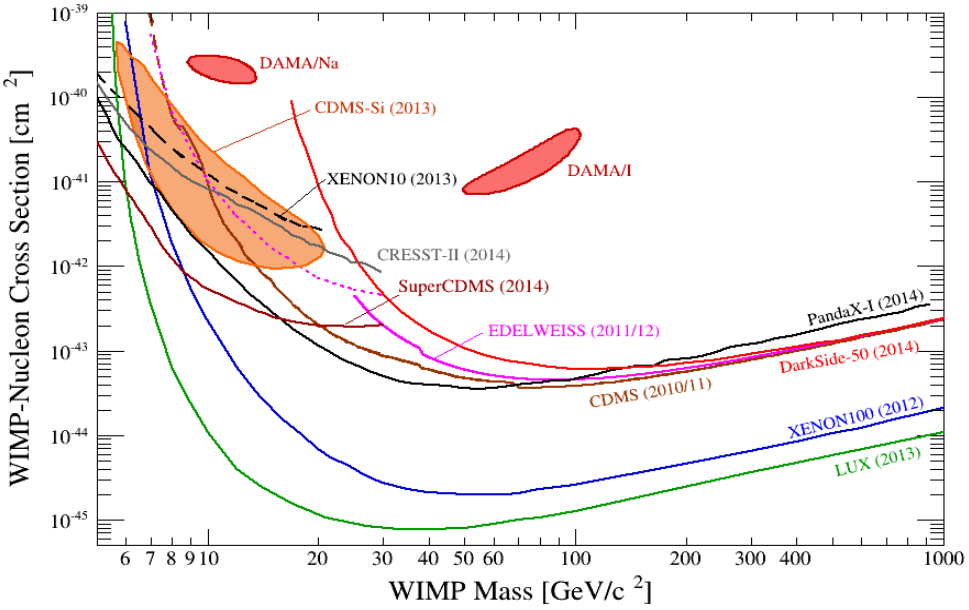

FIGURE 1.17 Results on spin-independent (scalar) WIMP-nucleon interactions as derived from direct detection experiments, showing the exclusion curves up to 1 TeV (high mass region). The results from DAMA/LIBRA and CDMS-Si (contours, which indicate possible signal hints) are challenged by the exclusion limits from many other experiments. The parameter space is currently dominated by the dual-phase liquid xenon time projection chambers (TPCs) XENON100 and LUX. Figure from [67].

Chapter 2

The EDELWEISS experiment

In this section, we will introduce the EDELWEISS experiment, which is currently in its third phase, called EDELWEISS III. As we have seen in Chapter 1, EDELWEISS is a WIMP direct detection experiment which relies on the identification of nuclear recoils in Germanium crystals. Unfortunately, these detectors are sensitive to several other particles: electrons, photons, neutrons as well as alpha and lead recoils. Because of radioactive contamination and cosmic rays, such events are abundant.

In the light of these observations, we will first take some time to discuss the various types of backgrounds expected in the experiment. We will then explain how background rejection can be efficiently implemented with dedicated Germanium bolometers, engineered within the collaboration. Lastly, we will present the complete setup of the experiment, designed to operate the detectors at very low temperatures while providing further background reduction. In this work, data from both the second and third stage of the experiment (EDELWEISS-II and EDELWEISS-III respectively) are analysed. Therefore, we will stress the major evolutions of the setup, with particular attention to changes in the detector design.

2.1 Expected backgrounds

We are now going to review the different types of backgrounds expected in the experiment and the strategies that were implemented to reduce their impact.

2.1.1 Muon-induced neutrons

Muons are a byproduct of cosmic rays. Cosmic ray interaction with the nuclei present in the Earth's atmosphere leads to a shower of particles which includes muons. Muons can penetrate deeply into matter and produce neutrons through a variety of mechanisms, both direct (negative muon capture, quasielastic scattering, muon spallation) and indirect (photonuclear production and hadronic interactions). See [68] for a detailed study of the muon-induced neutron background in the EDELWEISS laboratory. Neutrons are a very troublesome background for direct detection experiments as they have the same signature as WIMPs. This is the reason why all direct detection experiments are located in an underground laboratory: the rock overburden curbs the muon flux by several orders of magnitude. EDELWEISS is no exception; it is located in the Underground Laboratory of Modane (LSM), the deepest such laboratory in Europe. The muon flux in the laboratory was measured in[69]. This study found:

$$\Phi_\mu = (5.4 \pm 0.2^{+0.5}_{-0.9}) \text{ muons/m}^2\text{/d} \tag{2.1}$$

where Φ_μ denotes the muon flux. This is a full six orders of magnitude below the flux at sea level! Muon-induced activity is monitored by a muon veto, synchronised with the detectors. This enables the measurement of the muon-induced WIMP-like event rate in the detectors:

$$\Gamma^{\mu-n} = 0.008^{+0.005}_{-0.004} \text{ evts/(kg} \cdot \text{d)} \tag{2.2}$$

This rate was estimated using EDELWEISS-II data, requiring general quality cuts, identification of the event by the muon veto, an energy between 20 keV and 250 keV and location of the event in the 90% CL nuclear recoil band. The muon-induced neutron background is not yet available for EDELWEISS III. However, estimates from [69], which include the setup modifications predict an irreducible (i.e. muon-induced events which were not tagged by the muon veto) muon-induced neutron background of:

$$N^{\mu-n} = 0.6^{+0.7}_{-0.6} \tag{2.3}$$

for 3000 kg.d of exposure.

2.1.2 External radioactivity

The materials used for the experiment, the rocks, the laboratory air and walls are contaminated by heavy radioactive elements. We show their decay chains in Fig. 2.1 below. Through spontaneous fission, β and α radioactivity, neutrons, β and γ rays, α particles and heavy nuclei recoils can be produced.

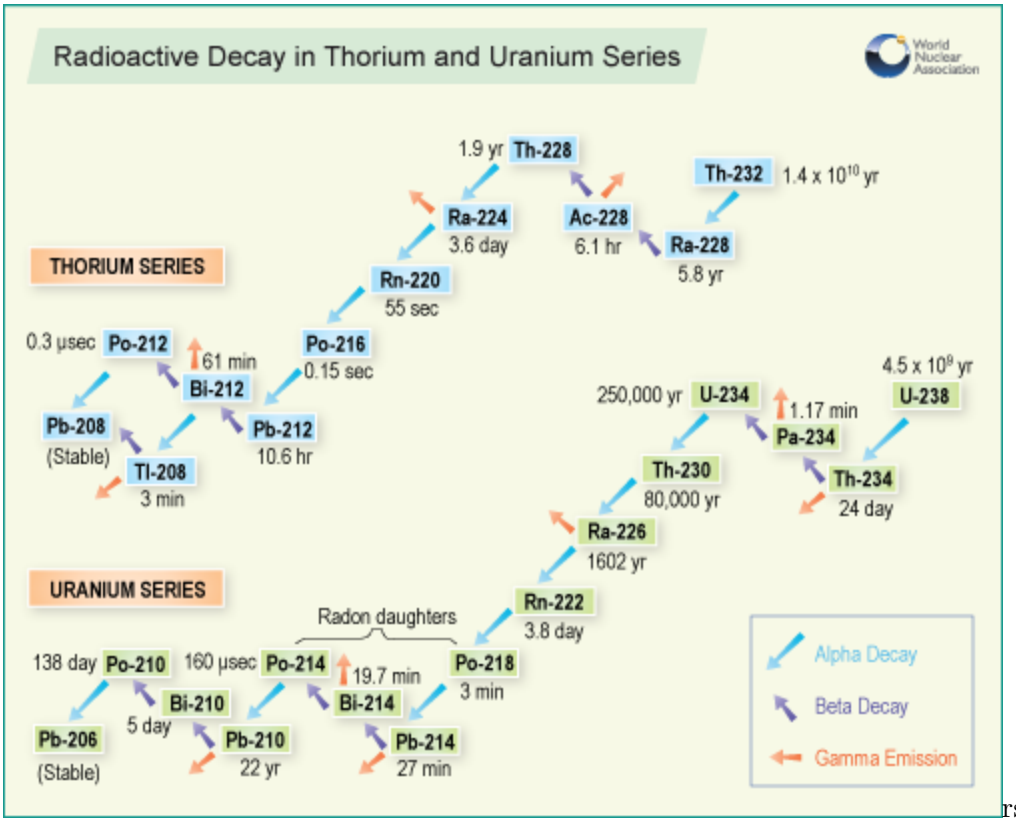

FIGURE 2.1 Decay chain of Uranium and Thorium. Radon 222, contained in the ambient air, is included in this decay chain. We can see that background events like β, α and γ are byproducts of many of these decay reactions.

A thorough understanding of background sources is crucial for the interpretation of a WIMP direct detection experiment. This is why we try to validate the observations with comprehensive Monte Carlo simulations. In [3], the EDELWEISS collaboration carried out GEANT4 simulations to estimate the gamma and neutron rate in the EDELWEISS-II setup. Using radiopurity measurements as inputs, this study found a Gamma event rate of 82 events/kg/day and a neutron rate of $(2.6 - 8.1) \times 10^{-3}$ events/kg/day in the 20-200 keV region. This is in good agreement with the observations. For illustrative purposes, we show the expected neutron background from various part of the EDELWEISS II setup in Table. 2.1 below. Similar studies for EDELWEISS-III are currently ongoing.

Source	Material	Composition (abundance %)	Neutron yield in n/g/s/ppb U	Th	Neutron events (384 kg×days)
Hall walls	Rock	H (17), C (8), O (53), Mg (1), Al (3), Si (4), Ca (13), Fe (1)	2.88×10^{-11}	7.52×10^{-12}	<0.01
Hall walls	Concrete	H (19), C (11), O (52), Mg (1), Si (2), Ca (15)	2.21×10^{-11}	3.96×10^{-12}	<0.1
Shielding	Polyethylene	H (67), C (33)	2.90×10^{-11}	6.25×10^{-12}	<0.01
Shielding	Lead	Pb (100)	1.35×10^{-11}	–	<0.08
Support	Stainless steel	Cr (17), Mn (0.02), Fe (69), Ni (12)	1.84×10^{-11}	5.92×10^{-12}	<0.01
Support	Mild steel	as above	1.84×10^{-11}	5.92×10^{-12}	<0.04
Warm electronics	PCB	H (22), B (2), C (19), N (6), O (35), Mg (1), Al (4), Si (8), Ca (3)	7.08×10^{-11}	2.21×10^{-11}	1.0±0.5
1K connectors	Aluminium	Al (100)	1.80×10^{-10}	8.59×10^{-11}	0.5±0.2
Thermal screens, crystal supports	Copper	Cu (100)	1.38×10^{-11}	9.36×10^{-13}	<0.1
Coaxial cables	PTFE	C (33), F (67)	8.40×10^{-10}	3.50×10^{-10}	<0.5
Crystal holders	PTFE	C (33), F (67)	8.40×10^{-10}	3.50×10^{-10}	<0.01
Electrodes	Aluminium	Al (100)	1.80×10^{-10}	8.59×10^{-11}	<0.01
Total					<3.1

TABLE 2.1 Number of neutron events expected for various components of the EDELWEISS-II setup. Table from [3].

These studies guided the elaboration of the EDELWEISS-III setup by identifying the major contributions to the background. However, it should be borne in mind that the predictions' precision is affected by uncertainties on the chemical composition of the components of the setup and on the measurement of radioactivity levels. In particular, it is difficult to estimate the contribution of partially shielded internal sources like the cabling and the electronics.

Surface radioactivity also plays an important role. Radon may be deposited close to the detectors. Its decay products can then reach the surface of the detector where they interact superficially (see Fig. 2.2). This background contribution is *local*: it may vary significantly even on the scale of a single detector. This makes it very hard to estimate through simulations. Models for such events will be discussed in Chap. 4.

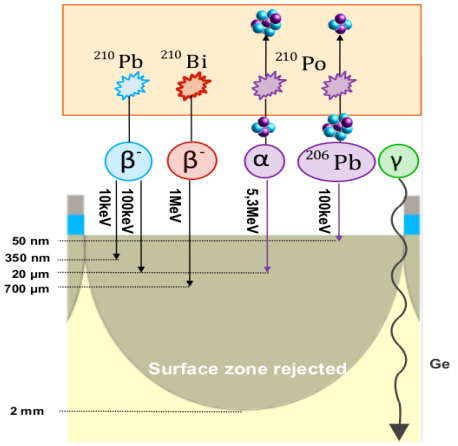

FIGURE 2.2 Surface interactions in a Ge bolometer.

2.1.3 Germanium internal radioactivity

Interactions with cosmic rays byproducts can lead to the production of long-lived radioisotopes *within* the Germanium crystal. This contamination occurs at sea-level, when the detectors are processed. Once they are installed in the Underground Laboratory, the activation is suppressed because of the rock overburden. Activated isotopes decay via electron capture (EC) or beta disintegration (see Fig. 2.3). Through EC, an orbital electron (usually from the K or L electron shell) is captured by a proton in the nucleus. The nucleus "loses" one proton and "gains" a neutron: EC changes the nuclide to a new element. This new element is in an excited state because it misses an electron in the inner shell. An electron in the outer shell will eventually fill the gap. In this process, X-rays or Auger electrons may be emitted, leading to the observation of lines (with various energies depending on the shell, K or L, that is filled) in the electronic recoil spectrum. Table 2.2 below lists some radioactive lines which are relevant to the axion and low mass WIMP searches of Chapter 3 and Chapter 4.

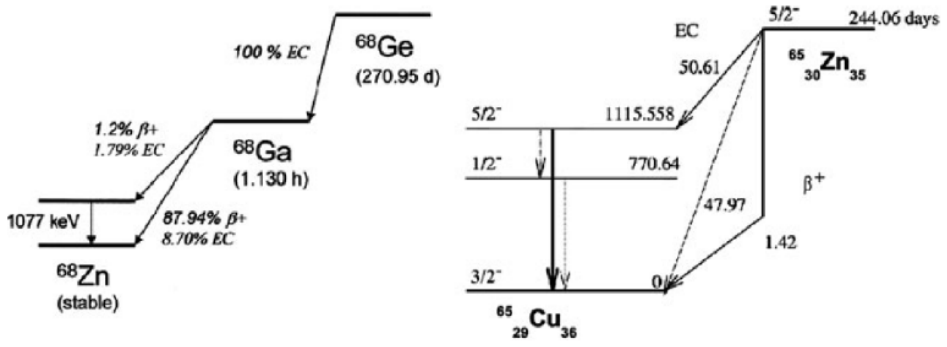

FIGURE 2.3 Decay scheme of ^{68}Ge, which produces a gamma ray line at 10.36 keV and ^{65}Zn, which produces a line at 8.98 keV.

Element	Half life	Gamma line(s)
^{71}Ge	11 days	10.37 keV, 1.297 keV
^{68}Ge	271 days	10.37 keV, 1.2977 keV
^{68}Ga	68 min	9.66 keV, 1.1936 keV
^{65}Zn	244 days	8.98 keV, 1.0961 keV
^{55}Fe	996 days	6.54 keV
^{68}Ge	312 days	5.99 keV
^{54}Mn	330 days	4.97 keV

TABLE 2.2 Radioactive peaks in the Germanium detectors of the EDELWEISS experiment. Source : http://www.nndc.bnl.gov/nudat2/.

2.1.4 Guidelines for background rejection

In Sec. 2.1.1,2.1.2,2.1.3, we have introduced several backgrounds, which we will seek to reject in EDELWEISS. This can be achieved in three major ways:

Nuclear recoil discrimination: Axions searches notwithstanding (see Chapter 3), we are looking for nuclear recoils triggered by WIMPs on Germanium nuclear. WIMP-induced electronic recoils are undetectable because of the kinematics of the reaction. Hence, we are not interested in electronic recoils. In Sec. 2.2.1, we will see that it is possible to discriminate electronic recoils from nuclear recoils in EDELWEISS, through the dual measure of the phonon and ionisation signal triggered by an interaction in the detectors. This allows us to reject background events like gamma rays, which trigger an electronic recoil.

Surface event rejection: In Sec. 2.1.2, we mentioned some background events which interact only near the surface of the detector. They are problematic for WIMP searches because the efficiency of the charge collection is reduced. This can impair significantly the discrimination between electronic and nuclear recoils. Surface events may also raise the low energy electronic recoil background which degrades the sensitivity of axion searches. This In Sec. 2.2.2,2.2.3, we will see how a clever electrode design (called InterDigit) can be used to reject surface events efficiently.

Shielding: The influx of background events can be effectively dampened by surrounding the detectors with shields which will screen incoming particles. All the shields of the experiment (both active and passive) will be described in Sec. 2.3.

2.2 The Germanium detectors

2.2.1 General principle

The cryogenic bolometers are built from a high purity Germanium monocrystal. The crystals are equipped with aluminium electrodes and one or two heat sensors (made of Ge-NTD: Germanium doped with neutrons). This enables the measurement of the ionisation signal deposited by an incident particle as well as the resulting phonon signal due to the temperature increase. Ionisation is measured by applying a bias voltage between the electrodes: charge carriers drift in the resulting electric field until they are collected by the electrodes. The NTD sensors' principle can be explained with a few equations: in the Germanium crystal, the relation between the deposited energy ΔE, the temperature change ΔT and the combined heat capacity of the NTD sensor and the crystal $C(T)$ is given by:

$$\Delta T = \frac{\Delta E}{C(T)} \tag{2.4}$$

where, following Debye's model, the heat capacity is proportional to the cube of the temperature T:

$$C \propto \left(\frac{T}{T_C}\right)^3 \tag{2.5}$$

This equation explains why the bolometers need to be cooled down: by lowering the temperature, they become sensitive to extremely small temperature variations such as those induced by particle interactions. The NTD sensor measures the temperature increase through the change of the resistance R of the crystal:

$$R \propto \exp(\sqrt{T_D/T}) \tag{2.6}$$

There is an additional contribution to the temperature increase (hence to the heat signal). When the charge carriers are accelerated in the electric field, additional phonons are created. This is the so-called Luke-Neganov effect. The additional contribution to the heat energy is given by:

$$E_{\text{Luke}} = N \times e \times V \tag{2.7}$$

where e is the fundamental charge, N the number of carriers and V the applied voltage. N is related to the recoil energy E_{R}: $N = \frac{E_{\text{R}}}{\epsilon}$. Here, ϵ is the average energy needed

to create an electron/hole pair which depends on the incident particle. For instance, $\epsilon_\gamma/\epsilon_{\text{neutron}} = 0.3$ means that γ rays produce approximately three times more charge carriers than neutrons. With this, Equation 2.7 becomes:

$$E_{\text{Luke}} = \frac{E_{\text{R}}}{\epsilon_{\text{particle}}} \times V \tag{2.8}$$

We have renormalised ϵ to absorb the fundamental charge e. Thus the total heat energy is equal to the sum of the recoil energy and the Luke energy:

$$E_{\text{heat}} = E_{\text{R}} + E_{\text{Luke}} = E_{\text{R}} \left(1 + \frac{QV}{\epsilon_\gamma}\right) \tag{2.9}$$

We have introduced the quenching factor Q:

$$Q = \frac{\epsilon_\gamma}{\epsilon_{\text{particle}}} \tag{2.10}$$

The usual practice is to rescale the heat energy so that, for a γ ray, the heat energy is equal to the recoil energy. We therefore define a new, calibrated heat energy E^C_{heat}:

$$E^C_{\text{heat}} = E_{\text{R}} \frac{1 + \frac{QV}{\epsilon_\gamma}}{1 + \frac{(Q_\gamma \equiv 1)V}{\epsilon_\gamma}} \tag{2.11}$$

For a gamma electronic recoil, we define:

$$E^\gamma_{\text{I}} = E^\gamma_{\text{R}} \tag{2.12}$$

where E^γ_{I} is the gamma ionisation energy. Since the ionisation signal is proportional to the number of electron/hole pairs, we can write, using Eq. 2.10:

$$E_{\text{I}} = QE_{\text{R}} \tag{2.13}$$

The dual heat and ionisation measure allows us to recontruct E_{R} independently of Q. Injecting Eq. 2.13 into Eq. 2.11, we obtain:

$$E_{\text{R}} = E^C_{\text{heat}} \left(1 + \frac{V}{\epsilon_\gamma}\right) - E_{\text{I}} \frac{V}{3} \tag{2.14}$$

The dual measure also allows us to estimate Q which can then be used as a discriminating variable since $Q_{\text{nuclear recoil}} \neq Q_{\text{electronic recoil}}$. This is why WIMP data are often shown in a Q-plot, with the quenching factor as a function of the recoil energy.

The nuclear recoil response is well understood thanks to various calibrations as in [70]. The current EDELWEISS parameterization for Q is:

$$Q = 0.16\ E_{\mathrm{R}}^{0.18} \tag{2.15}$$

In Fig. 2.4, we show an EDELWEISS-II nuclear recoil calibration . In this calibration, neutrons are generated by an Americium-Beryllium source placed in the vicinity of the detectors. As advertised above, electronic recoils ($Q = 1$) are separated from nuclear recoils ($Q \approx 0.3$). The red lines show the expected nuclear recoil response, according to the parameterization of Equation 2.15. In addition to pure electron and nuclear recoils, inelastic nuclear recoils are visible with associated electromagnetic energies of 13.26 and 68.75 keV, due to the deexcitation of short-lived states of ^{73}Ge created by neutron diffusion (dashed black lines).

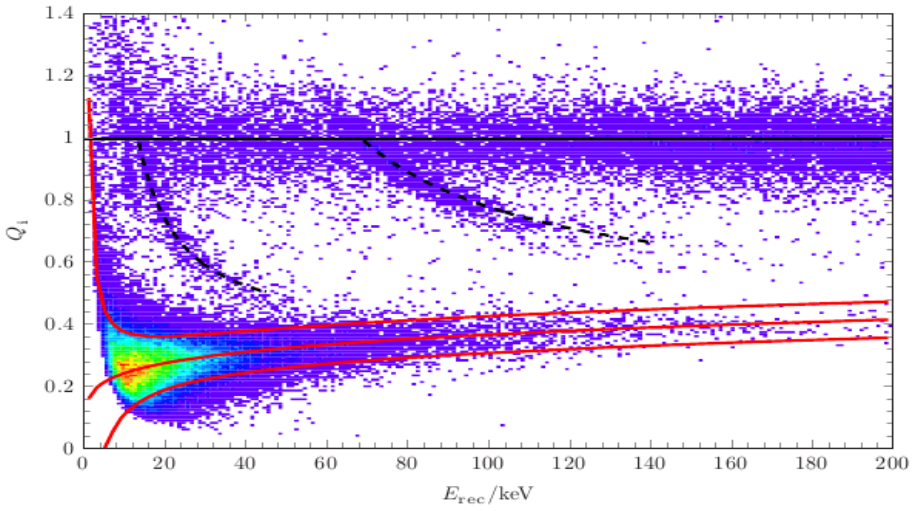

FIGURE 2.4 Q-plot for a neutron calibration in EDELWEISS-II.

As stated in Sec. 2.1, lead, beta and alpha recoils are a background for the EDELWEISS experiments. They have one important common feature: the interaction occurs on the surface of the detector (see Fig. 2.2). Surface events are problematic for WIMP searches because the efficiency of the charge collection is reduced. As a consequence, these events can fall in the WIMP signal region (delimited by red lines shown in Fig. 2.4). We are now going to describe the technology developed by the EDELWEISS collaboration to reject surface interactions. We will compare the designs used in EDELWEISS-II and EDELWEISS-III.

2.2.2 The Germanium detectors: EDELWEISS-II

The InterDigit design used in EDELWEISS-II features concentric electrode rings. Each ring is polarised alternatively (+4 V and -1.5 V at the top, -4 V and 1.5 V at the bottom). The resulting electric field configuration is shown in Fig. 2.5. Charge carrier transverse diffusion and anisotropy effects due to the crystalline nature of Germanium must be taken into account when modeling the ionisation response of the detector. However, for the sake of clarity, we will make the simplifying assumption that that the charge carriers' trajectory is only determined by the electric field. As a consequence, for a fiducial event (the green region of Fig. 2.5), the ionisation signal is collected at the top and bottom of the crystal. However, when a particle interacts near a given surface (the red region of Fig. 2.5), the charge is collected on this surface and there is no signal on the opposite surface. Surface rejection is obtained by requiring no veto signal (modulo resolution effects). The blue region in Fig. 2.5 is the so-called guard region. It defines an additional veto region for the sides of the detector.

With the InterDigit technology, the fiducial volume makes up about 42% of the total detector volume, and the detectors have a mass of 370 g. The measured gamma rejection factor is $(3 \pm 1) \times 10^{-5}$ [1] while the surface rejection factor was proved to be greater than 10^{-4} [71]. Fig. 2.6 below shows the final gamma calibration plot used to estimate the gamma rejection factor in EDELWEISS-II [1]. The anomalous events present in the nuclear recoil band will be discussed in Section 2.2.3.

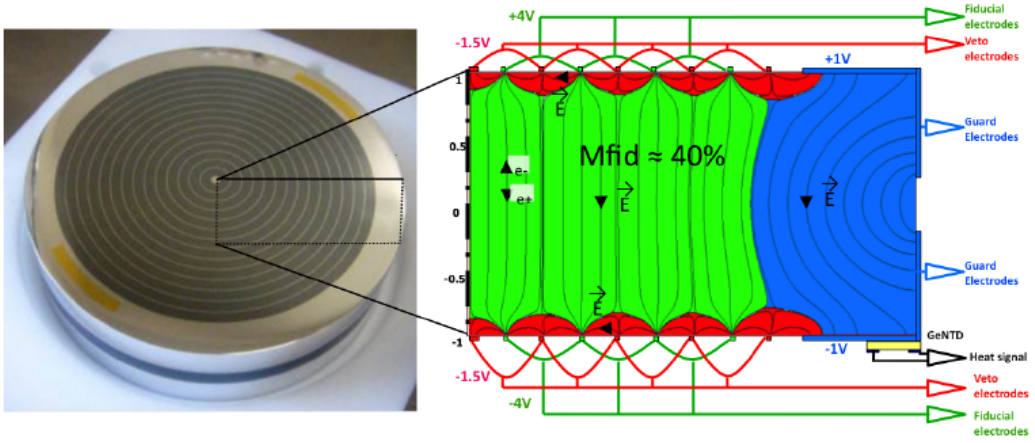

FIGURE 2.5 Left: EDELWEISS-II InterDigit detector. Right: Schematic view showing the electrode polarisation. The electrode design creates three distinct electric field regions which allow fiducialisation.

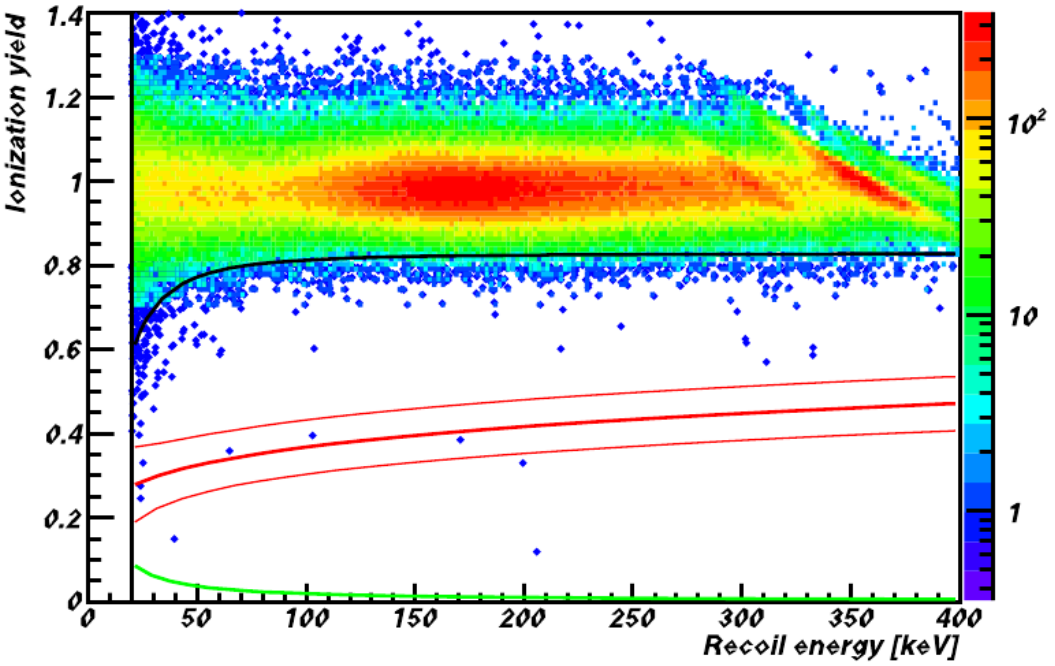

FIGURE 2.6 EDELWEISS-II gamma calibration plot from [1]. This plot shows the quenching factor Q as a function of the recoil energy for fiducial events recorded during the ^{133}Ba gamma calibration calibrations. The top line represents the 99.99% lower limit of the electron recoil band for typical noise conditions. The bottom (green) line is the typical ionization threshold, while the 90%CL nuclear recoil region is represented as a red band.

2.2.3 The Germanium detectors: EDELWEISS-III

The Full InterDigit (FID) design used in EDELWEISS-III is essentially the same as the InterDigit design. The technique of interleaved electrodes is once again used to allow surface event rejection. The main change lies in the replacement of the guard electrodes. The outer surface of the detector is now covered with alternated veto and collecting electrodes as shown in Fig. 2.8. This new design yields a significant increase of the fiducial volume which is now estimated at 75% of the total volume. It should also be noted that the FID detectors are more massive than their ID counterpart, with an average mass of 800 g. The FID design also improves the rejection of double scatter events. The EDELWEISS-II calibration plot in Fig. 2.6 shows that a few events leak in the WIMP signal region with a quenching between 0.1 and 0.5. These events cannot be explained by the tail of the fiducial gamma distribution. A possible explanation is that these events originate from double Compton scattering in the fiducial and guard region (see Fig. 2.7). Since charge collection may not always be under control in the guard region, this can degrade the reconstructed quenching factor. The FID design removes the guard volume, effectively reducing the likelihood of such events.

Fig. 2.9 below confirms our expectations: out of 411663 gamma calibration events, not a single anomalous event has been identified. A 90% CL upper limit on the gamma rejection factor is 6×10^{-6} [2] while the surface rejection factor was found to be greater than 4×10^{-5} [2] (see Fig. 2.10).

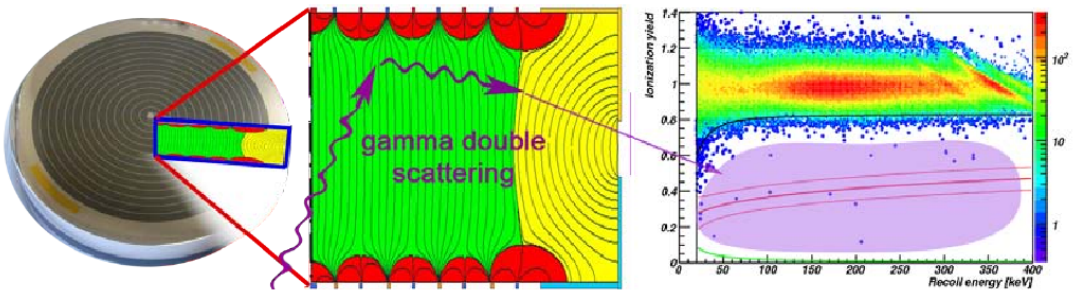

FIGURE 2.7 Scheme of the double Compton scattering in EDELWEISS II. If the double scatter occurs in the fiducial and guard region, the reconstructed quenching factor can be degraded, as shown by the calibration plot.

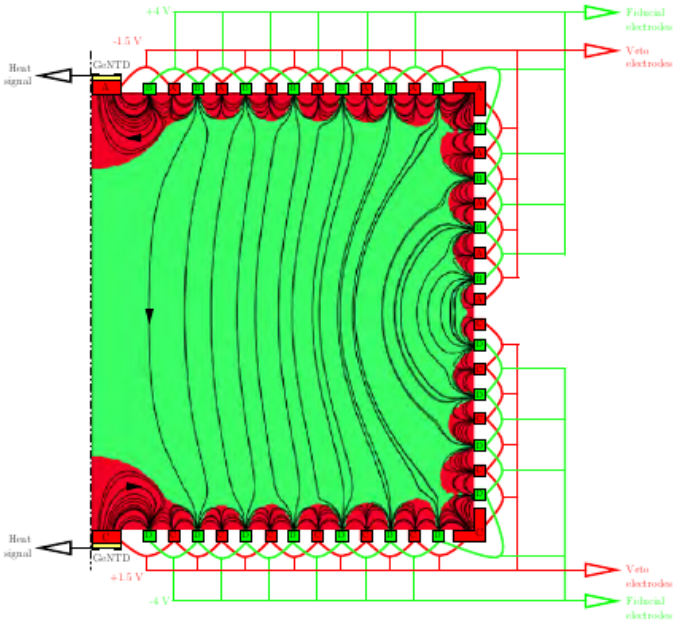

FIGURE 2.8 Schematic view of the Full InterDigit (FID) electrode design. This design increases the fiducial volume thanks to additional electrodes on the sides of the detector.

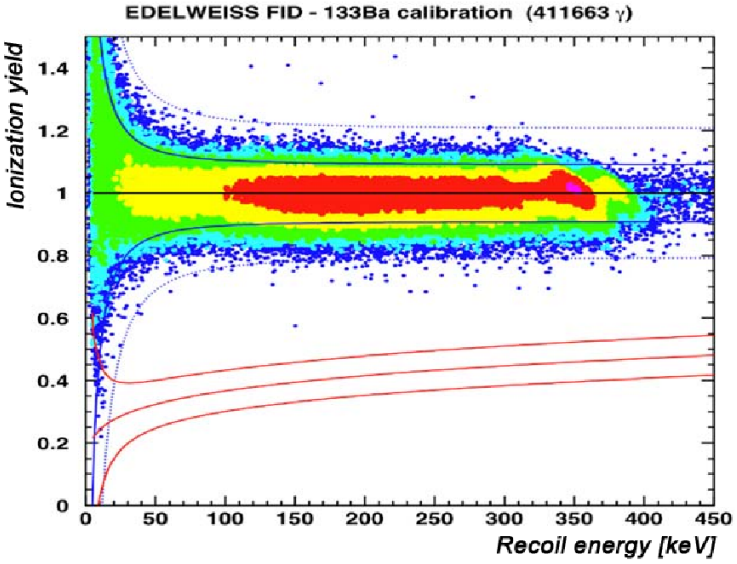

FIGURE 2.9 EDELWEISS-III gamma calibration plot from [2]. This plot shows the quenching factor Q as a function of the recoil energy for fiducial events recorded during the ^{133}Ba gamma calibration calibrations. The dashed line represents the 99.99% lower limit of the electron recoil band for typical noise conditions. The 90%CL nuclear recoil region is represented as a red band.

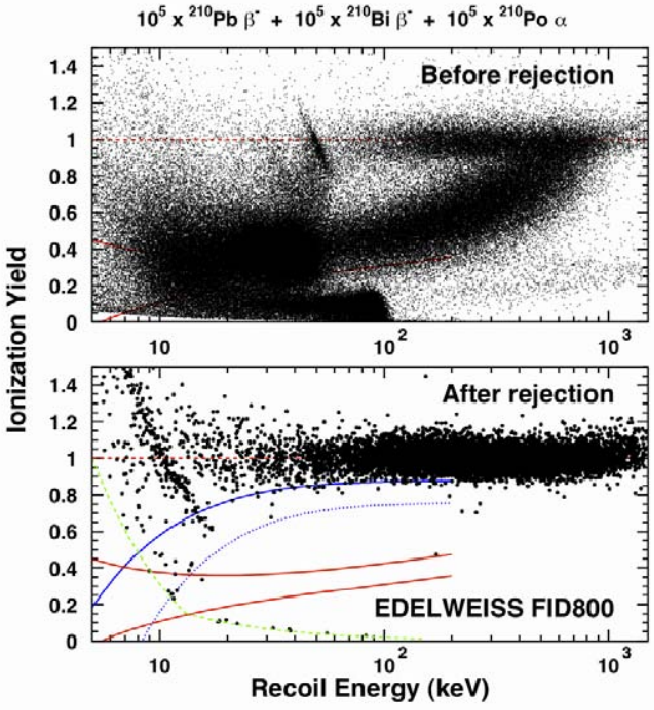

FIGURE 2.10 EDELWEISS-III surface calibration plot from [2]. These plot shows the quenching factor Q as a function of the recoil energy for surface events recorded during a surface calibration. Top: before rejection. Bottom: after rejection. A single event (above 15 keV) passed the fiducial cut out of roughly 100000 high and low energy betas and alphas.

2.3 The EDELWEISS infrastructure

Construction of the base infrastructure (shielding and cryostat) for EDELWEISS-II and EDELWEISS-III started in 2005, after the completion of the EDELWEISS-I physics reach. In this section, we will briefly describe the general setup of the experiment. Fig. 2.11 below shows the location of the Underground Laboratory of Modane, which houses the EDELWEISS experiment.

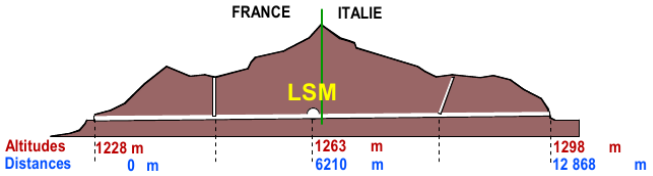

FIGURE 2.11 Laboratory location inside the Frejus tunnel.

2.3.1 Infrastructure: EDELWEISS-II

We are going to review the core components of the EDELWEISS setup, from the innermost (the detectors) to the outermost (the shieldings).

EDELWEISS-II's detectors are installed in a dilution cryostat built for the collaboration. More details will be given on the cryostat in Section 2.4. In the following, we may use the term "detector" or "bolometer" indifferently to refer to the Germanium crystals. Each detector is surrounded by an individual casing made of ultra-pure copper. The detectors are held by teflon inside the copper casings and arranged on disks in a hexagonal arrangement to maximise self-shielding. The disks are surrounded by a thermal screen on the sides and the top and supported by a thick plate on the bottom. The plate and the screen are kept at 10 mK and shield the detectors from radioactivity. The disks, the screen and the plate are also made of ultra-pure copper.

Radioactivity in the electronics and the dilution unit leads to the emission of γ rays. To protect the detectors from this background, a 14 cm-thick circular lead shield is inserted below the 10 mK plate. The lead is dubbed *Roman* lead because it was found in a Roman shipwreck. It spent more than a thousand years at the bottom of the ocean: the contamination in ^{210}Pb is 200 times less than that of modern lead [3]. The detectors are additionally surrounded by four thermal screens at 1 K, 4.2 K, 40 K, 100 K and the vacuum chamber at 300 K. All those screens are also made of copper, selected for its relative purity.

Additional shields protect the detectors from background events. They surround the whole cryostat. They include:
- A thick (18 cm) layer of non Roman lead shields .
- A thinner (2 cm) Roman lead layer has been cast directly on the modern lead.
- A thick (50 cm) polyethylene shielding.

The polyethylene protects the detectors from neutrons, while the lead layers shields them from γ rays.

The radon level in the laboratory room is kept at a low ($\sim$20 Bq/m^3) level thanks to a ventilation system. The entire room volume is renewed 1.5 times in an hour. Between the cryostat and the lead layer, there is a small air volume of about 0.1 cubic meters. The air is constantly resupplied with deradonized air: a radon trap facility further decreases the radon level down to approximately 20 mBq/m^3. The radon level is monitored by a dedicated detector so that any anomalous rise can be quickly detected and investigated.

In Section 2.1.1, we mentioned the muon veto, which is used to monitor and reject neutrons induced by cosmic muons. This veto is made of 46 modules of plastic scintillators, which cover a surface of $\sim$100 m^2 around the polyethylene.

The whole setup is shown in Fig. 2.12 below.

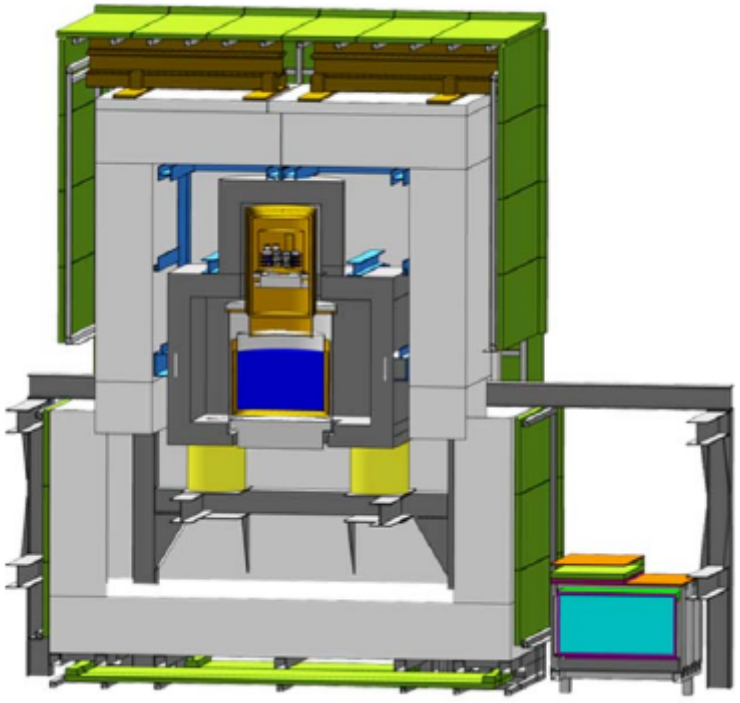

FIGURE 2.12 EDWELWEISS-II setup. The muon veto is shown in green. The polyethylene (PE) is shown in light gray. The lead shield is in dark gray and the copper thermal shields are shown in gold.

2.3.2 Infrastructure: EDELWEISS-III

The upgrade to EDELWEISS-III led to a few changes in the setup. The main change to the outer shielding lies in the addition of 4 new scintillator modules on top of the already existing ones (see Fig. 2.12). This addition was motivated by the change of the cryostat pulse tubes for a cryoline with different dimensions. With this new item, it was unclear whether the shields could close as tightly as before. New modules were therefore needed to cover for a possible central gap.

The Monte Carlo simulations we mentioned in 2.1.2 identified some internal components of EDELWEISS-II as major sources of background events (mostly neutrons and gammas). This led to a modification of the copper thermal shields and the addition of a PE shield above the circular Roman lead shield. The new copper thermal shields are made of ulra pure NOSV copper. The purity of this copper was ascertained at the Gran Sasso underground laboratory [72]. This study found that the remaining contamination was two order of magnitudes below that of the previous shields. The PE shield was installed to attenuate the neutron background emanating from the cold electronics at 1 K.

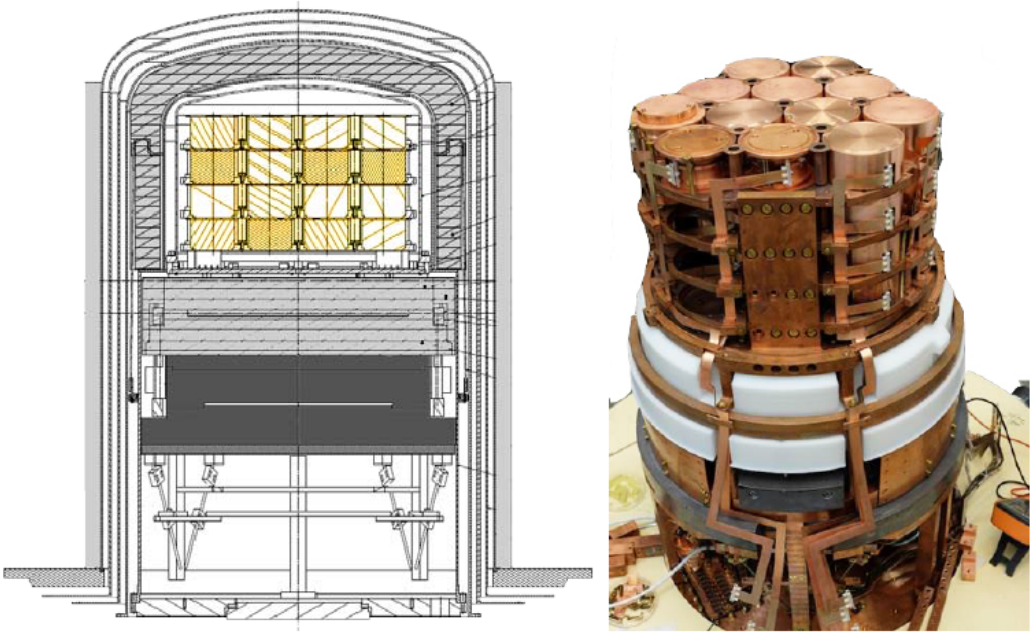

FIGURE 2.13 Left: scheme of the core setup for EDELWEISS-III. The gray (resp. dark gray) rectangles corresponds to the new PE shielding (resp. circular roman lead shield). The detector are shown in gold. Right: Photo of the FID detectors installed on the cryostat towers. This photo also shows the new PE shield (in white).

2.4 Cryogenics

2.4.1 Cryogenics: EDELWEISS-II

The EDELWEISS-II cryostat (see the left side of Fig. 2.14 for the detailed scheme) is a dilution cryostat whose cooling power is provided by the enthalpy of mixing of the two isotopes of Helium: ^{3}He and ^{4}He. It uses a reversed geometry design, with the experimental chamber on the top of the structure, allowing a lower level of vibrations and an easier access to the detectors. It is a nitrogen free system with three pulse tubes (for cooling) and a Helium reliquifier to reduce consumption. From the beginning, this cryostat was designed with a large volume, able to house up to 40 detectors. The cryostat design allows the detectors to operate at a stable temperature around 18 mK.

2.4.2 Cryogenics: EDELWEISS-III

The major difference in the cryogenic setup with respect to EDELWEISS-II consists in the replacement of the pulse tubes used to cool the 50 K and 100 K thermal shields. The new system combines a cryoline (see the right side of Fig. 2.14) and thermal machines, mounted on the walls outside of the lead and PE shields. This design aims at reducing vibration noise and microphonics.

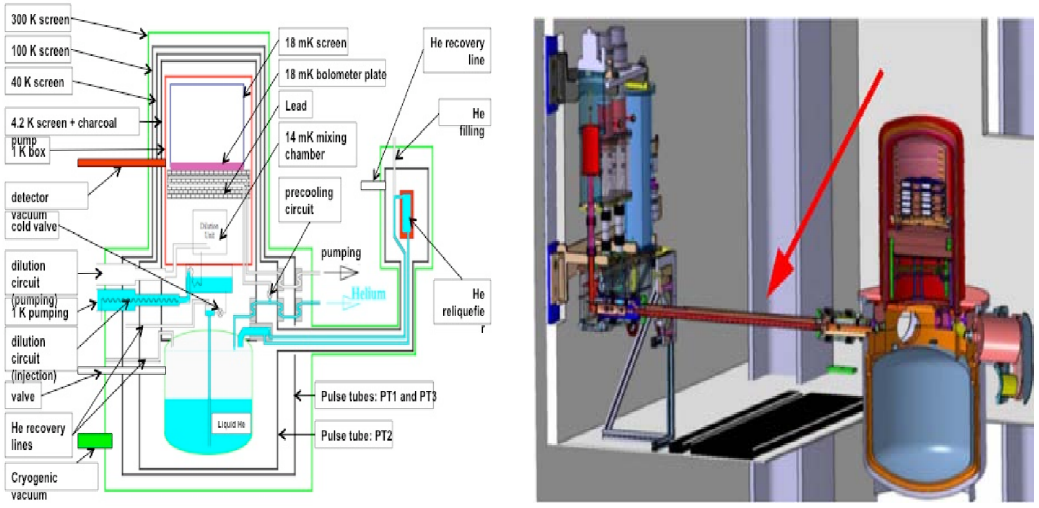

FIGURE 2.14 Left: Detailed scheme of the EDELWEISS cryostat. Right: Cryogenic setup showing the new cryoline. The thermal machines can be seen on the left side of this picture.

2.5 Electronics and data stream

2.5.1 Electronics and data stream: EDELWEISS-II

The read-out setup of EDELWEISS-II bolometers is made of a cold electronics part (FET preamplifier at the 100K stage and passive RC components at the 100K or 1K stage), and a room temperature part where a single module integrates various electronic components (such as the DAC for detector biasing and the components to amplify, filter and digitize the data). This module is called the bolometer box. These bolometer boxes deal with post-amplification, digitization and cold electronics management. They are directly plugged to the cryostat and send the data to the local network through optical fibers. The heat read-out relies on a differential AC measurement using a biFET. The signal is modulated so that contamination by low frequency noise is avoided. For the ionisation read-out, two 1 GΩ resistances are used for detector biasing and feedback capacitance discharging. More details can be found in [73]. The heat and ionization cold preamplifiers are shown in Fig. 2.15.

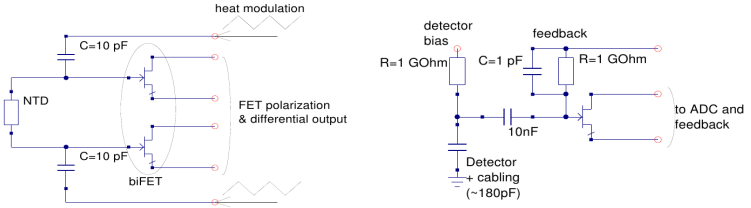

FIGURE 2.15 Cold electronics schemes used for EDELWEISS-II. Left: heat read-out. Right: ionisation read-out.

After digitization (at 100 kHz inside the bolometer box), the data is sent to acquisition computers via concentrators called "SuperCluzel". These computers provide a user interface to control the data acquisition process. A dedicated software called SAMBA is used to read the data and trigger when appropriate. The data acquisition chain is summarised in Fig. 2.16.

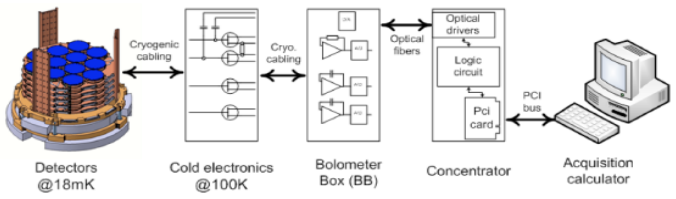

FIGURE 2.16 Overview of the EDELWEISS electronics from the detectors to data acquisition

2.5.2 Electronics and data stream: EDELWEISS-III

We have seen that the ionisation readout in EDELWEISS-II relies on a charge preamplifier with passive feedback. In EDELWEISS-III, a new version of the ionisation readout was designed. It works with an FET-based voltage follower, without feedback but with a gate potential periodically compensated (see Fig. 2.17): the capacitance is regularly discharged by an appropriate sequence of actions on the DAC commands. This new design allows long decay time constant for event pulses. The idea behind this is to use the low event rate to our advantage. Since there usually is a large gap between consecutive events, the signal can be recorded using long integration times. This allows us to extract important information at low frequencies where a better signal to noise ratio can be achieved. As a result, the resolution on the ionisation channel has improved substantially. This improvement is particularly relevant for low mass WIMP searches as we will see in Chapter 4.

The data acquisition was further modified by the introduction of a single crate tasked with the data redistribution. This crate replaces the "SuperCluzel" concentrators of EDELWEISS-II. The new solution is more robust and allows better synchronisation of the acquisition clock with the muon veto clock.

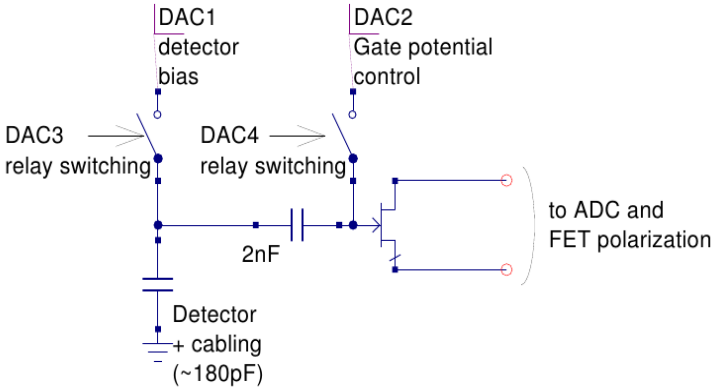

FIGURE 2.17 Cold electronics schemes used for EDELWEISS-II. Left: heat read-out. Right: ionisation read-out.

2.6 From EDELWEISS-II to EDELWEISS-III: a summary

While the overal setup did not change much, the detector evolution was a clear breakthrough. The new design has several new key benefits :

- **Size:** the detectors are more massive which allows increased exposure.
- **Fiducial volume:** In the new InterDigit schem, electrodes cover the full surface of the detector. We no longer need the guard electrodes and the fiducial volume increases relative to the full volume of the detector.
- **Background rejection:** The surface event rejection power has been increased and we saw no evidence of multiple Compton scatter events in the electronic response calibration.

The other major change lies in the improved electronics of the ionisation channels. The new design allows larger integration times and achieves an improvement of a factor two on the ionisation resolution. This is really important to ensure background rejection down to very low energies. As we will see later on, the ionisation resolution is also a key parameter for the reduction of the influence of a new type of background which we called the heat-only background. It will be discussed in detail in Chapter 4.

Chapter 3

Axion searches with EDELWEISS-II data

This chapter describes the analysis and results published in [74]. In this paper, we used EDELWEISS-II data to look for an elusive particle: the axion. We will first review the theoretical motivations for axions as well as their possible sources. We will then explain how they can be detected with the Germanium bolometers of the EDELWEISS experiment. After a brief description of the data selection procedure and backgrounds, we will explain how we were able to look for axions in four independent detection channels, with an emphasis on the various statistical procedures which we devised to interpret the data.

3.1 Axions: a theoretical introduction

The axion's early history is closely associated to the so-called QCD CP problem: the QCD lagrangian includes a CP violating term:

$$\mathcal{L}_\Theta = \Theta \left(\frac{\alpha_s}{8\pi}\right) G^{\mu\nu a} \bar{G}^a_{\mu\nu} \tag{3.1}$$

where G is the color field strength tensor, $\bar{G}$ its dual, α_s the strong coupling constant and Θ is a phase parameter. Experimental limits on the neutron electric dipole moment imply that $|\Theta| \lesssim 10^{-10}$ [75] even though a value of $\mathcal{O}(1)$ is otherwise perfectly satisfactory. This apparent fine-tuning of Θ is the CP problem.

A dynamical solution to the QCP CP problem was suggested by Peccei and Quinn [76] with later contributions by Weinberg [77] and Wilczek [78]. This theory postulates a new $\mathcal{U}(1)_{\mathrm{PQ}}$ (where PQ stands for Peccei-Quinn) symmetry, which is spontaneously broken. The corresponding Goldstone boson, is called the axion. Non perturbative QCD effects and the CP violating term induce a potential for the axion field. The relevant term can be written as:

$$\mathcal{L} = \left(\Theta - \frac{\phi_A}{f_A}\right) \left(\frac{\alpha_s}{8\pi}\right) G^{\mu\nu a} \bar{G}^a_{\mu\nu} \tag{3.2}$$

where ϕ_a is the axion field and f_A is the axion decay constant. The axion field will eventually settle to a value that minimises this effective potential. The minimum is reached for $\Theta = \frac{\phi_A}{f_A}$, leading to the dynamic cancelling of the CP violating term. This allows us to account for the very small value of the neutron electric dipole moment.

The axion mass and the strength of its couplings to Standard Model particles are inversely proportional to the axion decay constant f_A:

$$m_A = \left[\frac{z}{(1+z+w)(1+z)}\right]^{\frac{1}{2}} \frac{f_\pi m_\pi}{f_A} = 6\,\mathrm{eV} \times \left(\frac{10^6\,\mathrm{GeV}}{f_A}\right) \tag{3.3}$$

where $m_\pi = 135$ MeV is the pion mass, $f_\pi \approx 92$ MeV the pion decay constant, while $z = m_u/m_d = 0.56$ and $w = m_u/m_s = 0.029$ are the mass ratios of the lightest up, down and strange quarks, with significant uncertainties especially for z [79].

The original axion model, with f_A associated with the electroweak scale, was dismissed after extensive searches [79]. However, by allowing f_A to vary, the axion can be made to escape current detection constraints. Popular models include the so-called hadronic

models such as KSVZ (Kim-Shifman-Vainstein-Zakharov) [80, 81] and the GUT models such as the DFSZ (Dine-Fischler-Srednicki-Zhitnitskii) model [82, 83].

These models can be used to compute the effective coupling of axions to Standard Model particles, such as photons, electrons and nucleons. Of course, the computation depends on the underlying theory [84, 85]. For example, hadronic axions are coupled to new, heavy quarks and do not interact with ordinary quarks and leptons at tree level. This leads to a strong suppression of g_{Ae}. On the contrary, DFSZ axions require that Standard Model quarks and leptons carry a Peccei-Quinn charge, leading to no such suppression. Experimental searches and astrophysical constraints can be translated to limits on f_A, or equivalently on the axion mass, within a given axion model.

Besides axions, other pseudo scalar fields have been predicted by BSM theories, such as string theory [86]. These axion-like particles or ALPs can interact with known particles in much the same way as proper axions. However, unlike axions, their coupling to SM particles is not directly related to their mass. Because we want to report general results, which may apply for different candidate particles, we will adopt a mostly model-independent approach: we will report results on, say, the generic coupling of axions and ALPs to electrons independently of the underlying theory. It is then possible to pick a theory to interpret results. We will work with the following effective lagrangians:

$$\mathcal{L} = -\frac{1}{4} g_{A\gamma} F^{\mu\nu} \tilde{F}_{\mu\nu} \phi_A \qquad \text{(coupling to photons)} \tag{3.4}$$

$$\mathcal{L} = i\bar{\psi}_N \gamma_5 (g^0_{AN} + g^3_{AN}\tau_3)\psi_N \phi_A \qquad \text{(coupling to nucleons)} \tag{3.5}$$

$$\mathcal{L} = i g_{Ae} \bar{\psi}_e \gamma_5 \psi_e \phi_A \qquad \text{(coupling to electrons)} \tag{3.6}$$

where $F^{\mu\nu}$, ψ_e, ψ_N, g^0_{AN}, g^3_{AN}, g_{Ae} and $g_{A\gamma}$ are the electromagnetic field tensor, the electron field, the nucleon isospin double, the isoscalar axion-nucleon coupling, the isovector axion-nucleon coupling, the coupling electrons and the coupling to photons, respectively.

We will also interpret our results in terms of f_A (or equivalently m_A) in the context of the KSVZ and DFSZ axion models. In order to do that, we need to relate each coupling to SM particles to the axion decay constant f_A. Let us now give the relevant formulas with a systematic emphasis on the difference between the DFSZ and FSVZ axion models.

Axion photon coupling

The coupling to photons $g_{A\gamma}$ is related to the axion decay constant through:

$$g_{A\gamma} = \frac{\alpha}{2\pi f_A}\left[\frac{E}{N} - \frac{2(4+z+w)}{3(1+z+w)}\right] \text{ (energy)}^{-1} \tag{3.7}$$

where α is the fine structure constant and E/N is the ratio of the electromagnetic to color anomalies of the Peccei-Quinn symmetry ($E/N = 8/3$ and 0 for DFSZ and KSVZ models, respectively).

Axion nucleon couplings

In KSVZ models [84, 85], they are related to f_A by the following expressions:

$$\begin{aligned} g^0_{AN} &= -7.8\times10^{-8}\left(\frac{6.2\times10^6\text{GeV}}{f_A}\right)\left(\frac{3F-D+2S}{3}\right) \\ g^3_{AN} &= -7.8\times10^{-8}\left(\frac{6.2\times10^6\text{GeV}}{f_A}\right)\left[(D+F)\frac{1-z}{1+z}\right] \end{aligned} \tag{3.8}$$

Here, the dimensionless constants $F = 0.462$ and $D = 0.808$ [87] are invariant matrix elements of the axial current. S is the dimensionless flavor-singlet axial-vector matrix element. It is still poorly constrained. It can be estimated by measurements of the polarized nucleon structure function, but there are large uncertainties. Intervals for S proposed in the literature lie in the range $0.15 - 0.55$ [88, 89]. Whenever we interpret our results in the KSVZ model, we will use the benchmark value $S = 0.5$.

In non-hadronic axions such as the DFSZ model, the values for g^0_{AN} and for g^3_{AN} depend on two additional unknown parameters, X_u and X_d [84]. They are related to $\tan\beta_{DFSZ}$, the ratio of two Higgs vacuum expectation values of the model, by the relations $X_u + X_d = 1$ and $X_d = \cos^2\beta_{DFSZ}$. The expressions for g^0_{AN} and for g^3_{AN} are given in this case by [84]:

$$\begin{aligned} g^0_{AN} &= 5.2\times10^{-8}\left(\frac{6.2\times10^6\,\text{GeV}}{f_A}\right)\left[\frac{(3F-D)(X_u-X_d-3)}{6} + \frac{S(X_u+2X_d-3)}{3}\right] \\ g^3_{AN} &= 5.2\times10^{-8}\left(\frac{6.2\times10^6\,\text{GeV}}{f_A}\right)\frac{D+F}{2}\left(X_u - X_d - 3\frac{1-z}{1+z}\right)\ . \end{aligned} \tag{3.9}$$

For the interpretation of axion results in the DFSZ model, we will take $\cos^2\beta_{DFSZ} = 1$ as a benchmark value.

Axion electron coupling

For DFSZ axions, we have:

$$(g_{Ae})_{\mathrm{DFSZ}} = \frac{m_e}{3f_A}\cos^2\beta_{\mathrm{DFSZ}} \tag{3.10}$$

where m_e is the electron mass while $\tan\beta_{\mathrm{DFSZ}}$ was already defined in Section 3.2.1.2. Here again, for model-dependent studies we will fix $\cos\beta_{\mathrm{DFSZ}} = 1$. In that case g_{Ae} is given by:

$$(g_{Ae})_{\mathrm{DFSZ}} \simeq 1.68\times10^{-4}\frac{\mathrm{GeV}}{f_A} \simeq 2.84\times10^{-8}\frac{m_A}{\mathrm{keV}}. \tag{3.11}$$

As we remarked earlier, there is no axion-electron coupling at tree level for KSVZ axions. g_{Ae} is therefore only determined by radiative corrections [85]. As a consequence it is smaller than in the DFSZ model by a factor of about α^2. The expression for this parameter is:

$$(g_{Ae})_{\mathrm{KSVZ}} = \frac{3\alpha^2 N m_e}{2\pi f_A}\left(\frac{E}{N}\ln\frac{f_A}{m_e} - \frac{2}{3}\frac{4+z+w}{1+z+w}\ln\frac{\Lambda}{m_e}\right), \tag{3.12}$$

where $E/N = 0$ as discussed in Section 3.2.1.1 for hadronic axions, and $\Lambda \sim 1$ GeV is associated with the QCD confinement scale. We therefore obtain numerically:

$$(g_{Ae})_{\mathrm{KSVZ}} \simeq -5.7\times10^{-7}\,\frac{\mathrm{GeV}}{f_A} \tag{3.13}$$

In the following sections, we are going to study the couplings of Eq. 3.4,3.5,3.6. We will see that ALPs may be found in the Milky Way Dark Matter halo or may be produced in the Sun through various processes. We will compute the expected flux on Earth for each of these processes. We will then see that the Germanium bolometers of the EDELWEISS experiment are powerful axion detectors given that they are sensitive to ALPs through two independent detection channels: the coherent Bragg diffraction and the axio-electric effect, which is the analogue of a photo-electric effect with the absorption of an axion instead of a photon. This is how we were able to carry out four different axion searches, each associated with a different production/detection scenario. For each scenario, we will derive and discuss constraints on the ALP-SM couplings. In particular, these constraints will be translated into axion mass constraints, within the specific DFSZ and KSVZ axion models.

3.2 Possible axion sources: the Sun and the galactic halo

We now turn to possible axion sources. We will first describe the various mechanisms which can lead to axion production in the Sun (Section 3.2.1). We will then see how, under the hypothesis that axions make up all dark matter, the galactic halo may also be a major source of axions. (Section 3.2.2).

3.2.1 Axion production in the Sun

Below, we show the complete list of production mechanisms which we considered in our axion searches:

1. Primakoff production: $\gamma \rightarrow$ A in the presence of charged particles
2. Nuclear magnetic transition of ^{57}Fe nuclei: $^{57}\mathrm{Fe}^{*} \rightarrow ^{57}\mathrm{Fe}$ + A
3. Compton-like scattering: $\mathrm{e}^{-} + \gamma \rightarrow \mathrm{e}^{-}$ + A
4. Axion bremsstrahlung: $\mathrm{e}^{-} \rightarrow \mathrm{e}^{-}$ + A in the presence of charged particles
5. Axio-recombination: e^{-} + I $\rightarrow \mathrm{I}^{-}$ + A where I is an ion
6. Axio-deexcitation: $\mathrm{I}^{*} \rightarrow$ I + A where I^{*} is an excited state of I

From here on, we will refer to the sum of axio-recombination and axio-deexcitation as the axio-RD mechanism.

The intensity of each mechanism is model-dependent. For example, in the case of non hadronic axions such as those described by the DFSZ model, fluxes related to Compton and bremsstrahlung processes are far more intense than those predicted by hadronic models for the same value of f_A. In this case, the Compton and bremsstrahlung channels for axion production largely prevail over the Primakoff effect. On the contrary, the latter dominates hadronic axion emission. Fig. 3.1 shows the evaluated fluxes on Earth for the various processes.

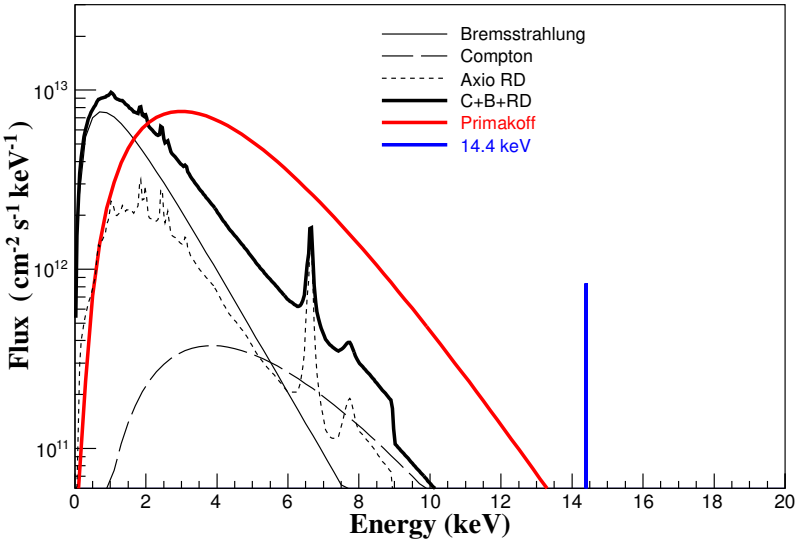

FIGURE 3.1 Predicted solar axion fluxes from different mechanisms. The thick solid black line corresponds to the sum of Compton, bremsstrahlung and axio-RD (recombination-deexcitation). Red: Primakoff axions. Blue: ^{57}Fe nuclear transition. The intrinsic width of this line, dominated by Doppler broadening, is 5 eV. The effective axion couplings corresponding to the represented fluxes are $g_{A\gamma} = 10^{-9}$ GeV^{-1}, $g_{Ae} = 10^{-11}$ and $g_{AN}^{\text{eff}} = 10^{-7}$.

3.2.1.1 Production by Primakoff effect

Axions can be efficiently produced in the Sun by the inverse Primakoff conversion of thermal photons in the electromagnetic field of the solar plasma.

The expected solar Primakoff axion flux was estimated in [90], and is well approximated by the expression where the energy E is in keV:

$$\frac{d\Phi}{d\mathrm{E}} = \frac{6.02 \times 10^{14}}{\mathrm{cm^2\,keV\,s}} \left(\frac{g_{A\gamma} \times 10^8}{\mathrm{GeV}^{-1}} \right)^2 \mathrm{E}^{2.481} e^{-E/1.205} \tag{3.14}$$

This corresponds to a broad spectrum, with an average energy of about 4.2 keV and a negligible intensity above 10 keV as shown in Fig. 3.1. The intensity of the resulting axion flux scales as $\mathrm{g}_{A\gamma}^2$.

N.B. This flux estimation is valid for ultra-relativistic axions. In [91], a calculation of the Primakoff flux is also given for non-relativistic axions. In the mildly relativistic regime ($m_A \lesssim 200$ eV), the corresponding correction to the flux is of the order of 1 %.

3.2.1.2 Production via ^{57}Fe nuclear magnetic transition

As axions couple to nucleons in many models, another possible mechanism of axion production in the Sun can be their emission following the de-excitation of the low-lying energy levels of some nuclei populated by the high solar temperature. In the context of the EDELWEISS experiment, the M1 transition of ^{57}Fe nuclei is of particular interest as it may lead to the emission of a 14.4 keV monochromatic axion line: this line can be readily measured by the Germanium bolometers as they are sensitive to keV-scale energy depositions with excellent resolution.

This particular isotope has many other advantages: it is stable and remarkably abundant among heavy elements in the Sun (the average ^{57}Fe density in the Sun's core is about 9×10^{19} cm^{-3} [92]). Last, but not least, its first excited nuclear state, placed at $E^* = 14.4$ keV above the ground state, is low enough to be thermally excited in the hot interior of the Sun, where the average temperature is $kT \sim 1.3$ keV [93, 94]. The relaxation of the excited ^{57}Fe nucleus is done mostly through the M1 channel (in this reaction the E2/M1 mixing ratio is 0.002) in which an axion or a photon can be emitted.

As we saw in Eq. 3.5, the effective Lagrangian which couples axions and nucleons involve the isoscale and isovector axion-nucleon coupling constants: g^0_{AN} and g^3_{AN}.

Let us now give the expected event rate for axion production in the deexcitation of ^{57}Fe. We start from the axion-to-photon emission rate ratio for the M1 nuclear transition in the long-wavelength limit [95]:

$$\frac{\Gamma_{\rm A}}{\Gamma_\gamma} = \left(\frac{k_{\rm A}}{k_\gamma}\right)^3 \frac{1}{2\pi\alpha} \frac{1}{1+\delta^2} \left[\frac{g^0_{\rm AN}\beta + g^3_{\rm AN}}{(\mu_0 - 1/2)\beta + \mu_3 - \eta}\right]^2 , \tag{3.15}$$

where $k_{\rm A}$ and k_γ are the momenta of the outgoing axion and photon respectively, and α is the fine structure constant. The quantities μ_0=0.88 and μ_3=4.71 are the isoscalar and isovector nuclear magnetic moments respectively, given in nuclear magnetons. The parameter δ denotes the E2/M1 mixing ratio for this particular nuclear transition, while β and η are nuclear structure dependent ratios. Their values for the 14.4 keV de-excitation process of an ^{57}Fe nucleus are δ=0.002, $\beta = -1.19$, and $\eta = 0.8$ [94].

Using these values in Eq. (3.15) we find:

$$\frac{\Gamma_{\rm A}}{\Gamma_\gamma} = \left(\frac{k_{\rm A}}{k_\gamma}\right)^3 1.82\ (-1.19 g^0_{\rm AN} + g^3_{\rm AN})^2 . \tag{3.16}$$

We can the write the 14.4 keV axion emission rate:

$$\mathcal{N}_{\rm a} = \mathcal{N}\ w_1\ \frac{1}{\tau_\gamma}\ \frac{\Gamma_{\rm a}}{\Gamma_\gamma} \quad {\rm g}^{-1}\ {\rm s}^{-1}\,, \tag{3.17}$$

where $\mathcal{N} = 3.0 \times 10^{17}$ g^{-1} is the number of ^{57}Fe nuclei per 1 g of solar matter [96], and $\tau_\gamma = 1.3 \times 10^{-6}$ s is the mean lifetime of the first excited nuclear state of ^{57}Fe associated with the partial gamma decay width of that state. w_1 is the probability to thermally excite ^{57}Fe to its first excited state with energy $E^* = 14.4$ keV.

The ^{57}Fe solar axion differential flux expected at the Earth is then given by :

$$\frac{d\Phi_{\rm a}(E_{\rm a})}{dE_{\rm a}} \;=\; \frac{1}{4\pi d_\odot^2} \int_0^{R_\odot} \mathcal{N}_{\rm a}\, \frac{1}{\sqrt{2\pi}\sigma(T(r))}\, e^{-\frac{(E_{\rm a}-E^*)^2}{2\sigma(T(r))^2}} \times \rho(r)\, 4\pi r^2\, dr \tag{3.18}$$

where $E_{\rm a}$ is the axion energy $d_\odot$ is the Earth-to-Sun distance, $R_\odot$ is the solar radius and $T(r)$ and $\rho(r)$ are the temperature and mass profile in the Sun interior.

In this formula, we had to account for Doppler broadening caused by the thermal motion of ^{57}Fe nuclei in the hot solar interior. This effectively convolves the distribution with a Gaussian with resolution $\sigma(T) = E^*\sqrt{\frac{kT}{m}}$. With T as the temperature of the Sun where the axion is produced and m as the ^{57}Fe mass, we have $\sigma(T) \sim$ eV. This is why the ^{57}Fe axion signal appears as a sharp blue line in Fig. 3.1.

Integrating over the axion energy, we find

$$\Phi_{14.4} = \left(\frac{k_{\rm A}}{k_\gamma}\right)^3 \times 4.56 \times 10^{23}\ (g_{AN}^{\rm eff})^2\ {\rm cm}^{-2}\,{\rm s}^{-1}. \tag{3.19}$$

where we used the Standard Solar Model [97] tables for $T(r)$ and $\rho(r)$. We have introduced $g_{AN}^{\rm eff}$, an effective axion to nucleon coupling:

$$g_{AN}^{\rm eff} \equiv (-1.19 g_{\rm AN}^0 + g_{\rm AN}^3) \tag{3.20}$$

This derivation follows that of [96]. However, we wanted to be able to compute the expected flux in the non-relativistic limit, which is why the factor $\left(\frac{k_{\rm A}}{k_\gamma}\right)^3$ has not been set to one. We are then free to interpret our results in the context of the DFSZ or KSVZ model with the help of the expressions given in Eq. (3.8) and Eq. (3.9).

3.2.1.3 Compton, bremsstrahlung and axio-RD processes

We are now interested in the coupling of axions to electrons in the solar plasma. Axions can be emitted within the Sun by the Compton process ($\gamma + e^- \rightarrow e^- + A$) and by bremsstrahlung ($e^- + X \rightarrow e^- + X + A$, where X is an electron, a hydrogen or helium nucleus) occurring in the hot plasma. We also consider emission processes associated with the electron capture by an ion (axio-recombination), and to the bound-bound "axio-deexcitation": from the reevaluation by [98], these processes lead to a non-negligible flux, which we call axio-RD. Since all these fluxes scale as g_{Ae}^2 we can easily add these axion production processes. For the axio-RD process we use a tabulated spectrum drawn in [98] (Fig. 3.1), while for the Compton-bremsstrahlung process we use the estimation [98]:

$$\begin{aligned}\frac{d\Phi}{d\mathrm{E}} &= \left(\frac{d\Phi}{d\mathrm{E}}\right)^{\mathrm{Compton}} + \left(\frac{d\Phi}{d\mathrm{E}}\right)^{\mathrm{bremsstrahlung}} \\ &= g_{Ae}^2 \times 1.33 \times 10^{33}\ \mathrm{E}^{2.987}\ e^{-0.776\ \mathrm{E}} \\ &\quad + g_{Ae}^2 \times 2.63 \times 10^{35}\ \mathrm{E}\ e^{-0.77\ \mathrm{E}} \frac{1}{1 + 0.667\ \mathrm{E}^{1.278}}\end{aligned} \tag{3.21}$$

where fluxes are in $\mathrm{cm}^{-2}\ \mathrm{s}^{-1}\ \mathrm{keV}^{-1}$ and energies in keV.

3.2.2 Axions as dark matter

We are now going to consider a fundamentally different axion source. We already remarked in Chapter 1 that axions may be credible Dark Matter candidates. Indeed, they have weak couplings and can account for the dark matter density (since axions are bosons, they are not subject to the Pauli exclusion principle and can compensate their small mass by large densities). The best motivated candidate is a QCD axion with a mass in the $\left[10^{-6}, 10^{-3}\right]$ eV range: it solves the QCD CP problem and provides the appropriate Dark Matter density without excessive tuning. However, other models exist [99], which predict keV-scale ALPs. In the following, we will assume that axions make up all of the Dark Matter halo in the Milky Way, with density $\rho_{\mathrm{DM}} = 0.3\ \mathrm{GeV/cm}^3$ in the solar neighborhood. This assumption is the same as that made for "standard" WIMP direct dection. The total, average flux of dark matter axions on Earth is then:

$$\Phi_{\mathrm{DM}}[/\mathrm{cm}^2/\mathrm{s}] = \rho_{\mathrm{DM}} \cdot \mathrm{v_A}/\mathrm{m_A} = 9.0 \times 10^{15} \left(\frac{\mathrm{keV}}{\mathrm{m_A}}\right) \cdot \beta \tag{3.22}$$

In this expression, m_A is the axion mass and v_A the mean axion velocity distribution with respect to the Earth, $\beta \simeq 10^{-3}$. The flux does not depend on any axion coupling (but it depends on the axion mass).

3.3 Axion interactions in EDELWEISS detectors

We are now going to introduce two different mechanisms which can be used for axion detection in EDELWEISS' Germanium bolometers.

- Through the Primakoff effect, axions can be converted into photons in the intense electric field of the germanium crystal [100]. The wavelength of relativistic solar axions, with an energy of a few keV, is of the same order of magnitude as the inter-atomic spacing of the detector. Therefore, depending on the direction of the incoming axion flux with respect to the lattice, the axion signal can be enhanced significantly through Bragg diffraction (EDELWEISS detectors are mono-crystals). The corresponding correlation of the count rate with the position of the Sun in the sky also helps further with an effective background rejection.

- Axions can also be detected through the axio-electric effect, the equivalent of a photo-electric effect with the absorption of an axion instead of a photon:

$$\mathrm{A}+\mathrm{e}^- + \mathrm{Z} \rightarrow \mathrm{e}^- + \mathrm{Z} \tag{3.23}$$

  The axio-electric cross-section as a function of the axion energy was computed in [99, 101, 102], and is represented for several values of its mass in Fig. 3.2:

$$\sigma_{Ae}(E) = \sigma_{\mathrm{pe}}(E)\frac{g_{Ae}^2}{\beta}\frac{3E^2}{16\pi\alpha m_e^2}\left(1-\frac{\beta^{\frac{2}{3}}}{3}\right) \tag{3.24}$$

  In this expression, β is the ratio of the axion velocity to the speed of light, α is the fine structure constant, m_e the electron mass σ_{pe} is the germanium photoelectric cross-section, taken from [103] and completed with [104].

  The photoelectric cross-section has a characteristic sawtooth shape owing to the shell structure of Germanium: if the incoming photon energy drops below the binding energy of a given shell, no electron from that shell can be ejected leading to sudden drops in the cross section. In the following analyses, we will set the electron recoil energy threshold at 2.5 keV. Hence, the only relevant shell is the K shell at 11 keV. These discontinuities in the signal shape play an important role in the analysis: the intricate signal shape allows for an easier background subtraction in likelihood analyses, which compare the shape of the signal to the shape of the expected background.

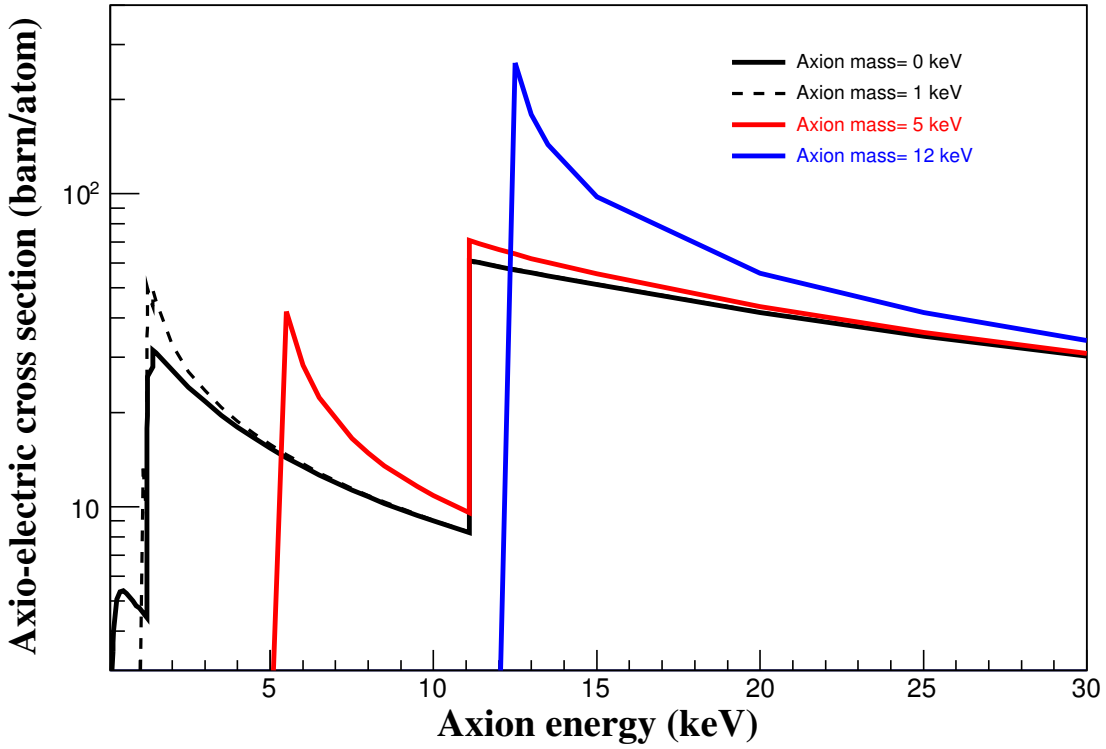

FIGURE 3.2 Axio-electric cross section for different axion masses, computed for germanium and normalized with $g_{Ae} = 1$. The discontinuities at $1.2 - 1.4$ keV and 11.1 keV are due to electron shell energies.

Let us conclude with a discussion of the choice of the analysis channels. We have 4 different axion sources and 2 detection channels, which gives a total of 8 possible combinations. We chose to restrict the analysis to four channels, summarised in Table 3.1 below. Even though the final choice was somewhat arbitrary, we used several guiding principles: we prioritise channels which involve a single coupling in order to report a simple interpretation of the results. Some channels have already been studied in previous experiments; it was decided to analyse them as well in order to situate the sensitivity of EDELWEISS.

Production channel	**Detection channel**
Primakoff in the Sun	Primakoff effect
CBRD in the Sun	axio-electric effect
^{57}Fe in the Sun	axio-electric effect
Axion Dark Matter	axio-electric effect

TABLE 3.1 Production and detection channels considered in this work.

3.4 EDELWEISS-II data and backgrounds

3.4.1 Data analysis for axion searches in EDELWEISS-II

All the axion searches presented here are based on data collected with ten ID bolometers during 14 months in 2009-2010 (the so-called Run12), as described in [1, 71].

As we have just seen, axions can generate electron recoils through their weak coupling either to photons (Primakoff effect) or to electrons (axio-electric effect). In Chapter 2, we saw that it was possible to use the dual heat-ionisation to specifically select electronic recoils: we will look for a potential axion or ALP signal in these events. We will also use the surface discrimination to our advantage as we want to look for axions in a clean, fiducial region with as little background contamination as possible.

The purpose of this section is to give a detailed account of the data selection procedure, which is the same as that used to derive the results published in [74]. We will also see that the dominant background comes from gamma events (unrelated to axions) for which we built a specific model.

The offline pulse reconstruction and calibration are the same as [1, 71] and simular to that described in Chapter 4. We looked for low-energy axion-induced recoils in the inner volume of the crystal by imposing a fiducial cut:

- Fiducial events were selected by requiring the absence of any signal above 4 sigma on the veto and guard electrodes and by constraining the difference in the measured values of the two collecting electrodes. The efficiency of this cut results in a fiducial mass of 160 g for each detector [71].
- For each fiducial event, we measured both the heat energy E_{heat} and a fiducial ionization energy E_{ion}, based on the combination of signals from both collecting electrodes. The combination is defined as follows. For two fiducial ionisation channels E_{ion1} and E_{ion2}, with resolutions σ_1 and σ_2, a combined ionisation estimator E_{ion} can be written as:

$$E_{\text{ion}} = w \times E_{\text{ion1}} + (1 - w) \times E_{\text{ion2}} \tag{3.25}$$

  The best estimator extremises the variance. Hence, solving for

$$\frac{d\left(w^2\sigma_1^2 + (1-w)^2\sigma_1^2\right)}{dw} = 0 \tag{3.26}$$

we obtain:

$$E_{\rm ion} = \frac{\sigma_2^2}{\sigma_1^2+\sigma_2^2} E_{\rm ion1} + \frac{\sigma_1^2}{\sigma_1^2+\sigma_2^2} E_{\rm ion2} \tag{3.27}$$

as the best ionisation estimator. Fiducial electron recoils are gaussian distributed along the line $E_{\rm ion} = E_{\rm heat}$. We rejected events beyond three standard deviations from this line.

To facilitate the analyses, it is better to work with a homogeneous data set for each detector. This is why we discarded time periods with noisy fiducial ionization or heat signals. This selection yields 280 live days per detector on average. The total exposure adds up to 448 kg.d in this analysis. It is larger than the WIMP-search exposure published in [1] mainly because the axion search does not depend as strongly on the purity of the fiducial selection, and requirements on the resolution on the heat and ionization guard signals can be relaxed. Misreconstructed pulses were also rejected: a cut was applied on the χ^2 of the fit to heat pulse shapes, with 98.7 % efficiency. We also rejected coincidence events in neighboring bolometers (we do not expect multiple scatters from axions) and events detected in the muon veto. The latter has negligible deadtime [69].

At low energies, an efficiency loss ϵ_{online} appears because of the online trigger (see Fig. 3.3). The efficiency function was computed from our knowledge of the time variations of this trigger. It was cross-checked with gamma calibrations. In addition, we selected events with both heat and fiducial ionization above a given threshold defined on a per-detector basis. The cut on fiducial ionization is essential to remove the large number of the so called heat-only pulses recorded during the experiment. Heat-only events are events which trigger no signal on the ionisation channels. A thorough analysis of heat-only events will be given in Chapter 4 in the context of the low mass WIMP analyses with EDELWEISS-III data. In the axion analyses of this Chapter though, the strict requirement on the fiducial ionisation threshold removes virtually all heat-only events.

Finally, for each selected event we combined the heat and fiducial ionization to obtain an optimal energy estimator for fiducial electron recoils: $\tilde{E} = w_{\rm heat}\, E_{\rm heat} + w_{\rm ion}\, E_{\rm ion}$ where $w_{\rm heat}$ and $w_{\rm ion}$ are defined as in Eq. 3.27. See Table 3.2 for the full list of weights. An analysis threshold on $\tilde{E}$ is set for each detector, by requiring that $\epsilon_{online}(\tilde{E}) > 50\%$ and $\epsilon_{other\ cuts}(\tilde{E}) > 95\%$. With these cuts, three detectors have a threshold at 2.5 keV, two at 3 keV and five at 3.5 keV. The average FWHM at low energy is 0.8 keV for $\tilde{E}$.

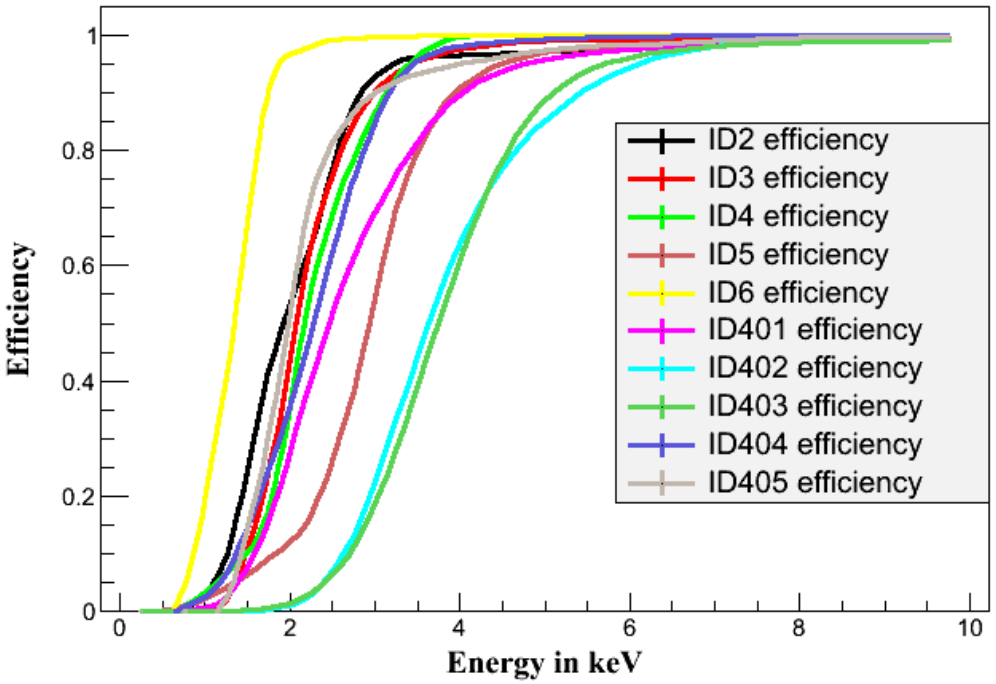

FIGURE 3.3 Online trigger efficiency as a function of the energy in keV. All bolometers are labeled as IDx.

Name	Estimator	FWHM (keV)	Live Days
ID2	$\tilde{E} = 0.7\,\mathrm{Efid} + 0.3\,\mathrm{Eheat}$	0.77	213.536
ID3	$\tilde{E} = 0.5\,\mathrm{Efid} + 0.5\,\mathrm{Eheat}$	0.49	311.03
ID4	$\tilde{E} = 0.3\,\mathrm{Efid} + 0.7\,\mathrm{Eheat}$	0.55	279.693
ID5	$\tilde{E} = 0.55\,\mathrm{Ecol2} + 0.45\,\mathrm{Eheat}$	0.68	317.682
ID6	$\tilde{E} = 0.3\,\mathrm{Efid} + 0.7\,\mathrm{Eheat}$	0.48	300.466
ID401	$\tilde{E} = 0.7\,\mathrm{Efid} + 0.3\,\mathrm{Eheat}$	0.67	283.881
ID402	$\tilde{E} = 0.7\,\mathrm{Efid} + 0.3\,\mathrm{Eheat}$	0.91	233.51
ID403	$\tilde{E} = 0.9\,\mathrm{Efid} + 0.1\,\mathrm{Eheat}$	0.67	295.232
ID404	$\tilde{E} = 0.5\,\mathrm{Efid} + 0.5\,\mathrm{Eheat}$	0.75	273.026
ID405	$\tilde{E} = 0.4\,\mathrm{Ecol1} + 0.6\,\mathrm{Eheat}$	0.72	295.053

TABLE 3.2 Estimator and live days table for the axion analysis. When a sensor is not functioning, it is not used in the estimator. For instance, we do not use collectrode 2 for ID405. Most dysfunctional channels are veto or guard electrodes, which is not detrimental to axion searches.

3.4.2 Backgrounds for axion searches in EDELWEISS-II

The background consists of a Compton profile with a smooth, slightly decreasing energy dependence, together with radioactive peaks, notably identified at 10.37 keV (^{68}Ge), 9.66 keV (^{68}Ga), 8.98 keV (^{65}Zn), 6.54 keV (^{55}Fe), 5.99 keV (^{54}Mn) and 4.97 keV (^{49}V). An additional smooth background increase at low energy may also be expected from unrejected surface interactions. Heat-only events and nuclear recoils are negligible. The former because of the imposed ionisation cut. The latter because we specifically select electron recoil events. In the axion searches described below, two different background models are used depending on the search:

1. *Primakoff solar axions.* In this study, we will exploit the time and energy dependence of the axion signal to quantify $g_{A\gamma}$. This results in an effective background rejection of about two orders of magnitude [105]. Furthermore the expected global energy distribution of the signal has a larger width than the detector FWHM. As a consequence we are allowed to include all radioactive peaks in the background model used for this analysis, in addition to a smooth component (see Section **??** for more details). The smooth time variation of these peaks is negligible with respect to the sharp and fast-varying axion signal. This analysis also requires that we first study each detector individually. For each detector, we define (and adjust) the following background model:

$$b_{\text{bolo}}(E) = C + \frac{1}{\sqrt{2\pi}} \sum_i \left(\frac{A_i}{\sigma_i} e^{\frac{-(E-E_i)^2}{2\sigma_i^2}} \right) \tag{3.28}$$

Fig. 3.4 below shows the typical low energy fiducial electron recoil spectrum and its fit with the above formula.

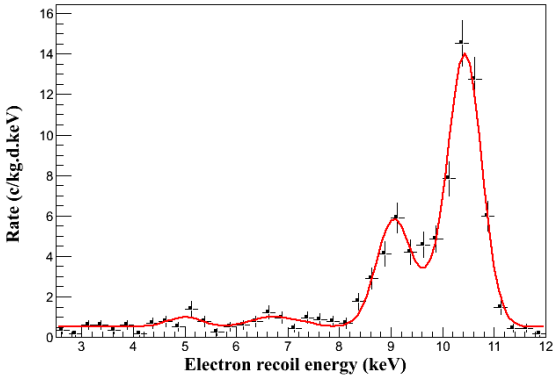

FIGURE 3.4 Efficiency-corrected electron recoil spectrum in the fiducial volume of a single detector called ID401 in the range [2.5-12] keV. Red: background model fit.

2. *Other axion searches.* In all other searches, the axion signal has no time dependence and is simply identified by its spectral shape (such as a line) in the stacked spectrum of all detectors. The time evolution of the 8.98 keV and 10.37 keV line intensities (with decay times of 243.7 and 271.0 days, respectively) allowed us to measure the intensity of these specific cosmogenic lines and include them in the background model, independently from a potential time-independent axion signal at the same energy. Let us explain how we fitted these amplitudes. In Fig. 3.5, we show the time distributions of the 10.37 and 8.98 peaks of the stacked recoil spectrum. For each peak, a specific energy window was selected so as to minimise pollution from other peaks. The peak amplitudes were then appropriately normalised to account for the size of the energy window. Sharp peaks are also visible. They occur after neutron calibrations which activate radioactive isotopes. For instance, neutron activation leads to the production of ^{71}Ge. It decays with half life of 11.43 days and boosts the gamma line at 10.37 keV.

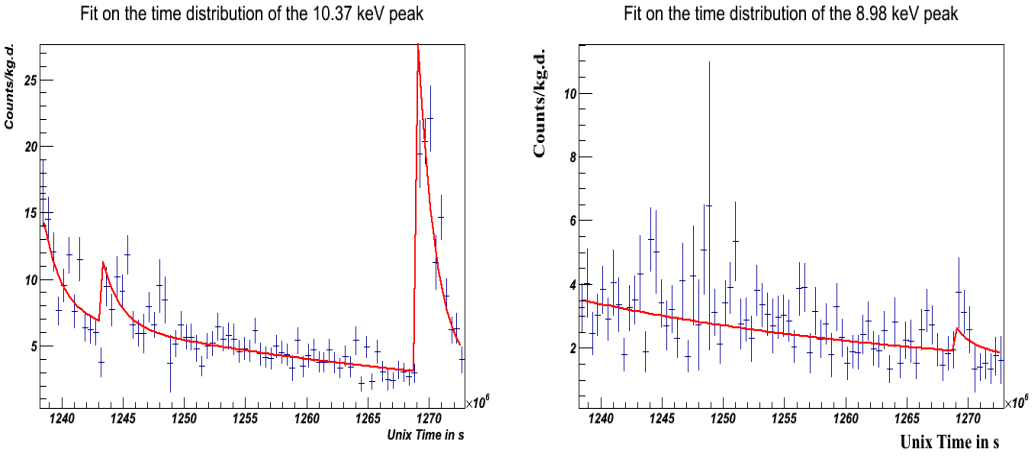

FIGURE 3.5 Left (resp. right): Time distribution of the 10.37 keV (resp. 8.98) peak events.

The red line in Fig. 3.5 above is the best fit for the following function:

$$\begin{aligned} \text{Rate} = & \; cst + \theta(t-t_0) N_{\text{n},0} \exp(-(t-t_0)/\tau_n) \\ & + \theta(t-t_0) N \exp(-(t-t_0)/\tau_{\text{peak}}) \\ & + \theta(t-t_{\text{n},1}) N_{\text{n},1} \exp(-(t-t_{\text{n},1})/\tau_n) \\ & + \theta(t-t_{\text{n},2}) N_{\text{n},2} \exp(-(t-t_{\text{n},2})/\tau_n) \end{aligned} \tag{3.29}$$

where *cst* is a flat background component, θ is the Heaviside function, N the unkown peak amplitude, $N_{\text{n},0}$ is the unknown initial neutron-induced contamination, $N_{\text{n},1}$ and $N_{\text{n},2}$ are the unknown neutron calibration amplitudes, t_0 is the initial

time, $t_{\mathrm{n},1}$ and $t_{\mathrm{n},2}$ are the neutron calibration times, τ_n is the neutron decay constant associated to neutron calibrations and τ_{peak} is the decay constant of the peak (10.37 or 8.98).

We see a good agreement with the time distribution. It is then possible to estimate the 10.37 (resp. 8.98) peak amplitude by integrating the fitted formula over the relevant time period. The other radioactive peaks cannot be confidently estimated from their decrease with time for lack of statistics. Therefore they are conservatively not included in the background model. Above 12 keV, the smooth component of the spectrum is adjusted by a polynomial fit. In this energy region, an increase of the count rate is observed when energy decreases as expected from simulations [3]. This smooth component is linearly extrapolated below 12 keV. Two detectors, called ID404 and ID405, have a significantly higher background than the others below 8 keV [63]. That is why they were discarded from the stacked spectrum below this energy. This results in an effective exposure of 357 kg.d at low energy for these analyses. Fig. 3.6 (bottom) shows the stacked, online trigger efficiency-corrected background rate of the detectors used in the analysis, together with the associated background model. We will refer to this model as $B(\tilde{E})$ in the following.

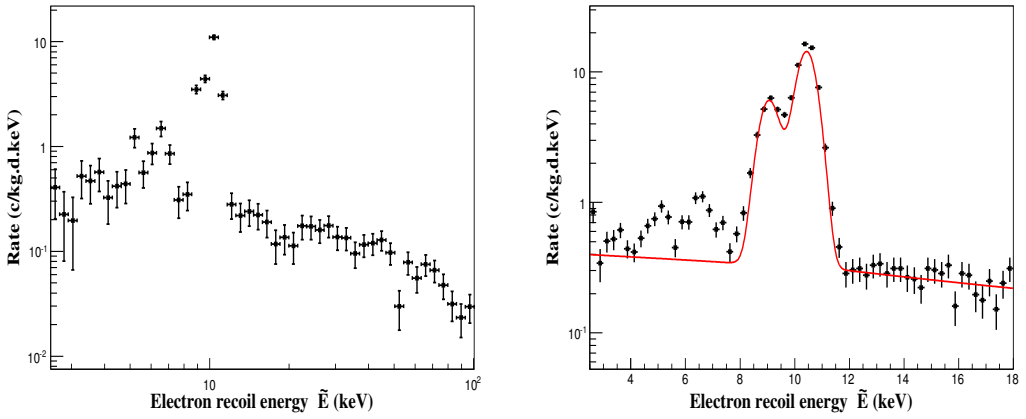

FIGURE 3.6 Left: Efficiency-corrected electron recoil spectrum in the fiducial volume of a single bolometer called ID3, in the energy range $2.5-100$ keV. The smooth Compton feature is visible as well as low-energy lines from induced radioactivity and cosmogenic activation of germanium. Right: Stacked, efficiency-corrected electron recoil spectrum for the full exposure in the $2.5-18$ keV range. The red line is the background model $B(\tilde{E})$ used in all analyses but Primakoff: a smooth Compton component linearly extrapolated below 12 keV, together with 10.37 keV and 8.98 keV cosmogenic lines.

3.5 Axion search: Primakoff solar axions

We consider the scenario in which axions are produced in the Sun by inverse Primakoff conversion, resulting in the flux given in Eq. (3.14), and are detected again by the Primakoff effect, using coherent Bragg diffraction. Similar searches have already been carried out by several crystal based experiments like CDMS [106], DAMA [107] or COSME [108]. The *modus operandi* is essentially the same as the one we are going to describe in this section. The only difference resides in the type of detector. COSME and CDMS use Germanium crystals while the DAMA collaboration operates NaI scintillators. As we will see shortly, the crystalline structure has a defining influence on the expected signal. We will now derive the expected count rate, using the same formalism as in [105].

3.5.1 Crystalline structure of Germanium

We are going to need a few crystallography notions for the computation of the event rate in a Germanium crystal. Germanium has a diamond crystalline structure (see Fig. 3.7) which may be described by a basis cell with 8 atoms at the following positions:

$$\begin{aligned}
\mathbf{r}_0 &= \frac{a_0}{4}(0,0,0) \\
\mathbf{r}_1 &= \frac{a_0}{4}(1,1,1) \\
\mathbf{r}_2 &= \frac{a_0}{4}(2,2,0) \\
\mathbf{r}_3 &= \frac{a_0}{4}(3,3,1) \\
\mathbf{r}_4 &= \frac{a_0}{4}(2,0,2) \\
\mathbf{r}_5 &= \frac{a_0}{4}(0,2,2) \\
\mathbf{r}_6 &= \frac{a_0}{4}(3,1,3) \\
\mathbf{r}_7 &= \frac{a_0}{4}(1,3,3)
\end{aligned} \tag{3.30}$$

Let $\mathbf{G}$ be a vector of the reciprocal lattice. Then:

$$\mathbf{G} = \frac{2\pi}{a_0}(h,k,l) \tag{3.31}$$

h, k and l are called the Miller indices. In Eq. 3.30 and Eq. 3.31 above, a_0 is the size of a single crystalline cell.

The nuclear structure factor, S, is defined as:

$$S(\mathbf{G}) = \sum_j e^{-i\mathbf{G}\cdot\mathbf{r}_j} \tag{3.32}$$

For the particular case of the diamond structure, it becomes:

$$S(\mathbf{G}) = \left[1 + e^{-i\frac{\pi(h+k+l)}{2}}\right]\left[1 + e^{-i\pi(h+k)} + e^{-i\pi(h+l)} + e^{-i\pi(l+k)}\right] \tag{3.33}$$

S takes non zero value in two cases only. When $h+k+l$ is odd, $S = 4(1+i)$ or $S = 4(1-i)$. When $h+k+l$ is even and divisible by 4, $S = 8$.

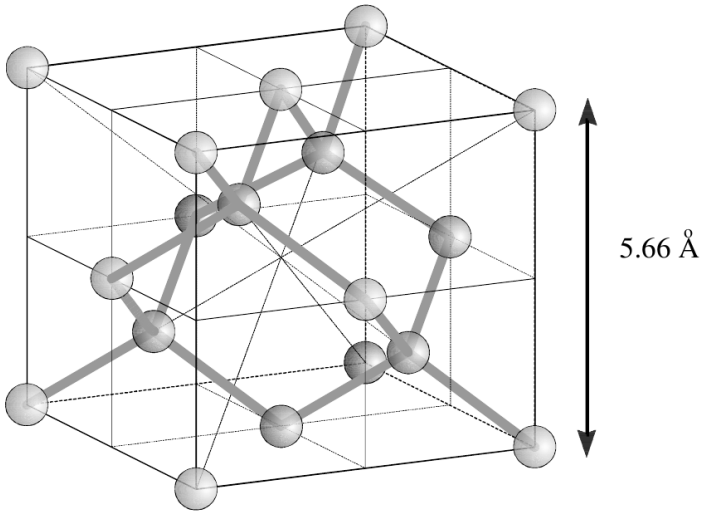

FIGURE 3.7 Scheme of the Germanium crystalline structure (diamond structure).

We will also need the form factor for a single atom and for the whole cell (respectively denoted as F_{atom} and F_{cell}). They are defined as the Fourier transform of the relevant electrostatic field ϕ :

$$\begin{aligned} F_{\text{cell}}(\mathbf{q}) &= k^2 \int \mathrm{d}^3x\, \phi^{\text{cell}}(\mathbf{x}) e^{-i\mathbf{q}\cdot\mathbf{x}} \\ F_{\text{atom}}(\mathbf{q}) &= k^2 \int \mathrm{d}^3x\, \phi^{\text{atom}}(\mathbf{x}) e^{-i\mathbf{q}\cdot\mathbf{x}} \end{aligned} \tag{3.34}$$

where $\mathbf{k}$ is the incoming particle's momentum while $\mathbf{q}$ is the transferred momentum from the scattering of the incoming particle on the crystal target. We model ϕ^{atom} by a screened Coulomb potential:

$$\phi^{\text{atom}}(\mathbf{x}) = \frac{Ze}{4\pi|\mathbf{x}|} e^{-\frac{|\mathbf{x}|}{r_0}} \tag{3.35}$$

where r_0 is the screening length. This gives:

$$F_{\text{atom}}(\mathbf{q}) = \frac{Zek^2}{\frac{1}{r_0^2} + \mathbf{q}^2} \tag{3.36}$$

Due to the periodic nature of the crystalline arrangement, the electric field is periodic as well so we can restrict the study to the electric field of a single cell. Using transformational invariance [109], this field can be written as:

$$\phi^{\text{cell}}(\mathbf{x}) = \sum_G n_G e^{i\mathbf{G}\cdot\mathbf{x}} \tag{3.37}$$

where the coefficients n_G are given by:

$$n_G = \frac{1}{v_a}\int_{\text{cell}} \mathrm{d}^3x\, e^{-i\mathbf{G}\cdot\mathbf{x}}\phi(\mathbf{x}) \tag{3.38}$$

In Eq. 3.38 above, v_a is the volume of the cell. ϕ^{cell} is actually the sum of the electric fields of each atom:

$$\phi^{\text{cell}}(\mathbf{x}) = \sum_i \phi^{\text{atom}}(\mathbf{x} - \mathbf{x}_i) \tag{3.39}$$

where the sum runs over all the atoms of the cell and $\mathbf{x}_i$ is the position of atom i. We can then rewrite Eq. 3.38 with a change of variables:

$$\begin{aligned} n_G &= \frac{1}{v_a}\int_{\text{cell}} \mathrm{d}^3x \sum_i \phi^{\text{atom}}(\mathbf{x}) e^{-i\mathbf{G}\cdot\mathbf{x}} e^{-i\mathbf{G}\cdot\mathbf{x}_i} \\ &= \frac{1}{v_a}\int_{\text{cell}} \mathrm{d}^3x\, \phi^{\text{atom}}(\mathbf{x}) e^{-i\mathbf{G}\cdot\mathbf{x}} S(\mathbf{G}) \\ &= \frac{1}{v_a\, k^2} F_{\text{atom}}(\mathbf{G})\, S(\mathbf{G}) \end{aligned} \tag{3.40}$$

Combining Eq. 3.34, Eq. 3.37 and Eq.3.40, we obtain:

$$F_{\text{cell}}(\mathbf{q}) = \frac{1}{v_a}\int \mathrm{d}^3x \sum_G F_{\text{atom}}(\mathbf{G})\, S(\mathbf{G}) e^{i\mathbf{G}\cdot\mathbf{x}} e^{-i\mathbf{q}\cdot\mathbf{x}} \tag{3.41}$$

With these notions in mind, we can now focus on the event rate computation.

3.5.2 Event rate computation

Let us first show that the recoil of the nucleus and the electrons remain negligible in the Bragg process. In the extreme case where all the axion energy is transferred to the nucleus or the electrons, the transferred momentum is:

$$\Delta p = E_a \approx \text{ keV} \tag{3.42}$$

As a consequence,

$$\Delta E_{\text{nuc}} \approx \frac{\Delta p^2}{m_{\text{nuc}}} \approx 10^{-6} \text{ keV} \ll \text{ keV} \tag{3.43}$$

and

$$\Delta E_{\text{elec}} = \frac{\Delta p^2}{m_{\text{elec}}} \approx 2 \times 10^{-3} \text{ keV} \ll \text{ keV} \tag{3.44}$$

We see that we can neglect momentum transfer to the electrons or to the nucleus, for keV scale axions. This means that the energy of the outgoing photon equals that of the incoming photon: $E_a = E_\gamma$.

Let us neglect the axion mass for now. Let us denote the incoming axion momentum as $\mathbf{k}_a$, the outgoing photon momentum as $\mathbf{k}_\gamma$ and $\mathbf{G}$ a vector of the Germanium reciprocal lattice. Then, the Bragg condition is:

$$\mathbf{k}_\gamma - \mathbf{k}_a = \mathbf{G} \tag{3.45}$$

Equivalently, this may be written in terms of the incoming axion energy E_a:

$$E_a = \frac{|\mathbf{G}^2|}{(2\mathbf{u} \cdot \mathbf{G})} \tag{3.46}$$

where $\mathbf{u}$ is a unit vector directed towards the Sun. Fig. 3.8 below shows a schematic view of the experiment.

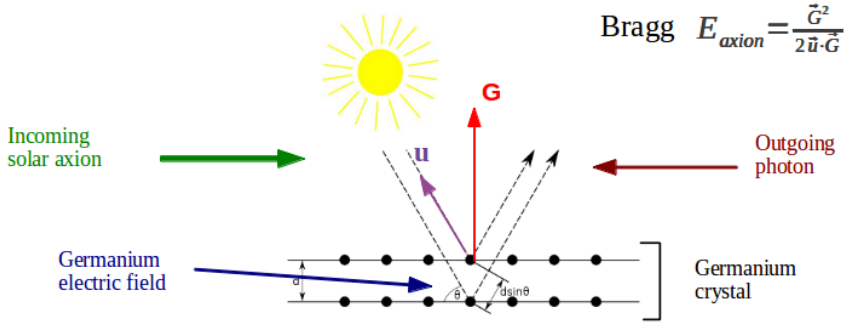

FIGURE 3.8 Bragg enhancement of the signal.

We can now compute the event rate from the Primakoff conversion of axions into photons. This rate is simply written as the product of the differential axion flux and the differential cross section, which are then integrated over:

$$\frac{dR}{dE_\gamma} = \int_0^\infty \mathrm{d}E_a \frac{d\Phi}{dE_a}(E_a) \int \mathrm{d}\Omega \frac{d\sigma}{dE_\gamma d\Omega} \tag{3.47}$$

As before, E_γ is the energy of the outgoing photon while E_a is the energy of the incoming axion. Since $E_a = E_\gamma$ (recall that the nuclear and electronic recoils can be neglected in the axion to photon reaction), we have:

$$\frac{d\sigma}{dE_\gamma d\Omega} = \frac{d\sigma}{d\Omega}\delta(E_\gamma - E_a) \tag{3.48}$$

The cross section $\frac{d\sigma}{d\Omega}$ for this process was given in [110]:

$$\frac{d\sigma}{d\Omega} = \frac{g_{A\gamma}^2}{16\pi^2} F_{\mathrm{cell}}^2(\mathbf{q}) \sin(2\theta)^2 \tag{3.49}$$

As before, 2θ is the scattering angle (see Fig. 3.8).

We are then ready to compute the count rate $R(\tilde{\mathrm{E}})$ in the detector. To this end, we further integrate $\frac{dR}{dE_\gamma}$ to account for the detector resolution (denoted as Δ):

$$\begin{aligned} R(\tilde{\mathrm{E}}) &= \int\int\int dE_\gamma \mathrm{d}E_a \mathrm{d}\Omega \frac{1}{\Delta\sqrt{2\pi}} e^{-\frac{(\tilde{E}-E_\gamma)^2}{2\Delta^2}} \frac{d\Phi}{dE_a}(E_a) \frac{d\sigma}{d\Omega}\delta(E_\gamma - E_a) \\ &= \int\int dE_\gamma \mathrm{d}\Omega \frac{1}{\Delta\sqrt{2\pi}} e^{-\frac{(\tilde{E}-E_\gamma)^2}{2\Delta^2}} \frac{d\Phi}{dE_a}(E_\gamma) \frac{g_{A\gamma}^2}{16\pi^2} F_{\mathrm{cell}}^2(\mathbf{q}) \sin(2\theta)^2 \end{aligned} \tag{3.50}$$

From Eq. 3.41 above, we compute:

$$F_{\mathrm{cell}}^2(\mathbf{q}) = (2\pi)^3 \frac{V}{v_a^2} \sum_G \left| S(\mathbf{G}) F_{\mathrm{atom}}^0(\mathbf{G}) \right|^2 \delta(\mathbf{G} - \mathbf{q}) \tag{3.51}$$

Plugging Eq. 3.51 in Eq. 3.50 we can integrate over $\mathbf{q}$ with the following change of variables:

$$dE_\gamma \, \mathrm{d}\Omega = \frac{2\mathrm{d}^3 q}{q^2} \tag{3.52}$$

We obtain:

$$R(\tilde{\mathrm{E}}) = 2(2\pi)^3 \frac{V}{v_a^2} \sum_G \frac{d\phi}{dE_a} \frac{g_{A\gamma}^2}{16\pi^2} \sin(2\theta)^2 \frac{1}{|\mathbf{G}|^2} \left| S(\mathbf{G}) F_A^0(\mathbf{G}) \right|^2 e^{-\frac{(\tilde{E}-E_\gamma)^2}{2\Delta^2}} \tag{3.53}$$

In Eq. 3.53 above, E_γ, $\mathbf{G}$ and 2θ are related through the Bragg condition: $E_\gamma = \frac{\mathbf{G}^2}{2\mathbf{u}\cdot\mathbf{G}}$ with $\mathbf{u}$ as the direction of the incoming axion.

If we know the position of the sun in the lab referential and the orientation of the axis of the detectors, we can then predict the expected axion count rate. In the following, we will reexpress Eq. 3.53 as:

$$\begin{aligned} R(\tilde{E},t,\alpha) &= 2(2\pi)^3 \frac{V}{v_a^2} \sum_G \frac{d\phi}{dE_a} \frac{g_{A\gamma}^2}{16\pi^2} \sin(2\theta)^2 \frac{1}{|\mathbf{G}|^2} \left|S(\mathbf{G})F_A^0(\mathbf{G})\right|^2 \; e^{-\frac{(\tilde{E}-E_\gamma)^2}{2\Delta^2}} \\ &= \left(\frac{g_{A\gamma}\times 10^8}{\mathrm{GeV}^{-1}}\right)^4 \overline{R}(\tilde{E},t,\alpha) \quad \equiv \quad \lambda \overline{R}(\tilde{E},t,\alpha) \end{aligned} \tag{3.54}$$

in Eq. 3.54 above, α, the azimuthal orientation of the detector, is not explicitly written. However, it is needed to compute $\mathbf{u}\cdot\mathbf{G}$ in the Bragg relation. A typical axion signal is shown in Fig. 3.9, where we have picked an arbitrary detector orientation in local (terrestrial) coordinates.

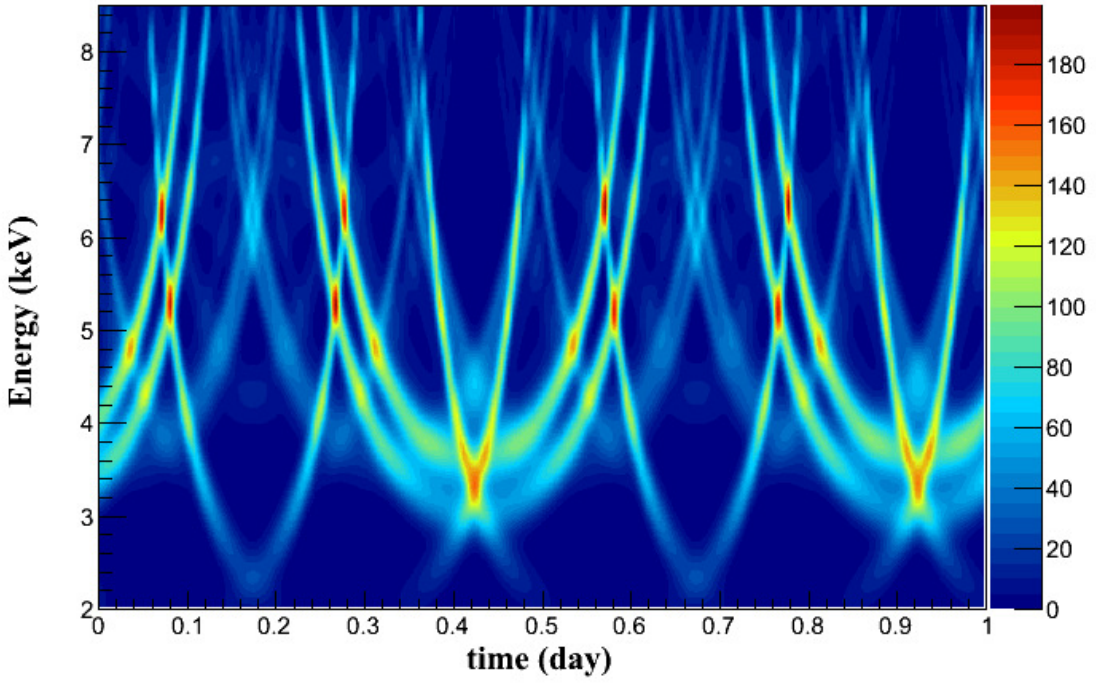

FIGURE 3.9 Example of the theoretical Primakoff conversion signal in a single detector, in counts per kg.d.keV, for a detector resolution of 0.5 keV and $g_{A\gamma} = 10^{-8}$ GeV^{-1}.

3.5.3 Statistical analysis: one detector

The geodesic location of the Underground Laboratory of Modane is (45.14° N, 6.68° E). While the vertical axis of the bolometer tower is aligned with the [001] axis of each detector, with a precision of about one degree, the individual azimuthal orientation (angle between the [110] axis and the North Pole direction) α of each detector was not measured. Therefore, in a first step we will adapt the method developed in the same context by [105] for a single bolometer. We use the following time correlation function assuming a given orientation α:

$$\chi_k(\alpha) = \epsilon_k \sum_i \left[\overline{R_k}(t_i) - \left\langle \overline{R_k} \right\rangle\right] \cdot n_{ik} \equiv \sum_i^n W_{ik} \cdot n_{ik} \tag{3.55}$$

where ϵ_k is the detector efficiency, n_i indicates the number of measured events in the time interval $[t_i, t_i + \Delta t]$, the index k refers to the energy interval $[\tilde{E}_k, \tilde{E}_k + \Delta\tilde{E}]$ and the sum is over the total period of data taking. We use the analysis window $3 - 8$ keV, which contains most of the expected signal. The Dirac-like brackets indicate an average over time. The distribution of $n_{i,k}$ is given by a Poisson distribution with average:

$$\langle n_{ik} \rangle = \epsilon_k \left[\lambda \overline{R_k}(t_i) + b_k\right] \Delta t \Delta\tilde{E} \tag{3.56}$$

where b_k is the individual detector background in the relevant energy interval. We can compute the average of χ_k:

$$\begin{aligned}
\langle \chi_k \rangle &= \epsilon_k \sum_i^n \left[\overline{R_k}(t_i) - \left\langle \overline{R_k} \right\rangle\right] . \langle n_{ik} \rangle \\
&= \epsilon_k^2 \sum_i^n \left[\overline{R_k}(t_i) - \left\langle \overline{R_k} \right\rangle\right] . \left[\lambda \overline{R_k}(t_i) + b_k\right] \Delta t \Delta\tilde{E} \\
&= \epsilon_k^2 \lambda \sum_i^n W_{ik}^2 \Delta t \Delta\tilde{E} + 0 \\
&\equiv \lambda . A_k
\end{aligned} \tag{3.57}$$

where the zero comes from averaging W_{ik} over time multiplied by something independent of time. Likewise, we can compute the variance of χ_k:

$$\begin{aligned}\sigma^2(\chi_k) &= \epsilon_k^2 \sum_{i,j} W_{ik} W_{jk} \left[\langle n_{ik} n_{jk}\rangle - \langle n_{ik}\rangle \langle n_{jk}\rangle\right] \\ &= \epsilon^2 \sum_i W_{ik}^2 \langle n_{ik}\rangle ,\end{aligned} \tag{3.58}$$

In the derivation of Equation 3.58, we assumed that the n_{ik} and n_{jk} are independent. Thus, assuming background dominates,

$$\sigma^2(\chi_k) = f(\lambda) + \epsilon_k b_k A_k \approx \epsilon_k b_k A_k \tag{3.59}$$

In practice, the χ_k are well approximated by a gaussian distribution since they are obtained by summing a large number of random variables. This was verified with Monte Carlo simulations. Consequently, we can write a simple likelihood fit:

$$L(\lambda) = \prod_k \exp\left[-\frac{(\chi_k - \langle\chi_k\rangle)^2}{2\sigma^2(\chi_k)}\right] \tag{3.60}$$

Minimizing the likelihood function, we derive simple estimators for the reduced coupling λ and its error[1]:

$$\tilde{\lambda}(\alpha) = \frac{\sum_k \frac{\chi_k}{\epsilon_k b_k}}{\sum_k \frac{A_k}{\epsilon_k b_k}} \qquad \text{and} \quad \sigma(\tilde{\lambda}(\alpha)) = \left(\sum_k \frac{A_k}{\epsilon_k b_k}\right)^{-1/2} \tag{3.61}$$

Since we do not know the precise orientation of the detector, we scan over all possible orientations (see Fig. 3.10). $\alpha \in [0, \pi/2]$ because of symmetry considerations. Then we pick the most conservative value of $\tilde{\lambda}$: $\tilde{\lambda} = \lambda_{\max}$. Given $\sigma(\tilde{\lambda})$, we can compute a limit on $g_{A\gamma}$ at the desired confidence level.

3.5.4 Statistical analysis: naive multi-detector analysis

How do we combine the data from several bolometers? We can run the previous analysis over all bolometers: we get a conservative, worst-case limit for each detector. Following a naive conservative approach, we can then combine the worst case of each detector together:

[1] **N.B.** The formula for λ in Eq. 3.61 corrects that of [108], which did not correctly account for the background b_k.

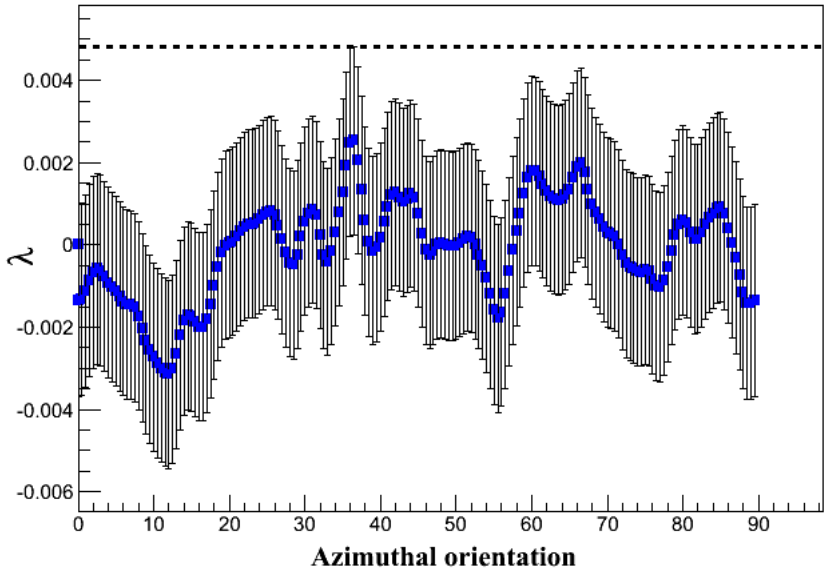

FIGURE 3.10 Results for the scan over α in degrees for a bolometer called ID6. Error bars are 1.64 σ The maximum of λ is reached for $\alpha = 36.5$ degrees. The results are compatible with zero signal.

$$\chi_k^{tot} = \epsilon_k \sum_{n_{bol}} \sum_i \left[\overline{R_k^{n_{bol}}}(t_i) - \left\langle \overline{R_k^{n_{bol}}} \right\rangle \right] .n_{ik}^{n_{bol}} \equiv \epsilon_k \sum_{n_{bol}} \sum_i W_{ik}^{n_{bol}} .n_{ik}^{n_{bol}} \tag{3.62}$$

where for each detector, we select the orientation yielding the highest value of λ. As before, we can construct the likelihood function:

$$L(\lambda) = \prod_k \prod_{n_{bol}} exp \left[- \frac{(\chi_k^{n_{bol}} - \langle \chi_k^{n_{bol}} \rangle)^2}{2\sigma^2(\chi_k^{n_{bol}})} \right] \tag{3.63}$$

which yields by maximisation:

$$\lambda = \frac{\sum_k \sum_{n_{bol}} \frac{\chi_k^{n_{bol}}}{\epsilon_k^{n_{bol}} b_k^{n_{bol}}}}{\sum_k \sum_{n_{bol}} \frac{A_k^{n_{bol}}}{\epsilon_k^{n_{bol}} b_k^{n_{bol}}}} \tag{3.64}$$

and

$$\sigma(\lambda) = \left[\sum_k \sum_{n_{bol}} \frac{A_k^{n_{bol}}}{b_k^{n_{bol}} \epsilon_k^{n_{bol}}} \right]^{-1/2} \tag{3.65}$$

However, this leads to a strong bias of the analysis towards a positive λ. Indeed, the estimator is a combination of the biggest fluctuations of each detector. This does not take

into account the fact that the detector orientations should be at random, which provides a smoothing of fluctuations. We will now explain how the issue may be bypassed, through the introduction of a more robust observable.

3.5.5 Statistical analysis: Monte Carlo procedure for multi-detector analysis

In order to combine all the detectors and at the same time take into account the lack of knowledge of the azimuthal orientation of each crystal, we apply the following procedure. Combining all detectors and scanning over all possible orientations, we obtain from the data an overall distribution for $\tilde{\lambda}$: $D_{\text{real data}}(\tilde{\lambda})$. Let us give more details. For each detector, we compute the estimator for $\tilde{\lambda}$ given possible azimuthal orientations as in Fig. 3.10. With a step of 0.5°, this gives us 180 values of $\tilde{\lambda}$ per detector, that is 1800 values in total. These 1800 values for $\tilde{\lambda}$ are then histogrammed (see Fig. 3.11) to constitute what we call $D_{\text{real data}}(\tilde{\lambda})$.

We then performed Monte Carlo simulations including the detector exposures, efficiencies and backgrounds as well as a potential axion signal. These simulations reproduce the conditions of the EDELWEISS-II experiments assuming various values for the coupling $g_{A\gamma}$: we picked an initial, random set of detector orientations: $\{\alpha_0^{\text{detector}}\}$. Then we drew events from the distribution of the expected event rate for each detector:

$$R_{\text{bolo}}(t, E, \alpha_0^{\text{detector}}) = b_{\text{bolo}}(E) + \lambda \overline{R_{\text{bolo}}}(t, E, \alpha_0^{\text{detector}}) \tag{3.66}$$

Using the same procedure as the one outlined above, we obtained a simulated overall distribution for $\tilde{\lambda}$: $D_{\text{sim}}(\tilde{\lambda})$. These simulations show that, in the presence of an axion signal, D_{sim} charts a tail at high $|\tilde{\lambda}|$ (see Fig. 3.11). There is tail at both positive and negative $\tilde{\lambda}$. This is because D_{sim} combines values of $\tilde{\lambda}$ reconstructed by assuming different values for the orientation: depending on the orientation, there may be correlations or anti-correlations.

Based on the simulations, we therefore introduce a statistical observable I given by:

$$I = \int_{|\tilde{\lambda}|<\tilde{\lambda}_c} D(\tilde{\lambda}) - \int_{|\tilde{\lambda}|>\tilde{\lambda}_c} D(\tilde{\lambda})$$

where $\tilde{\lambda}_{\text{cutoff}} = 0.003$. The cutoff was tuned by Monte Carlo simulations so as to provide the most robust sensitivity.

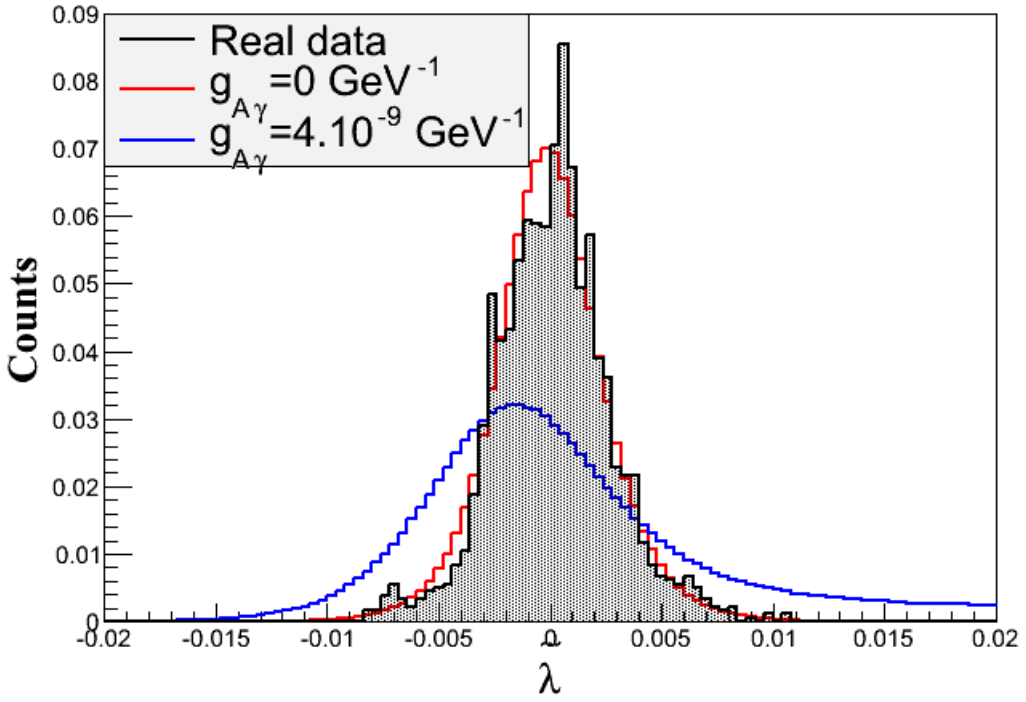

FIGURE 3.11 Grey: $D_{\text{real data}}(\tilde{\lambda})$. Red and blue: $D_{\text{sim}}(\tilde{\lambda})$ for different values of $g_{A\gamma}$. The tail at high $\tilde{\lambda}$ will be used to define a statistical observable.

The simulations allow us to obtain the expected distribution of I for a given λ_0 and $\{\alpha_0^{\text{detector}}\}$. The measured value $I_{\text{real data}}$ is compatible with simulations carried out for $\lambda_0 = 0$. By scanning over λ_0 and comparing the resulting distributions of I with $I_{\text{real data}}$, we can place a 95% CL upper limit on the axion-photon coupling:

$$g_{A\gamma} < 2.15 \times 10^{-9}\,\text{GeV}^{-1} \quad (95\%\text{CL}).$$

This limit is shown in Fig. 3.12 and compared with constraints from other experiments and astrophysical bounds. We may wonder how the limit would change if we had known the orientation of the detectors. If all the azimuthal angles are known, a simple combination of estimators from Eq.3.61 can be computed. In the absence of observed signal, the expected average upper limit on lambda is given by $1.64\,\sigma$ where $1/\sigma^2 = \Sigma_{\text{bolo}_i} 1/\sigma_i^2$, which yields the expectation $g_{A\gamma} < 1.8 \times 10^{-9}\,\text{GeV}^{-1}$, a slightly better sensitivity than the one effectively achieved without knowing the azimuthal orientations. This shows that we are not too penalised by the lack of knowledge on the orientation.

It is therefore enlightening to compare our results with those of the CDMS collaboration [106] which measured the azimuthal orientation of its detectors. With similar exposure, the EDELWEISS experiment improves slightly on the eventual limit. There

are two main reasons: the first one, as we have just seen, is that the penalty from the lack of knowledge on the orientation is low. The second one lies in the background rate. Thanks to the InterDigit scheme, fiducialisation and surface event rejection allows EDELWEISS to obtain a very low electron recoil background, about four times lower than that of the CDMS collaboration in the region of interest.

Comparison to the CAST experiment[111] is fruitful as well. The two experiments are complementary since CAST's sensitivity degrades for axion masses higher than 0.02 eV. This comes from coherence loss due to the size of the helioscope. This loss can be somewhat mitigated by the introduction of a buffer gas inside the helioscope, extending the reach to masses of 0.64 eV. Crystal based experiments do not suffer from such difficulties. However, their sensitivities does degrade eventually, as the axion mass becomes large enough to trigger non-relativistic effects. These will be discussed in Sec. 3.5.6

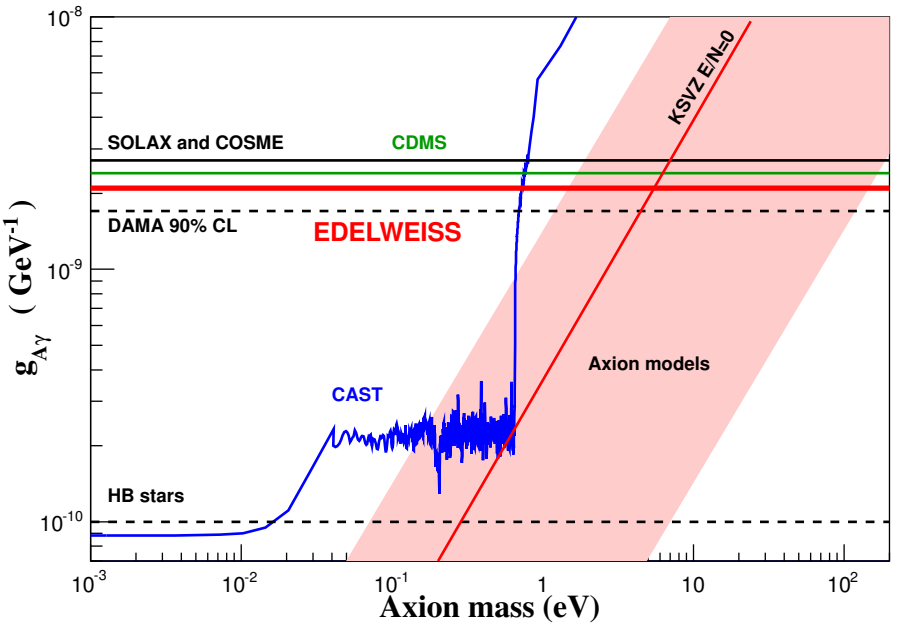

FIGURE 3.12 95 % CL limit on the $g_{A\gamma}$ coupling from the solar Primakoff flux obtained by EDELWEISS-II (red), compared to other crystal experiments such as SOLAX [112], COSME [108], CDMS [106] (green) and DAMA [107] (90 % CL)). We also show the CAST limit [111] (blue) and indirect bounds from HB stars [113]. The light red band labeled 'Axion models' represents typical theoretical models with $\mid E/N - 1.95 \mid$ =0.07-7. The red solid line inside this band represents the case E/N=0 (KSVZ model).

3.5.6 Validity of the results

In this section, we have made a number of assumptions to compute the eventual limit. We are now going to discuss their domain of validity.

Dependence on the Monte Carlo orientation choice

Our Monte Carlo procedure, which we used to compute the combined limit from several detectors selected an initial random set of detector orientations: $\{\alpha_0^{\text{detector}}\}$. For our results to be valid, we must show that the statistical inference does not depend on the initial choice of $\{\alpha_0^{\text{detector}}\}$. This was verified by generating various initial random sets and comparing the eventual simulated distributions $D_{\text{sim}}(\tilde{\lambda})$ in each case. Remarkably, there was an excellent agreement, as shown on Fig. 3.13.

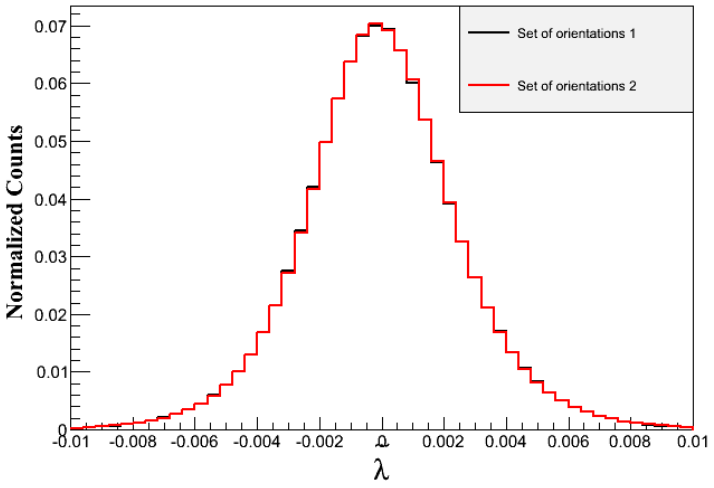

FIGURE 3.13 $D_{\text{sim}}(\tilde{\lambda})$ for two different sets of initial orientations $\{\alpha_0^{\text{detector}}\}$ and the same initial $g_{A\gamma}$.

Dependence on the axion mass

In Fig. 3.12, we have reported results up to axion masses of 200 eV. We are now going to explain why this is valid, even though we approach the non-relativistic limit.

The first thing we want to look at is the axion flux from the Sun, which varies with the axion mass. The flux dependence with the axion mass is taken from [91], where the expected Primakoff flux of massive axions was computed with a precision better than 15%:

$$\frac{d\Phi}{d\mathrm{E}} = \frac{4.2\times10^{10}}{\mathrm{cm^2\,keV\,s}}\left(\frac{g_{A\gamma}\times10^{8}}{\mathrm{GeV^{-1}}}\right)^2 \frac{E(E^2-{m_a}^2)}{e^{E/1.1}-0.7}(1+0.02\,m_a) \tag{3.67}$$

The mass dependence is plotted in Fig. 3.14 below.

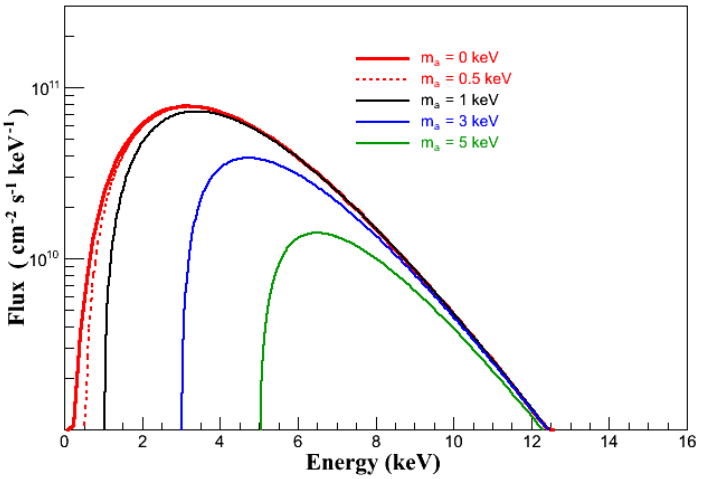

FIGURE 3.14 Expected spectra of solar axions for the Primakoff mechanism with various masses. The effective axion coupling corresponding to the represented fluxe is $g_{A\gamma} = 10^{-9}$ GeV^{-1} .

Integrating the differential flux from in our region of interest, the [2.5, 8] keV interval, we find that there is less than a 1% difference between a massless axion and an $m_a = 0.2$ keV axion, which is small with respect to the flux uncertainties: we can apply the massless formula for axions with masses up to 200 eV.

The axion mass may have more important consequences on the computation of the eventual detected signal. Indeed, it is involved in the computation of the Bragg relation. We will now investigate any change that may be required to properly take the mass into account. For axion masses of 200 eV, the recoil of the nucleus and the electrons remain negligible so we can write, as before,

$$E_a = E_\gamma \quad \Rightarrow \quad k_a^2 + m_a^2 = k_\gamma^2 \tag{3.68}$$

Then, the Bragg condition becomes:

$$\begin{aligned} G^2 &= k_\gamma^2 + k_a^2 - 2\mathbf{k}_a \cdot \mathbf{k}_\gamma \cos(2\theta) \\ &= 2E_a^2 - m_a^2 - 2E_a^2\sqrt{1 - \frac{m_a^2}{E_a^2}}\left(1 - 2\left(\frac{\mathbf{u}\cdot\mathbf{G}}{G}\right)^2\right) \end{aligned} \tag{3.69}$$

We set our threshold at 2.5 keV. That means the minimum axion energy we can detect is $E_a = 2.5$ keV. With an axion mass ≤ 0.5 keV the ratio $\frac{m_a^2}{E_a^2}$ remains very small. Restricting our study to masses ≤ 0.5 keV, we can then compute the Bragg condition

for massive axions:

$$E_a^2 = \frac{G^4}{4(\mathbf{u}\cdot\mathbf{G})^2} + \frac{m_a^2}{2} \Rightarrow \Delta E_a^2 = \frac{m_a^2}{2} \tag{3.70}$$

Then

$$\Delta E_a^2 = 2E_a\Delta E_a \Rightarrow \Delta E_a = \frac{m_a^2}{4E_a} \approx 10^{-2}\,\mathrm{keV} \ll E_a \tag{3.71}$$

We see that the Bragg condition is essentially the same energy-wise. However, what is really important is to know whether the scattering angle changes. If it changes significantly, it may impact the correlator in our statistical study. Because of the crystal symmetries, it is sufficient to restrict studies to $\theta \in [0, \frac{\pi}{2}]$. Rewriting $\mathbf{u}\cdot\mathbf{G}$ as $\mathrm{G}\sin(\theta)$, we can express Eq. 3.70 as

$$\sin^2\theta = \frac{G^2}{4E_a^2 - 2m_a^2} \approx \frac{G^2}{4E_a^2} + \frac{G^2 m_a^2}{8E_a^4} \Rightarrow \Delta\sin^2\theta = \frac{G^2 m_a^2}{8E_a^4} \tag{3.72}$$

Then

$$\Delta\sin^2\theta = 2\,\sin\theta\Delta\sin\theta \Rightarrow \Delta\sin\theta = \frac{Gm_a^2}{4E_a^3} = \epsilon \ll 1 \tag{3.73}$$

We restricted our study to the interval $[0, \frac{\pi}{2}]$ in which the sine function is strictly (increasing) monotonous function of θ. Given $\Delta\sin\theta$, the largest corresponding variation of θ (i.e. $\Delta\theta_{\max}$) occurs in the smallest slope region: near $\theta = \frac{\pi}{2}$. Solving for

$$\sin(\frac{\pi}{2}) - \sin(\frac{\pi}{2} - \Delta\theta_{\max}) = \epsilon \tag{3.74}$$

we obtain, assuming that $\Delta\theta_{\max}$ remains small:

$$\Delta\theta_{\max} = \sqrt{2\epsilon} \tag{3.75}$$

For an axion mass of 0.5 keV, a conservative estimate gives about 6°. For an axion mass of 0.2 keV, the same estimate gives 2°.

The rather large uncertainty at an axion mass of 0.5 keV means that the Bragg amplification will take place when θ is slightly different: there is a small time-offset. This may have an influence on the time-correlator. A precise computation should be carried out to fully understand it. However, we should bear in mind that we have an uncertainty on the scattering angle because of the energy resolution of the detector. Differentiating the Bragg relation we find:

$$\Delta\theta\cos(\theta) = \frac{G\Delta E}{2E^2} \tag{3.76}$$

Given that ΔE is of the order of the detector resolution (0.7 keV), the uncertainty on the angle can be computed. We find $\Delta\theta \approx 5°$. So we see that the uncertainty caused by resolution effect (included in the signal model) outweighs that made for axion masses below 0.2 keV. The fact that we do not know the azimuthal orientation of the detectors and that we sum contributions of all possible orientations in our MC simulations should also smooth out variations of θ. With all these remarks, we can safely conclude that our results are valid at least up to axion masses of 0.2 keV.

Dependence on the background model

We have made several background assumptions: we stated that we could include radioactive peaks in the background model and that the background dominated over signal. Fig. 3.15 below provides an *a posteriori* justification. With a single detector and a conservative hypothesis (no peaks included in the background model), we can exclude axions with $g_{A\gamma} > 2.7 \times 10^{-9}$. The corresponding signal is plotted in blue in Fig. 3.15. We see that, as expected, background dominates. Furthermore, the width of the signal is much larger than that of the peaks. This verification validates our assumptions.

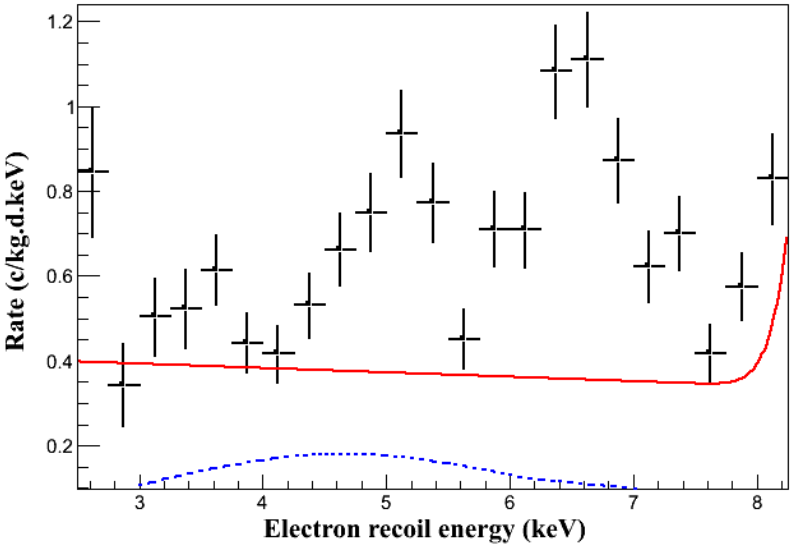

FIGURE 3.15 Stacked, efficiency-corrected electron recoil spectrum in the fiducial volume. The red line is the conservative background model.

3.6 Axion search: 14.4 keV solar axions

We now test the scenario in which solar axions are produced in the ^{57}Fe magnetic transition and detected by the axio-electric effect in a Ge crystal, resulting in a 14.4 keV electron recoil. The expected rate in counts per keV is the product of the flux $\Phi_{14.4}$ (Eq. 3.19), the axio-electric cross section given in Eq. (3.24), the individual detector resolution σ_i and exposure $M_i T_i$, summing over all detectors i:

$$\begin{aligned} R_{14.4}(\tilde{E}) &= \Phi_{14.4}\,\sigma_{\mathrm{Ae}}(14.4)\sum_i M_i T_i \frac{1}{\sqrt{2\pi}\sigma_i} \times e^{-\frac{(\tilde{E}-14.4)^2}{2\sigma_i^2}} \\ &\equiv \lambda \times \overline{R}_{14.4}(\tilde{E}) \qquad \text{where } \lambda = (g_{Ae} \times g_{AN}^{\mathrm{eff}})^2 \end{aligned} \tag{3.77}$$

At 14.4 keV, the online trigger efficiency is equal to 1 for all 10 detectors. Fig. 3.16 shows a zoom on the stacked electron recoil spectrum in the $12-18$ keV interval. There is no hint of a line at 14.4 keV and we therefore derive a limit on the line intensity using a binned likelihood function and assuming Poisson statistics for the background:

$$L = \prod_i e^{-N_i^{\mathrm{th}}} \frac{(N_i^{\mathrm{th}})^{N_i^{\mathrm{exp}}}}{N_i^{\mathrm{exp}}!} \tag{3.78}$$

Here N_i^{exp} is the observed number of events in the energy bin i and $N^{th}(\tilde{E}) = \lambda\overline{R}_{14.4}(\tilde{E}) + B(\tilde{E})$.

The likelihood function is gaussian to a very good approximation. In order to deal with possible negative background fluctuations, we use the following prescription. If the likelihood best fit is positive we use a standard gaussian 90% upper limit. If the value is negative we assume it is equivalent to a zero measurement. This is a conservative approach (presented in Appendix A) which solves issues of undercoverage and empty intervals. We find $R_{14.4} < 0.040$ counts/kg/d. This method was validated with MC simulations.

For a low-mass axion, this result translates to a 90% CL constraint on the couplings:

$$g_{AN}^{\mathrm{eff}} \times g_{Ae} < 4.7 \times 10^{-17}$$

Using the relationships given in Eq.(3.19) and Eq.(3.24), it is possible to obtain the upper limits for $g_{AN}^{\mathrm{eff}} \times g_{Ae}$ as a function of the axion mass m_A for axion masses up to 14 keV. Fig. 3.17 shows this model independent limit.

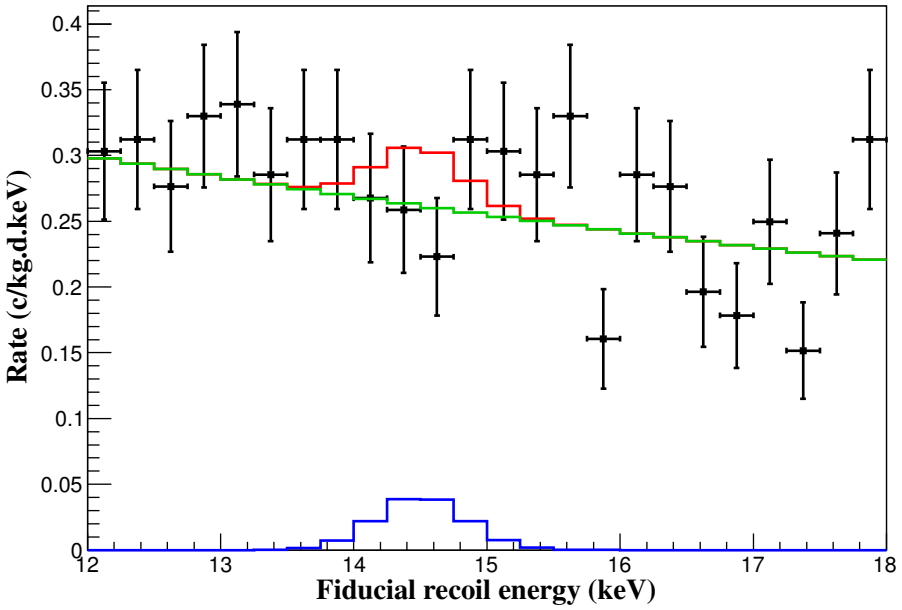

FIGURE 3.16 Stacked electron recoil spectrum around 14.4 keV. Blue: detector response to 14.4 keV solar axions using axio-electric conversion at the 90% CL limit. Green: background model. Red: axion signal with coupling at the 90% CL limit superimposed on the background model.

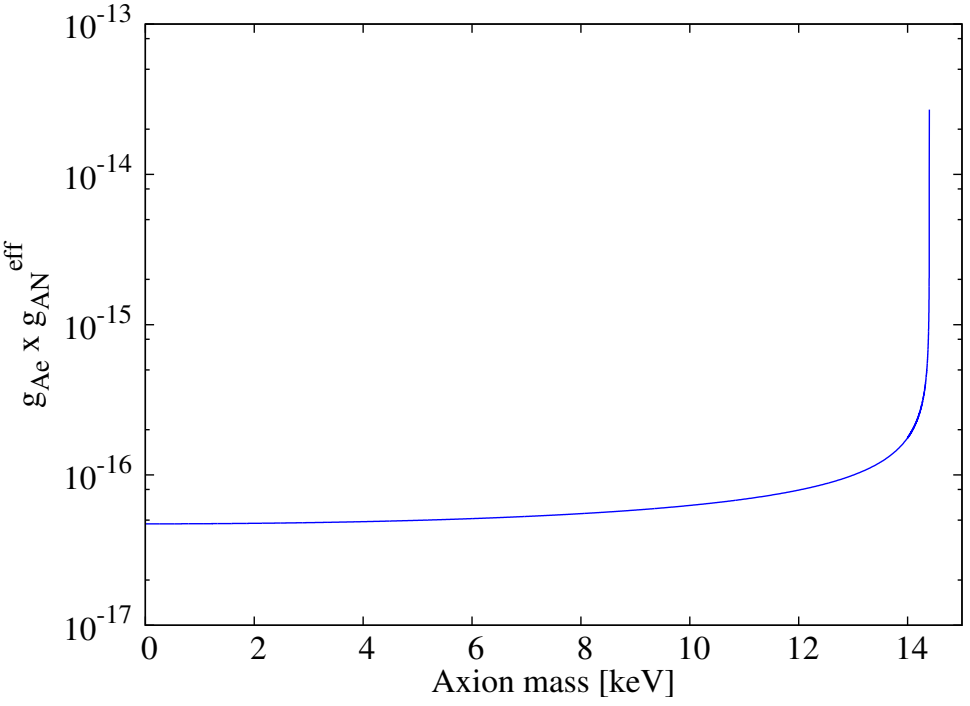

FIGURE 3.17 90 % CL upper limits for $g_{Ae} \times g_{AN}^{\text{eff}}$ as a function of the axion mass m_A obtained with the EDELWEISS-II data.

3.7 Axion search: Compton, bremsstrahlung and axio-RD

In this scenario, solar axions are produced through Compton, bremsstrahlung and axio-RD processes, resulting in the flux given by Eq. (3.21). These axions can be detected by the axio-electric effect in the crystal, resulting in an expected count rate given by:

$$\begin{aligned} R_{\text{C-B-RD}}(\tilde{E}) &= \int dE_A\, \sigma_{\text{A}}(E_A) \left(\frac{d\Phi^{\text{C-B-RD}}}{dE_A} \right) \times \sum_i \epsilon_i(\tilde{E}) M_i T_i \frac{1}{\sqrt{2\pi}\sigma_i} \times e^{-\frac{(\tilde{E}-E_A)^2}{2\sigma_i^2}} \\ &\equiv \lambda \times \overline{R}_{\text{C-B-RD}}(\tilde{E}) \qquad \text{where } \lambda = g_{Ae}^4 \end{aligned} \tag{3.79}$$

The notations are identical to Eq. (3.77), ϵ_i being the efficiency function for a given detector i, which is relevant at low energy. We look for Compton-bremsstrahlung-axio-RD solar axions in the 2.5-30 keV energy window. We use the same likelihood procedure described in the previous section, where $N^{th}(\tilde{E})$ becomes:

$$N^{th}(\tilde{E}) = \lambda \overline{R}_{\text{C-B-RD}}(\tilde{E}) + B(\tilde{E}) \qquad (\lambda = g_{Ae}^4) \tag{3.80}$$

The expected signal is not a line feature, so the likelihood analysis window has been tailored to each axion mass. Fig. 3.18 shows the essential case of massless axions, for which the expected signal stands mostly below 5 keV, and therefore the likelihood is not strongly affected by the presence of activation peaks. However the interpretation of the data at low energies remain difficult: we cannot exclude that some surface events pollute the signal region since discrimination degrades as the energy decreases. The lack of statistics also makes it difficult to analyse the apparent increase of the background. It may be a threshold effect or a mere statistical fluctuation. For each axion mass, a 90 % CL limit is found using the same prescription as before. The constraint found for axions with $m_A \ll$ few keV is $R_{\text{C}-\text{B}-\text{RD}} < 0.46$ counts/kg/day. This translates to a constraint on the axio-electric coupling: $g_{Ae} < 2.59 \times 10^{-11}$ at 90% CL. The sensitivity attained with this channel improves that of previous experiments [114, 115] and is even slightly better than the indirect bound obtained from constraints on the solar neutrino flux[116]. In this channel, the assets of the EDELWEISS experiment are the same as those we highlighted in the Primakoff search: excellent fiducialisation of the detector and very low (0.5 dru) event rate. Since the results were published in 2013, only Xenon100 [117] has attained a better sensitivity. The evolution of the limit on g_{Ae} as a function of m_A can be found on Fig. 3.19.

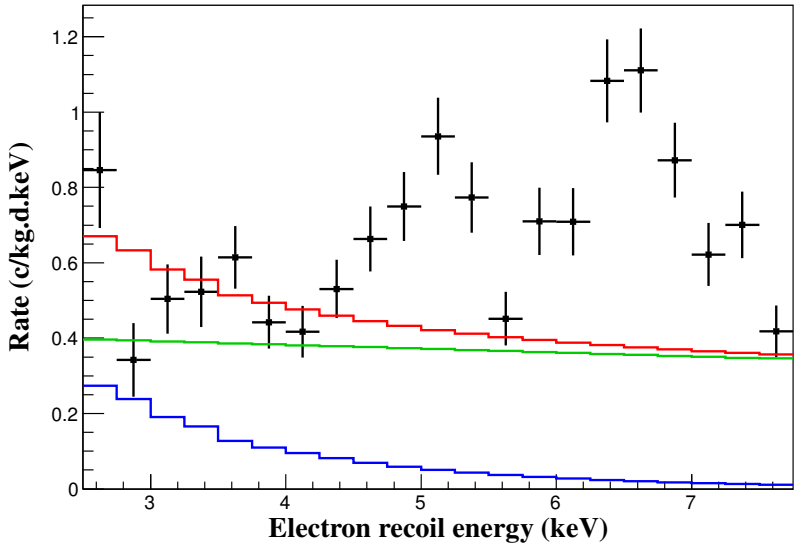

FIGURE 3.18 Efficiency-corrected stacked electron recoil spectrum for the whole exposure, close to the analysis threshold. The detector response for a Compton Bremsstrahlung axio-RD, zero-mass axion signal at the 90% confidence limit is represented by the blue curve, while the green curve shows the conservative background model. Red curve: signal superimposed over the background model. Note that the number of detectors used to compute the spectrum depends on the energy range considered.

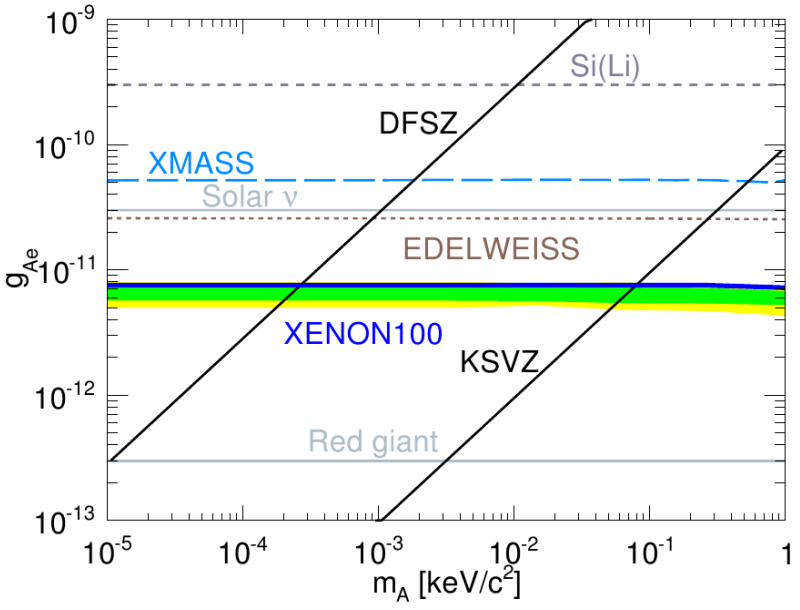

FIGURE 3.19 Constraints on the g_{Ae} axion coupling as a function of m_A. The EDELWEISS limit is the dotted brown line. Also shown are the limits from Derbin (Si(Li)) [114], XMASS [115] and XENON100 [117]. Benchmark DFSZ and KSVZ models are represented by straight black lines. Indirect astrophysical bounds from solar neutrinos [116] and red giants [118] are shown as gray lines.

3.8 Axion search: dark matter axions

We now focus on the scenario in which axions constitute the entire dark matter halo of our galaxy. Since the galactic DM is non-relativistic, the resulting signal due to the axio-electric coupling will consist in electron recoils at an energy equal to the axion mass m_A. Hence, this search is fundamentally different from the other searches presented so far. We also stress that the axion or ALP we are looking for is not the standard QCD dark matter axion, which solves the QCD CP problem and has a mass in the $\left[10^{-6}, 10^{-3}\right]$ eV range.

From Eq. (3.22) and Eq. (3.24), the expected axion count rate is:

$$\begin{aligned} R_{\rm DM}(\tilde{E}) &= \Phi_{\rm DM}\sigma_{\rm A}(m_A) \times \sum_i \epsilon_i(\tilde{E}) M_i T_i \frac{1}{\sqrt{2\pi}\sigma_i} \times e^{-\frac{(\tilde{E}-m_A)^2}{2\sigma_i^2}} \\ &= \lambda \times \overline{R}_{\rm DM}(\tilde{E}) \qquad \text{where } \lambda = g_{Ae}^2 \end{aligned} \tag{3.81}$$

The notations are the same as above. We look for galactic axions in the [2.5 keV - 100 keV] mass window. We proceed with a binned likelihood as in Eq. (3.78), where:

$$N^{th}(\tilde{E}) = \lambda \overline{R}_{\rm DM}(\tilde{E}) + B(\tilde{E}) \tag{3.82}$$

Over the whole energy range, no statistically significant excess was found, except at energies where potential cosmogenic lines are expected. We therefore report a 90% CL limit on the axion coupling as a function of its mass. We use the same prescription as above to derive the appropriate limit. The shape of our electron recoil background implies that the strongest constraint is found for 12.5 keV axions, for which we found $R_{\rm DM} < 0.05$ counts/kg/d. This translates to a constraint on the dark matter axio-electric coupling at this mass: $g_{ae} < 1.07 \times 10^{-12}$.

A typical signal at limit is shown in Fig. 3.20. The final limit on $g_{\rm Ae}$ within this scenario is represented as a function of m_A in Fig. 3.21. For masses below 10 keV, the oscillations are due to the radioactive peaks which as we explained before, were conservatively not included in the background model. For higher masses, the oscillations are due to background fluctuations. Our results above 2.5 keV are similar to those of the CDMS collaboration[106] although they are somewhat penalised by our conservative background model. Since we set our threshold at 2.5 keV, we have no sensitivity to axions with masses below this value. The CDMS and CoGeNT[119] collaborations exclude a wider region of the parameter space thanks to their lower threshold. The Xenon100 collaboration [117]

also published results in this channel, with an improvement in sensitivity for masses in the [1,10] keV range.

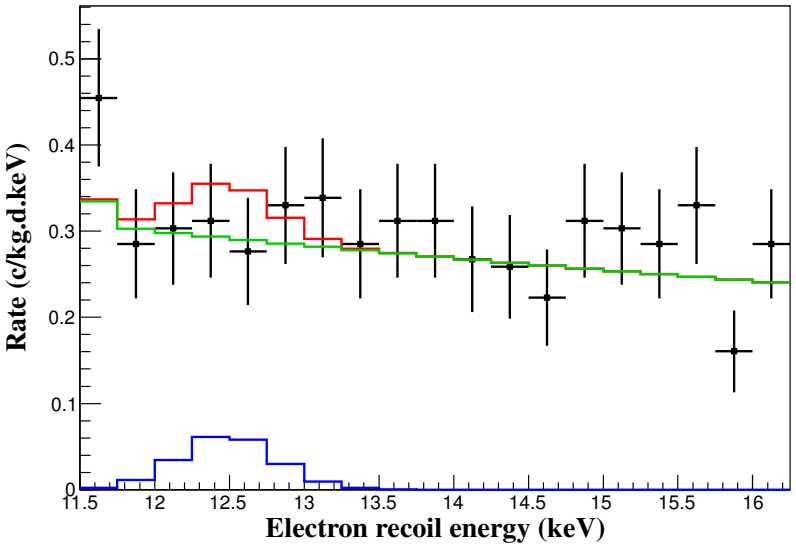

FIGURE 3.20 Efficiency-corrected stacked electron recoil spectrum for the whole exposure, close to the analysis threshold. The detector response for a 12.5 keV Dark Matter axion signal at the 90% confidence limit is represented by the blue curve, while the green curve shows the conservative background model. Red curve: signal superimposed over the background model.

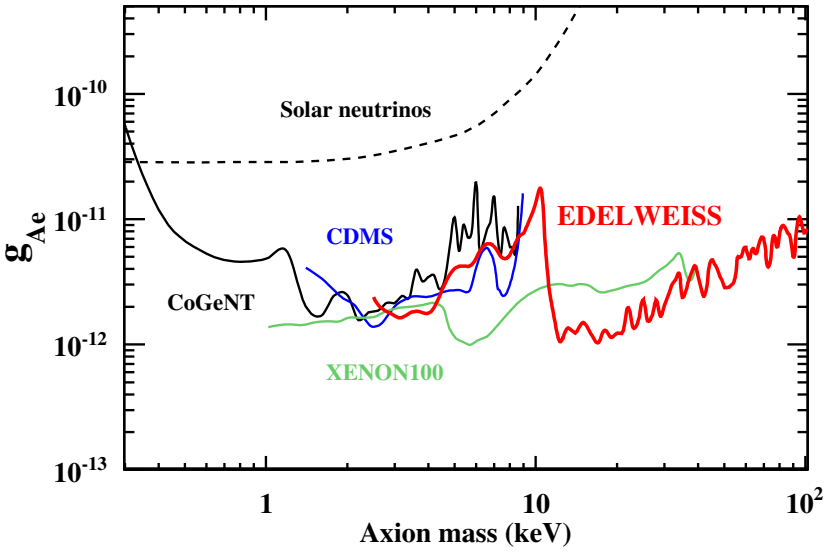

FIGURE 3.21 Limit on the axion-electron coupling as a function of m_A assuming the local dark matter halo of our galaxy is made entirely of axions. The black and blue curves are constraints set by the CoGeNT [119] and CDMS [106] germanium detectors respectively. The green curve shows the constraints from the XENON100 experiment [117]. Dashed line: indirect bound derived from the solar neutrino flux measurement [116].

3.9 Derivation of model dependent mass bounds

In Table 3.3 below, we summarise the model independent constraints we obtained on each axion coupling under study. Within the framework of a given axion model, KSVZ or DFSZ, the only free parameter is the axion mass, or equivalently the Peccei-Quinn symmetry-breaking scale f_A (see Eq. (3.3)). Therefore, our limits on the couplings constrain m_A directly. We calculate the exclusion range for m_A from each of the three solar axion channels previously studied, within both models assuming the model-dependent couplings and hadronic physics parameters given in Section 3.2.

Channel	14.4 ($g_{Ae} \times g_{AN}^{\text{eff}}$)	DM (g_{Ae})	C-B-RD (g_{Ae})	P ($g_{A\gamma}$)
Limit	$< 4.82 \times 10^{-17}$	$< 1.07 \times 10^{-12}$	$< 2.59 \times 10^{-11}$	$< 2.15 \times 10^{-9}$ GeV^{-1}

TABLE 3.3 Summary of the limits on the different axion couplings. 14.4 stands for 14.4 keV solar axions, DM for dark matter axions, C-B-RD for Compton-bremsstrahlung and axio-RD axions, and P for Primakoff axions. The quoted values are in the limit $m_A = 0$, except for the dark matter case, which is given for $m_A = 12.5$ keV. All limits are at 90% CL except P (95% CL).

Let us now compute these mass constraints for all channels with the exception of the Dark Matter channel (as these axions are not standard QCD axions). In Table 3.4, the derived limits on the axion mass are summarized for both benchmark models. Within the DFSZ model we completely exclude the mass range $0.92\,\text{eV} < m_A < 14.4$ keV from the combination of the Compton-bremsstrahlung-RD channel and the 14.4 keV channel. Within the KSVZ framework, combining the same channels channels, we exclude the mass range $155\,\text{eV} < m_A < 14.4$ keV. The Primakoff channel also excludes relativistic solar axions with $m_A > 5.78$ eV, therefore closing the window for $5.78\,\text{eV} < m_A < 1$ keV axion masses.[2]

Channel	14.4 ($g_{Ae} \times g_{AN}^{\text{eff}}$)	C-B-RD (g_{Ae})	P ($g_{A\gamma}$)
KSVZ	$155\,\text{eV} < m_A < 14.4$ keV	$272\,\text{eV} < m_A < 1$ keV	5.78 eV$< m_A \lesssim 200$ eV
DFSZ	$8\,\text{eV} < m_A < 14.4$ keV	$0.92\,\text{eV} < m_A < 1$ keV	15 eV$< m_A \lesssim 200$ eV

TABLE 3.4 Excluded ranges of axion masses derived from EDELWEISS-II constraints within two benchmark models, KSVZ and DFSZ. We assume axion and hadronic parameters described in Section 3.2. The channels considered are solar 14.4 keV axions (14.4), solar Compton-bremsstrahlung-RD axions (C-B-RD) and solar Primakoff axions (P).

[2]The EDELWEISS results published [74] were more constraining as we pushed the CBRD exclusion to non relativistic axions. After discussin the issue with J. Redondo, it became apparent that this was not fully justified. The correction to the limit is now under study.

Chapter 4

Low mass WIMP searches with EDELWEISS-III data

Theoretically, WIMP masses can span many orders of magnitudes. The canonical WIMP mass is at the electroweak scale (10 to 100 GeV). Within SUSY models, the latest LHC searches typically favour masses in the range 100 - 1000 GeV [29]. However, outside of specific SUSY frameworks, low-mass WIMPs are also a heavily scrutinised possibility. There are several motivations. On the one hand, some direct detection experiments have reported excesses of events [58, 61] and there may also be evidence of WIMP annihilation in the galactic center [120]. All these hints point to a Dark Matter mass of a few GeV. On the other hand, credible theoretical frameworks that naturally require low mass WIMPs have emerged. One such model is called Asymmetric Dark Matter (ADM). By postulating an initial DM particle-antiparticle asymmetry, it seeks to explain the concordance of the baryon and dark matter densities. In such models, the Dark Matter relic density is set by the baryon asymmetry, not by the properties of a thermal freeze-out. This mechanism predicts $\Omega_{\mathrm{DM}} \approx \frac{m_{\mathrm{DM}}}{m_b}\Omega_b$, hence $m_{\mathrm{DM}} \approx 5$ GeV.

The quest for low mass WIMPs in EDELWEISS-III raises an immediate challenge: the expected recoil energy ($\mathcal{O}(1$ keV)) are even lower than for high mass WIMPs which means that the bulk of the expected signal will be found near the threshold of the experiment, where backgrounds are hard to control and event discrimination becomes more difficult.

In this chapter, we will present the EDELWEISS-III dataset. Then, we will introduce the experimental backgrounds and a novel statistical tool (classification with machine learning), that we used to improve event discrimination. We will eventually describe the full analysis pipeline, as applied in the analysis of a first, single-detector dataset.

4.1 The EDELWEISS-III dataset

The data analysed in this work was recorded during a single physics run, called Run308. In this section, we will give a general presentation of Run308. In particular, we will explain how data reconstruction works, from raw traces and event triggering to the calibration of the data and definition of the variables of interest for the data analyst. Over the course of my PhD, I have made contributions to the calibration procedure and the heat processing which helped towards the production of the final n-tuples and the creation of a pulse simulation pipeline.

4.1.1 Presentation of Run308

The bolometer configuration for this run is shown in Fig. 4.1 below.

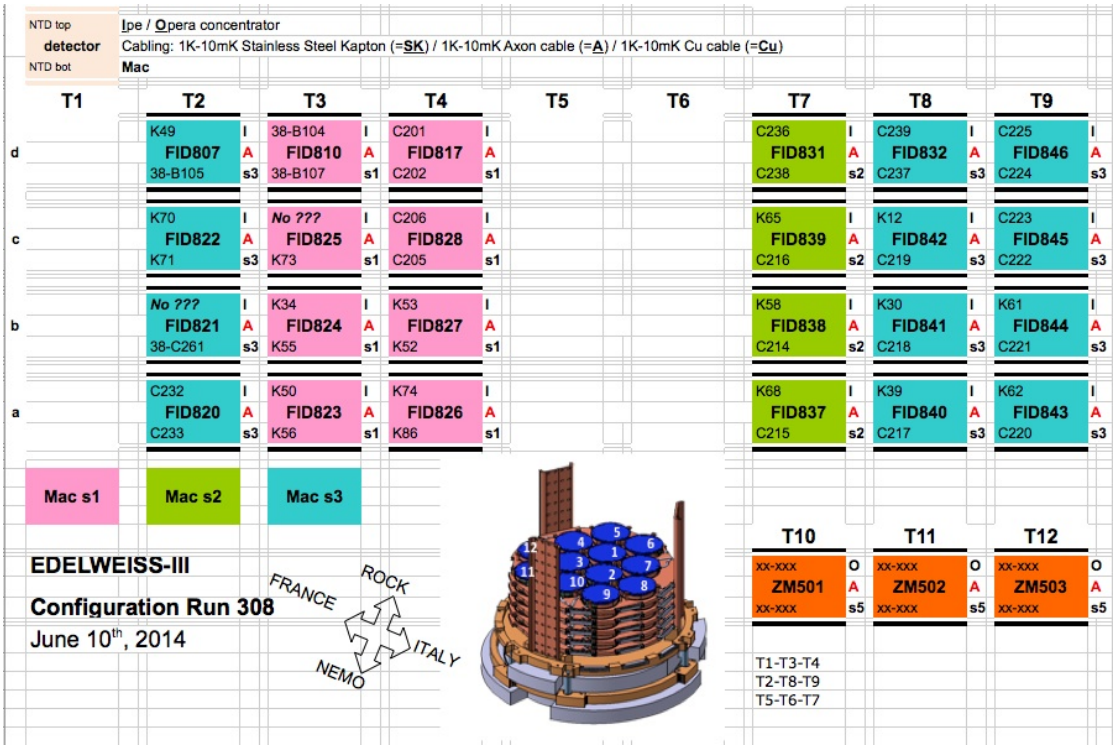

FIGURE 4.1 EDELWEISS-III Run 308 setup

In Run308, 36 FID Germanium bolometers and three scintillating ZnMoO detectors operated by the LUMINEU collaboration [121] were installed. Owing to cabling issues, only 24 FID detectors were actually read-out. Run308 started in July 2014 and ended in April 2015 after a cryogenic incident.

In this time interval, the data acquisition progressed steadily, as shown in Fig. 4.2. In addition to WIMP search runs, calibration runs were dedicated to the understanding of the

nuclear and electronic recoil response (with Americium-Beryllium and Baryum sources respectively). The nuclear response of the EDELWEISS detectors is well understood down to sub keV energies [122].

The Baryum gamma source charts a peak at 356 keV which is used to calibrate the six measurement channels (4 ionisations and 2 heats) of the detector. The full calibration process will be described in more details in Section 4.1.4.

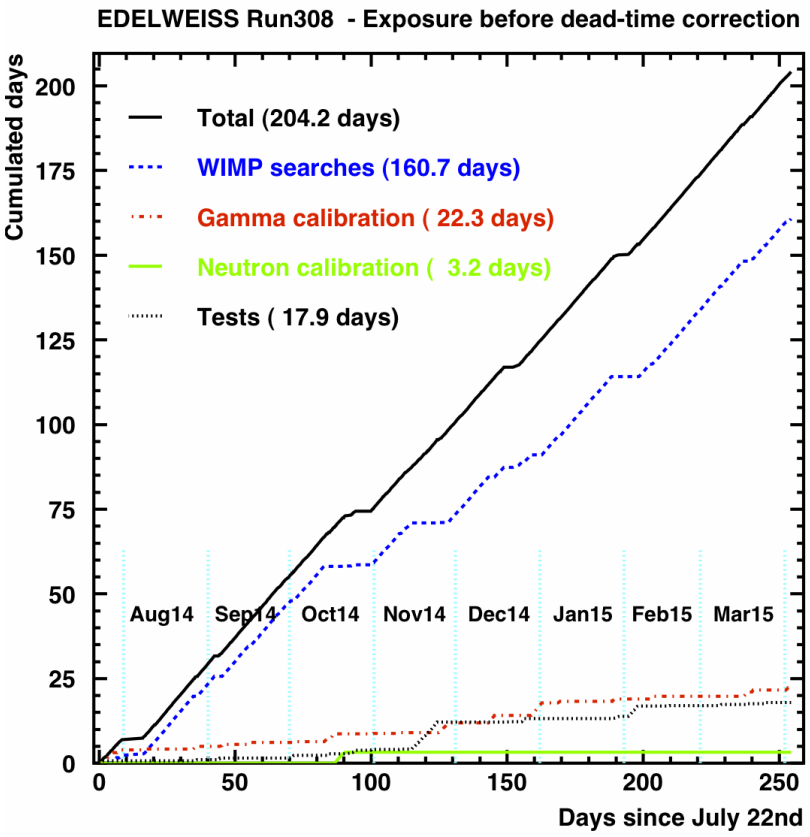

FIGURE 4.2 EDELWEISS-III Run 308 exposure.

4.1.2 EDELWEISS-III trigger

In order to understand the threshold limitations of the EDELWEISS experiment, it is essential to describe how triggering works. In EDELWEISS-III, the ionisation channels are sampled at 100 kHz. Each heat channel is also sampled at 100 kHz but it is subsequently demodulated yielding an effective sampling of 500 Hz. The trigger is set off by the heat channel since it typically achieves lower threshold for nuclear recoils than the ionisation channel. To this end, the heat data are filtered through a bandpass Butterworth filter,

fixed at the beginning of the run. They are then convolved by a template pulse, obtained by the convolution of the raw signal pulse shape with the Butterworth filter. This template is fixed at the beginning of the run as well. The bolometer then triggers if the convolved data overshoots a given threshold. The threshold varies over time because the heat baselines may vary. Hence, it is designed in order to meet two requirements: ensure an approximately constant event rate while maintaining the threshold at the lowest possible value. These requirements allow the threshold to regulate itself: when there is a sudden noise increase, the event rate increases and the threshold will rise as well to maintain a constant event rate. In low noise periods, the threshold can be more agressive and reach lower values without perturbing the event rate.

Once a bolometer has triggered, all channels (heat and ionisation) are stored on disk. The heat channel is recorded in a single demodulated trace of 1024 points centered around the event time. Each ionisation channel is stored in two traces. The first one is dubbed the "slow" ionisation, obtained by downsampling the full ionisation trace to 1 kHz. This yields a window of 2048 points centered around the event time. This downsampling allows us to solve issues related to the limitations of the available data storage and processing capabilities. It does not lead to significant loss of information since the low frequency part of the ionisation trace is where the highest signal to noise ratio can be achieved. A small part of the full ionisation trace, sampled at 100 kHz, is recorded as well. This is the so-called "fast" ionisation: it is used for precision identification of the time of the event. This is sometimes needed to search for coincidences between bolometers or with the muon veto.

We also remark that there is another ionisation channel, sampled at a much higher frequency (40 MHz). This sampling frequency is high enough to allow the measurement of the rise time of the ionisation pulse. However, it has been tested on one bolometer only with an independent acquisition. We will not make use of this information here.

The channels of the triggered detector's nearest neighbors are also recorded. This serves a double purpose: it can allow us to detect rare coincidences when a particle (a gamma in most cases) interacts in one detector and then leaves a very small energy deposit in another detector such that the other detector does not trigger. A careful offline analysis of the heat and ionisation traces then allows us to detect the event which the trigger did not see. On the other hand, traces with no such events play the role of a random trigger. This gives us a sampling of the noise condition for this particular detector which is useful for event processing like optimal filtering where one needs to compute the noise spectrum and for pulse simulations.

4.1.3 EDELWEISS-III offline pulse processing

Let us now give a few words on the offline processing. For all traces, the general procedure is the same: after a pre-processing step (with operations such as baseline subtraction and slope correction) the data is filtered and then fitted to a template pulse. The pre-processed traces are shown in Fig. 4.3 (low energy pulses relevant to the low mass WIMP analysis) and Fig. 4.4 (high energy pulses).

Optimal filtering has been implemented for the heat processing. This procedure, as defined in EDELWEISS, is equivalent to applying a filter with transfer function $H(f) = \frac{T(f)}{N(f)}$ where $T(f)$ is the Fourier transform of the template pulse and $N(f)$ reflects the noise conditions relevant to the corresponding time period (power spectrum density of the noise, estimated by averaging pure noise traces over time periods of an hour).

The ionisation signal is the Heaviside step function. This makes it hard to use optimal filtering (because of effects generated by an infinite derivative and non finite support). That is why optimal filtering is not implemented as of now for the ionisation processing in Run308. Instead, a Butterworth filter adapted to the noise conditions is used. Regardless the processing type, we are able to extract an amplitude (in ADU) for each channel.

The goodness of fit can be estimated by a simple chi-square with respect to the template. The chi-squared is well normalised for the heat processing because the noise was estimated in the optimal filtering procedure. No such normalisation is possible for the ionisation chi-square because the noise is not estimated during the amplitude estimation process. As a consequence, good ionisation pulses are selected by constraining the difference between the measured ionisation CHI2 and the average chi-square of clean noise pulses on the relevant time period.

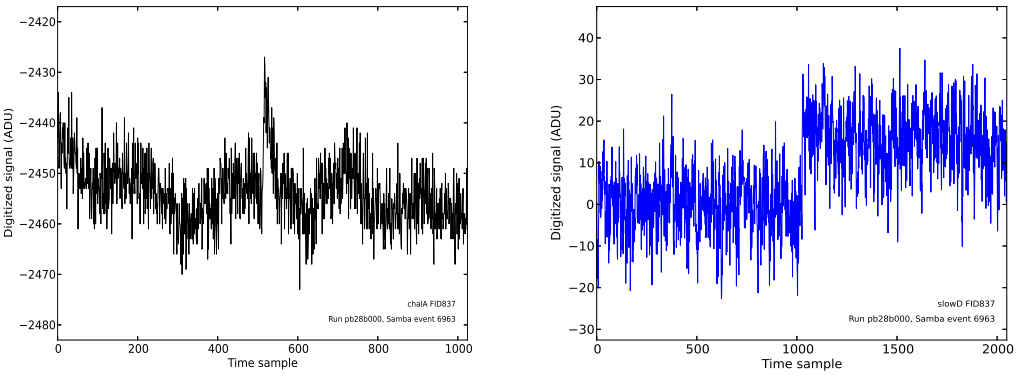

FIGURE 4.3 EDELWEISS-III pulses for a low-energy (3 keV) event. Left: Heat trace for which the influence of low frequency noise is clearly visible. Right: Ionisation B pulse.

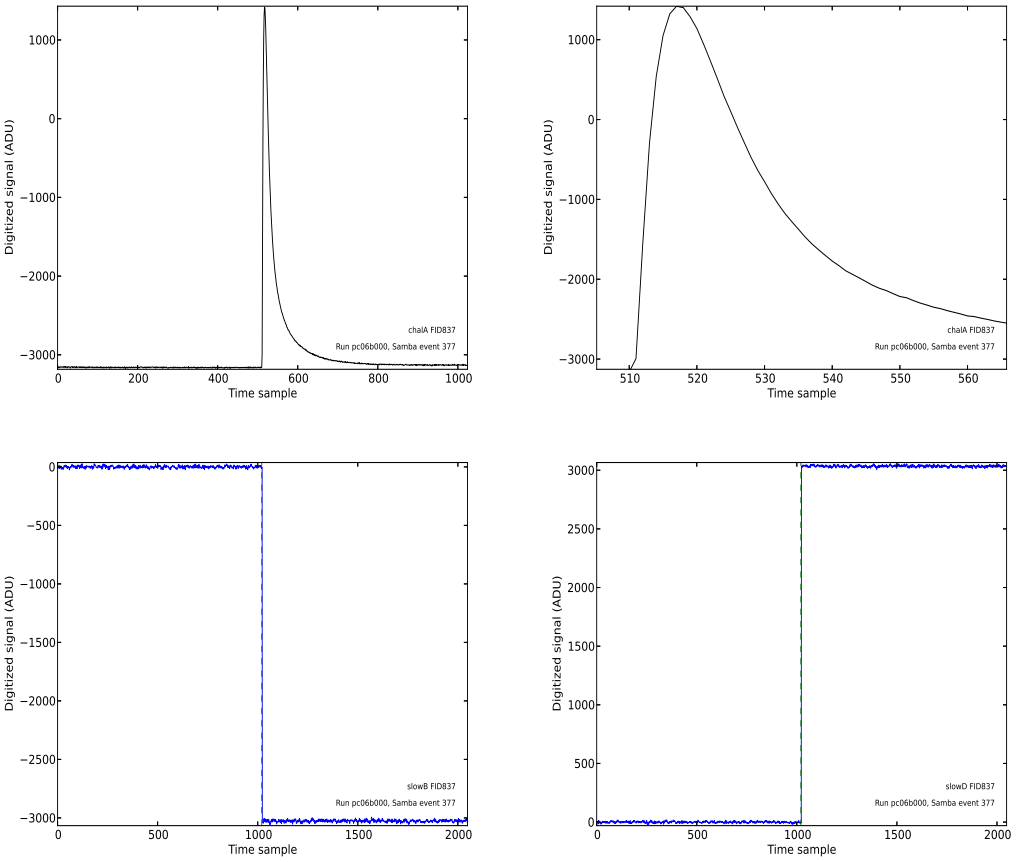

FIGURE 4.4 EDELWEISS-III pulses for a high-energy (600 keV) gamma event. Top Left: Full heat trace. Top Right: Zoom on the heat pulse. Bottom Left: Ionisation B pulse. Bottom Right: Ionisation D pulse. The signs of the ionisation pulses are opposite because the electrodes are polarized at opposite voltages.

4.1.4 EDELWEISS-III calibration

As we mentioned earlier, the energy calibration of all channels rely on the measurement of the 356 keV peak which appears in Baryum calibrations. The first step actually consists in measuring the ionisation cross-talk. Indeed, the heat and ionisation readout of each detector are carried out by two bolometer boxes (BBs). One BB reads four ionisations and one heat. The other BB reads the remaining heat channel. Because of the proximity of the cables, electromagnetic interferences can occur, causing cross-talk on the two ionisation channels of a single BB. This cross-talk is a linear effect which can be simply negated with the appropriate linear correction (see Fig. 4.5).

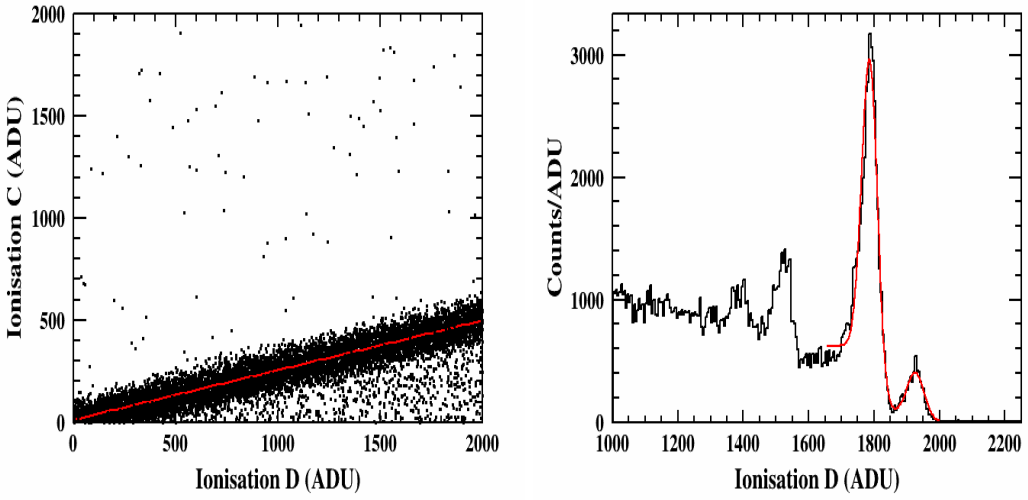

FIGURE 4.5 EDELWEISS-III calibration. Left: Crosstalk estimation, showing veto2 data as a function of collectrode2 data. Right: Baryum calibration 356 keV peak on collectrode D.

Once the crosstalk is estimated, we can look at the fiducial gamma electronic recoil spectrum where we expect to see a sharp peak at 356 keV (see Fig. 4.5). By fitting the position of the peak, we obtain the conversion coefficient to go from ADU to keV for each collecting electrode. The ionisation gain is very stable over time so we usually do not need to account for time variations. The 356 keV peak is sometimes difficult to identify for the innermost bolometers, which are shielded by their neighbours.

The veto electrodes cannot be calibrated in the same way since the 356 keV is harder to identify. Indeed 356 keV gamma rays usually deposit their energy through multiple scattering. These scatterings do not in general take place all at the same time within the small, shell-shaped non-fiducial volume. Hence, the standard procedure is to look for well identified surface events, for which we know that the veto energy should be the

same as the collecting electrode energy. Correcting for the cross talk, we can then obtain the appropriate calibration coefficient for each veto electrode.

The heat calibration is done in two steps. The first step consists in selecting fiducial events in the $[100, 200]$ keV interval. Then we look at the heat/ionisation ratio evolution over time for the same events (see Fig. 4.6, 4.7). Indeed, unlike the ionisation, the heat gain is suspect to changes, although it can remain stable over large periods of time. Accounting for these time variations, we then calibrate the heat thanks to the - already calibrated - ionisation. Hence, the heat is calibrated in terms of fiducial electronic recoils. By construction, the heat energy is equal to the ionisation energy (modulo resolution effects) for these events. For other events, this is no longer the case (because of the ionisation quenching factor and/or a different Luke effect).

The second step consists in correcting for the non linearities. Schematically, non-linearities arise because the detector's heat capacitance depends on its temperature. High energy particles can heat up the crystal and hence change its capacitance. Recalling Eq. 2.4, we see that this impacts the heat energy measurement. In practice, we get rid of those non-linearities by making an empirical fit to the observed dispersion and then correcting by the appropriate amount.

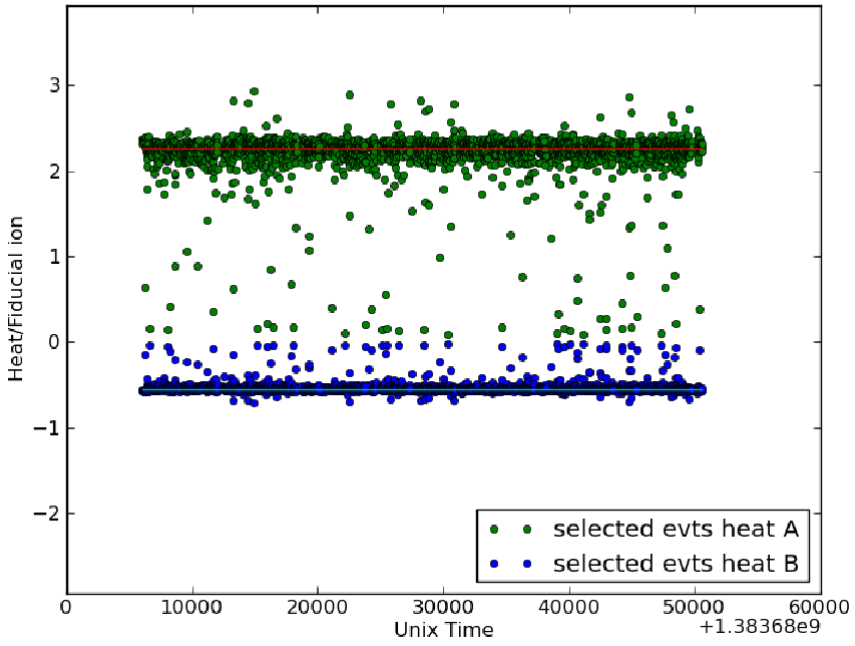

FIGURE 4.6 EDELWEISS-III calibration. Left: Linear heat calibration, which accounts for possible time variation of the heat gain. Both heat channels (A and B) are shown. The gain for A and B differ in sign because they have, for technical reasons, slightly different electronics readouts.

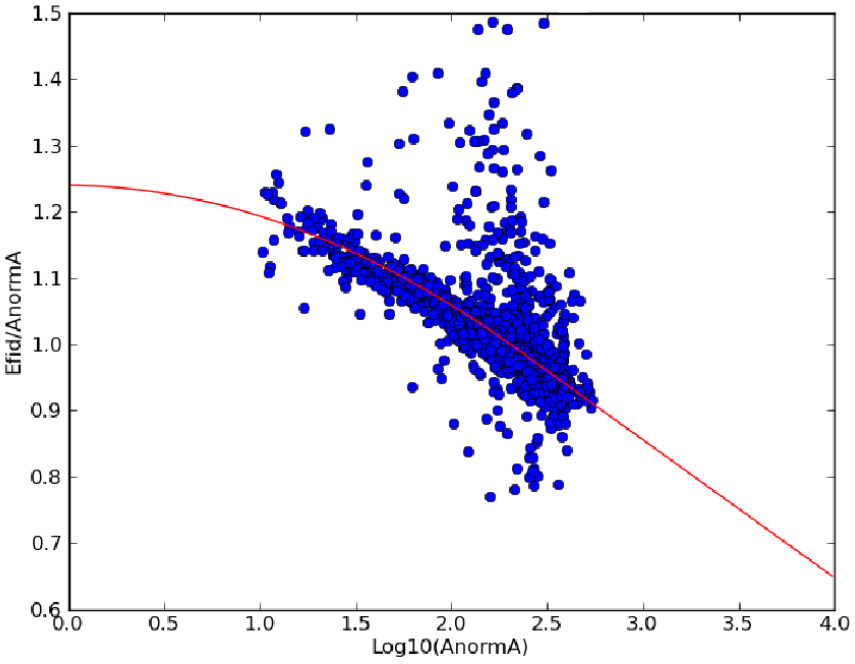

FIGURE 4.7 EDELWEISS-III calibration. Non linear heat calibration, which shows the heat over ionisation ratio as a function of the heat amplitude.

4.1.5 EDELWEISS-III n-tuples

EDELWEISS-III full-processed data are stored in ROOT TTree format with many different variables. Only a subset of these variables is of interest to us for the low mass analysis. We will now introduce some notations which will be used throughout the analysis. All variables are summarised in Table 4.1 and Table 4.2.

As stated before, we have four sets of electrodes and two heat sensors. Each set of electrodes is identified by a letter in (A, B, C or D). The heat sensors are identified as C1 and C2. The basic variable is the energy (ionisation or heat). This is accompanied by a measure of the resolution of the sensor (FWHM) and the chi-square of the fit to the template pulse. The experimental time is obtained by combining two variables, UT1 and UT2. The fiducial bias voltage is stored in VOLT while the veto bias is stored in VVET. Other variables of interest are the online threshold level (KTH), a multiplicity tag to identify multiple scatters (MULT) and the time before and after each event (TBEF, TAFT) which can be used to reject pile-up events.

Variable name	Definition
EIA/B/C/D	Ionisation energy for channels A/B/C/D
FWIA/B/C/D	Ionisation FWHM for channels A/B/C/D
CHIA/B/C/D	Ionisation χ^2 for channels A/B/C/D
RCIA/B/C/D	Average Ionisation χ^2 (over the hour) for channels A/B/C/D
OC1/C2	Heat energy for channels 1/2
OW/C1/C2	Heat FWHM for channels 1/2
XOC1/C2	Heat χ^2 for channels 1/2
UT1, UT2	Unix time = 1E6*UT1+UT2
VOLT, VVET	Fiducial and Veto bias voltage
KTH	Online trigger level
MULT	Event multiplicity count
TBEF	Time since last event in the detector
TAFT	Time before next event in the detector

TABLE 4.1 Base analysis variables.

We further introduce combined variables (like the heat estimator from the combination of the two heat channels) when needed.

Variable name	Definition
EI	Total ionisation. EI = (EIA+EIB+EIC+EID)/2
EFID	Fiducial ionisation (weighted sum of EIB and EID)
EIS1	Surface 1 ionisation (weighted sum of EIA and EIB)
EIS2	Surface 2 ionisation (weighted sum of EIC and EID)
EC	Heat energy (weighted sum of EC1 and EC2)
ER	Recoil energy ER = (1+VOLT/3) EC -1/3 (VVET (EIA +EIC) + 0.5 VOLT(EIB + EID))
FWFID	Fiducial ionisation baseline
FWS1	Surface 1 ionisation baseline
FWS2	Surface 2 ionisation baseline
FWC	Combined heat baseline
Q	Ionisation quenching factor Q = EI/ER

TABLE 4.2 Combined analysis variables.

Lastly, we created a new variable called HR which corresponds to the magnitude of the heat-only background (see Section 4.2.5 for a detailed discussion of this background) at the time of the event. The idea is that the rate of heat-only events varies steeply with time and is uncorrelated with the WIMP rate: many heat-only events occur when HR is high, while potential WIMPs occur uniformly (if we neglect the annual modulation). Hence, the HR distribution for heat-only events should be skewed to high values of HR with respect to that of WIMPs. We will use this new variable to improve discrimination. For legibility's sake, we summarise this paragraph in Table 4.3

Variable name	Definition
HR	Heat-only rate at the time of the event It is obtained from the time distribution of heat-only events selected in a sideband and histogrammed with a binning of 1 day.

TABLE 4.3 New heat-only rate variable.

4.2 Backgrounds

We have already discussed possible sources for background events in Section 2.1. Here, we are going to study their distribution in WIMP search data. All the plots shown in this section come from the unblinding of a fraction of the WIMP-search data set. We selected one "good" but relatively standard detector, FID837, with data taking between July 2014 and January 2015. The resulting exposure is 35 kg.d.

A Q plot, which shows the quenching factor as a function of the recoil energy is very helpful to visualise the data. In Fig. 4.8 below, we can easily identify 4 different background populations. Gamma events are centered around the value $Q = 1$. The radioactive lines from the decay of ^{68}Ge and ^{65}Zn around 10 keV are also clearly visible. At lower values of the quenching factor, near Q = 0.4, lies another important contribution to the background, originating from β surface radioactivity. At even lower values of Q, near Q = 0.08, we can see another surface background, this time caused by ^{210}Pb recoils. The largest contribution of all can be seen at Q = 0. Recalling that $Q = \frac{E_I}{E_R}$, we see that these events must have zero ionisation. Hence, we will refer to them as *heat-only* events. Given the magnitude of this background, specific attention will be devoted to its understanding in this work.

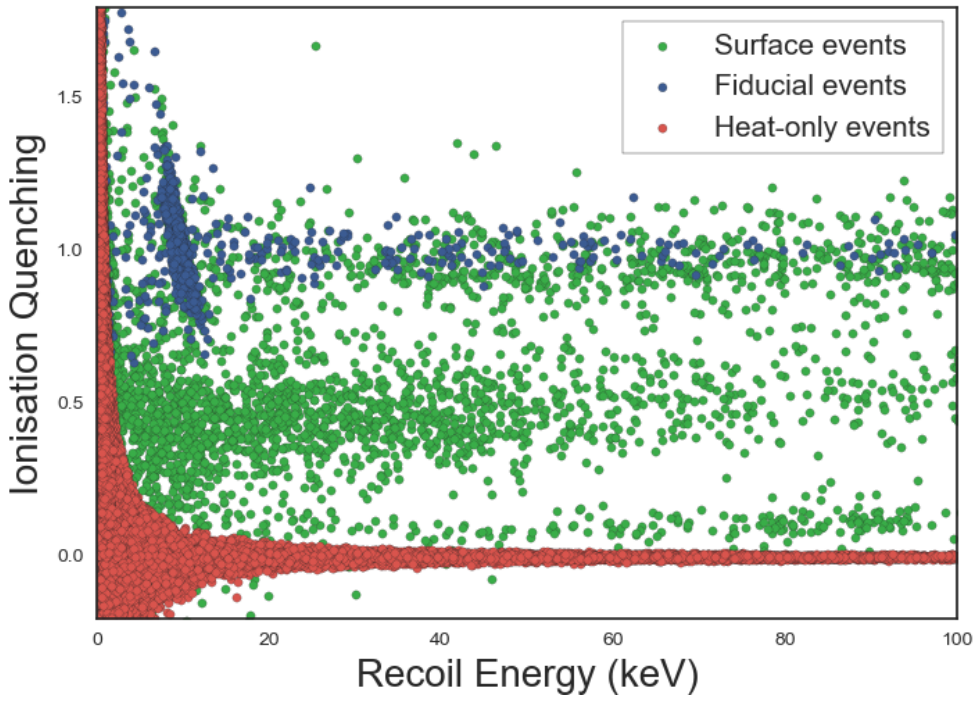

FIGURE 4.8 Q plot for WIMP search data. The data shown here passes general quality cuts (heat and ionisation baseline and chi-square cuts).

A neutron background would appear in this plot as a band of fiducial events around Q= 0.3. Given the low exposure considered it is not expected to be visible.

One may also remark that the separation between different background bands is not always clear cut (especially between the gamma and β band), even when resolution effects are taken into account: there is actually another background, induced by poor charge collection near the surface. Hence, some gammas, which interact close to the surface, fall outside of the usual Q= 1 gamma band. However, they are of little importance for our WIMP searches.

In order to better characterise these backgrounds, we are now going to describe typical one-dimensional distributions of the count rate as a function of the combined heat energy. Special emphasis will be put on heat-only events as we will try to find hints of their origin. Let us first describe the data selection procedure. The mean of a random variable X will be written as $\mu(X)$ and its standard deviation will be written as $\sigma(X)$.

General quality cuts:

- Remove coincident events with MULT=1,
  Remove pile-up events with a TBEF > 0.5 and TAFT > 0.5.
- Select good data acquisition periods by imposing KTH$<$ 1 keVee and
  FWChannel $< 5\sigma$(FWChannel) for all channels.
- Impose XOC $< \mu$(XOC) $+4\sigma$(XOC) for all heat channels.
- Impose CHI-RCI $< 5\sigma$(CHI-RCI) for all ionisation channels.
- Impose EC> 0 and $|$EC1$-$EC2$| < 1$.

Selection of fiducial events:

- Require EIA $<$ 1.2 FWIA, EIC $<$ 1.2 FWIC, EIB $>$ 1.2 FWIB, EID $>$ 1.2 FWID and EC > 0.5 to select fiducial events

Selection of pure surface events:

- Require EIC $<$ 1.2 FWIC, EID $<$ 1.2 FWID, EIA $>$ 1.2 FWIA, EIB $>$ 1.2 FWIB to select Surface 1 events
- Require EIA $<$ 1.2 FWIA, EIB $<$ 1.2 FWIB, EIC $>$ 1.2 FWIC, EID $>$ 1.2 FWID to select Surface 2 events

Population selection:

- Require $Q > 0.7$ to select gamma events
- Require $0.2 < Q < 0.7$ to select beta events
- Require $0.04 < Q < 0.15$ to select lead recoil events
- Require $EI < 1$ keVee to select heat-only events

4.2.1 Fiducial Gamma background

As we saw in Chapter 3, the low-energy fiducial gamma background (shown in Fig.4.9 below) is made of a mostly flat Compton component and radioactive peaks at well-identified energies.

We have selected the events according to the procedure we mentioned in Section 4.2 and we did not correct the spectrum for the online trigger efficiency (shown in red here).

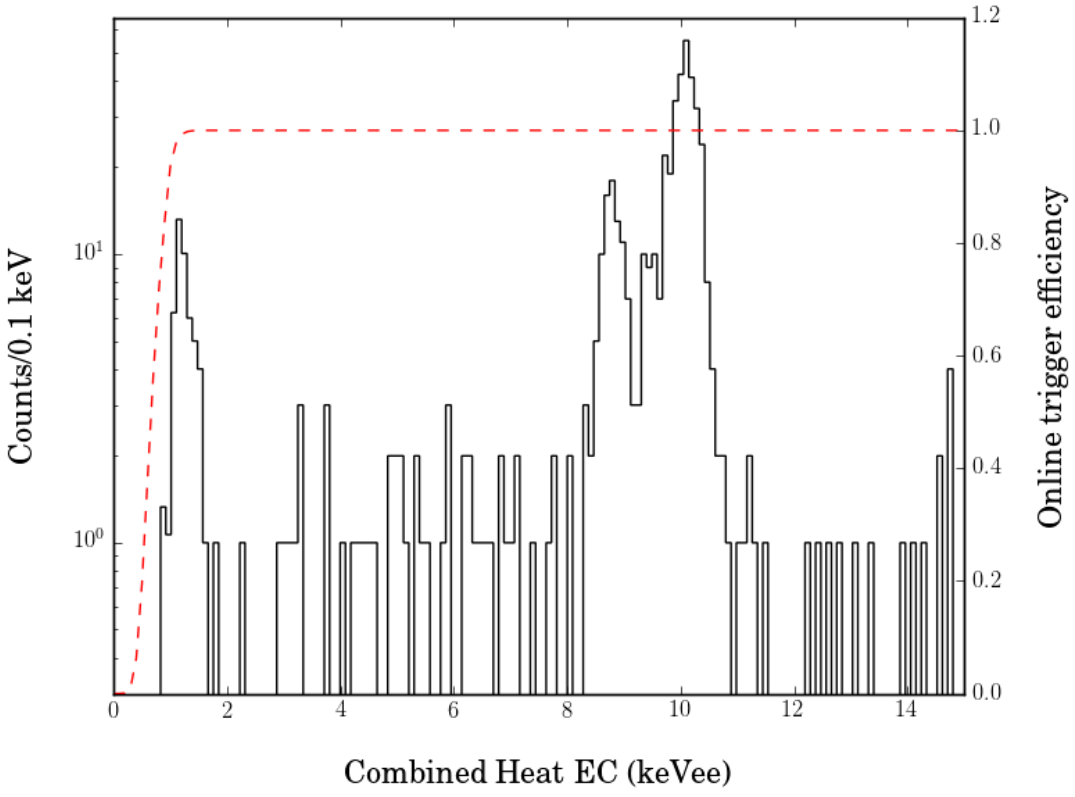

FIGURE 4.9 Fiducial gamma background for the FID837 bolometer. The red line shows the online trigger efficiency as a function of the combined heat energy.

The main novelty with respect to EDELWEISS-II is that the resolution and threshold have improved. We are now able to clearly identify the 1.1-1.3 keV peaks from the L-shells of ^{68}Ge and ^{65}Zn. The L-shell peaks are related to the K-shell peaks (found at 10.37 and 8.98 keVee respectively). Hence, their amplitude can be predicted from the knowledge of the K-shell peak's amplitudes. The amplitude ratios were measured by Bahcall in 1963 [123]. In the following, we will use L/K= 0.1175 for ^{68}Ge and L/K = 0.119 for ^{65}Zn.

4.2.2 Surface Gamma background

The surface gamma background is very similar to the fiducial gamma one: we can identify a flat Compton component and radioactive lines identical to those of the fiducial gamma background. There are a few important differences however:

- The Compton background is usually higher than that of fiducial events. This is because fewer external low energy gammas can reach the fiducial volume.
- The amplitudes of the cosmogenic peaks is reduced by a factor 1/3 (with respect to fiducial gammas) approximately. This is because the active elements are uniformly distributed in the crystal, and the fiducial mass is over three times the surface mass.
- The cosmogenic peaks' energies are different from those of fiducial events. Indeed, the Luke-Neganov effect is not the same for surface and volume events, because the applied biases (V_{surf} and V_{fid} respectively) are not the same. This shifts the lines by a factor $\frac{1+\text{V}_{\text{surf}}/3}{1+\text{V}_{\text{fid}}/3}$.

In Fig. 4.10 below, we show the surface gamma spectrum. The data selection follows the procedure of Section 4.2 and we stacked the Surface 1 and Surface 2 spectra. We do not show data below 2 keV as the correct idenfication of surface Gamma becomes more difficult since they overlap with other backgrounds. As a consequence we cannot see the 1.3 keV lines in the non-fiducial volume.

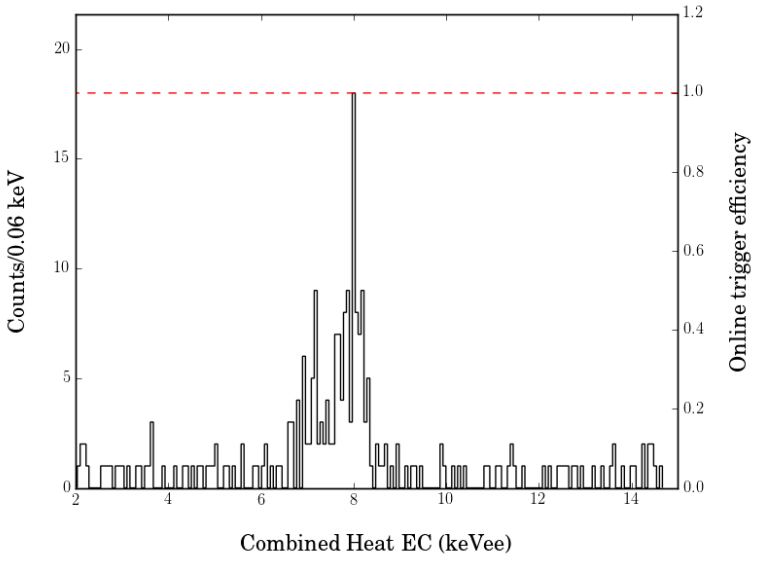

FIGURE 4.10 Surface gamma background for the FID837 bolometer. In the heat spectrum, the lines' energies are shifted by a factor $\frac{1+\text{V}_{\text{surf}}/3}{1+\text{V}_{\text{fid}}/3}$.

4.2.3 Surface Beta background

To this date, the beta background of the EDELWEISS experiment remains poorly known. The collaboration has run Monte Carlo simulations to reproduce the observed distributions and understand the major contributions to the beta spectrum. Unfortunately, there are large uncertainties in these simulations. It was shown that the observed spectrum could vary significantly with the position of the beta source and its implantation depth. In the face of these uncertainties, we chose to resort to data-driven methods to model the beta background.

In addition to WIMP search data, we can use surface calibration data to understand the Beta (or lead recoil) background. These calibrations were carried out by depositing ^{210}Pb on the surface of the detector holder of two bolometers, called FID808 and FID803 during another run, called run305, which took place between November 2013 and February 2014. The obtained distribution has high statistics; it is therefore instructive to compare it to the distribution obtained under WIMP-search conditions as it can guide the background modeling. There are some limitations to this comparison: the calibration source on FID808 does not necessarily reflect the true source (position, implementation depth....), different detectors might have different spectra and the data taking conditions during run305 are different from those of run308. All these remarks explain why we used calibration data for comparison purposes only: the beta background model is built entirely from the WIMP-search data of the bolometer under study.

In Fig. 4.11 below, we show the surface beta spectrum obtained for FID837. The data selection follows the procedure of Section 4.2 and we stacked the Surface 1 and Surface 2 beta spectra. We do not show data below 2 keV as the correct idenfication of surface beta events becomes more difficult since they overlap with surface gamma events. The black histogram corresponds to actual run308 FID837 data. The red histogram shows the calibration data of FID808 during run305. We have rescaled the red histogram to make the comparison easier.

At face value, our black data does not seem to reproduce the “bump” feature observed near 15 keVee. However, this is likely due to statistical fluctuations and stacking the two surfaces. To verify that, we randomly downsampled the calibration data to match the size of our actual data for each surface. We then ran a Kolmogorov-Smirnov (KS) test. Iterating 100 times, we obtain a mean p-value of 0.25 (respectively 0.12) for surface 1 betas (respectively surface 2 betas): there is no significant deviation from the null hypothesis, which states that the two samples come from the same distribution.

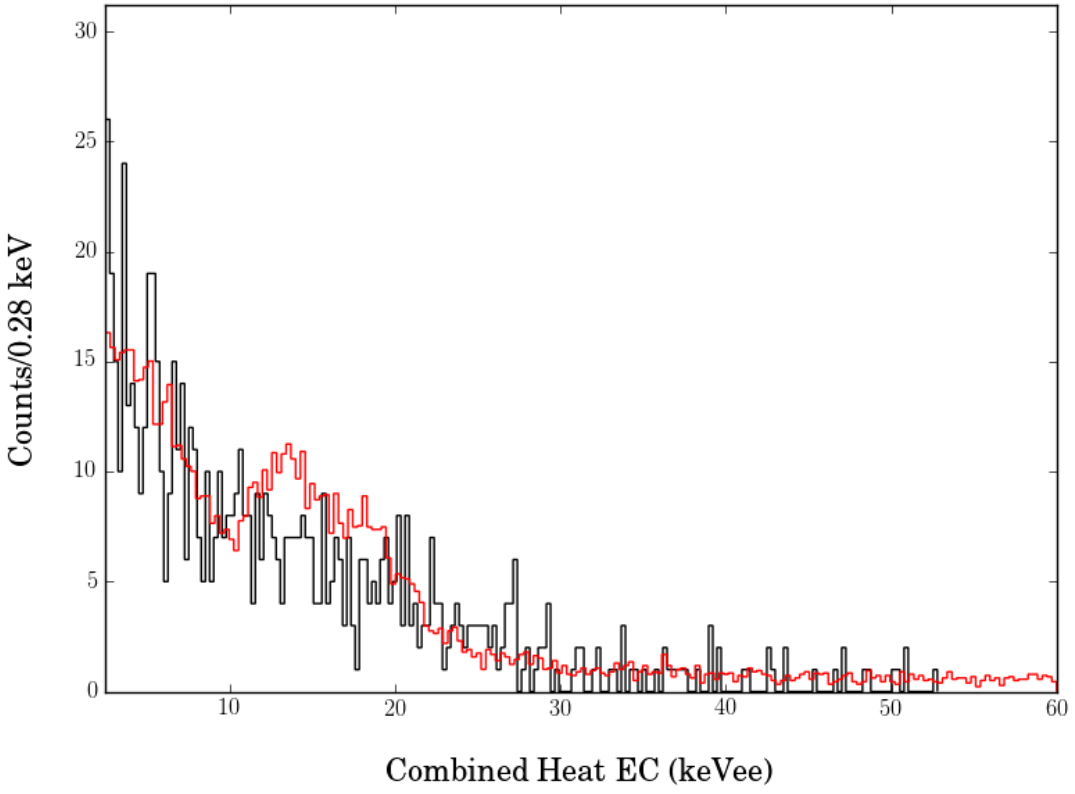

FIGURE 4.11 Surface β background for the FID837 bolometer. Black histogram: FID837 run308 data. Red histogram: FID808 run305 calibration data (rescaled).

4.2.4 Surface lead recoil background

The comments we made on the beta background are also valid for the lead recoil background: it is difficult to provide a theoretical model and the most robust procedure is to base simulations on actual data. The lead recoil background from a single detector is shown in Fig. 4.12 below. The data selection once again follows the procedure of Section 4.2 and we stacked the Surface 1 and Surface 2 lead recoil spectra. As above, the red histogram shows the calibration data of FID808 during run305. We have rescaled this histogram to make the comparison easier.

The decay of ^{210}Po leads to the emission of a ^{206}Pb with 100 keV recoil energy. Recalling that:

$$\mathrm{ER} = (1 + \mathrm{VOLT}/3)\ \mathrm{EC} - 1/3\ (1.5\ \mathrm{EIA} + 4\ \mathrm{EIB} + 1.5\ \mathrm{EIC} + 4\ \mathrm{EID}) \tag{4.1}$$

we can compute the associated heat energy; we find EC = 28 keVee which indeed matches the energy of the peak of Fig. 4.12. This distribution charts a tail. This is because the ^{206}Pb can deposit part of its energy in the detector holder from which it was emitted (or escape the Germanium surface in case it was deposited directly on the detector).

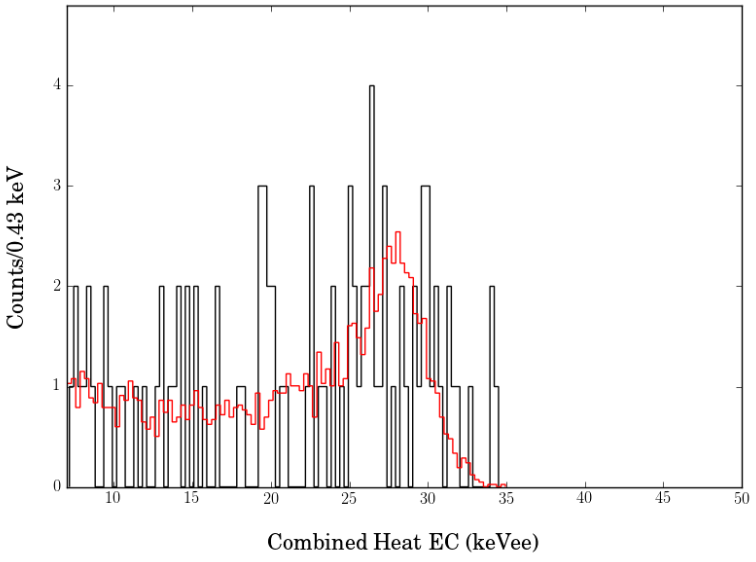

FIGURE 4.12 Surface lead recoil background for the FID837 bolometer. Black histogram: FID837 run308 data. Red histogram: FID808 run305 calibration data (rescaled).

As for the beta background, an appropriate downsampling followed by a KS test shows a good agreement between WIMP-search and calibration data (p-values of 0.65 and 0.25 for surface 1 and surface 2 lead recoils respectively).

4.2.5 Heat-only background

We have already stated that heat-only events were the most prominent low mass background. This is well evidenced by Fig. 4.8 where it is clear that the band at $Q = 0$ outweighs all other contributions.

From previous EDELWEISS runs, we knew that internal radioactivity in NTD sensors could lead to the production of ionisationless events, with a distinctive pulse shape. We call such events "NTD events". The new design of the FID detectors (two heat sensors instead of one) allows us to confirm the origin of these events. A typical NTD event is shown in Fig. 4.13. In one sensor (left panel), we observe an intense pulse, with much faster decay time than a standard pulse. In the other sensor (right panel), we observe a low energy, slowly decaying pulse. These peculiar pulse shapes are interpreted as follows: because the energy deposition of an NTD event occurs in a very distinct region of the detector, the resulting thermal signal is not filtered in the same way as normal events. For instance, the heat signal detected by the NTD in which the NTD event was produced was not filtered by the glue used to couple the heat sensor to the crystal. More importantly, the event couples directly to the electrons of the NTD.

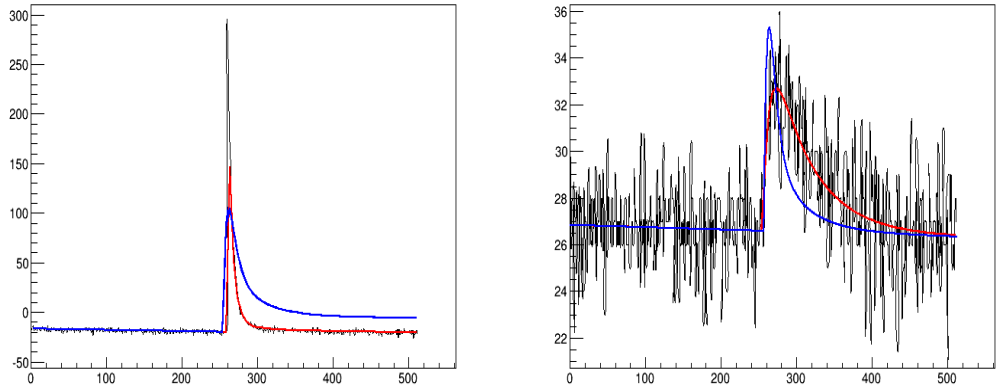

FIGURE 4.13 Left: Heat pulse of an NTD event as detected by the NTD from which it originates. Right: Heat pulse of an NTD event as detected by the other NTD. In each plot, the red line shows a fit to the anomalous pulse while the blue line represents the shape of standard pulses

An efficient way to get rid of NTD events is to impose chi-square cuts on the heat pulse shape. Indeed, the template used for standard events is not adapted to the shape of the pulses shown in Fig. 4.13. Hence the fit should result in a large chi-square which allows us to separate NTD events from real events. In addition, NTD events will typically exhibit very different values of EC1 and EC2 while these should be equal (modulo resolution

effects) for real events. Hence, a cut on the difference between the two heat channels can further help us reject NTD events.

Is it sufficient to get rid of all heat-only events? Unfortunately, the answer is no. In Fig. 4.14, we show all the events satisfying the general quality cuts of Section 4.2 and EI$<$ 1. We have also relaxed the constraints on EC1$-$EC2 and the heat chi-square. The blue and red populations are separated by a heat chi-square cut. The red dots correctly match the standard heat template and chart a good chi-square while the blue dots do not. The chi-square cut is strict enough to remove most NTD events. In spite of this cut, we see that many heat-only events (most of which statisfy EC1=EC2) remain. This shows that there is a new, distinct population of heat-only events.

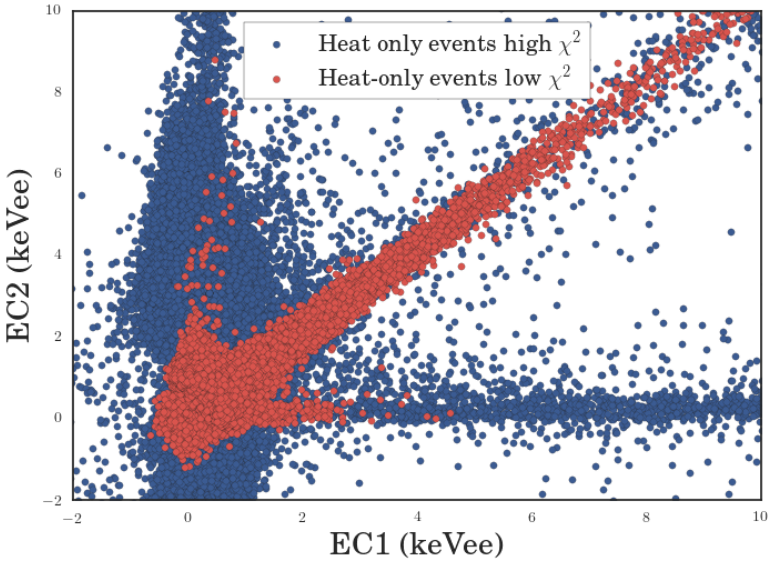

FIGURE 4.14 FID837 EC2 versus EC1 for ionisation-less events. The blue population is made of events such that XOC$>$ μ(XOC)+2σ(XOC) for at least one heat channel. The red population is made of events such that XOC$<$ μ(XOC)+2σ(XOC) for both heat channels.

In the following, we will always impose a cut on the difference between EC1 and EC2 and a heat chi-square cut. "Heat-only" will then only denote the ionisation-less events that pass these cuts.

We can now exclude NTD events as the primary contribution to the heat-only background. Do we have other candidates? A potential contribution may come from lead recoil events. Indeed, some of them may fall directly on a collecting electrode. In that case, no ionisation is collected and the event looks just like a heat-only event. However, this contribution remains marginal as shown in Fig. 4.15. This figure shows the proportions of lead recoils at $Q = 0$ (red histogram) and at $Q = 0.08$ (black histogram)

for calibration data in Run305. The ratio of the number of events is about 0.13. From Fig. 4.8, this is clearly insufficient to account for the whole heat-only background.

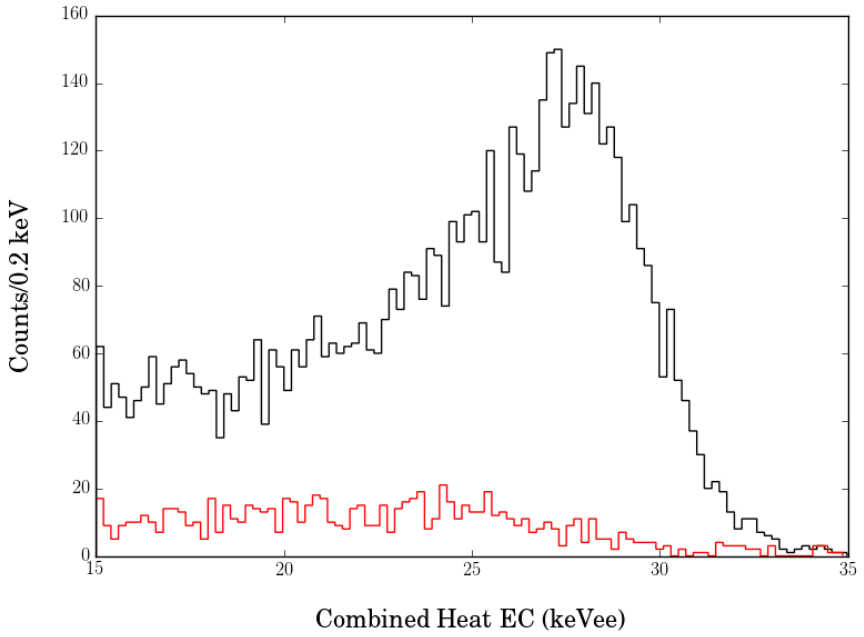

FIGURE 4.15 Lead recoil spectra for FID808.

So what are these heat-only events made of? To answer this question, we need to find other clues. Let us look at the heat-only spectrum, shown in Fig. 4.16. In this plot, we have selected events passing all the general quality cuts of Section 4.2 and the heat-only selection cut. The spectral shape is not particularly informative. Above 2 keV, it is well fitted by a simple exponential. Below this value, the slope changes, threshold effects start to kick in as we hit the noise wall.

The time distribution of heat-only events, shown in Fig. 4.17, is much more interesting as it exhibits several key features. For this plot, we have selected events passing all the general quality cuts of Section 4.2 and the heat-only selection cut. We have also imposed EC> 1.5 keVee. There are so-called calm periods where the heat-only rate is low and approximately flat. A burst of the event rate has also been observed. Then, there is a tentative exponential decay (with decay time 20 days) starting at day 65. The radioactive hypothesis is currently disfavored: the tables of the decay chains of the usual radioactive isotopes show no species with the corresponding decay time. Moreover, day 65 coincides with a cryogenic and hardware intervention which may account for the feature. What is remarkable is that all these characteristics are observed simulateneously in the other detectors.

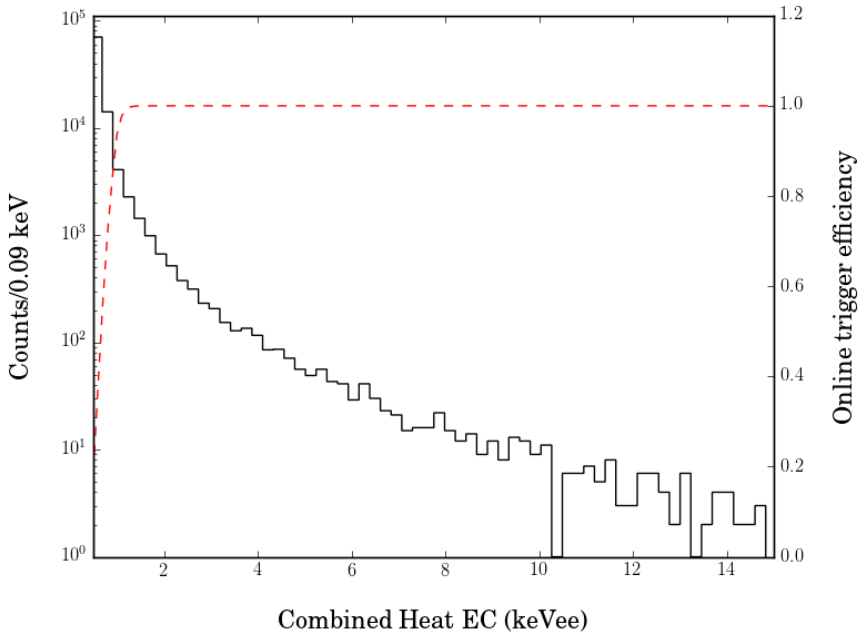

FIGURE 4.16 Heat-only spectrum for the FID837 bolometer.

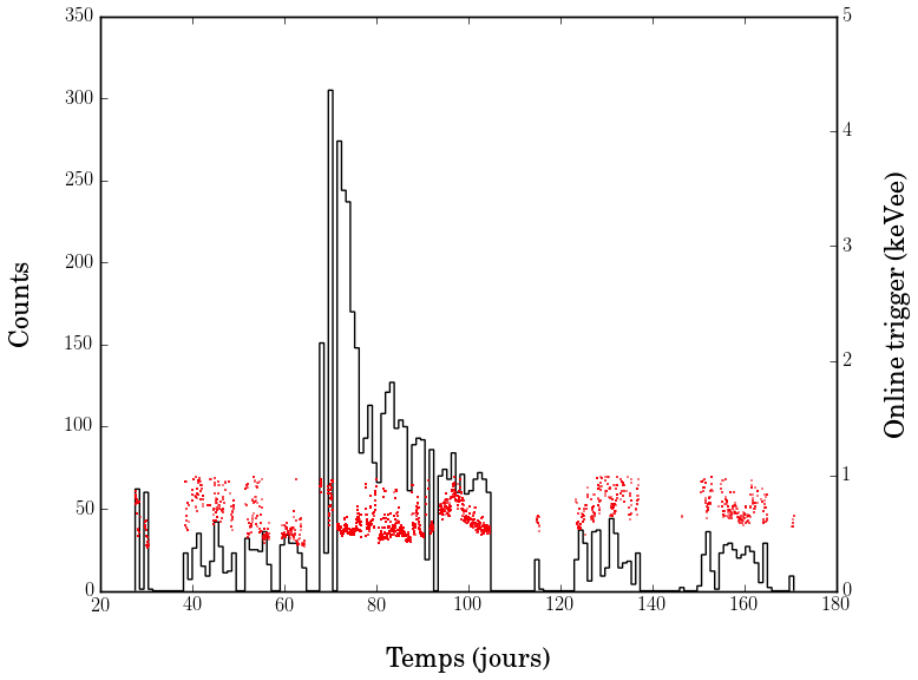

FIGURE 4.17 FID837 heat-only event rate over time. The red dots indicate the online trigger level.

The large variations of the time-distribution of heat-only events points to potentially distinct heat-only populations. We can learn more about these by looking at the evolution of the heat-only background's spectral form over time. With the same data selection

cuts as above, we have split the WIMP search data into four periods. In Fig. 4.18, we superimpose the heat-only heat spectrum obtained for each periods. Periods 1 and 2 are less noisy than periods 3 and 4 as evidenced by a noise wall located at lower energies. However, these periods do not necessarily coincide with those were the heat-only rate is high. This shows that heat-only events are not correlated to the baseline noise.

Despite all these observations, the origin of heat-only events remains unclear. A possible interpretation is to invoke mechanical noise like friction between the crystal and its teflon-coated support. The possibility of a Helium leak has also been put forward. What is clear is that the heat-only rate needs to be very closely monitored. The collaboration is now thinking about new ways to hold the detectors in order to reduce the mechanical stress.

Heat-only events are also seen by the SCDM collaboration and were understood as low frequency noise in a recent work [124]. Unlike EDELWEISS, most of these events were rejected with pulse shape discrimination. The difference may come from their phonon sensor technology, which operates at higher frequencies.

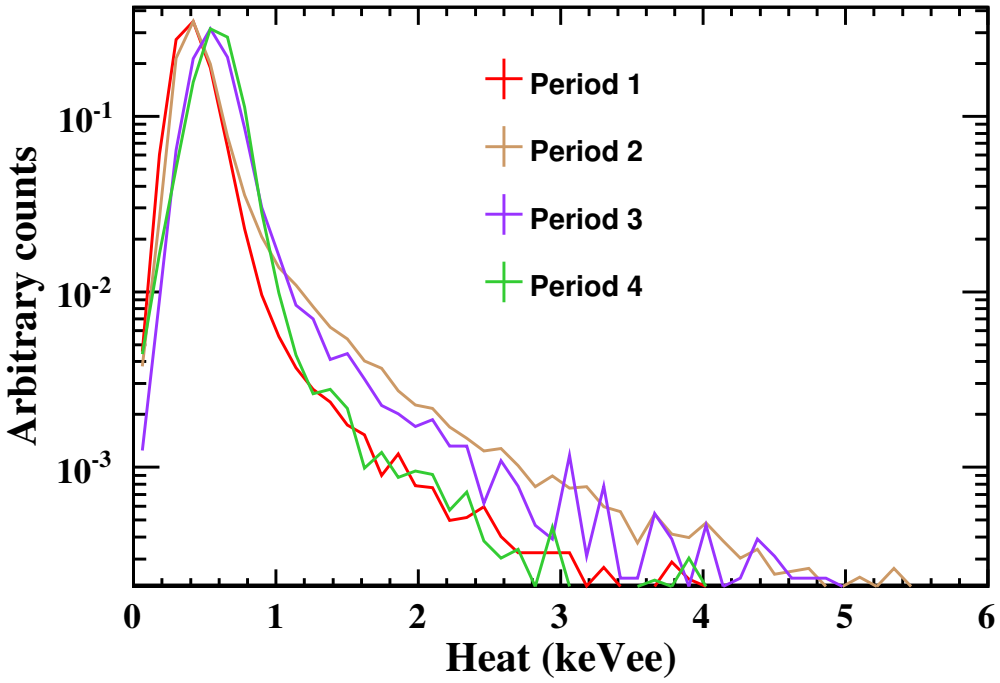

FIGURE 4.18 FID837 heat spectrum for different periods. The histograms have been rescaled to unit norm. Period 1: from day 1 to day 65. Period 2: from day 65 to day 110. Period 3: from day 110 to day 150. Period 4: from day 150 to day 200.

4.3 Boosted Decision Trees

4.3.1 Principle

Boosted Decision Trees (BDTs) are a **classification method** which solves the following problem: we are given different classes of events and a data sample. The goal is to find the correct class for each event in the data sample. In most physically relevant instances, there are two classes: background and signal events.

A set of features is attached to each event. The algorithm uses theses features to classify events. In the EDELWEISS experiment, the basic features are the ionisation and heat measures. With 4 ionisation channels and 2 heat channels, we have a 6D parameter space.

BDT belong to the so-called **supervised learning** methods which typically work in two steps. Classified, known events are fed to the algorithm, which learns their characteristics. This is the training phase. Once the training is over, new, unidentified data is fed to the algorithm. The algorithm classifies these new events based on what it has learnt in the training phase: this is the application phase.

The basic idea of a decision tree is to make successive rectangular cuts in the parameter space. Usually, the size of the tree (its depth/number of node) is fixed beforehand. At each node, the algorithm determines the optimal (in terms of the classification error) variable X_i and cut value c_i to partition the space into two complementary subsets $\{X_i > c_i\}$ and $\{X_i < c_i\}$. If the tree is too large (i.e. it makes numerous specific cuts to correctly separate the classes), it might not generalise well. This is called overfitting. This is why the tree should first be "grown" large and then pruned by optimizing a cost-complexity function.

Boosting is a powerful technique that combines "weak" classifiers to get better results. The first step consists in training a simple decision tree. At the end of the training, some events are misclassified. The events are then reweighted according to their classification score. This reweighting puts more emphasis on poorly classified events: at the next stage, a new tree is trained with the reweighted data. This procedure is iterated as desired. Then, the final classification is averaged over all the decision trees.

For more details on the fundamentals of multivariate analyses, the interested reader may refer to *The elements of Statistical learning* by T. Hastie, R. Tibshirani and J. Friedman.

4.3.2 BDT model selection and validation

In order to train the BDT, one has to choose the values of so-called hyperparameters which are inherent to the algorithm. For instance, one must choose the number of boosting instances (how many trees are combined to estimate the target), the depth of each individual tree or the value of regularisation parameters (which add a cost to model complexity to constrain overfitting). Feature seletion is also an important part of the model selection. With too few features, the model might lack discriminative power. With too many features, the large phase space induces prohibitive computation costs. Hence, the challenge is to find the combination of parameters that give the best performance. Then, there is another issue which is to evaluate whether the model generalises well to new data: is it able to correctly predict the class labels of data which it has not seen before ?

The choice of hyperparameters induces a bias-variance tradeoff situation as illustrated by Fig. 4.19. In this simulated classification, the data was divided into different sets: a training set, to train the classifier and a test set, to evaluate the classification error on new data. Here, the "error" is a function that quantifies how poorly the set was labeled by the machine learning algorithm.

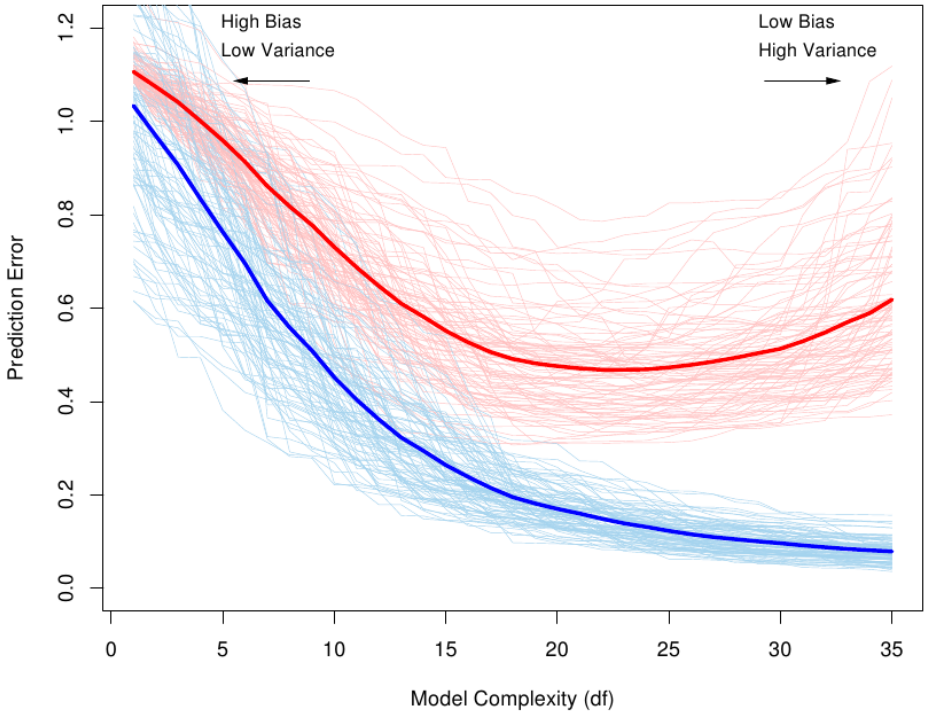

FIGURE 4.19 Illustration of the bias-variance tradeoff. Figure from *The elements of Statistical learning.*

The light blue curves (respectively light red curves) show the training (respectively testing) errors on 100 training (respectively testing) sets of equal size as a function of model complexity. The thick line corresponds to the average of all curves in both cases. The spread of the curves gives an idea of the variance of the classifier. The training error generally tends to decrease with model complexity. This is because we allow the model to be perfectly tuned to the data. For the test error, we see two distinct regimes. Simple models generalise well to new data, which is why there is little variance. However, they may fail at capturing all the relations between the features, resulting in poor classification performance (high bias). With increased model complexity, the model becomes more powerful. However, it may not generalise well given that it adapts itself too closely to the training data: the variance increases.

In order to estimate the optimum model complexity and the generalisation error (i.e. the error on a new, independent dataset), we may split the data into three samples: a training sample to train the classifier, a test sample for model selection and a validation sample to estimate the generalisation error. The idea is that the validation sample should remain hidden until all the parameters have been fixed through training and testing. Indeed, the test sample may not provide an accurate estimation of the generalisation error. Since model selection is guided by the error on the test set (which we seek to minimise), there is a chance that this leads the algorithm to overfit the test set. That is why an independent set must be used to estimate the generalisation error.

This procedure is rather wasteful as significant chunks of the dataset are left out (for testing and validation). This is where K-fold cross validation comes into play: the data set is divided into K equal size datasets. Then, one set is used for testing, while the four others are used for training. This procedure is repeated K-1 times, until all sets have been singled out exactly once for testing. Given a set of parameters, the testing error is then estimated as the average of the K testing errors at each stage of the K-fold cross validation procedure. This procedure can be iterated for all sensible hyperparameter values (and possibly different feature choices). The best parameters are chosen as the ones which minimise the cross validation testing error. The generalisation error can then be computed on a validation set which was isolated beforehand.

4.4 Analysis of a single detector: FID837

We are now going to present the details of the single detector analysis. This is mostly a prospective analysis, with a very conservative approach: we looked at a fraction of the data available for a single detector (FID837) and imposed a relatively high threshold at 1.5 keVee. We used this data to construct a detailed background model for a typical detector.

4.4.1 Data selection

The data selection follows the general cuts outlined in Section 4.2. Let us give the precise cut values for chi-square and baseline cuts. We will also track the evolution of the efficiency after successive cuts.

- As before, we require KTH< 1 keVee. This reduces the livetime to 73 days, from 100 days.
- Require FWIA< 1.5, FWIB< 1.5, FWIC< 1.5, FWID< 1.5
  and OWC1< 1, OWC2< 1. This further reduces the livetime to 66 days.
- Require (CHIA-RCIA, CHIB-RCIB) $< (0.28, 0.22)$
  and (CHIC-RCIC, CHID-RCID) $< (0.18, 0.23)$
- Require (XOC1, XOC2) $< (0.114, 0.114)$

We have checked that the efficiency loss induced by the chi-square cuts is less than 1%. All other efficiency losses were shown to be negligible. In particular, Fig. 4.20 below shows that the online threshold efficiency is 100% for the 1.5 keVee threshold of this analysis. The computation of the efficiency was obtained independently in two ways.

- Given the online trigger KTH, the efficiency is[1]:

$$\epsilon = 0.5 \left(1 + \mathrm{Erf} \left(\frac{\mathrm{EC} - \mathrm{KTH}}{\sqrt{2} \frac{\mathrm{FWC}}{2.3548}} \right) \right) \tag{4.2}$$

  We have to account for the time variations of the online trigger level. So we split the livetime into periods of equal KTH. We then computed the contribution of each period to the total livetime. Finally, we computed the weighted sum of the efficiency for each period. The resulting curve falls under the label "samba" in Fig. 4.20.

[1] assuming the resolution measured by samba is the same as the offline resolution.

- The efficiency can also be measured by studying coincidences between neighbour detectors. Let us take 2 bolometers, A and B. We want to compute the trigger efficiency of A. To this end, we first select events on which B has triggered. In these events, we look for the population P of events on which A has triggered as well. The ratio of the energy distribution of P and the energy distribution of all events then gives the online trigger efficiency. The resulting histogram (with error bars) is labeled "coincidences" in Fig. 4.20.

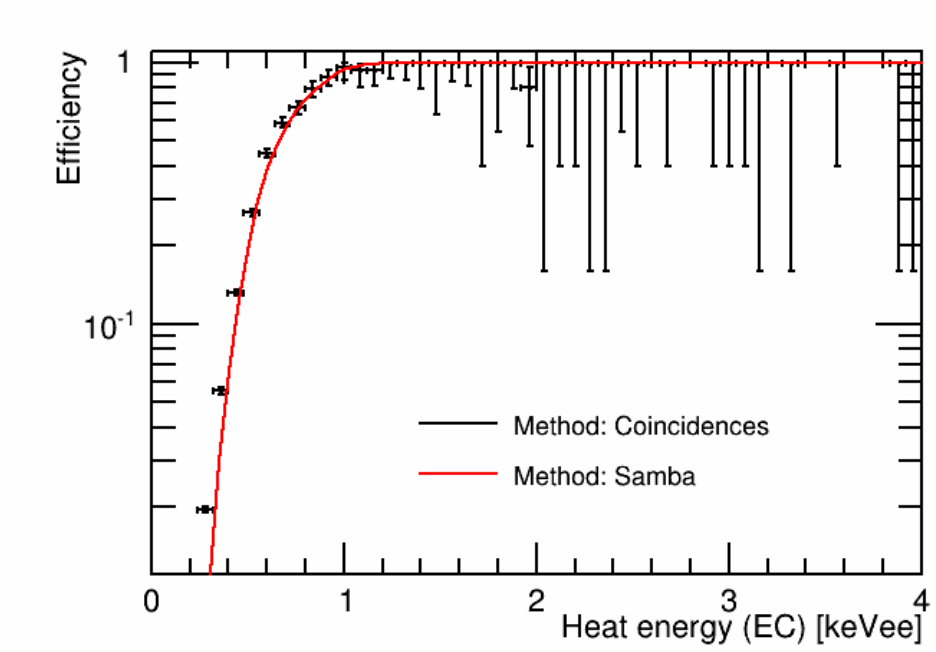

FIGURE 4.20 FID837 online trigger efficiency. The efficiencies were estimated using coincidences (black crosses) and using an anlytical model based on the estimation of the online trigger level. (Red curve)

So far, we have defined quality cuts which ensure a homogeneous data set and reject some events incompatible with WIMPs. For the purpose of the low-mass WIMP analysis, we will further define a region of interest, where most of the signal is expected to lie. This specific low-mass cut is not implemented for the background studies since it removes many background events and prevents us from building a data-driven model.

The low mass cut is defined as follows:

- Require EIA/C $< \frac{5}{2.35} \times$ FWIA/C
  Veto cut. We look for WIMPs interacting in the volume of the Ge detector: no surface signal is expected. This 5σ-cut is loosely defined on purpose as it is only designed to facilitate the work of the multivariate analises we will use later on.

- Require EFID$\in [0, 15]$ keVee and EC$\in [1.5, 15]$ keVee
  This is a box cut which captures the region in the fiducial ionisation / combined heat plane where most of the low mass WIMP signal is expected. Given a 1.5 keVee heat threshold, the signal efficiency loss further induced by the requirement EFID>0 is smaller than 0.1%.

The efficiency loss resulting from the fiducial selection (we will only be looking for WIMPs in the fiducial volume) is included in the computation of the fiducial mass. Given that the total mass of the crystal and the fiducial mass are respectively 800 and 600 g, this leads to a 25% efficiency loss. An additional 10% efficiency loss is included in the final computation of the exposure to account for deadtime losses. The final exposure after all cuts is 35.4 kg.d.

4.4.2 Background models

All our background models are essentially data-driven. In some cases, we have a well-founded theoretical model with free parameters. This is the case of the gamma background: as we said before, we know there are radioactive peaks and a flat Compton component. However, we cannot predict the value of the free parameters beforehand. Hence they are adjusted by fitting the data to the model. In other cases, such as surface beta events, we have no clear parameterisation. In this case, we resort to non-parametric fits, generally based on splines, to fit the data. These models are then used to simulate the training samples necessary to the Boosted Decision Trees analysis, as we will see in Section 4.4.3.

4.4.2.1 Gamma backgrounds

To build the Gamma background model (for surface or fiducial gammas), events are selected thanks to the Q-plot shown in Fig. 4.8. The gamma band is well separated from the WIMP band down to a few keV so the sideband region in which we are allowed to build a data-driven background model stretches down to a few keV. The model (shown in Fig. 4.21) is then linearly extrapolated down to lower energies.

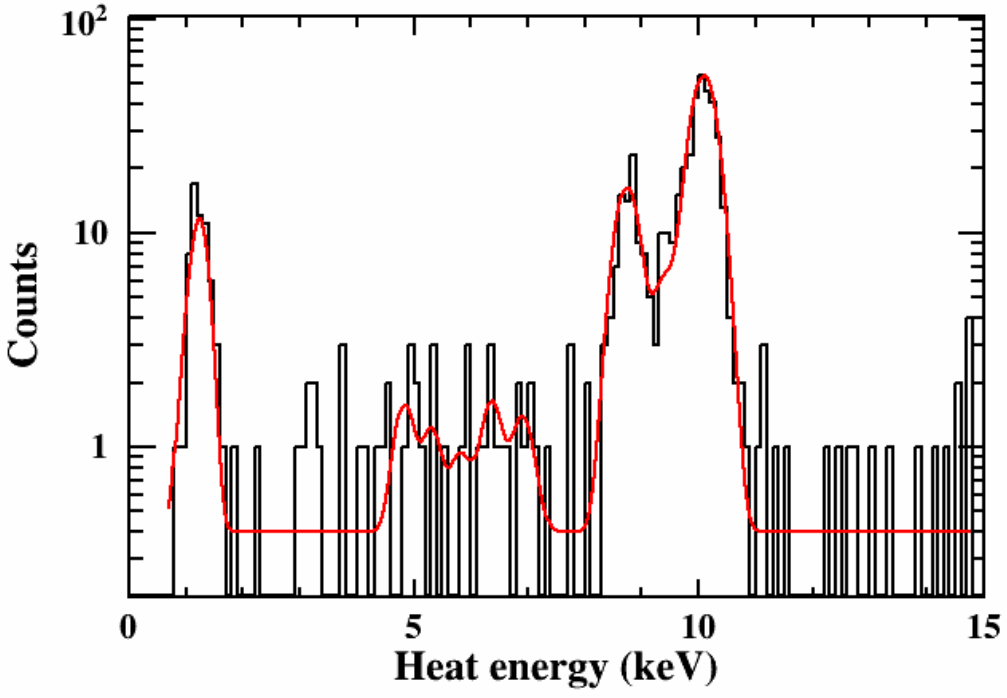

FIGURE 4.21 FID837 fiducial gamma spectrum. The fit includes some known radioactive peaks and a flat Compton component

The formula below shows the complete parameterisation of the background model:

$$\mathrm{B(EC)} = \mathrm{C} + \sum_{\mathrm{peak}} \frac{\mathrm{A_{peak}}}{\sqrt{2\pi}\sigma(\mathrm{EC_{peak}})} \exp\left[-0.5\left(\frac{\mathrm{EC} - \mathrm{EC_{peak}}}{\sigma(\mathrm{EC_{peak}})}\right)^2\right] \tag{4.3}$$

As in Chapter 3, we have a flat component and radioactive peaks. There are a few important differences. We now include new peaks corresponding to the L-shells of ^{68}Ge and ^{65}Zn with energies 1.297 keVee and 1.096 keVee respectively. As we stated in Section 4.2.1, the amplitudes of these peaks are fixed by the corresponding K-shell amplitudes. Indeed, at these energies, the definition of the sideband is no longer clear-cut. This is why it is more robust to rely on the higher-energy model (for both the Compton continuum and the peaks' amplitudes) to estimate the low-energy gamma background.

Through the comparison of our model with the real data, we saw that we needed to take another phenomenon into account, namely charge trapping. Charge trapping is caused by the presence of impurities in the crystal, which prevent full charge collection. Hence, it is directly proportional to the impurity density. A direct consequence of trapping is the deterioration of the resolution, with increasing importance at high energies. Trapping has more serious effects in large detectors (indeed, the charge path length increases with the size of the detector which increases the trapping probability at equal impurity density). This explains why trapping could be neglected in Chapter 3 (the EDELWEISS-II detectors are much smaller than the new EDELWEISS-III detectors) while we now have to take it into account.

The trapping-induced energy dependency for the resolution is well modeled by:

$$\sigma(\mathrm{EC})^2 = \sigma_0^2 + (\mathrm{a} \times \mathrm{EC})^2 \tag{4.4}$$

where σ_0 is the resolution at 0 keV while the parameter a (measured at 0.017 for FID837) is adjusted by fitting the prominent 10.37 keV peak. Hence, at 10.37 keV, this leads to a 57% increase of the resolution.

The construction of the surface gamma background model follows the same procedure. Surface events are selected by selecting events in the $Q = 1$ region with signal on the two electrodes of the same surface. However, we only adjust the flat component of the background to the data. Indeed, the ratio of the amplitudes of the surface to fiducial background is the same as the ratio of the fiducial mass to the total mass. Hence, once we know the amplitude of the fiducial lines, we also know that of the surface lines.

4.4.2.2 Beta and Pb backgrounds

The event selection is similar to the one outlined in Sec. 4.4.2.1. When the veto signal is sufficiently large, beta and lead recoils can be clearly tagged as surface events which are outside the WIMP search region: it is once again perfectly legitimate to use them to build a data driven model. To make sure we are outside the WIMP search region, we require a surface ionisation signal greater than 5 standard deviations. Using simple quenching hypotheses and the Luke Neganov formulas, we computed the corresponding heat signal. These results, which define a safe surface sideband are summarised in Table 4.4 below.

Background	Quenching	Heat signal @ 2 keVee ionisation
Beta	0.4	2.3 keVee
Pb	0.08	7.5 keVee

TABLE 4.4 Heat energy at ionisation identification threshold

Using this sideband, we built the 1D heat spectrum for the surface backgrounds as shown in Fig. [4.22-4.23]. We then derive a one dimensional background model by fitting a spline to the data. The model is then linearly extrapolated outside of the surface sideband. The spline fit performs rather poorly for lack of statistics. However, we only really need the low energy extrapolated part (high energy surface events are rejected by the veto cut) which is the main source of uncertainty for our model. Fortunately, this is not problematic as we will see that surface events are a sub-dominant background for this analysis. Future modeling will include more statistics which will reduce the uncertainties.

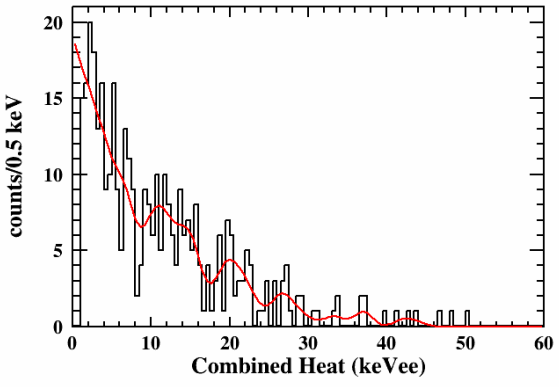

FIGURE 4.22 Surface Beta spectrum. Black histogram: FID837 WIMP search Beta. Red curve: Spline fit to the data.

For background simulations, we also need to know the relation between heat and ionisation. Once again, we derive this relation from the data in the sideband. The results

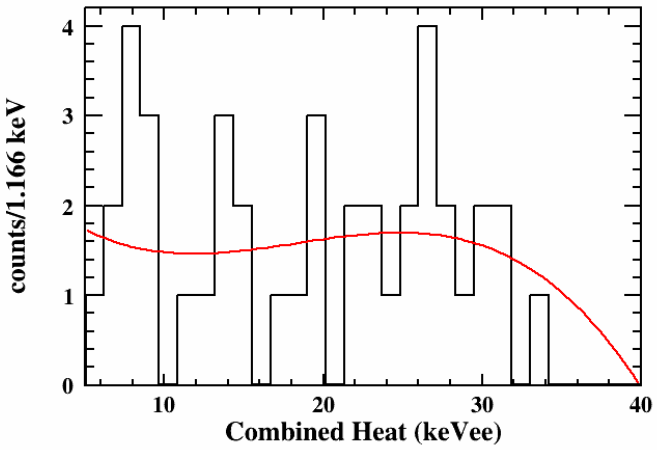

FIGURE 4.23 Surface Lead recoil spectrum. Black histogram: FID837 WIMP search lead recoils. Red curve: Spline fit to the data.

are shown in Fig. 4.24. We see that the dispersion increases at higher energies: we need to add an intrinsic scatter to take this effect into account. In practice, the effect is negligible for surface events that survive the veto cut.

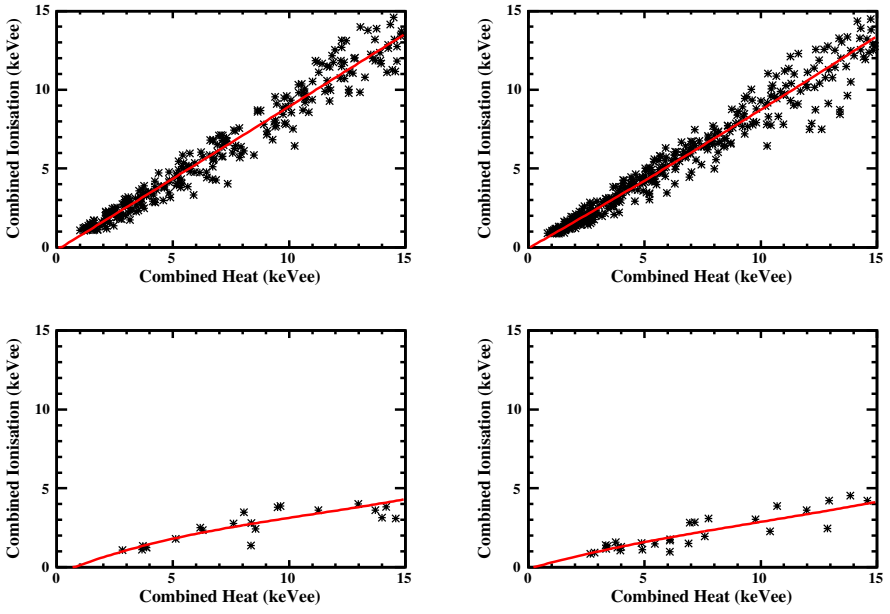

FIGURE 4.24 Top left: Surface 1 Beta. Top right: Surface 2 Beta. Bottom left: Surface 1 Pb. Bottom right: Surface 2 Pb. The beta and lead selection cuts have not effect on the width of this distribution at the energies relevant to our analysis.

N.B. An accurate model above 10 keVee is unnecessary because of the veto cut which effectively rejects all surface events above this energy

4.4.2.3 Heat-only background

In Sec. 4.2.5, we stated that the heat-only background was rather poorly understood. This is problematic given that heat-only events are the most intense background. However we will show that even if we are not sure of the physical mechanisms behind these events, the data allow us to build a model for these events in the context of a WIMP search.

It turns out that the ionisation amplitude reconstruction of pure noise events is absolutely unbiased - ie. the EFID distribution is perfectly symmetric around zero for events with no ionisation signal. As a consequence we can use EFID<0 events to fully characterize the heat behaviour of the heat-only background. From Fig. 4.25, we see that is little to no overlap between the signal region (black dots) and the heat-only background in the $\{\text{EFID} < 0\}$ region, as long as the heat energy is above 1.5 keV. In Fig. 4.25, a 7 GeV WIMP signal is shown. We verified that the above assertion was true for all the WIMP masses considered in this analysis.

The heat background model for heat-only event is then simply obtained by drawing events from the histogrammed 2D EC1,EC2 distribution. This is needed to account for possible correlations between the two heat channels close to the threshold.

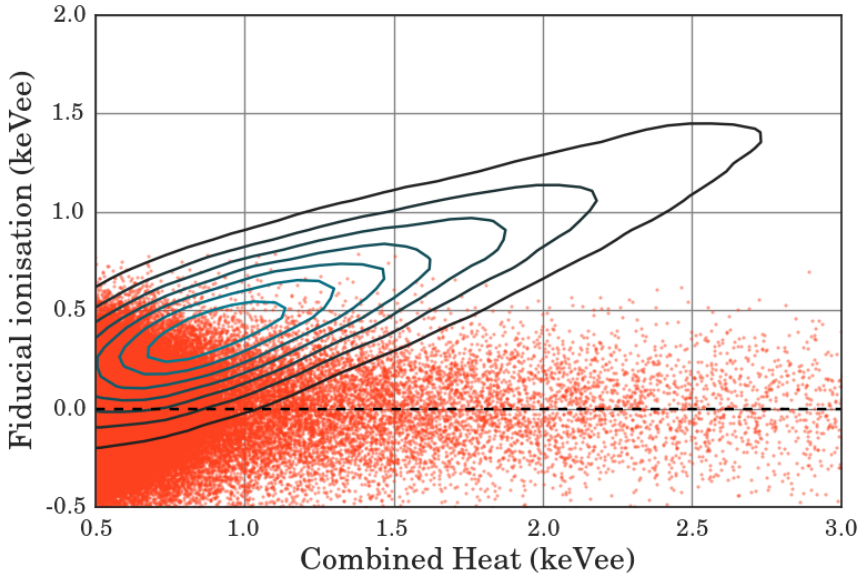

FIGURE 4.25 Contour lines: simulated WIMP signal at 10 GeV. Red dots: FID837 heatonly events.

4.4.3 Event simulations

In this section, we will describe the procedure we used in the single detector analysis in order to simulate six dimensional background data (4 ionisations and 2 heats). Full simulation details, with code samples can be found in Appendix B. Here, we only give the guiding principles of the simulation.

4.4.3.1 Signal simulation

We generate a 6-tuple with the following procedure:

- Draw an event with recoil energy $E_{\mathrm{R,sim}}$ from the WIMP rate given in Eq. 1.28. Compute $Q_{\mathrm{sim}} = 0.16\, E_{\mathrm{R,sim}}^{0.18}$.
- For each heat channel, draw a random float ϵ from a zero mean gaussian with resolution equal to the channel's resolution.
- The ionisations are correlated and the noise distributions are well described by a multivariate gaussian. We selected pure ionisation noise events by imposing EC < 0.5 and fitted a zero mean multivariate gaussian to the distribution. Ionisation noise is then simulated by drawing samples from this multivariate distribution.
- If the channel is a veto channel, set the simulated veto energy $E_{\mathrm{vet}} = \epsilon_{\mathrm{vet}}$
- If the channel is a heat channel, set the simulated heat energy:

$$E_{\mathrm{heat}} = E_{\mathrm{R,sim}} \times \frac{1 + Q_{\mathrm{sim}} V_{\mathrm{fid}}/3.}{1 + V_{\mathrm{fid}}/3.} + \epsilon_{\mathrm{heat}} \tag{4.5}$$

- If the channel is a collecting electrode channel, set the simulated collecting electrode energy:

$$E_{\mathrm{col}} = E_{\mathrm{R,sim}}\, Q_{\mathrm{sim}} + \epsilon_{\mathrm{col}} \tag{4.6}$$

- Compute the combined estimators for the heat and the fiducial ionisation
- Simulate online threshold effects by defining an acceptance probability based on the event's energy.
- Impose analysis cuts (WIMP box cut and veto cut)

4.4.3.2 Background simulation

The simulation of background samples is essentially the same as the signal simulation. Of course, the details of the simulations are changed, to account for the location of the event (surface or fiducial) and its specific quenching factor.

There is one major difficulty though. For the signal simulation, we had the theoretical event rate, before convolution with the resolution of the detector. The addition of gaussian noise to simulated events from this distribution then effectively includes resolution effects on each channel. However, for background events, we fitted event rates which already included resolution effects: we need to deconvolve the distribution before drawing background samples. Else, we effectively add more noise than needed, and the simulated samples may not match the actual data.

There are additional subtleties, specific to each population, which we are now going to detail:

- **Surface gammas:**

  Our 1D background model shows the count rate as a function of the heat energy. As we stated in Section 4.2.2, the heat energy is shifted by a factor $\frac{1+V_{\mathrm{surf}}/3}{1+V_{\mathrm{fid}}/3}$ which we need to include for the ionisation simulation.

- **Surface Betas and lead recoils:**

  In Section 4.4.2.2, we fitted the ionisation-heat relation. We use this fitted function to get the correct ionisation corresponding to an event drawn from the 1D heat distribution. We neglected the influence of the intrinsic scattering that we identified earlier given that only low energy events survive the final analysis cuts.

- **Heat-only events:**

  In Section 4.4.2.3, we fitted the OC1-OC2 distribution of FID837. This fit includes threshold and resolution effects (since it is a fit of the actual data without extrapolation). Hence we do not need to deconvolve; we can simply draw the two heat energies from this distribution without modification. We then simulate the ionisation energies with four uncorrelated gaussians with appropriate resolution.

4.4.4 Optimisation of the BDT through cross-validation

We are now going to explain how we tuned the BDT parameters and the features of interest. As we saw in Section 4.3.2, this is usually done by monitoring the evolution of the classification error on the test set. In order to do this, we first need to define the metric, with which we will evaluate the classification performance. For binary classification problems (as is the case here), it is usual to study the Receiver Operating Curve (ROC) which plots the true positive rate (signal events correctly identified as signal) as a function of the false positive rate (background events misclassified as signal events) for various discrimination thresholds. One such curve is shown in Fig. 4.26

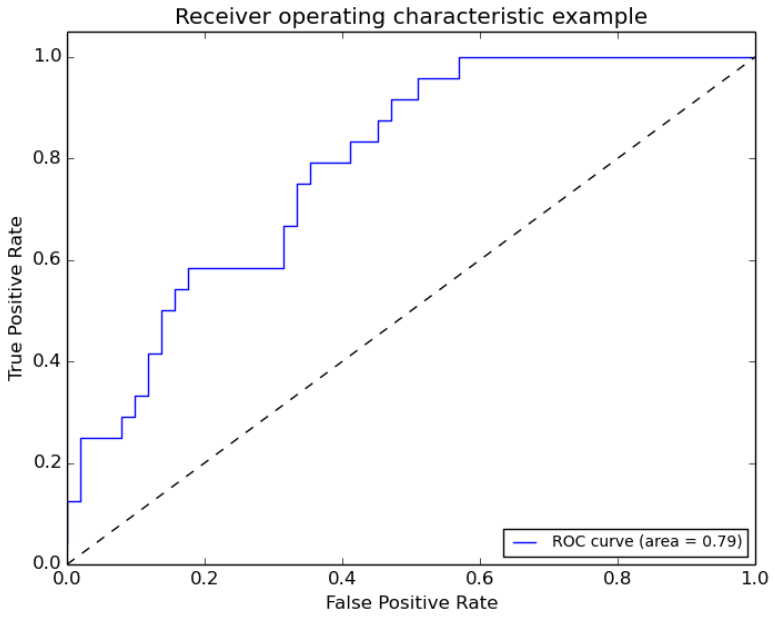

FIGURE 4.26 Typical example of a ROC curve for a binary classification problem. The dashed straight line indicates the average performance of a classifier which randomly classify events as background or signal. Figure from the scikit-learn website.

The objective of classification is, of course, to maximise the true positive rate while minimising the false positive rate. Hence, the "optimal" ROC curve would have a point in the top left corner: no false positives, and 100% true positives. This cannot be achieved in most practical cases but it does indicate that classifiers with a large area under the ROC curve typically perform better. In the remainder of this section, we will therefore use this metric (called AUC for Area Under Curve) to estimate the performance of our BDT classification algorithm.

Before using cross validation (cf. Section 4.3.2) it is interesting to plot so-called "learning curves" which show the evolution of the error metric (the AUC in our case) as a BDT hyperparameter is varied. Fig. 4.27 shows two such learning curves. We see that

the general behaviour outlined in Section 4.3.2 is well respected: for low model complexity, the bias is high (low AUC score). With increasing complexity (more depth, more boosting rounds), the bias decreases at the cost of overfitting: the algorithm is tuned to the training sample and the AUC score of the training and test samples diverge.

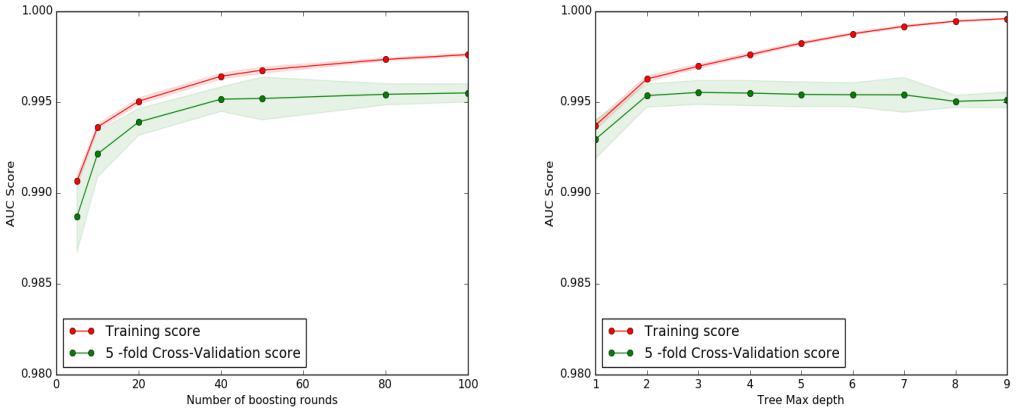

FIGURE 4.27 Learning curves for BDT hyperparameters. Left: evolution of the AUC as a function of the number of boosting rounds. Right: evolution of the AUC as a function of the tree depth. The shaded regions indicate a 1-sigma confidence interval around the measured AUC.

The curves shown above are merely illustrative as the optimisation of the BDT hyperparameters is a multidimensional problem: the hyperparameters must be tuned simultaneously. To this end, we used grid-search cross validation. That is, we selected an acceptable range for each hyperparameter and computed the cross validation score for all possible combinations. The best parameters are then those which give the highest AUC score.

Similarly, cross validation can be used to choose the best features for classification. Indeed, the basic approach is to use the 6 standard variables (EC1, EC2, EIA, EIB, EIC, EID). However, it may be possible to increase the classification performance by taking the square root or logarithm of a feature, combining several features etc. This approach is mostly empiric as there are no *a priori* criteria for feature selection. In our case, however, we can rely on physics intuition. For instance, we can introduce the feature EC1−EC2 (at low energies, heat-only events may slightly depart from the equality between EC1 and EC2) or EFID−Q×ER (which is centered on zero for WIMPs, not for other populations). The eventual choice of features is guided by two things: the BDT algorithm ranks its features by importance (schematically, this corresponds to how often a feature is used to partition the feature space) so irrelevant features can be discarded. Then, the cross validation score is once again used to select the best features. During this feature engineering phase, we have tried many different combinations, some

of which are plotted in Fig. 4.28. This figure shows the AUC score for the training and Cross validation test samples for four distinct feature selections detailed in the figure legend. The lower and upper boundaries of the boxes correspond the first and third quartiles of the AUC score distribution, the black line within the box is its median and the whiskers are the extremum values. This plot shows a clear gain when the 6 analysis variables are used (as opposed to EC and EFID only, as in EDELWEISS-II). While the gain from the use of further variables does not seem large, we observed an improvement (with respect to the 6 features analysis) of the sensitivity as high as 60% below 7 GeV in the final analysis.

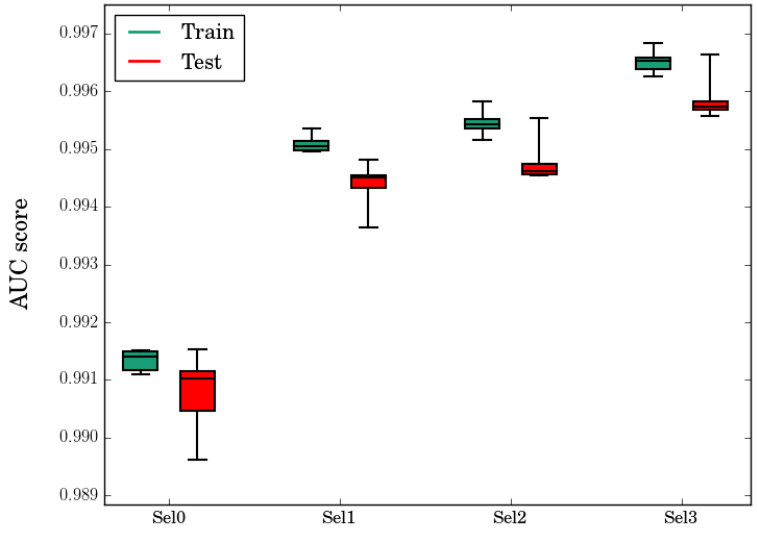

FIGURE 4.28 Training and Cross-validation test errors for the following feature selections: Sel0: {EC, EFID}, Sel1: {EC1, EC2, EIA, EIB, EIC, EID}, Sel2 = Sel1 + {EFID-QER}, Sel3 = Sel2 + {HR}.

The final parameters, derived from the prodcedure outlined in this section, are summarised in Table 4.5 below.

Features	EC1, EC2, EIA, EIB, EIC, EID HR, EFID-QER
Tree depth	3
Number of boosting rounds	150
Learning rate	0.1

TABLE 4.5 BDT hyperparameters and feature selection.

4.4.5 Single detector multivariate analysis

We simulated data samples for all backgrounds and the expected signal, which we then fed as inputs to Boosted Decision Trees (BDT). In this specific analysis, we use the BDT method from the xgboost[2] package. The number of trees is set to 150 and the depth to 3. We have controled overtraining by evaluating the p-value of a Kolmogorov test between the training and test samples. For all WIMP masses, the p-value is always above 0.5, indicating excellent agreement and hence limited overtraining. In Fig. 4.29, we show the results of the BDT analysis at four different masses: 5 GeV, 6 GeV, 7 GeV and 25 GeV.

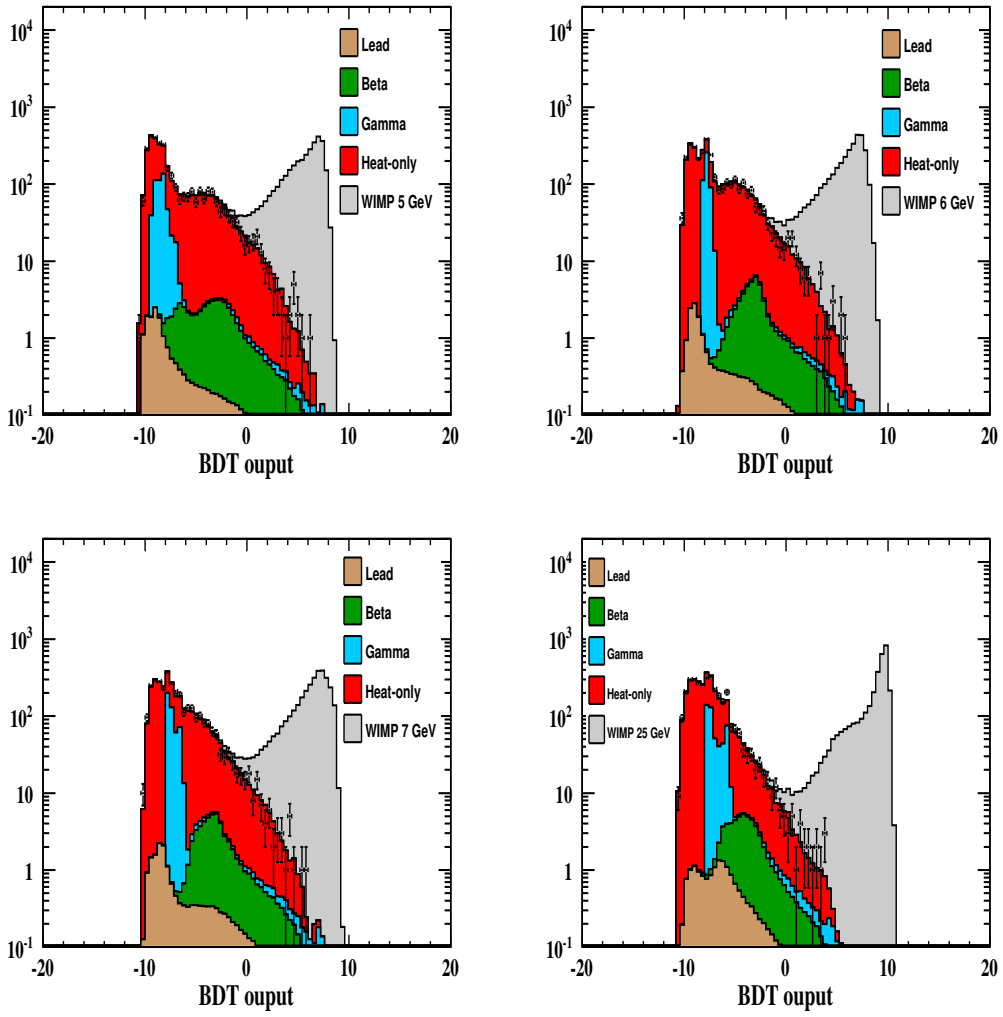

FIGURE 4.29 FID837 BDT plot for several WIMP masses. The data is shown as black dots (with an error bar).

[2]https://github.com/dmlc/xgboost

The x axis shows the BDT output, which can be viewed as a one dimensional quantity that indicates whether an event is more background-like (the output is close to -10) or signal-like (the output is larger). The filled histograms show the expected responses for background and signal events. Additionally, we have applied the trained classifier to FID837 data. We then superimposed the output (black dots) over the background and signal models.

Fig. 4.29 validates our background simulations as there is a good agreement between the background prediction and the observed data. This is confirmed by the computation of the p-value of a chi-square test between the two distributions. For all masses, the p-value is equal to or greater than 0.2. Let us make a few more comments.

As expected, heat-only events are the dominating background, even though they are less of a factor for high masses. This, of course, is expected since the majority of a high mass WIMP signal is found outside of the heat-only band. We also see that the influence of surface events (lead recoils or betas) is very limited: all other species have more overlap with the WIMP distribution. This is a tribute to the new FID detector design, which allows remarkable surface event rejection.

We now introduce the statistical procedure we used to derive an upper limit on the WIMP cross section. Starting from the simulated one dimensional BDT output, we define a cut value on this output in order to maximise the experimental sensitivity. Once the value is set, we apply the BDT classification to the real data and count the events which pass the BDT output cut. We then place a Poisson upper limit on the number of events, which we translate to an upper limit on the WIMP-nucleon cross section.

Let us give more details on the computation of the cut value. Given a BDT output cut value, we use the histograms of Fig. 4.29 to compute the expected number of background events that pass the cut: $N_{\mathrm{bckg}}(\mathrm{cut})$, obtained by integrating the predicted background contributions in the allowed region. We compute the signal efficiency given the same value of the cut: $\epsilon_{\mathrm{WIMP}}(\mathrm{cut})$. We then seek to minimise the ratio:

$$R = \frac{\sum_n \mathcal{P}_{90}\left(n\right) \mathrm{P}\left[\mathrm{X} = \mathrm{n}; \mathrm{N}_{\mathrm{bckg}}(\mathrm{cut})\right]}{\epsilon_{\mathrm{WIMP}}(\mathrm{cut})} \tag{4.7}$$

where $\mathcal{P}_{90}(n)$ indicates the Poisson 90% CL upper limit on the Poisson mean given n observations and $\mathrm{P}\left[\mathrm{X} = \mathrm{n}; \mathrm{N}_{\mathrm{bckg}}(\mathrm{cut})\right]$ is the Poisson probability to observe n events given a mean of $N_{\mathrm{bckg}}(\mathrm{cut})$. Below, R is shown as a function of the BDT cut in Fig. 4.30 for a WIMP mass of 5 GeV.

Fig. 4.30 is a great visualisation of the impact of the Boosted Decision Trees method. For small values of the BDT cut, very few background events are rejected and the sensitivity is completely background dominated. If we increase the BDT cut, the rejection of background events improves while little signal efficiency is lost because signal and background are well separated. Hence, the sensitivity improves until it reaches an optimal point.

Beyond this point (for larger BDT cuts), the sensitivity degrades. What happens is that the gain in background rejection does not compensate the signal efficiency loss caused by the BDT cut. For very high values of the BDT cut, all the signal is rejected as well and we are no longer sensitive to it.

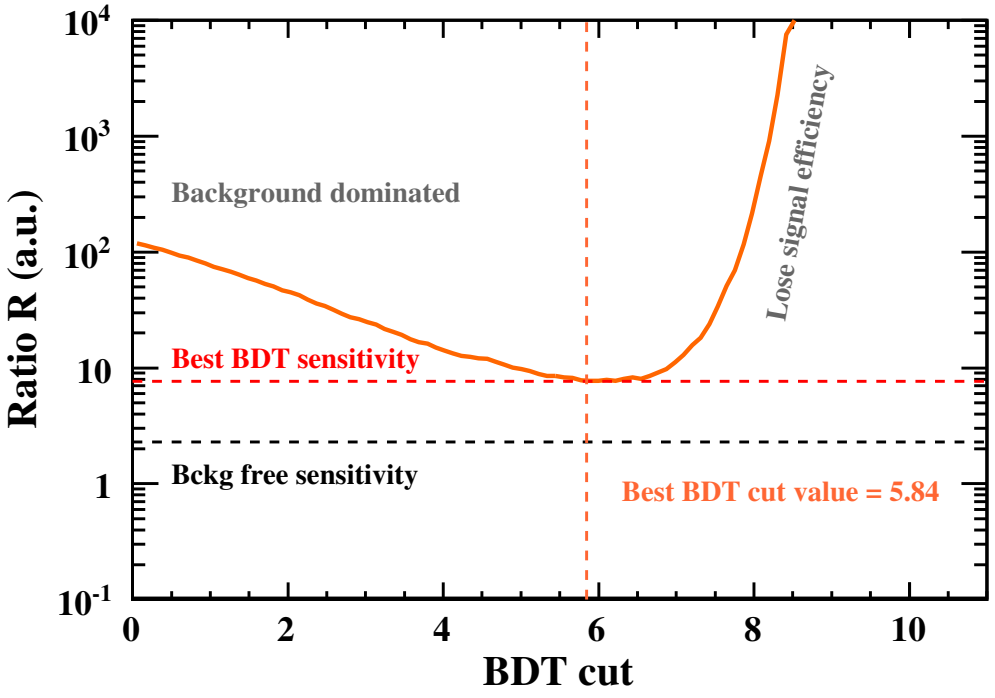

FIGURE 4.30 Sensitivity for a 5 GeV WIMP, given different values of the BDT cut.

By setting the BDT cut to the optimal value, we see that we are able to increase the sensitivity by one order of magnitude at 5 GeV. The ultimate goal of a BDT analysis is to reach the so-called "background free sensitivity" which is simply the 90% CL Poisson sensitivity for an experiment where no background event is observed. The difference between this "background free sensitivity" and the optimal BDT sensitivity shows the influence of the residual background after BDT cut. Indeed, signal and background cannot be completely separated hence background contamination cannot be avoided. For this analysis, there is approximately a factor 4 between the best BDT sensitivity and the background free sensitivity for a 5 GeV WIMP mass.

We now have a clear procedure to derive limits on the WIMP-nucleon cross section. For each WIMP mass, we minimise the ratio R of Equation. 4.7 to obtain the optimal BDT cut value. We then apply this cut to the real data. Next, we compute the 90% CL Poisson limit of the number of real data events that pass the BDT cut. This limit on a number of events is the converted to a limit on the WIMP-nucleon cross section through the integration of the WIMP PDF in the signal region.

Cut values, observed and expected events are shown in Table 4.6

WIMP mass	BDT cut value	Signal efficiency	Expected – Observed events
5	6.1	46 %	0.77 – 0
6	5.9	58 %	0.84 – 0
7	5.9	64 %	0.74 – 0
10	6.1	70 %	0.48 – 0
25	6.3	85 %	0.06 – 0

TABLE 4.6 BDT cut value, signal efficiency, expected and observed events given the WIMP mass.

The resulting limit[3] is shown in Fig. 4.31. In fact, we show two versions of the single detector limit. The first one, in light dashed red, was shown as a preliminary result in Moriond 2015. The only differences with the analysis presented in this work are: only 6 variables are used, ionisation noises are supposed to be independent and another machine learning package was used. The second one, in thick red, is the limit obtained with the analysis described in this work. These limits show competitive results in spite of the small exposure and relatively high threshold. This clearly demonstrates the potential of EDELWEISS bolometers for low mass WIMP searches.

[3]A previous version of this plot did not take the BDT cut efficiency into account correctly. This is the corrected limit.

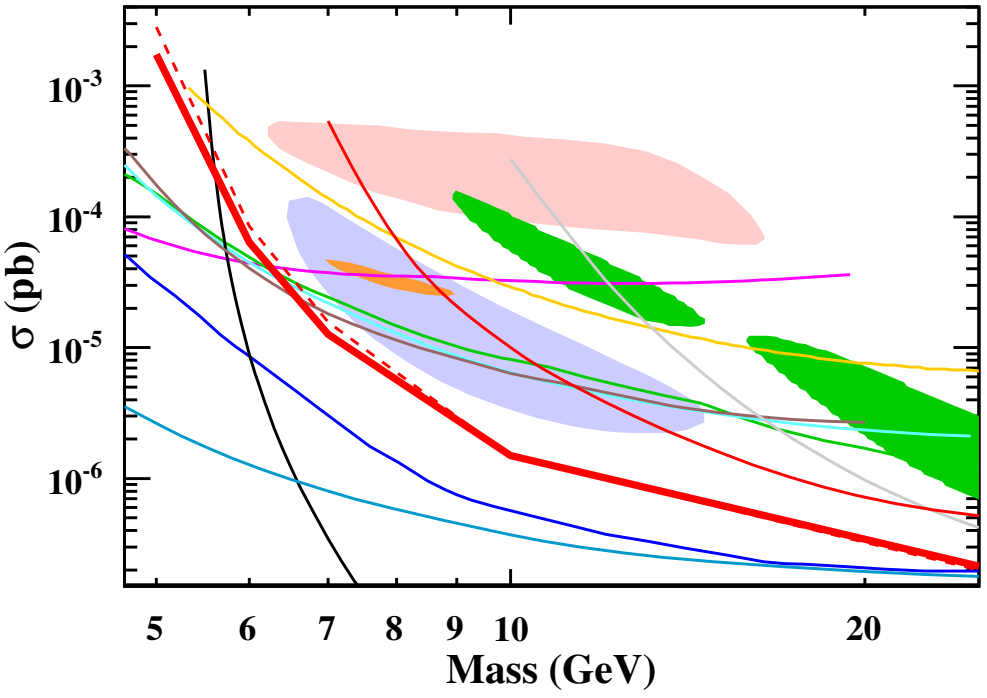

FIGURE 4.31 Limit on the WIMP cross section from the analysis of a single detector, FID837. Color code: SCDMS (*blue*), CDMS-Si 68% contour (*light blue*), CDMSlite (*purple*), DAMA (*salmon*), CRESST limit and contours (*green*), SIMPLE (*yellow*), COUPP (*gray*), PICO (*teal*), Xenon10 (*brown*), LUX (*black*), CoGeNT (*orange*), EDELWEISS-II (*thin red*) and EDELWEISS-III 35 kg.d in (*red*) (this work). Also shown in light dashed red is the corrected Moriond limit.

Chapter 5

Conclusions and prospects

In summary, two distinct physics analyses were carried out in this work: axion searches (in Chapter 3) and low-mass WIMP searches (in Chapter 4).

Axion searches:
Axions are new particles which were first introduced to solve the strong CP problem. They can be produced in the Sun and in some theories make up interesting Dark Matter candidates. If they exist, they can induce electronic recoils in the EDELWEISS detectors, thus enabling us to constrain their properties.

We introduced a novel statistical approach to bypass the lack of determination of the detector's orientation for the Primakoff channel. No signal was found, however, so we reported an upper-limit on the axion-photon coupling : $g_{A\gamma} < 2.15 \times 10^{-9}$ GeV^{-1}.

Other studies revolved around the use of the axio-electric effect for axion detection under the assumption of different possible origins. We combined several axion-producing reactions in the sun into a single channel which we called CBRD (for Compton, Bremsstrahlung, Recombination and Deexcitation) and then implemented a simple likelihood analysis to identify axion recoils in EDELWEISS-II's electronic recoil spectrum. We also envisaged the possibility of axions being produced through magnetic transition in the practical case of ^{57}Fe. The combination of the three channels above allowed us to obtain strong constraints on the axion mass within specific QCD axion models: $0.92\,\text{eV} < m_A < 80$ keV within the DFSZ framework and $5.78\,\text{eV} < m_A < 40$ keV for KSVZ axions.

Finally, we looked at a Dark Matter scenario where the galactic halo is made of keV-scale axion-like particles. These non-relativistic axions generate a line at the axion mass in the electronic recoil spectrum. We ran a likelihood scan between 2.5 and 100 keV without finding conclusive evidence for a signal. The best exclusion limit on the axion electron coupling was found for a 12.5 keV axion: $g_{Ae} < 2.59 \times 10^{-11}$.

Future searches will benefit from increased exposure and better thresholds.

Low mass WIMP searches:

WIMPs are the leading Dark Matter candidates. Low-mass WIMPs (1 to 10 GeV) have drawn interest recently because of signal hints in both direct and indirect detection experiments. They are also motivated by theories like Asymmetric Dark Matter which naturally requires $M_\chi = \mathcal{O}(5)$ GeV.

In this work, we introduced a new multivariate analysis, specifically tailored for low mass WIMPs. The analysis pipeline includes a comprehensive data-driven modeling of all background sources in the six basic analysis variables (EC1, EC2, EIA, EIB, EIC and EID). The simulation correctly accounts for threshold effects and the time variation of each channel's resolution. We then trained a classifier called BDT (Boosted Decision Trees) on simulated data before applying it to real-world data, taken from a good, standard bolometer called FID837 with an exposure of 35 kg.d after cuts. We validated this pioneer analysis with extensive use of 5-fold cross validation. No excess over background was found in the final analysis so we set an upper limit on the WIMP-nucleon cross-section for the masses of interest (5 to 25 GeV), reaching a limit of 1.48 $\times 10^{-6}$ pb for a 10 GeV WIMP.

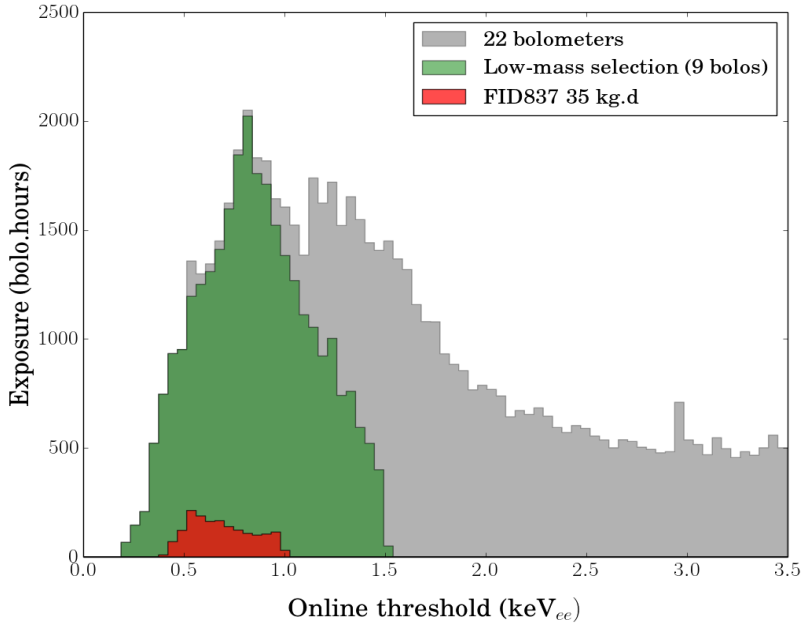

FIGURE 5.1 Future dataset for low mass analyses.

In this pilot analysis, we only scratched the surface of available EDELWEISS-III data, as shown in Fig. 5.1 which shows the valid data as a grey histogram, a selection of

good detectors as a green histogram and this work's FID837 as a red histogram for comparison. From this, it is clear that significant gains can be achieved through the combination of the different detectors and the decrease of the analysis threshold (we have plenty of high quality data below the analysis threshold that we set at 1.5 keVee in this work).

Beyond that, the success of our background models should encourage us to introduce a background analysis instead of the cut-based method we used in this work. This will require extensive control of the sideband regions (especially for the heat-only events) and a careful study of the systematics.

A broader view of the low mass WIMP field is given by Fig. 5.2, showing recent results of low mass WIMP searches, the solar neutrino floor and the parameter space that remains to be scanned.

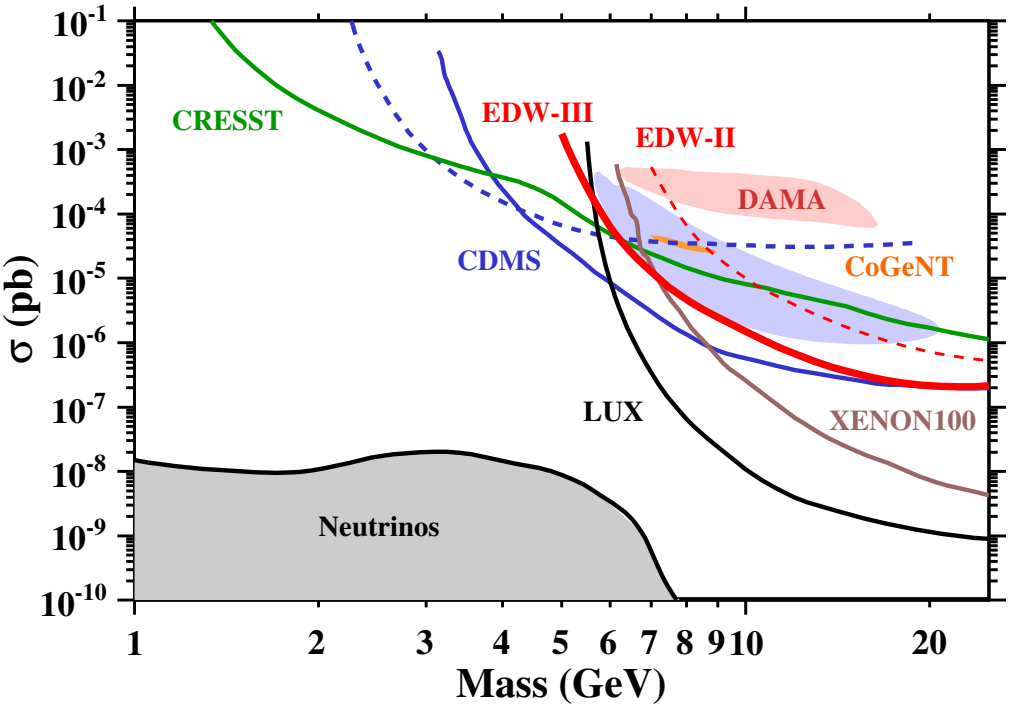

FIGURE 5.2 Overview of the low mass WIMP search region.

Let us make a few comments.

The CRESST experiment looks promising: thanks to its very light nuclei, its sensitivity does not degrade as quickly as other experiments. However, it remains to be seen whether it can decrease its background contamination to make significant progress.

The Xenon-based experiments (LUX and Xenon100) unquestionably lead the field for high mass WIMPs. However, their energy threshold is effectively limited by how

many photoelectrons they can detect. This explains the quick degradation in sensitivity for masses below 7 GeV.

EDELWEISS and CDMS lie somewhere in the middle as their target nuclei is heavier than that of CRESST while they have shown more control over their backgrounds.

EDELWEISS currently aims to improve the low mass sensitivity with research efforts in three directions:

- **Reduction of the heat-only background:** The collaboration is testing new designs for the detector holders. This should help in reducing the heat-only background if these events indeed originate from mechanical vibrations.
- **Improvement of the ionisation resolution:** An R&D program aims at replacing JFET by HEMT to further improve the ionisation resolution by a factor 2. This will also help against the heat-only background as the heat-only distribution will be compressed closer the the EFID = 0 line, away from the signal region.
- **Improvement of the heat threshold:** An idea to improve the heat threshold is to increase the bias voltage of the detector to amplify the heat signal. This high voltage strategy should therefore increase the sensitivity for very low mass WIMPs. However, background discrimination through ionisation measurements is not possible in this setup.

What is clear is that the low mass WIMP field will remain very open in the years to come: significant improvements in sensitivity are required before the low mass window can be fully closed and no technology has clearly emerged as the uncontested leader. This is an opportunity for EDELWEISS, which has a clear roadmap for hardware improvements.

Appendix A

A word on statistics

In statistics, we are interested in making inferences about a hypothesized model. This has many applications in physics where one often repeats experiments in order to determine the parameters of a theory. For instance, one might be looking for the decay constant of a given particle: the lifetime of the particle should obey the following probability distribution function- $f(t) = \frac{1}{\tau}e^{-t/\tau}$. This model has one observable, the lifetime of the particle and one parameter, the decay constant. We must then design an experiment to measure the observable. The result of the experiment is a set of observables $\{t_1, t_2, t_3, ...t_n\}$ from which the experimenter has to reconstruct the value of τ.

Several issues require the experimenter's attention. First, one should bear in mind the existence of two conflicting interpretations of statistics: the frequentist school and the Bayesian point of view. In frequentist statistics, one should carefully pick an *estimator* for the parameters of interest. In Bayesian statistics, prior, potentially subjective knowledge about the true value of the estimated parameter must be incorporated in the model. Specific attention should be given to the stated confidence level as conflicting approximations/interpretations can lead to surprising results. The purpose of this appendix is to clarify the differences between these two interpretations. Most of the following work is inspired by [125]. It is also an attempt at answering this naive question: which point of view should I take when making probabilistic inference about a model? A concrete example will be given with the search for Dark Matter.

We will start with an explanation of the differences between Bayesian and frequentist statistics. Then we will focus on the frequentist interpretation and see how we can use likelihood methods to interpret data. We will conclude with a few remarks on the Feldman-Cousins method [126] which was introduced to solve issues arising from the frequentist interpretation.

A.1 Frequentist versus Bayesian

A.1.1 Frequentist (Classical) statistics

A.1.1.1 Foundations of frequentist statistics

In frequentist statistics, probability is interpreted as the frequency of the outcome of a repeatable experiment. A confidence interval has the following interpretation: assume you build a confidence interval for the true value of the parameter p_t. This is a 68% CL interval for p_t if, in the limit of a large number of experiments, the intervals constructed the same way contain p_t 68% of the time. We say that the interval "covers" p_t. Thus, in the frequentist sense, a confidence interval is not a statement about the true value of p_t. This has been the source of many confusions. The coverage property of frequentist intervals is at the heart of frequentist inference.

Frequentist statistics allow the experimenter to report the outcome of an experiment objectively. No prior beliefs concerning the parameter being measured or the theory being tested need to be incorporated. This explains why they are used for reporting most measurements and their statistical uncertainties in high-energy physics.

A.1.1.2 Parameter estimation

An estimator $\hat{p}$ for a parameter p is a function of the data that is used to estimate the true value p_t of this parameter. No rules state how the estimator must be chosen. However, the choice may be guided by how well the estimator does with respect to some important properties:

- *Consistency:* $\hat{p}$ is consistent if it converges to p_t.
- *Bias:* $b = E(\hat{p}) - p_t$ where $E(\hat{p})$ is the expectation value of $\hat{p}$.
- *Efficiency:* $\hat{p}$ is efficient if its variance converges to the Cramer bound (under general conditions, this is the lowest possible variance for any estimator).
- *Robustness:* How the estimator fares with departures from original assumptions for the probability density function.

Usually, choosing an estimator implies a trade-off between these properties. For instance, decreasing the variance often increases the bias and vice versa.

One of the most important estimator is the Maximum Likelihood Estimator (MLE). It relies on the maximization of the likelihood function:

$$L(p) = \prod_{i=1..N} f(x_i, p) \tag{A.1}$$

where f is the probability density function evaluated at the data points x_i. The MLE $p_{\hat{ML}}$ for p_t maximises $L(p)$. Equivalently, one often minimizes the negative log-likelihood function $-\ln(L(p))$. This estimator does well with respect to the properties above. It is consistent and for large data samples, it is approximately unbiased, normal distributed and efficient. It is also invariant under 1-1 reparameterization: if $p_{\hat{ML}}$ is the MLE for $p_{\hat{ML}}$ then $g(p_{\hat{ML}})$ is the MLE for $g(p)$.

In frequentist statistics, the likelihood function is not a probability density function for the parameter p. Hence, it is not legitimate to integrate the likelihood function to extract confidence intervals. So why do physicists quote their likelihood function to report confidence intervals? The reason lies in the following important approximation. In the gaussian case one may find the s-standard deviation errors from:

$$\ln L(p) = \ln L(p)_{max} - \frac{s^2}{2} \tag{A.2}$$

the intervals derived using this procedure satisfy the coverage property. In non gaussian cases, the same method is used but the intervals will only have *approximate* coverage. In practice, using a gaussian approximation to compute confidence intervals is often valid because the likelihood function is asymptotically normal.

A.1.2 Bayesian statistics

A.1.2.1 Foundations of Bayesian statistics

In the frequentist case discussed above, one makes inference about the value that the data will take when performing an experiment. No inference is made on the true values of the parameters in the model. This is no longer true of Bayesian statistics which invoke an interpretation of Bayes' theorem where one builds a probability density function (p.d.f) for the true value of the parameter(s) of interest (POI). This p.d.f depends on

the experimental data and on a "prior" distribution for the POI which reflects our beliefs on the POI *prior* to the experiment. Bayes' theorem then gives the following expression for the p.d.f of the POI:

$$f(p_t|x) = \frac{L(x|p_t)\pi(p_t)}{\int L(x|p'_t)\pi(p'_t)dp'_t} \tag{A.3}$$

where L is the likelihood function as defined above and π is the prior distribution for p_t.

Since we now have a p.d.f for the true value p_t of the POI, it is perfectly sensible to integrate it to build a confidence interval for p_t. The interpretation of this confidence interval is different from the frequentist interpretation. In Bayesian statistics, the confidence interval (sometimes called credible interval) is a statement about the true value of the parameter p_t.

Now, taking a uniform prior, the p.d.f for p_t is simply proportional to the likelihood function so one integrates the likelihood function to obtain confidence intervals. Although this looks similar to the procedure described above to find frequentist intervals, the interpretation is fundamentally different. Since the likelihood function is a p.d.f for the true value of p_t, it is legitimate to integrate it in Bayesian statistics. This is not the case in frequentist statistics where a p.d.f for the true value of p_t is not defined and one relies on gaussian approximations of the likelihood function to find confidence intervals.

A.1.2.2 Bayesian priors

In Bayesian statistics, there are no predefined rules for determining the prior $\pi(p_t)$. The prior may be chosen so as to reflect objective knowledge before doing the experiment. For instance, when measuring a mass m, the experimenter may build a prior that excludes the $m < 0$ region of the parameter space. If the experimenter wants to incorporate complete ignorance about p_t, he might be tempted to choose the so-called *uninformative* uniform prior. This naive choice leads to tricky issues: in which metric should the prior be uniform? A prior constant in p_t, p_t^2 or $\ln(p_t)$ may lead to different confidence intervals, an unsettling prospect for many physicists. Can we accept a non integrable prior? Can we accept a non reparameterization-invariant prior? Attempts have been made at finding a prior from formal rules. Jeffrey suggested a reparameterization-invariant prior using the Fisher information matrix. Bernardo and Berger introduced a prior based on the

maximization of the information gain one may expect from the data. This prior is usually identical to Jeffrey's prior for a single continuous parameter.

In spite of these objective formal rules, pure Bayesian physicists remain a minority. The main reason is that Bayesian credible intervals may not satisfy the coverage property of frequentist intervals and that thorough discussions of prior are needed for Bayesian results to be accepted by the community. The search for neutrino masses is a notable exception as some experiments with a frequentist interpretation reported a negative best fit for the neutrino mass. This problem is solved elegantly by adopting the Bayesian interpretation and including a prior excluding negative masses.

A.1.3 Choosing the correct statistical interpretation

A.1.3.1 A few examples

In a famous paper [127], R. Cousins showed the pitfalls faced by either interpretations in a very simple counting experiment involving Poisson statistics. In this case, picking a uniform prior for the expected number of event μ_t yields the same confidence intervals as in the frequentist interpretation. However, when using a prior uniform in a different metric, say $\pi(1/\mu_t) = 1$ new confidence intervals are found, which do not cover in the frequentist sense!

In another seemingly innocent example, he shows how a perfectly rigorous frequentist construction leads to counter-intuitive results. The experiment is once again a counting experiment that is used to constrain say a branching ratio. The sensitivity S_t of the experiment is not known exactly. He assumes the estimated sensitivity follows a gaussian distribution centered around the true value: $\hat{S} \sim N(S_t, \sigma_S)$. He then shows (this is easily verified with Monte Carlo simulations) that in order to have proper coverage, an upper-limit on the branching ratio is more restrictive than the one found when the sensitivity is known perfectly! This contradicts common sense as one would expect uncertainty on the sensitivity to actually degrade the limit. This unexpected result stems from the interaction between a discrete probability law (Poisson) and a continuous one (Gaussian) which leads to the paradoxical relaxation of the upper limit. Conversely, he shows that a Bayesian analysis, which includes a prior distribution for S, treated as a nuisance parameter, leads to sensible results. The prior can be tuned to yield coverage in the frequentist sense.

A.1.3.2 A proposed rule of thumb

Physicists should be well aware of the distinction between frequentist and Bayesian statistics. However, as evidenced from the section above, it makes little sense to stand firmly behind a given interpretation as incongruous inferences can arise from the most simple situations. The only essential requirement is the frequentist property of coverage.

In any case, the guideline for statistical studies in physics should be:

- Adopt the frequentist point of view whenever it is possible (i.e. does not give rise to unphysical result as in the neutrino mass case). This is the standard framework of the community.
- In frequentist statistics, the confidence intervals should inherently cover. However, some authors have shown [126] that undercoverage may arise from a frequentist procedure. The claimed coverage should be systematically verified with MC simulations.
- In some situations, it may be easier to adopt a mixed Bayesian-Frequentist interpretation. For instance, nuisance parameters often have acceptable priors (like a gaussian distribution for the sensitivity uncertainty) and are naturally dealt with in the Bayesian framework by marginalizing the p.d.f over the nuisance parameter. It should be verified that the confidence intervals found with this method give the proper coverage.
- A fully Bayesian treatment is acceptable if there is a strong motivation for the prior of the parameter of interest.

A.2 Profile Likelihood analysis for dark matter searches

A.2.1 Statistical formalism

A.2.1.1 Useful definitions

Following [128], we introduce the (frequentist) Profile Likelihood formalism used in tests for new physics, with a direct application to the identification of possible direct-detection dark matter signals.

Definition 1. A ***statistical test*** is a rule that states for which values of $\boldsymbol{x}$ a given hypothesis called H_0 should be rejected.

Definition 2. A ***critical region*** w is a region such that there is no more than a specified probability α under H_0, called the ***size of the test***, to find $\boldsymbol{x} \in w$. If $\boldsymbol{x} \in w$, H_0 is rejected.

Definition 3. A ***type-I error*** occurs when H_0 is rejected even though it is true. By construction, it happens with probability α.

Definition 4. A ***type-II error*** occurs when accepting H_0 even though the alternate hypothesis H_1 is true. Let β the probability of making such a mistake. Then $1 - \beta$ is the ***power*** of the test H_0 with respoect to the alternative H_1.

Lemma 1. Neyman-Pearson lemma: To maximize the power of a test of H_0 with respect to the alternative hypothesis H_1, the critical region w should be chosen such that

$$\lambda(\boldsymbol{x}) = \frac{L(H_0|\boldsymbol{x})}{L(H_1|\boldsymbol{x})} \leq \eta \tag{A.4}$$

where η is defined by $P(\lambda(\boldsymbol{x}) \leq \eta|H_0) = \alpha$

Definition 5. Let t a test statistic for a hypothesis H_0. The ***p-value*** is the probability to find t in the region of equal or lesser compatibility with H_0 than the level of compatibility observed in the actual data.

Definition 6. The p-value is often converted into an equivalent ***significance Z***, defined by

$$Z = \Phi^{-1}(1 - p) \tag{A.5}$$

where Φ^{-1} is the inverse Gaussian cumulative distribution function.

With this definition, the standard 5σ threshold for discovery corresponds to a p-value $p = 2.87 \times 10^{-7}$.

A.2.1.2 The profile likelihood

Definition 7. Assume an experiment involves a parameter of interest σ and nuisance parameters $\boldsymbol{\theta}$ in vector form. The ***profile likelihood ratio*** is defined as

$$\lambda(\sigma) = \frac{L(\sigma, \hat{\hat{\boldsymbol{\theta}}})}{L(\hat{\sigma}, \hat{\boldsymbol{\theta}})} \tag{A.6}$$

where L is the likelihood function, the denominator is maximized over the whole parameter space (in σ and $\boldsymbol{\theta}$) while the numerator is maximized over $\boldsymbol{\theta}$ only. Thus, $\hat{\hat{\boldsymbol{\theta}}}$ is a function of σ.

Theorem 1. WILKS THEOREM: In the large sample limit, $-2\ln(\lambda(\sigma)) \sim \chi^2_n$ where n is the difference in dimensionality between the spaces spanned by H_0 and H_1

Because of Wilks' theorem, the test statistic $t = -2\ln(\lambda(\sigma))$ is often preferred to the original form. With this definition, higher values of t correspond to increasing incompatibility with the hypothesis for σ. We can compute the p-value for this test statistic:

$$p = \int_{t_{obs}}^{\infty} f(t|\sigma)dt \tag{A.7}$$

There are numerous reasons supporting the use of the profile likelihood.

- It should be noted that the best fit obtained by maximizing the profile likelihood is the same as the one obtained with the usual likelihood function.
- In the frequentist interpretation, it provides a convenient framework for eliminating nuisance parameters. If there are several POI, 2D contours can be plotted by effectively taking uncertainties on the nuisance parameters into account. This has many applications in physics.
- Using the form $t = -2\ln(\lambda(\sigma))$ and Wilks theorem, it is easy to compute (approximate) confidence intervals without having to resort to Monte Carlo simulations.
- Neyman-Pearson lemma and several tests indicate that using the profile likelihood as a test statistics has good power [125, 128–130].

A.2.2 Application to Dark Matter searches

A.2.2.1 Exclusion

In this section, we want to test the signal hypothesis where there is a Wimp signal at a given mass M_χ and cross-section σ. We first assume the mass is fixed: only σ is a parameter of interest. Then the analysis can be repeated for a different mass.

Following [128], we build the test statistic t_σ:

$$t_\sigma = \begin{cases} -2\ln\lambda(\sigma) & \text{if } \hat{\sigma} < \sigma \\ 0 & \text{if } \hat{\sigma} > \sigma \end{cases} \tag{A.8}$$

where $\lambda(\sigma)$ is the profile likelihood of the analysis. It includes the p.d.f for the expected signal and backgrounds and may include uncertainties about the parameters (nuisance parameters). Here we set t_σ=0 for $\hat{\sigma} > \sigma$ because we are trying to set an upper limit. Data with $\hat{\sigma} > \sigma$ do not represent less comptability with the data obtained. Higher values of t_σ represent greater incompatibility between the data and the hypothesized value of σ.

The p-value is:

$$p_\sigma = \int_{t_{\sigma,obs}}^{\infty} f(t_\sigma|H_\sigma)dt_\sigma \tag{A.9}$$

In order to compute a 90% CL interval, we have to scan over values of σ until we find σ_{lim} such that $p_{\sigma_{lim}} = 10\%$.

If background events are expected in the Dark Matter search experiment, a modified p-value can be used. Indeed, it may happen that the data fluctuate downwards with respect to the background expectation, in which case the resulting upper-limit on the cross section may be very low. From Monte-Carlo simulations, it is possible to estimate the median expectation for the exclusion limit assuming no signal is found. A real-data exclusion limit found significantly lower than this median limit may indicate a poor

background estimate or a strong downward fluctuation of the data. In this case, the Particle Data Group [125] suggests using a statistic called CLs defined as:

$$CLs \equiv p'_\sigma = \frac{p_\sigma}{1 - p_b} \tag{A.10}$$

where

$$p_b = 1 - \int_{t_{\sigma=0,obs}}^{\infty} f(t_\sigma|H_0)dt_\sigma \tag{A.11}$$

is the p-value of the background-only hypothesis. As before, the signal hypothesis H_σ is rejected at 90% CL if $p'_\sigma \leq 10\%$. As the denominator is less than unity, the requirement $p'_\sigma \leq 10\%$ is stronger than $p_\sigma \leq 10\%$. In fact, this procedure introduces a slight *conservative* overcoverage as can be verified by Monte Carlo simulations. We see that downward background fluctuations are effectively dealt with:

When testing a region where the experiment has good sensitivity (for instance, the exclusion of the region with a cross-section much higher than the eventual sensitivity), we will have the following results:

- The best fit for the cross section is much lower than the hypothesized value.
- From the definition of our test statistic, this means that $t_{\sigma,obs}$ is large and equivalently, that p_σ is small.
- Under this assumption, all data should be background events. So assuming the background is well modelled, fitting under the background only hypothesis should be in very good agreement with the (background) model which means a low $t_{\sigma=0,obs}$ and consequently $1 - p_b \approx 1$

So in this case, we see that the test statistic is hardly modified. If there is a small background fluctuation, no significant deviation should be expected because $p'_\sigma = \frac{p_\sigma}{1-p_b}$ should remain very small under the assumption of a high cross-section.

The test statistic will change in low-sensitivity regions (i.e. testing cross-sections close to the eventual sensitivity). When fitting a hypothesized signal in this region, the best

fit for the cross-section should be close to the hypothesized value. This will yield to a high value for p_σ which will prevent the experimenter from confidently excluding this region. However, if the background fluctuates downard with respect to the background model, the best fit for the cross section may be significantly lower than the hypothesized value, which brings p_σ to a value such that the experimenter may be tempted to exclude the hypothesized cross-section. We see that using $p'_\sigma = \frac{p_\sigma}{1-p_b}$ protects us from background fluctuations because due to the disparity between the background model and the observed data, $1 - p_b$ will decrease as well, preventing $p'_\sigma < \alpha$ from being satisfied.

As before, in order to compute a 90% CL interval, we have to scan over values of σ until we find σ_{lim} such that $p'_{\sigma_{lim}} = 10\%$. We then repeat this for every WIMP mass m_χ to report the usual WIMP $M_\chi - \sigma$ exclusion limit.

A.2.2.2 Discovery

A similar test statistic may also be used to evaluate the significance of a potential signal discovery. We simply have to test a background only hypothesis and see if we can reject it at the required confidence level. In this case, we will use the test statistic [128]:

$$t_0 = \begin{cases} -2\ln\lambda(0) & \text{if } \hat{\sigma} > 0 \\ 0 & \text{if } \hat{\sigma} < 0 \end{cases} \tag{A.12}$$

To quantifiy the disagreement between the observed data and the hypothesized background only model, we compute the p-value:

$$p_0 = \int_{t_{\sigma,obs}}^{\infty} f(t_0|H_0)dt_0 \tag{A.13}$$

With a p-value sufficiently low, we may report on the discovery of something that looks like the signal. However, the physical origin of the signal should be studied with caution given some persistent uncertainties in the signal model and the background estimations.

A.2.2.3 2D contours

In the case where the experimenter finds strong hints for a signal, it is possible to draw 2-D contours in the $M_\chi - \sigma$ plane to identify the region favoured by the experimental results.

Once again, we build the profile likelihood:

$$\lambda(\sigma, M_\chi) = \frac{L(\sigma, M_\chi, \hat{\hat{\boldsymbol{\theta}}})}{L(\hat{\sigma}, \hat{M}_\chi \hat{\boldsymbol{\theta}})} \tag{A.14}$$

According to Wilks' theoreme, this follows a χ^2 distribution with two degrees of freedom in the limit of a large number of events. With Monte Carlo simulations of the experiment, it is possible to verify whether this is satisfied by our Profile Likelihood. Then it is easy to report a joint 2D confidence interval on the parameters of interest: the mass and the cross-section. We will see how this works in practice in the following section.

A.3 The Feldman-Cousins method revisited

In order to find a correct 90% CL on the limit, we can use the Feldman and Cousins [126] method (with some modifications explained below) Feldman and Cousins introduced this method in part to avoid the flip-flopping problem. (see Fig. A.1)

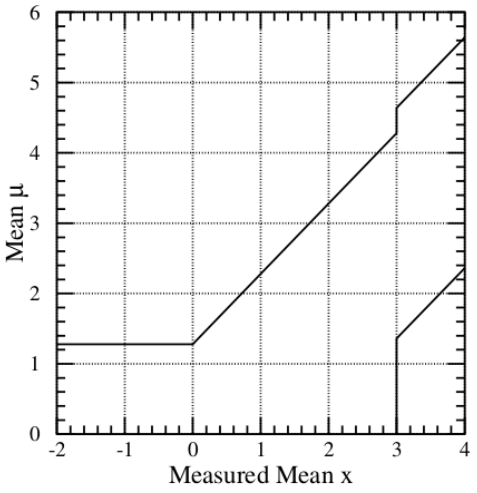

FIGURE A.1 Gaussian CL in the flip-flop case. The expected signal is a gaussian with rms=1 and unknown true mean μ. We measure a mean x.

Feldamn and Cousins insight is the following: Let us suppose, for example, that Physicist X takes the following attitude in an experiment designed to measure a small quantity: If the result x is less then 3σ, I will state an upper limit from the standard tables. If the result is greater than 3σ, I will state a central confidence interval from the standard tables. We call this policy flip-flopping based on the data. Furthermore, Physicist X may say: If my measured value of a physically positive quantity is negative, I will pretend that I measured zero when quoting a confidence interval, which introduces some conservatism. These CL intervals are not valid confidence belts, since they can cover the true value at a frequency less than the stated confidence level. For $1.36 < \mu < 4.28$, the coverage (probability contained in the horizontal acceptance interval) is 85%.

Feldman and Cousins use a so-called likelihood ordering principle that avoids flip-flopping and provides confidence intervals which are never empty. However, as we will see in Fig. A.2, this leads to difficulties in the physical interpretation of data. We will use a more conservative approach which may lead to less stringent constraints but provides a sound physical interpretation.

The black lines correspond to Feldman-Cousins' confidence intervals. The red line corresponds to a standard gaussian 90% upper CL. For the black line, when the measured

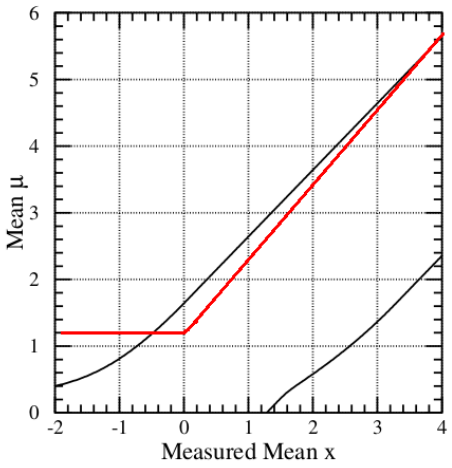

FIGURE A.2 Feldman Cousins confidence intervals for a gaussian with boundary. The expected signal is a gaussian with rms=1 and unknown true mean μ. We measure a mean x.

$x < 1.28$ an upper limit μ is given. This transition smoothly (and with some conservatism which is why the black line is above the red line for $x > 1.28$) to a two sided 90% CL for higher values of x. We can see that these intervals are never empty and computations show that such intervals have exactly 90% coverage, thus avoiding flip-flopping. The red line is the prescription we recommend. Indeed, the problem with FC is that in case of a negative fit result (negative x) due to a background fluctuation, the prescription leads to a better limit on the signal which makes little sense: since background and signal are uncorrelated, a negative background fluctuation should not lead to a better limit. To bypass this difficulty, we assume a negative measurement is equivalent to a zero measurement. For a non negative measurement we pick a standard gaussian 90% upper CL. This avoids the flip flopping problem, guarantees a coverage of 90% or more and leads to physically sound results.

Appendix B

Background simulation code

B.1 Signal: WIMP events

We start from the usual equation for the WIMP rate:

$$R = \int_{E_T}^{\infty} dE_R \frac{\rho_0}{M_N M_\chi} \int_{v_{min}}^{\infty} v f(v) \frac{d\sigma_{WN}}{dE_R}(v, E_R)\, dv \tag{B.1}$$

We run Monte-Carlo simulations in order to obtain a sampling of the WIMP distribution for the masses of interest. Each event is then converted into the usual (EIA, EIB, EIC, EID, EC1, EC2) 6-tuple by adding gaussian noise and taking the Luke-Neganov effect into account. The C++ code below shows the exact procedure:

```
1
2  // Simulate num_events events.
3  for (int k=0; k<num_events; k++)
4  {
5
6    ERsimu = frecoil->GetRandom(0,30);
7    Qsimu = 0.16*pow(ERsimu,0.18);
8
9    //Get heat rate
10   float jour = hJOUR->GetRandom();
11   HR = heatrate->GetBinContent(heatrate->FindBin(jour));
12
13   // Get resolution for heat, with time dep
14   float s_EC1 = hOWC1->GetBinContent(hOWC1->FindBin(jour))/2.3548;
15   float s_EC2 = hOWC2->GetBinContent(hOWC2->FindBin(jour))/2.3548;
16   float s_heat = compute_resolution(s_EC1*2.3548, s_EC2*2.3548);
17   float coeff_EC1 = compute_coeff(s_EC1*2.3548, s_EC2*2.3548);
18
```

```
19   //Draw ionisation from multivariate gaussian
20   TArrayD reso_coeff(4);
21   for (int k = 0; k<4; k++) {reso_coeff[k] = u.Gaus(0,1);}
22   TMatrixD reso_matrx(4,1);
23   reso_matrx.SetMatrixArray(reso_coeff.GetArray());
24   TMatrixD ion_matrx = Lmatrx*reso_matrx;
25
26   EIA = ion_matrx(0,0);
27   EIC = ion_matrx(2,0);
28   EC1 = (1+Qsimu*V_fid/3.)/(1+V_fid/3.)*ERsimu + u.Gaus(0,s_EC1);
29   EC2 = (1+Qsimu*V_fid/3.)/(1+V_fid/3.)*ERsimu + u.Gaus(0,s_EC2);
30   EIB = ERsimu*Qsimu + ion_matrx(1,0);
31   EID = ERsimu*Qsimu + ion_matrx(3,0);
32
33   float EC =coeff_EC1*EC1+(1-coeff_EC1)*EC2;
34   float EI =0.413*EIB+0.587*EID;
35   float accept = 0.5*(1 + TMath::Erf( (EC-heat_thresh) / (TMath::Sqrt(2)*
       s_heat) ) );
36
37   // Select data that pass analysis cuts
38   if (abs(EC1-EC2)< 1 && ECinf < EC && EC < ECsup && EIinf<EI  && EI<EIsup
       && EIA < cut_vetA && EIC < cut_vetC)
39   {
40           //Simulate threshold effects
41           if (u.Binomial(1,0.9999*accept)==1)
42           {
43               t_new->Fill();
44           }
45   }
46
47
48
49 }
```

B.2 Background: Gamma events

Likewise, the Gamma training events are generated from the background model of Sec. 4.4.2.1. The background model was deconvolved first, so that resolution effects are incorporated in the simulation by the simple addition of gaussian noise.

The C++ implementation for fiducial Gammas can be found below:

```
1
2  for (int k=0; k<num_event; k++)
3  {
4    // Draw data from 1D distribution
5    float evt_heat = func_FidGamma->GetRandom(0,20);
6    //Get heat rate
7    float jour = hJOUR->GetRandom();
8    HR = heatrate->GetBinContent(heatrate->FindBin(jour));
9    // Get resolution for heat, with time dep
10   float s_EC1 = hOWC1->GetBinContent(hOWC1->FindBin(jour))/2.3548;
11   float s_EC2 = hOWC2->GetBinContent(hOWC2->FindBin(jour))/2.3548;
12   float s_heat = compute_resolution(s_EC1*2.3548, s_EC2*2.3548);
13   float coeff_EC1 = compute_coeff(s_EC1*2.3548, s_EC2*2.3548);
14   //Draw ionisation from multivariate gaussian
15   TArrayD reso_coeff(4);
16   for (int k = 0; k<4; k++) {reso_coeff[k] = u.Gaus(0,1);}
17   TMatrixD reso_matrx(4,1);
18   reso_matrx.SetMatrixArray(reso_coeff.GetArray());
19   TMatrixD ion_matrx = Lmatrx*reso_matrx;
20
21   EIA = ion_matrx(0,0);
22   EIC = ion_matrx(2,0);
23   EIB = evt_heat + ion_matrx(1,0);
24   EID = evt_heat + ion_matrx(3,0);
25   EC1 = evt_heat + u.Gaus(0,s_EC1);
26   EC2 = evt_heat + u.Gaus(0,s_EC2);
27   float EC =coeff_EC1*EC1+(1-coeff_EC1)*EC2;
28   float EI =0.413*EIB+0.587*EID;
29   float accept = 0.5*(1 + TMath::Erf( (EC-heat_thresh) / (TMath::Sqrt(2)*
       s_heat) ) );
30   // Select data that pass analysis cuts
31   if (abs(EC1-EC2)<1 && ECinf < EC && EC < ECsup && EIinf<EI  && EI<EIsup
       && EIA < cut_vetA && EIC < cut_vetC)
32   {
33     //Simulate threshold effects
34     if (u.Binomial(1,0.9999*accept)==1) {t_new->Fill();}
35   }
36 }
```

B.3 Background: Beta and Pb events

Likewise, the Beta and Lead training events are generated from the background model of Sec. 4.4.2.1. The background model was deconvolved first, so that resolution effects are incorporated in the simulation by the simple addition of gaussian noise. We also add an additional contribution to the resolution, corresponding to the intrinsic scatter.

The C++ implementation of the simulation of Surface 1 Betas can be found below:

```
for (int k=0; k<num_event; k++)
{
  // Draw data from 1D distribution
  float evt_heat = func_S1Beta->GetRandom(0,20);
  //Get heat rate
  float jour = hJOUR->GetRandom();
  HR = heatrate->GetBinContent(heatrate->FindBin(jour));
  // Get resolution for heat, with time dep
  float s_EC1 = hOWC1->GetBinContent(hOWC1->FindBin(jour))/2.3548;
  float s_EC2 = hOWC2->GetBinContent(hOWC2->FindBin(jour))/2.3548;
  float s_heat = compute_resolution(s_EC1*2.3548, s_EC2*2.3548);
  float coeff_EC1 = compute_coeff(s_EC1*2.3548, s_EC2*2.3548);
  //Draw ionisation from multivariate gaussian
  TArrayD reso_coeff(4);
  for (int k = 0; k<4; k++) {reso_coeff[k] = u.Gaus(0,1);}
  TMatrixD reso_matrx(4,1);
  reso_matrx.SetMatrixArray(reso_coeff.GetArray());
  TMatrixD ion_matrx = Lmatrx*reso_matrx;

  EIA = func_convS1Beta->Eval(evt_heat) + ion_matrx(0,0);
  EIC = ion_matrx(2,0);
  EIB = func_convS1Beta->Eval(evt_heat) + ion_matrx(1,0);
  EID = ion_matrx(3,0);
  EC1 = evt_heat + u.Gaus(0,s_EC1);
  EC2 = evt_heat + u.Gaus(0,s_EC2);

  float EC =coeff_EC1*EC1+(1-coeff_EC1)*EC2;
  float EI =0.413*EIB+0.587*EID;
  float accept = 0.5*(1 + TMath::Erf( (EC-heat_thresh) / (TMath::Sqrt(2)*
    s_heat) ) );
  // Select data that pass analysis cuts
  if (abs(EC1-EC2)<1 && ECinf < EC && EC < ECsup && EIinf<EI  && EI<EIsup
    && EIA < cut_vetA && EIC < cut_vetC)
  {
    //Simulate threshold effects
    if (u.Binomial(1,0.9999*accept)==1) {t_new->Fill();}
  }
}
```

B.4 Background: Heatonly events

The C++ implementation of the simulation can be found below:

```
for (int k=0; k<num_event; k++)
{

  // Draw events from file where the 2D heat signal was simulated
  fheatonly >> heat_EC1 >> heat_EC2 >> jour;
  // Get Heat rate
  HR = heatrate->GetBinContent(heatrate->FindBin(jour));
  // Get resolution for heat, with time dep
  float s_EC1 = hOWC1->GetBinContent(hOWC1->FindBin(jour))/2.3548;
  float s_EC2 = hOWC2->GetBinContent(hOWC2->FindBin(jour))/2.3548;
  float s_heat = compute_resolution(s_EC1*2.3548, s_EC2*2.3548);
  float coeff_EC1 = compute_coeff(s_EC1*2.3548, s_EC2*2.3548);
  //Draw ionisation from multivariate gaussian
  TArrayD reso_coeff(4);
  for (int k = 0; k<4; k++) {reso_coeff[k] = u.Gaus(0,1);}
  TMatrixD reso_matrx(4,1);
  reso_matrx.SetMatrixArray(reso_coeff.GetArray());
  TMatrixD ion_matrx = Lmatrx*reso_matrx;

  EC1 = heat_EC1 ;
  EC2 = heat_EC2 ;
  EIA = ion_matrx(0,0);
  EIB = ion_matrx(1,0);
  EIC = ion_matrx(2,0);
  EID = ion_matrx(3,0);

  float EC =coeff_EC1*EC1+(1-coeff_EC1)*EC2;
  float EI =0.413*EIB+0.587*EID;
  float accept = 0.5*(1 + TMath::Erf( (EC-heat_thresh) / (TMath::Sqrt(2)*
    s_heat) ) );
  // Select data that pass analysis cuts
  // No threshold to be simulated (already included in the simulation)
  if (abs(EC1-EC2)<1 &&  ECinf < EC && EC < ECsup && EIinf<EI  && EI<EIsup
    && EIA < cut_vetA && EIC < cut_vetC) {t_new->Fill();}
}
```

Appendix C

Synthèse en Français

C.1 Introduction à la matière noire

Le modèle standard de la cosmologie, aussi appelé ΛCDM, est une immense réussite qui parvient à rendre compte d'un très grand nombre d'observations. En dépit de ces succès, la majeure partie de l'univers demeure mal connue. En effet, le modèle ΛCDM indique que l'univers est aujourd'hui dominé par des composants "sombres" : l'énergie noire et la matière noire (voir Fig. C.1) qui sont essentielles pour le modèle mais dont la vraie nature demeure mal comprise. Dans cette thèse, nous allons nous intéresser en premier lieu à la matière noire. Dans cette partie, nous allons expliquer comment les observations cosmologiques tendent vers l'hypothèse d'une matière noire froide non baryonique et interagissant faiblement. Nous passerons rapidement en revue les candidats avant de nous pencher sur les expériences de détection.

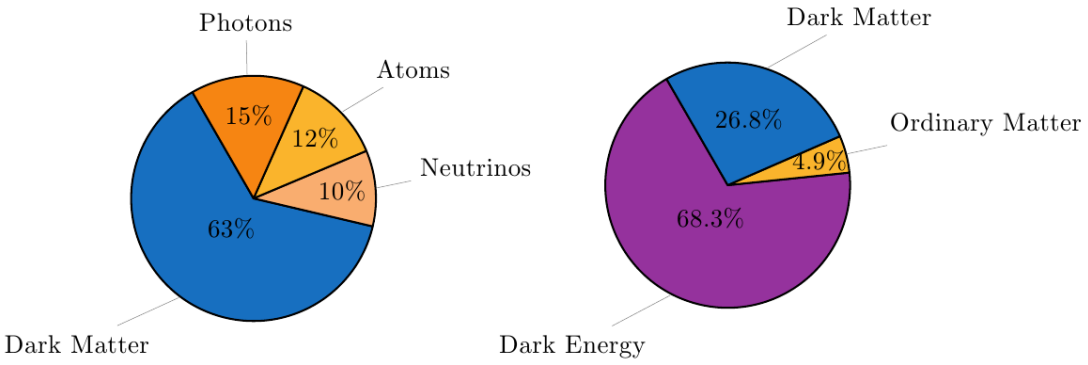

FIGURE C.1 À gauche : Contenu de l'univers 380 000 ans après le Big Bang (recombinaison). À droite : Contenu aujourd'hui.

C.1.1 Motivations pour la matière noire sous forme de WIMPs

La paternité du terme "matière noire"" est attribué à Zwicky. Avec Smith, il a mesuré les vitesses des galaxies dans les amas Coma et Virgo. Ils ont mis en évidence un désaccord entre la masse prédite par Hubble et la masse nécessaire pour expliquer les vitesses par interaction gravitationnelle. Pour résoudre ce problème, Zwicky a postulé l'existence de matière invisible ("noire"). Aujourd'hui, les preuves les plus robustes proviennent du fond diffus cosmologique (CMB), de l'oscillation acoustique de baryons (BAO) et de la nucléosynthèse primordiale (BBN). Ces sondes contraignent la densité baryonique ainsi que la densité de matière avec une grande précision et mettent en évidence l'existence d'une composante froide, non baryonique.

C.1.2 Candidats pour la matière noire

L'existence de la matière noire étant établie, il reste à savoir ce qui la constitue. La particule candidate doit satisfaire aux propriétés suivantes : stabilité (sinon elle ne serait pas observable aujourd'hui), neutralité de charge (sinon elle laisserait une empreinte visible sur le CMB) et caractère non relativiste (sinon cela conduirait à une suppression de la formation de structures incompatible avec les observations).

Parmi les nombreux candidats prédits par les théories au-delà du modèle standard (BSM), deux vont retenir notre attention. En premier lieu, les axions. Ces particules ont été introduites pour résoudre le problème de la symétrie CP en chromodynamique (plus de détails dans la Section C.3). Ces particules peuvent être créées non thermiquement et contribuer à la totalité de la densité de matière noire tout en ayant une masse très faible (de l'ordre de 10^{-6} eV). Le second candidat est appelé WIMP et désigne une particule massive ($\mathcal{O}$(GeV)-$\mathcal{O}$(TeV)) interagissant faiblement. Ces particules interagissent avec le plasma primordial et leur densité décroit exponentiellement à mesure que l'univers se refroidit. Lorsque leur densité devient suffisamment faible, l'équilibre avec le plasma est rompu et la densité n'évolue plus (hormis le facteur de dilution causé par l'expansion de l'univers). La densité relique observée aujourd'hui suffit à expliquer toute la matière noire si la section efficace d'annihilation du WIMP est de l'ordre de $3 \cdot 10^{-26}\,\mathrm{cm}^3\mathrm{s}^{-1}$. Il est remarquable que cette section efficace coïncide avec celle attendue pour des particules prédites par des théories BSM. Cette coïncidence est parfois appelée le miracle WIMP. La supersymétrie, une théorie BSM, prédit un candidat très étudié, le neutralino.

C.1.3 Détection de la matière noire

Il existe trois grandes classes de recherche de matiere noire sous forme de WIMPs. La détection directe repose sur la diffusion de WIMPs sur des noyaux cibles. La détection dans les collisionneurs de particules consiste à produire de la matière noire grâce à l'énergie générée par des collisions de particules du modèle standard. Enfin, la détection indirecte cherche les produits de l'annihilation de WIMPs dans des régions du ciel soupçonnées d'héberger de grandes quantités de matière noire.

Nous allons maintenant nous concentrer sur la détection directe de matière noire car c'est à cette classe qu'appartient l'expérience EDELWEISS.

Le principe est simple : notre galaxie, la Voie Lactée, est piégée gravitationnellement dans un halo de matière noire. Si ce halo est composé de WIMPs, il est alors facile d'estimer le flux sur Terre : $\Phi \approx 10^5 \left(\frac{100\,\mathrm{GeV}}{M_\chi}\right)\ \mathrm{cm}^{-2}\ \mathrm{s}^{-1}$ où M_χ est la masse du WIMP. Les WIMPs du halo ont une vitesse du même ordre de grandeur que celle des étoiles, de l'ordre de quelques centaines de kilomètres par seconde. À cette vitesse, les WIMPs diffusent élastiquement sur un noyau cible donné. Le calcul du taux d'interaction donne la formule suivante :

$$\mathcal{R} \equiv \frac{\mathrm{d}R}{\mathrm{d}E_\mathrm{R}} = \frac{\sigma(q)}{2M_\chi \mu^2}\,\rho_0\,\eta(E_\mathrm{R}, t) \qquad \text{en coups/kg.jour.keV} \tag{C.1}$$

où E_R est l'énergie de recul, μ est la masse réduite du système noyau-WIMP, $\sigma(q)$ est la section efficace de diffusion WIMP-noyau, ρ_0 est la densité de WIMP locale et η est défini par :

$$\eta(E, t) = \int_{u > v_\mathrm{min}} \frac{f(\mathbf{u}, t)}{u}\,\mathrm{d}^3 u\,. \tag{C.2}$$

où u est la vitesse du WIMP, $f(u)$ est la distribution des vitesses et v_min est la vitesse minimale nécessaire à la diffusion élastique.

Toutes les expériences de détection directe partagent le même principe, mais de nombreuses différences de technologie existent. En effet, de nombreuses particules bien connues peuvent diffuser dans le détecteur et il faut donc être capable de les rejeter. Pour cela plusieurs solutions existents. Les expériences au gaz noble comme XENON ou LUX utilisent typiquement une chambre à projection temporelle (TPC) diphasique qui permet de mesurer un signal de scintillation et un signal d'ionisation (résultant d'une interaction dans le détecteur). La comparaison du signal ionisation au signal de scintillation permet de discriminer le bruit de fond par rapport au signal. D'autres expériences, comme EDELWEISS ou CDMS utilisent des détecteurs bolométriques solides pour mesurer le

signal d'ionisation et le signal de phonons à chaque interaction. Là encore, la comparaison des deux permet la discrimination.

La figure C.2 montre des résultats expérimentaux récents. On peut dégager deux grandes régions : une région haute masse (> 30 GeV), dominée par les expériences à base de Xenon et une région à basse masse (< 10 GeV) où les résultats sont plus contrastés : certaines expériences ont observé un excès par rapport aux prédictions de bruit de fond et en déduisent un contour de confiance. D'autres ne voient rien d'anormal et en déduisent une limite d'exclusion. A l'heure actuelle, tout conclusion fiable est prématurée, car les signaux observés sont très proches du seuil expérimental. La prochaine génération d'expériences à bas seuil devrait permettre de lever le voile sur ces incertitudes.

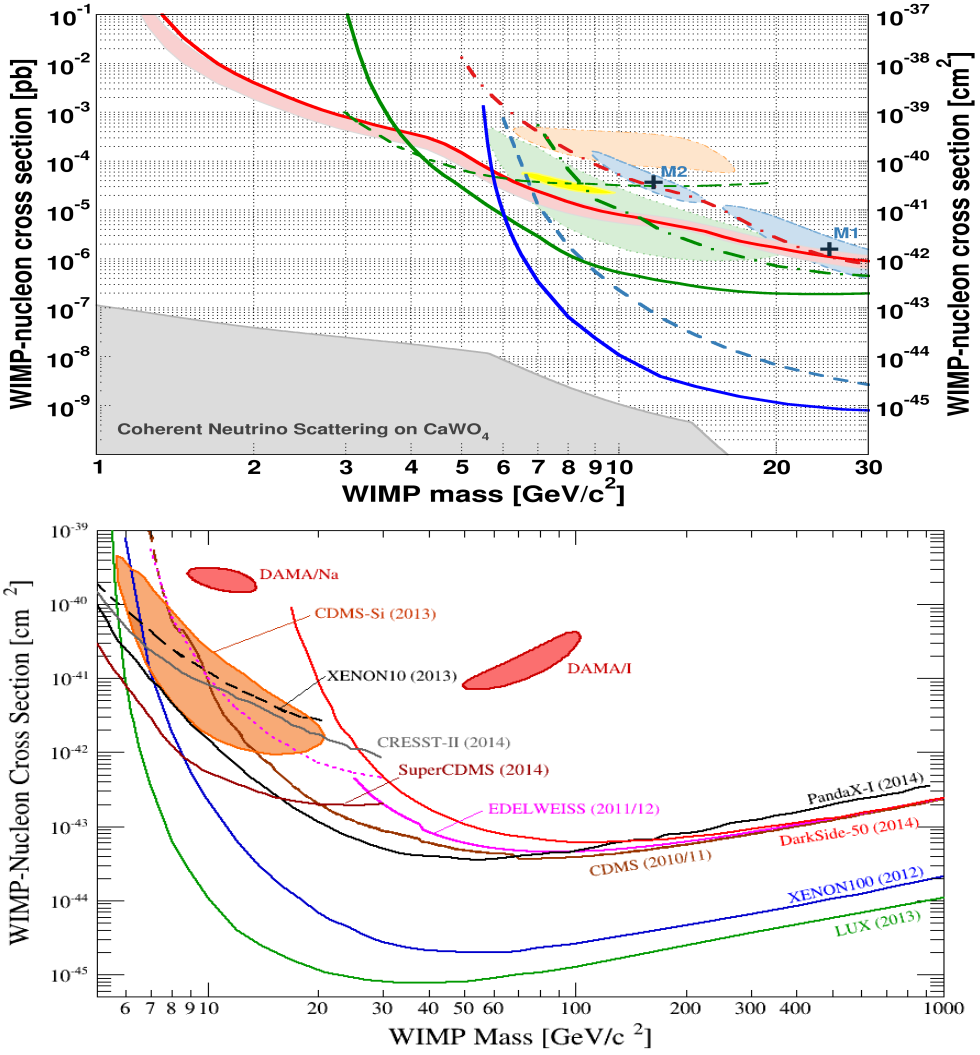

FIGURE C.2 Limites sur la section efficace WIMP-nucleon. Haut: zoom sur la région des basses masses. Bas: Présentation des limites à haute masse (1 TeV).

C.2 Présentation de l'expérience EDELWEISS

Dans cette section, nous allons présenter l'expérience EDELWEISS, actuellement dans sa troisième phase : EDELWEISS-III. Comme nous l'avons indiqué dans la section C.1.3, de nombreuses particules peuvent interagir avec le noyau cible : il y a de nombreux bruits de fond à rejeter. Nous allons donc articuler cette section autour des bruits de fond : quels sont-ils ? Comment faire pour s'en protéger ?

- **Les neutrons**. Les neutrons ont plusieurs origines : ils peuvent provenir de muons cosmiques ou bien de chaînes de radioactivité naturelle (Uranium/Thorium). Ils interagissent avec le noyau de la cible.
- **Les gammas** ont également plusieurs origines : les rayons cosmiques peuvent activer des isotopes radioactifs du détecteur. Leur désexcitation génère des gammas avec une énergie bien précise. Les plus intenses se trouvent à 10.37 keV et 8.98 keV (^{68}Ge et ^{65}Zn respectivement). Les gammas peuvent également être produits dans les chaînes de radioactivité naturelles ou bien par radioactivité des composants électroniques. Les gammas interagissent avec les électrons de la cible.
- **Radioactivité de surface.** La contamination des composants du dispositif expérimental en éléments lourd conduit à l'émission de betas, de particules alpha et de reculs de plomb. Ces bruits de fond pénètrent très peu profondément dans le détecteur. Comme les gamma, ils interagissent avec les électrons.

Cette description des bruits de fond va nous permettre de bien comprendre le dispositif expérimental choisi par EDELWEISS. L'expérience est située sous la montagne, dans le tunnel du Fréjus : la roche atténue grandement le flux de muons et permet de limiter le bruit de fond neutron. La figure C.3 ci-dessous montre le dispositif expérimental dans le laboratoire. Les détecteurs sont placés dans un cryostat (en doré) et protégés par une série de blindages, en polyéthylène et en plomb. Ces blindages permettent de nettement réduire le taux d'événement de bruit de fond.

Malgré toutes les précautions prises dans le choix des blindages et de la pureté des composants, le bruit de fond n'est pas entièrement supprimé. La description des bruits de fond donne de nouvelles pistes : la plupart des bruits de fond interagissent avec les électrons alors que les WIMPs interagissent avec les noyaux (le recul d'un électron après collision avec un WIMP est indétectable). Il suffit donc d'être capable de discriminer reculs nucléaires et reculs électronique pour rejeter beaucoup de bruit de fond. La fiducialisation du détecteur est une autre piste qui permet de rejeter les événements de

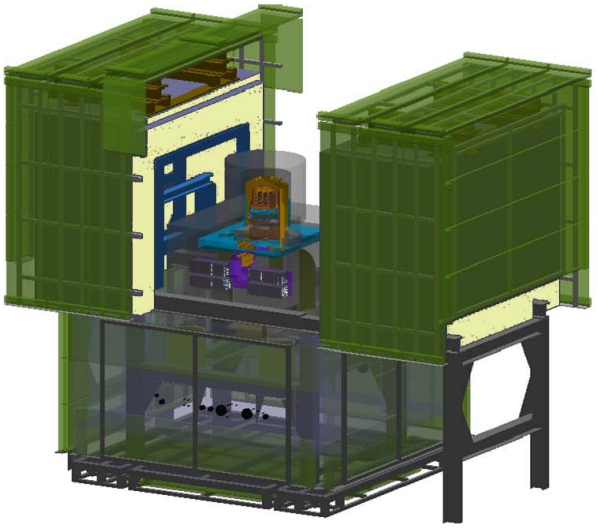

FIGURE C.3 Dispositif EDWELWEISS-III.

surface. À travers la description du détecteur, nous allons expliquer comment ces idées ont été appliquées dans le cadre d'EDELWEISS.

Les détecteurs d'EDELWEISS-III sont des cristaux de Germanium, dont la température est maintenue proche de 17 mK, équipés de senseur chaleur et placés sous tension pour permettre la lecture d'un signal ionisation (les paires électron trous se déplacent jusqu'à une série d'électrodes sous l'effet du champ électrique). Il y a 4 voies ionisation en tout (voir Fig. C.4) pour fiducialiser le détecteur : du fait des polarisations alternées, un événement de surface ne générera du signal que sur une des surfaces du détecteur alors qu'un événement de volume générera du signal sur les deux faces. C'est ainsi que l'on peut rejeter les événements de surface.

La distinction recul nucléaire/recul électronique se fait à travers la comparaison du signal chaleur et du signal ionisation. Schématiquement, le signal chaleur est la somme de l'énergie de recul et d'une composante due à l'accélération des électrons (effet Luke) :

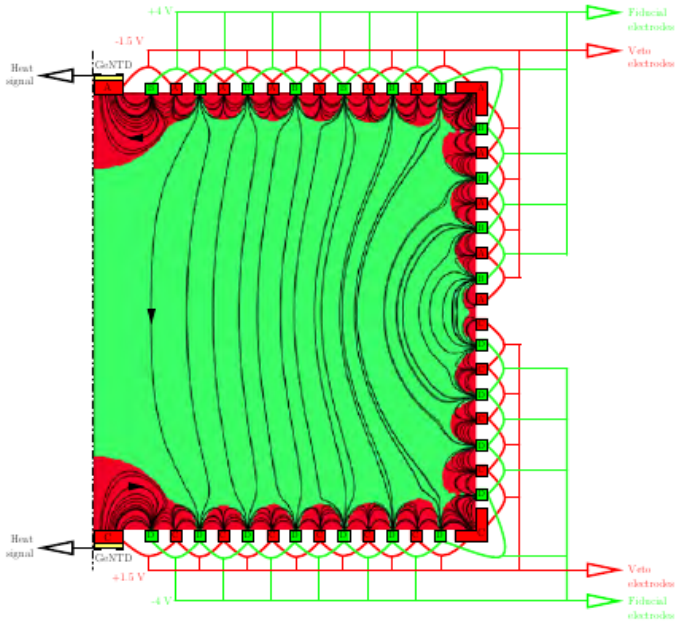

FIGURE C.4 Schéma du détecteur the Full InterDigit (FID) utilisé dans EDELWEISS-III

$$E_{\text{heat}} = E_{\text{R}} + E_{\text{Luke}} = E_{\text{R}}\,(1 + \epsilon V) \tag{C.3}$$

Cette dernière composante vient du fait que les électrons accélérés chauffent le cristal. Elle est bien sûr proportionnelle à la tension appliquée (V) mais dépend aussi de l'énergie nécessaire à la production d'une paire électron-trou. Cette énergie, qui dépend du type de particule est noté ϵ. Par convention, on normalise par rapport à ϵ_γ et on écrit alors

$$E_{\text{heat}} = E_{\text{R}} + E_{\text{Luke}} = E_{\text{R}}\left(1 + \frac{QV}{\epsilon_\gamma}\right) \tag{C.4}$$

où $Q = \epsilon_\gamma/\epsilon$. Le signal ionisation est proportionnel au nombre de charges produites : on peut donc écrire $E_{\text{R}} = E_{\text{I}}/Q$. On voit ainsi comment la double mesure chaleur-ionisation permet la mesure de Q et donc la discrimination entre gammas (recul électronique, Q=1) et WIMPs (recul nucléaire, Q=0.3).

C.3 Recherche d'axions avec les données EDELWEIS-II

Nous allons maintenant présenter une première analyse, conduite avec les données d'EDELWEISS-II, et consacrée à la recherche d'axions. Après une courte introduction théorique, nous commenterons les canaux d'analyse et discuterons les résultats.

C.3.1 Une introduction aux axions

Le problème de la symétrie CP en chromodynamique est un problème de *fine-tuning*. Le lagrangien QCD inclut un terme qui viole la symétrie CP :

$$\mathcal{L}_\Theta = \Theta\left(\frac{\alpha_s}{8\pi}\right) G^{\mu\nu a}\bar{G}^a_{\mu\nu} \tag{C.5}$$

où G est le tenseur du champ de couleur, $\bar{G}$ son dual, α_s la constante de couplage forte et Θ est un paramètre de phase. La mesure du moment electrique du neutron implique : $|\Theta| \lesssim 10^{-10}$ alors même qu'une valeur de l'ordre de 1 est tout à fait satisfaisante. C'est le problème de la symétrie CP. Peccei et Quinn, puis Weinberg, ont alors postulé une nouvelle symétrie $\mathcal{U}(1)$ qui est brisée spontanément et dont le boson de Goldstone acquiert une masse par des effets non perturbatifs : c'est l'axion ! Le champ de l'axion oscille dans le potentiel créé par ces effets et finit par atteindre le minimum, ce qui annule dynamiquement le terme de violation CP.

L'axion peut interagir avec des particules du modèle standard comme les électrons, les photons et les nucléons. La valeur du couplage dépend du modèle choisi. Dans la suite, nous adopterons une approche modèle-indépendante en introduisant des couplages génériques (qui peuvent ensuite être interprétés dans le cadre d'un modèle particulier)

C.3.2 Production et détection d'axions

Nous allons maintenant nous intéresser aux mécanismes de production et de détection d'axions. Le champ d'axions sera noté A.

Production

- Effet Primakoff dans le soleil : $\gamma \rightarrow$ A en présence de particules chargées. Cette réaction fait intervenir le couplage aux photons $g_{A\gamma}$.
- Processus Compton, Bremsstrahlung, Recombinaison et déexcitation dans le soleil (avec des réactions du type de $e^- + \gamma \rightarrow e^- +$ A ou $e^- +$ I $\rightarrow I^- +$ A où I est un ion). Ces réactions font intervenir le couplage aux électrons g_{Ae}
- Transition nucléaire magnétique du noyau ^{57}Fe dans le soleil: $^{57}Fe^* \rightarrow ^{57}$Fe + A. Cette réaction fait intervenir le couplage aux nucléons g_{AN}
- Axion en tant que particule de matière noire. (Pas de couplage)

Détection

- Effet Primakoff inverse dans le cristal : A $\rightarrow \gamma$ dans le champ électrique du détecteur. Cette réaction fait intervenir $g_{A\gamma}$.
- Effet axio-electrique. C'est l'équivalent de l'effet photoélectrique pour les axions. La section efficace peut s'écrire :

$$\sigma_{Ae}(E) = \sigma_{\mathrm{pe}}(E)\frac{g_{Ae}^2}{\beta}\frac{3E^2}{16\pi\alpha m_e^2}\left(1 - \frac{\beta^{\frac{2}{3}}}{3}\right) \tag{C.6}$$

  Dans cette équation, β est le quotient de la vitesse de l'axion et de la lumière, α est la constante de structure fine, m_e est la masse de l'électron et σ_{pe} est la section photoélectrique du Germanium.

La figure C.5 ci-dessous montre les différents flux d'axions solaires à gauche et la section efficace axio-électrique pour plusieurs masses différentes à droite.

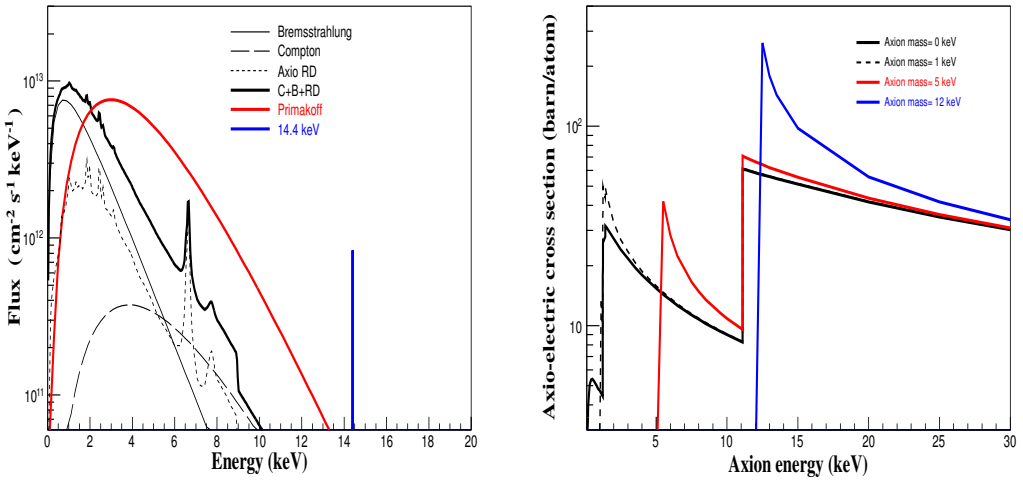

FIGURE C.5 Gauche : Flux d'axions solaires pour les canaux de production d'intérêt. Les constantes de couplage ont les valeurs suivantes : $g_{A\gamma} = 10^{-9}$ GeV^{-1}, $g_{Ae} = 10^{-11}$ et $g_{AN}^{\text{eff}} = 10^{-7}$. Droite : Section efficace axio-électrique pour différentes masses.

Nous avons donc, en tout, 8 paires production-détection. Pour faciliter l'interprétation, nous avons favorisé les paires ne faisant intervenir qu'un seul couplage. Nous nous sommes donc limités à 4 canaux d'analyse, résumés dans la table C.1 ci-dessous .

Production	**Detection**
Primakoff dans le soleil	Détection Primakoff
CBRD dans le soleil	Effet axio-électrique
^{57}Fe dans le soleil	Effet axio-électrique
Axion matière noire	Effet axio-électrique

TABLE C.1 Canaux étudiés. CBRD désigne Compton-Bremsstrahlung-Recombinaison-Désexcitation.

C.3.3 Le spectre des reculs électroniques

Les axions génèrent des reculs électroniques. Il est donc nécessaire de bien comprendre le bruit de fond de reculs électroniques pour pouvoir conclure sur la présence ou non d'un signal. La figure C.6 ci-dessous montre le spectre des reculs électroniques (combiné sur l'ensemble des détecteurs). C'est dans ce spectre que l'on va recherche un éventuel signal axion.

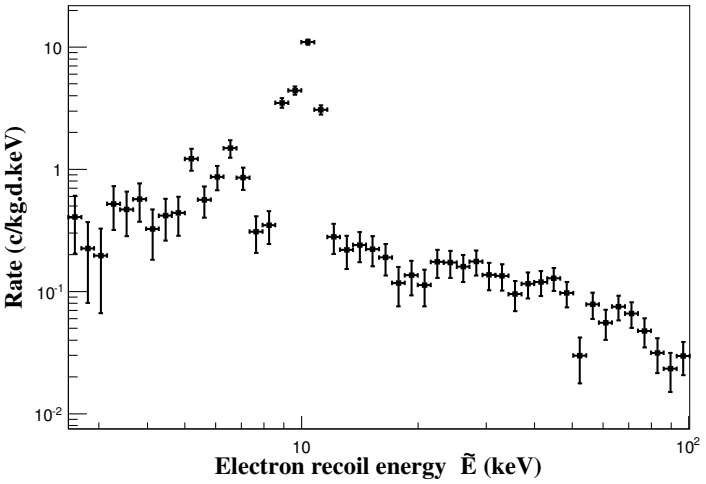

FIGURE C.6 Spectre combiné (plusieurs détecteurs), avec correction de l'efficacité. On remarque le fond plat Compton et la présence de pics dus à l'activation d'isotopes radioactifs.

C.3.4 Résultats

Nous allons maintenant présenter les analyses conduites pour chacun des 4 canaux.

Détection Primakoff

La détection Primakoff repose sur la diffraction de Bragg (voir schéma explicatif C.7). En effet, les axions émis par effet Primakoff ont une longueur d'onde comparable à la distance interatomique du cristal de Germanium : il n'y aura d'interférences constructrices que pour des valeurs bien particulière de l'énergie de l'axion incident (condition de Bragg). Prenant cette condition en compte, nous obtenons l'expression finale du taux d'interaction dans le cristal :

$$R(\tilde{E},t,\alpha) = 2(2\pi)^3 \frac{V}{v_a^2} \sum_G \frac{d\phi}{dE_a} \frac{g_{A\gamma}^2}{16\pi^2} \sin(2\theta)^2 \frac{1}{|\mathbf{G}|^2} \left| S(\mathbf{G}) F_A^0(\mathbf{G}) \right|^2 \; e^{-\frac{(\tilde{E}-E_a)^2}{2\Delta^2}} \qquad \text{(C.7)}$$

où θ est l'angle de diffraction, la somme porte sur les vecteur $\mathbf{G}$ du réseau réciproque et $\frac{d\phi}{dE_a}$ est le flux Primakoff venant du soleil. S et F_A^0 sont respectivement les facteurs de structure et de forme du Germanium dans la maille diamant. $\tilde{E}$ est l'énergie mesurée par le détecteur et Δ sa résolution.

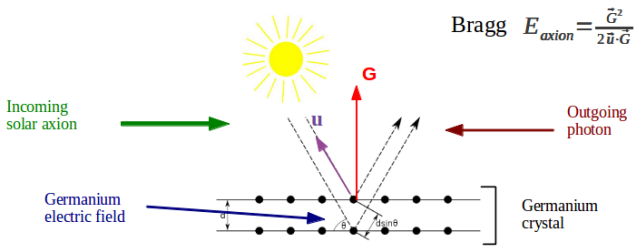

FIGURE C.7 Schéma de Bragg pour la détection d'axions.

Pour faire l'analyse statistique des résultats, nous avons introduit un corrélateur en temps pour le taux d'événement. A partir de ce corrélateur, il est possible de mettre en évidence un signal ou, le cas échéant, d'en déduire une limite sur le couplage $g_{A\gamma}$. Les résultats obtenus avec la combinaison de plusieurs détecteurs de l'expérience EDELWEISS sont montrés figure C.8

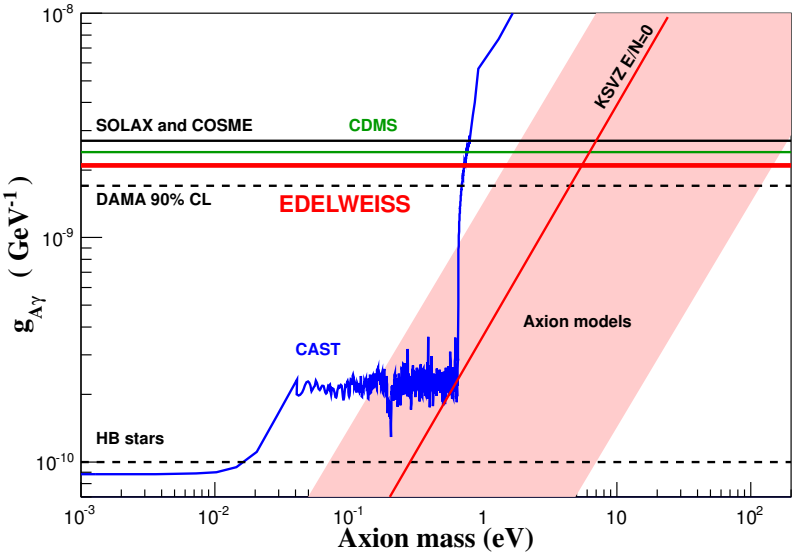

FIGURE C.8 Limite à 95 % de confiance sur le couplage $g_{A\gamma}$ (en rouge). Cette limite est comparée à d'autres expériences à base de détecteurs cristallins (SOLAX, COSME, CDMS et DAMA). Nous montrons également la limite de CAST (en bleu) ainsi que des limites indirected astrophysques (pointillés noirs) La bande rouge indique les régions favorisées par des modèles d'axions standards.

Détection par effet axio-électrique

La détection par effet axio-électrique est très simple : il s'agit d'identifier un signal dans le spectre des reculs électroniques. Pour ce faire, une simple analyse de vraisemblance est menée avec le modèle de bruit de fond et le modèle de signal. Aucune de ces analyses n'indique la présence d'un signal, nous en avons donc déduit des limites sur le couplage g_{Ae} (et aussi g_{AN} dans le cas du ^{57}Fe). Ces limites (à l'exception de la limite ^{57}Fe qui ne peut pas être montrée dans le plan $g_{Ae} - m_A$ sans faire d'hypothèse sur le modèle d'axion) sont résumées dans la figure C.9.

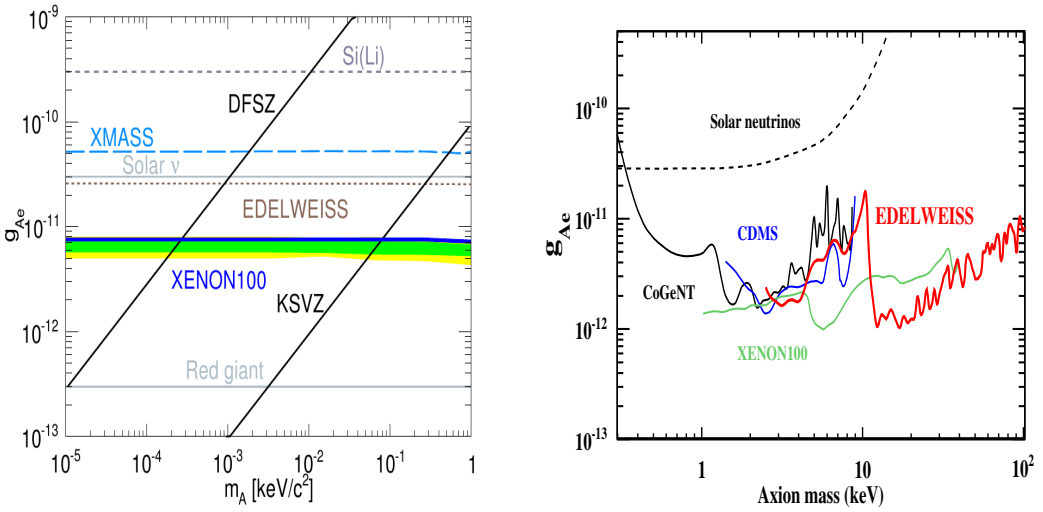

FIGURE C.9 Contraintes sur g_{Ae}. A gauche : canal CBRD, la limite d'EDELWEISS est en marron. A droite : limite pour des axions matière noire. La limite d'EDELWEISS est en rouge. Les autres courbes correspondent à des limites d'autres expériences (Xenon, CoGeNT, CDMS, DAMA, XMASS) ou astrophysiques (neutrinos solaires et géantes rouges).

C.3.5 Conclusions

L'analyse menée ici permet de poser des contraintes compétitives sur trois couplages de l'axion en utilisant 4 canaux différents : c'est un excellent résultat pour un unique lot de données. En interprétant les résultats dans le cadre d'un modèle d'axions particulier, le modèle DFSZ, nous excluons 4 ordres de grandeur de masses d'axion !

C.4 Recherche de WIMPs de basse masses

Dans cette section, nous allons présenter un nouvelle méthode d'analyse, adaptée tout particulièrement aux WIMPs de basse masse. Comme nous l'avons indiqué plus haut, les WIMPs de basse masse sont motivés par plusieurs résultats expérimentaux indiquant un excès possible pour des masses de l'ordre du GeV, ainsi que par certaines théories BSM comme la matière noire asymétrique. Après une brève description du jeu de données, nous présenterons la construction des modèles de bruit de fond puis nous introduirons un nouvel outil de statistique: les arbres de décision boostés (BDT). Cette nouvelle méthode va nous permettre d'améliorer les performances de l'analyse à basse énergie.

C.4.1 Le jeu de données

Dans cette analyse, nous n'utilisons qu'une fraction du lot total. L'objectif est de préparer la construction des modèles de bruit de fond avant de faire une analyse en aveugle sur le lot restant. Pour cela, nous avons sélectionné un détecteur, nommé FID837, avec des performances "standard" pour une période d'environ 100 jours (de prise réelle de données) de Juillet 2014 à Janvier 2015. Nous avons imposé un seuil relativement élevé à 1.5 keV afin de pouvoir négliger les perte d'efficacité dues au seuil de déclenchement. Nous avons ensuite sélectionné les données passant des coupures qualité bien définies: coupure sur le niveau du seuil de déclenchement en ligne, sur la forme des pulses, sur la valeur de la ligne de base de chaque voie. Ces coupures réduisent l'exposition à 58 jours environ.

C.4.2 Les modèles de bruit de fond

Les données sont montrées sous la forme d'un Q-plot (Q en fonction de l'énergie de recul) sur la figure C.10. Nous avons souligné la différence entre les événements fiduciels, les événements de surface et les événements dits "chaleur-seule" (ils ne génèrent pas de signal ionisation).

Les différentes populations sont sélectionnées à partir de ce Q-plot, ce qui permet de construire les modèles de bruits de fond à partir des données. Nous allons maintenant expliquer la procédure exacte pour chacune des populations.

- **Gammas Fiduciels :** Le fond chaleur à une dimension consiste d'une composante plate (due aux gammas Compton) et de pics radioactifs (pour la plupart situés en dehors de la zone de signal WIMPs). Il est donc possible d'ajuster un modèle à

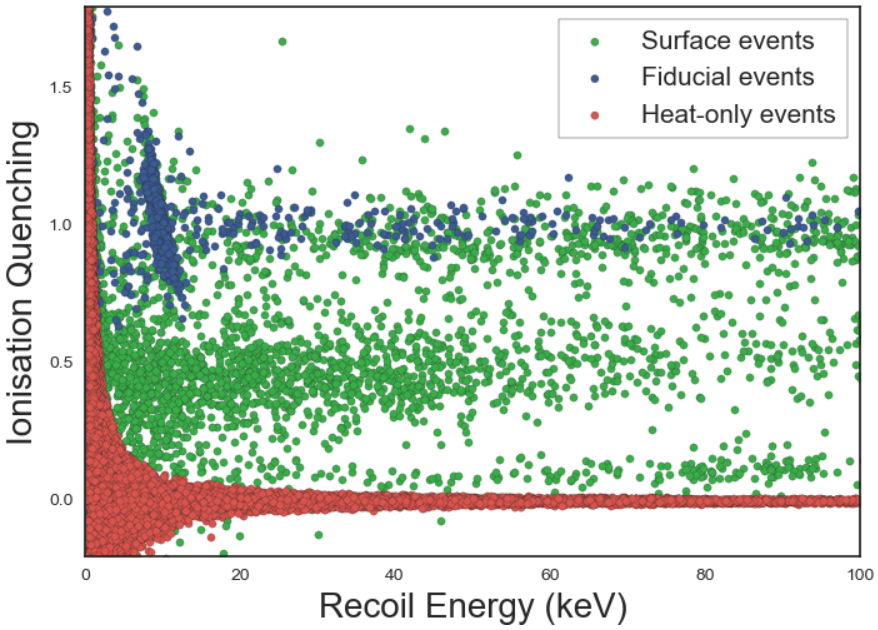

FIGURE C.10 Q plot pour les données de recherche WIMP du FID837 passant les coupures générales de qualité mentionnées plus haut.

ces données. Ce modèle est ensuite extrapolé aux plus basses énergies. N.B. Un des pics (en fait plusieurs pics d'énergie similaire) se situe dans la zone WIMP. Leur amplitude peut néanmoins être correctement estimée car elle est directement reliée à celle de pics de plus haute énergie (niveaux L/K).

- **Gammas de surface :** Le modèle est immédiatement dérivé du modèle des gammas fiduciels (avec une correction de l'échelle d'énergie chaleur) et du rapport masse fiducielle/masse de surface. Seul le fond plat est ajusté. Il peut en effet être plus intense que le fond fiduciel car moins de gamma pénètrent dans le volume du cristal.

- **Betas et reculs de plomb :** Ces deux espèces sont ajustées de la même manière. Leur spectre en chaleur est ajusté avec une spline dans un région en dehors de la région de signal et est ensuite extrapolé linéairement. La relation chaleur/ionisation est également ajustée par une fonction polynomiale.

- **Fond chaleur seule :** C'est le fond le plus intense, comme le montre le Q-plot ci-dessus. Il est donc crucial de l'estimer correctement. Toute la zone à ionisation négative est une zone sans signal pour le seuil considéré (1.5 keV). Il est donc possible de simuler le signal chaleur des événements chaleur seule à partir de l'histogramme des données dans cette région.

C.4.3 La simulation du signal et des bruits de fond

Pour les besoins de notre analyse multivariée, nous avons réalisé des simulations à 6 dimensions, pour reproduire les informations données par les 6 senseurs du détecteur EDELWEISS (4 ionisations, 2 chaleurs). Voici comment.

- **Simulation de signal**. Partant de la formule à 1D du taux d'événément (voir équation C.1), nous avons simulé des énergies de recul. Cette simulation 1D est ensuite convertie en un 6-tuple en ajoutant le bruit correspondant à chacune des voies et en corrigeant l'échelle d'énergie ou les effets de "quenching". Le bruit chaleur est simulé à partir de gaussiennes non corrélées. Le bruit ionisation est tirée d'une gaussienne à 4 dimensions qui prend en compte les corrélations ionisation. Nous ne simulons du signal que pour les WIMPs de volume.

- **Simulation des événement chaleur-seule.** Nous simulons le signal en énergie chaleur en tirant des événements de la distribution chaleur à 2 dimensions. Le signal ionisation est tirée de la même gaussienne à 4 dimensions que pour le signal.

- **Simulation des autres bruits de fond**. Comme pour les simulations de signal, nous partons de la distribution à une dimension en énergie chaleur du bruit de fond considéré. On ajoute ensuite le bruit correspondant à chacune des voies, en corrigeant les effetts de quenching pour les gammas de surface et en prenant en compte la dispersion chaleur-ionisation pour les betas et les reculs de plomb.

C.4.4 Les arbres de décision boostés

Les arbres de décision boostés (BDT) sont une méthode de classification supervisée. À partir d'événements déjà bien classifiés, le BDT apprend à reconnaître chaque classe (phase d'entraînement) et est ensuite capable de classifier correctement des données entièrement nouvelles (phase d'évaluation). Le principe d'un arbre de décision est de faire des coupures rectangulaires dans l'espace des paramètres afin d'optimiser la discrimination entre les différentes classes. La phase dite de *boosting* consiste à combiner plusieurs arbres en affectant une importance différente à différents événements pour améliorer la classification : À l'entraînement, les événements mal classifiés se voient accorder un poids plus important pour pénaliser d'autant plus les futurs arbres qui ne le classifieraient pas correctement. Le BDT peut être affinés en contrôlant ses hyper-paramètres. Par exemple, on peut modifier la profondeur des arbres, ou bien le nombre d'arbres utilisés.

C.4.5 Application des BDT à EDELWEISS

La figure C.11 ci-dessous montre le résultat du BDT appliqué aux données EDELWEISS. La grandeur histogrammée est une variable à 1D, obtenue en sortie du BDT. Cette variable est liée à la probabilité d'appartenance à la classe signal (valeurs élevées) ou à la classe bruit de fond (valeurs faibles).

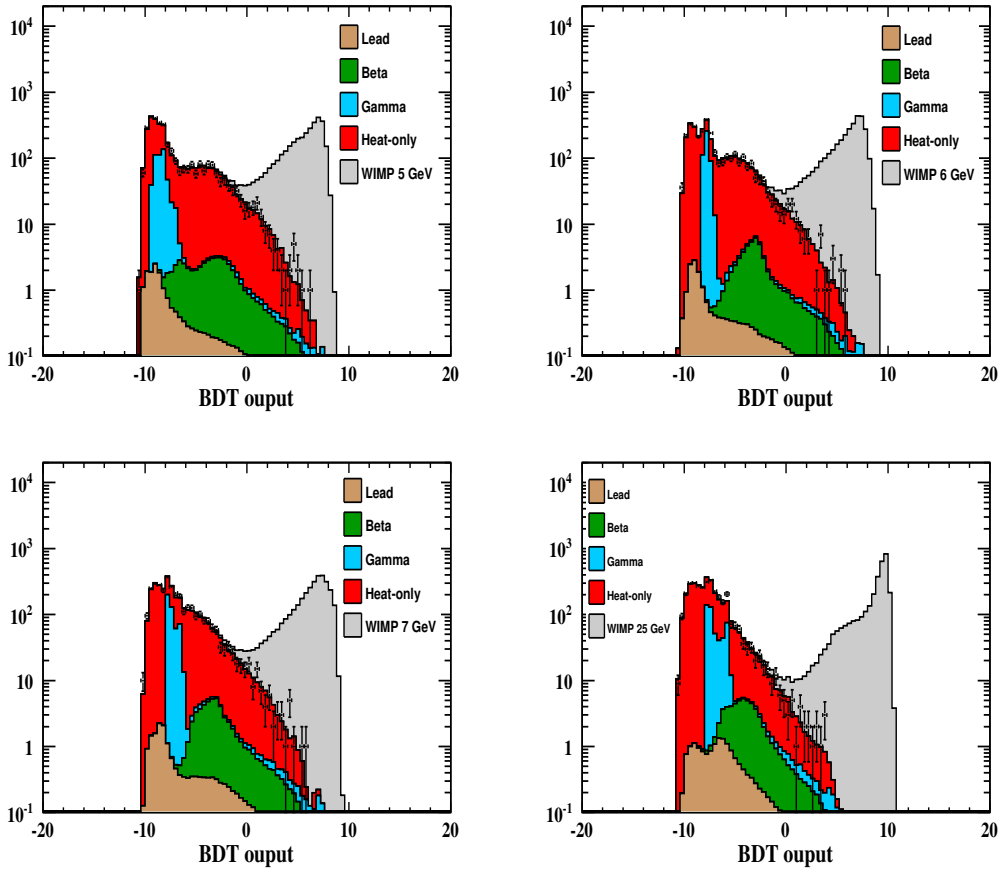

FIGURE C.11 Histogrammes de BDT pour FID837 BDT pour différentes masses. Les histogrammes colorés sont issus des simulations. Les données en noir avec une barre d'erreur sont les données réellement enregistrées pour FID837.

On remarque un très bon accord entre les prédictions des simulations de bruit de fond et les vraies données. Aucun excès notable n'a été observé pour les masses de WIMPs d'intérêt, nous avons donc calculé une limite d'exclusion sur la section efficace WIMP-noyau à partir des distributions BDT. Le principe est simple, il s'agit de choisir la coupure (sur la variable BDT) qui minimise le rapport bruit/signal suivant:

$$R = \frac{\sum_n \mathcal{P}_{90}\,(n)\,\mathrm{P}\,[\mathrm{X}=\mathrm{n};\mathrm{N}_{\mathrm{bckg}}(\mathrm{cut})]}{\epsilon_{\mathrm{WIMP}}(\mathrm{cut})} \tag{C.8}$$

Il ne reste plus qu'à compter le nombre d'événements passant la coupure. Une fois cela fait, on calcule la limite de Poisson correspondante. Ce nombre d'événements correspond à une section efficace donnée qui est obtenue simplement par intégration de la distribution de signal WIMP. La limite finale est montrée figure C.12. En fait, deux limites sont montrés (ligne rouge épaisse et ligne rouge en pointillés). Ces deux courbes correspondent à 2 optimisations de BDT différentes. Pour la courbe rouge épaisse, nous avons cherché à améliorer la performance du BDT en ajoutant de nouvelles variables. Les simulations menées nous ont indiqué qu'il était avantageux d'utiliser la variable EFID-QER (EFID est l'ionisation fiducielle, Q est le quenching et ER l'énergie de recul) ainsi qu'une variable indiquant l'amplitude du taux d'événement chaleur seule au cours du temps. Les limites montrent des résultats compétitifs malgré la faible exposition, le fond élevé et le choix du seuil d'analyse (qui pénalise les basses masses). Nous montrons ainsi clairement le potentiel de la technologie FID d'EDELWEISS pour les recherches de WIMPs de basse masse.

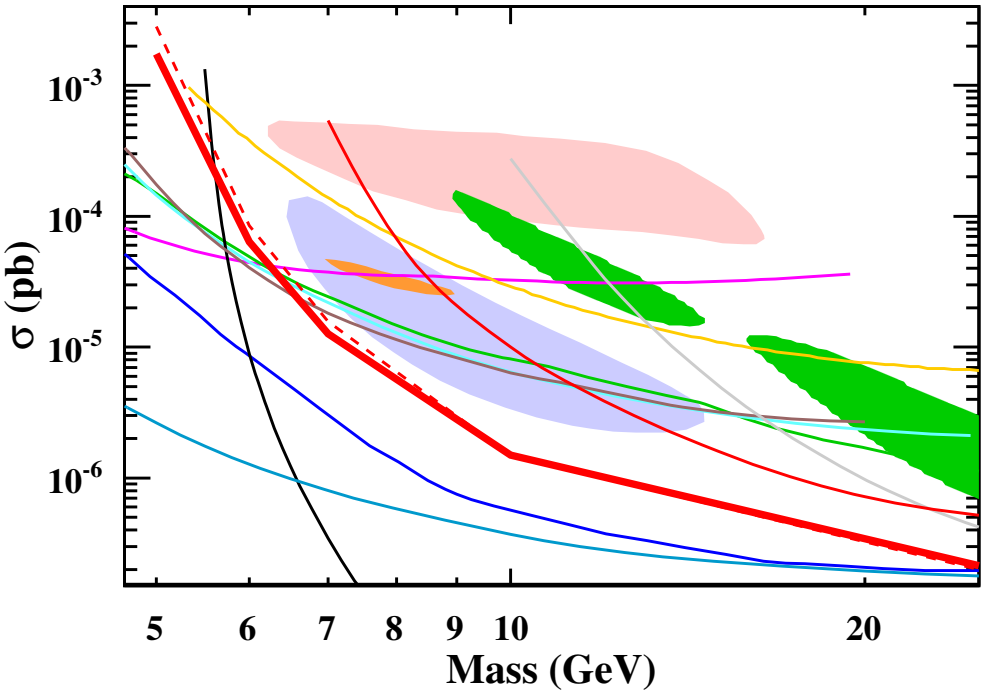

FIGURE C.12 Limite sur la section efficace WIMP pour l'analyse du FID837. Code couleur: SCDMS (*bleu*), CDMS-Si contour (*bleu clair*), CDMSlite (*violet*), DAMA (*saumon*), CRESST (limite et contours en *gris*), SIMPLE (*jaune*), COUPP (*gris*), PICO (*cyan*), Xenon10 (*marron*), LUX (*noir*), CoGeNT (*orange*), EDELWEISS-II (*rouge, trait fin*) and EDELWEISS-III 35 kg.d in (*rouge*). Nous montrons aussi en pointillés l'autre version de la limite EDELWEISS-III pour FID837.

Bibliography

[1] The EDELWEISS collaboration. Final results of the EDELWEISS-II WIMP search using a 4-kg array of cryogenic germanium detectors with interleaved electrodes. *Physics Letters B*, 702(5):329–335, August 2011. ISSN 03702693. doi: 10.1016/j.physletb.2011.07.034. URL http://arxiv.org/abs/1103.4070. arXiv: 1103.4070.

[2] Benjamin Schmidt. *Background discrimination of EDELWEISS-III cryogenic Ge-detectors for dark matter search* . PhD thesis, 2015.

[3] The EDELWEISS collaboration. Background studies for the EDELWEISS dark matter experiment. *Astroparticle Physics*, 47:1–9, July 2013. ISSN 0927-6505. doi: 10.1016/j.astropartphys.2013.05.004. URL http://www.sciencedirect.com/science/article/pii/S0927650513000790.

[4] S. Perlmutter, G. Aldering, G. Goldhaber, R. A. Knop, P. Nugent, P. G. Castro, S. Deustua, S. Fabbro, A. Goobar, D. E. Groom, I. M. Hook, A. G. Kim, M. Y. Kim, J. C. Lee, N. J. Nunes, R. Pain, C. R. Pennypacker, R. Quimby, C. Lidman, R. S. Ellis, M. Irwin, R. G. McMahon, P. Ruiz-Lapuente, N. Walton, B. Schaefer, B. J. Boyle, A. V. Filippenko, T. Matheson, A. S. Fruchter, N. Panagia, H. J. M. Newberg, W. J. Couch, and The Supernova Cosmology Project. Measurements of ω and λ from 42 high-redshift supernovae. *ApJ*, 517(2):565, June 1999. ISSN 0004-637X. doi: 10.1086/307221. URL http://iopscience.iop.org/0004-637X/517/2/565.

[5] M. Colless et al. The 2df galaxy redshift survey: Final data release. June 2003. URL http://arxiv.org/html/astro-ph/0306581.

[6] Adam G. Riess, Alexei V. Filippenko, Peter Challis, Alejandro Clocchiatti, Alan Diercks, Peter M. Garnavich, Ron L. Gilliland, Craig J. Hogan, Saurabh Jha, Robert P. Kirshner, B. Leibundgut, M. M. Phillips, David Reiss, Brian P. Schmidt, Robert A. Schommer, R. Chris Smith, J. Spyromilio, Christopher Stubbs, Nicholas B. Suntzeff, and John Tonry. Observational evidence from supernovae

for an accelerating universe and a cosmological constant. *The Astronomical Journal*, 116(3):1009, September 1998. ISSN 1538-3881. doi: 10.1086/300499. URL http://iopscience.iop.org/1538-3881/116/3/1009.

[7] Planck Collaboration. Planck 2015 results. XIII. Cosmological parameters. *arXiv:1502.01589 [astro-ph]*, February 2015. URL http://arxiv.org/abs/1502.01589. arXiv: 1502.01589.

[8] G. Hinshaw, D. Larson, E. Komatsu, D. N. Spergel, C. L. Bennett, J. Dunkley, M. R. Nolta, M. Halpern, R. S. Hill, N. Odegard, L. Page, K. M. Smith, J. L. Weiland, B. Gold, N. Jarosik, A. Kogut, M. Limon, S. S. Meyer, G. S. Tucker, E. Wollack, and E. L. Wright. Nine-year wilkinson microwave anisotropy probe (WMAP) observations: Cosmological parameter results. *arXiv:1212.5226 [astro-ph]*, December 2012. URL http://arxiv.org/abs/1212.5226. arXiv: 1212.5226.

[9] Planck Collaboration P A R Ade, N Aghanim, M Arnaud, M Ashdown, J Aumont, P Bielewicz, D Harrison, and G Helou. Planck 2013 results. I. Overview of products and scientific results. 2013.

[10] D Scott, British Columbia, and G F Smoot. 26 . COSMIC MICROWAVE BACKGROUND. 010001(September 2013):1–22, 2014.

[11] D. J. Eisenstein, I. Zehavi, D. W. Hogg, R. Scoccimarro, M. R. Blanton, R. C. Nichol, R. Scranton, H. Seo, M. Tegmark, Z. Zheng, S. Anderson, J. Annis, N. Bahcall, J. Brinkmann, S. Burles, F. J. Castander, A. Connolly, I. Csabai, M. Doi, M. Fukugita, J. A. Frieman, K. Glazebrook, J. E. Gunn, J. S. Hendry, G. Hennessy, Z. Ivezic, S. Kent, G. R. Knapp, H. Lin, Y. Loh, R. H. Lupton, B. Margon, T. McKay, A. Meiksin, J. A. Munn, A. Pope, M. Richmond, D. Schlegel, D. Schneider, K. Shimasaku, C. Stoughton, M. Strauss, M. SubbaRao, A. S. Szalay, I. Szapudi, D. Tucker, B. Yanny, and D. York. Detection of the baryon acoustic peak in the large-scale correlation function of SDSS luminous red galaxies. *The Astrophysical Journal*, 633(2):560–574, November 2005. ISSN 0004-637X, 1538-4357. doi: 10.1086/466512. URL http://arxiv.org/abs/astro-ph/0501171. arXiv: astro-ph/0501171.

[12] Daniel J Eisenstein, Hee-Jong Seo, and Martin White. On the Robustness of the Acoustic Scale in the Low-Redshift Clustering of Matter. *The Astrophysical Journal*, 664:660–674, August 2007. URL http://adsabs.harvard.edu/abs/2007ApJ...664..660E.

[13] A. H. Broeils K. G. Begelan and R. H. Sandersh. Extended rotation curves of spiral galaxies: dark haloes and modified dynamics. *MNRAS*, 249:523, 1991.

[14] Y. N. Parijskij. Search for Primordial Perturbations of the Universe: Observations with Ratan-600 Radio Telescope. In M. S. Longair and J. Einasto, editors, *The Large Scale Structure of the Universe*, number 79 in International Astronomical Union / Union Astronomique Internationale, pages 315–316. Springer Netherlands, 1978. ISBN 978-90-277-0896-0, 978-94-009-9843-8. URL http://link.springer.com/chapter/10.1007/978-94-009-9843-8_33.

[15] C. S. Frenk S. D. M. White. Clustering in a neutrino-dominated universe. *The Astrophysical Journal*, 274:L1–L5, 1983. ISSN 0004-637X. doi: 10.1086/184139.

[16] George R. Blumenthal, S. M. Faber, Joel R. Primack, and Martin J. Rees. Formation of galaxies and large-scale structure with cold dark matter. *Nature*, 311(5986):517–525, October 1984. doi: 10.1038/311517a0. URL http://www.nature.com/nature/journal/v311/n5986/abs/311517a0.html.

[17] Revised October, Trieste Observatory, Standard Model, and Thus Bbn. 22. big-bang nucleosynthesis. 010001(October 2013):1–15, 2014.

[18] M. Betoule, R. Kessler, J. Guy, J. Mosher, D. Hardin, R. Biswas, P. Astier, P. El-Hage, M. Konig, S. Kuhlmann, J. Marriner, R. Pain, N. Regnault, C. Balland, B. A. Bassett, P. J. Brown, H. Campbell, R. G. Carlberg, F. Cellier-Holzem, D. Cinabro, A. Conley, C. B. D'Andrea, D. L. DePoy, M. Doi, R. S. Ellis, S. Fabbro, A. V. Filippenko, R. J. Foley, J. A. Frieman, D. Fouchez, L. Galbany, A. Goobar, R. R. Gupta, G. J. Hill, R. Hlozek, C. J. Hogan, I. M. Hook, D. A. Howell, S. W. Jha, L. Le Guillou, G. Leloudas, C. Lidman, J. L. Marshall, A. Möller, A. M. Mourão, J. Neveu, R. Nichol, M. D. Olmstead, N. Palanque-Delabrouille, S. Perlmutter, J. L. Prieto, C. J. Pritchet, M. Richmond, A. G. Riess, V. Ruhlmann-Kleider, M. Sako, K. Schahmaneche, D. P. Schneider, M. Smith, J. Sollerman, M. Sullivan, N. A. Walton, and C. J. Wheeler. Improved cosmological constraints from a joint analysis of the SDSS-II and SNLS supernova samples. *arXiv:1401.4064 [astro-ph]*, January 2014. URL http://arxiv.org/abs/1401.4064. arXiv: 1401.4064.

[19] Kevork Abazajian. Linear Cosmological Structure Limits on Warm Dark Matter. *Physical Review D*, 73(6), March 2006. ISSN 1550-7998, 1550-2368. doi: 10.1103/PhysRevD.73.063513. URL http://arxiv.org/abs/astro-ph/0512631. arXiv: astro-ph/0512631.

[20] Vijay K. Narayanan, David N. Spergel, Romeel Davé, and Chung-Pei Ma. Lyman-alpha Forest Constraints on the Mass of Warm Dark Matter and the Shape of the Linear Power Spectrum. *arXiv:astro-ph/0005095*, May 2000. URL http://arxiv.org/abs/astro-ph/0005095. arXiv: astro-ph/0005095.

[21] P. Colin, V. Avila-Reese, and O. Valenzuela. Substructure and halo density profiles in a Warm Dark Matter Cosmology. *The Astrophysical Journal*, 542(2):622–630, October 2000. ISSN 0004-637X, 1538-4357. doi: 10.1086/317057. URL http://arxiv.org/abs/astro-ph/0004115. arXiv: astro-ph/0004115.

[22] P. Tisserand, L. Le Guillou, C. Afonso, J. N. Albert, J. Andersen, R. Ansari, E. Aubourg, P. Bareyre, J. P. Beaulieu, X. Charlot, C. Coutures, R. Ferlet, P. Fouqué, J. F. Glicenstein, B. Goldman, A. Gould, D. Graff, M. Gros, J. Haissinski, C. Hamadache, J. de Kat, T. Lasserre, E. Lesquoy, C. Loup, C. Magneville, J. B. Marquette, E. Maurice, A. Maury, A. Milsztajn, M. Moniez, N. Palanque-Delabrouille, O. Perdereau, Y. R. Rahal, J. Rich, M. Spiro, A. Vidal-Madjar, L. Vigroux, and S. Zylberajch. Limits on the macho content of the galactic halo from the EROS-2 survey of the magellanic clouds. *Astronomy and Astrophysics*, 469(2): 387–404, July 2007. ISSN 0004-6361, 1432-0746. doi: 10.1051/0004-6361:20066017. URL http://arxiv.org/abs/astro-ph/0607207. arXiv: astro-ph/0607207.

[23] Scott Dodelson and Lawrence M. Widrow. Sterile neutrinos as dark matter. *Phys. Rev. Lett.*, 72(1):17–20, January 1994. doi: 10.1103/PhysRevLett.72.17. URL http://link.aps.org/doi/10.1103/PhysRevLett.72.17.

[24] Palash B. Pal and Lincoln Wolfenstein. Radiative decays of massive neutrinos. *Phys. Rev. D*, 25(3):766–773, February 1982. doi: 10.1103/PhysRevD.25.766. URL http://link.aps.org/doi/10.1103/PhysRevD.25.766.

[25] Esra Bulbul, Maxim Markevitch, Adam Foster, Randall K. Smith, Michael Loewenstein, and Scott W. Randall. Detection of an Unidentified Emission Line in the Stacked X-Ray Spectrum of Galaxy Clusters. *ApJ*, 789(1):13, July 2014. ISSN 0004-637X. doi: 10.1088/0004-637X/789/1/13. URL http://iopscience.iop.org/0004-637X/789/1/13.

[26] Alexey Boyarsky, Oleg Ruchayskiy, Dmytro Iakubovskyi, and Jeroen Franse. An unidentified line in X-ray spectra of the Andromeda galaxy and Perseus galaxy cluster. *Physical Review Letters*, 113(25), December 2014. ISSN 0031-9007, 1079-7114. doi: 10.1103/PhysRevLett.113.251301. URL http://arxiv.org/abs/1402.4119. arXiv: 1402.4119.

[27] Leanne D. Duffy and Karl van Bibber. Axions as dark matter particles. *New Journal of Physics*, 11(10):105008, October 2009. ISSN 1367-2630. doi: 10.1088/1367-2630/11/10/105008. URL http://arxiv.org/abs/0904.3346. arXiv: 0904.3346.

[28] G. Bertone. *Particle Dark Matter Observations Models And Searches | Cosmology, relativity and gravitation | Cambridge University Press.* URL http://www.cambridge.org/fr/academic/subjects/physics/cosmology-relativity-and-gravitation/particle-dark-matter-observations-models-and-searches.

[29] M. Cahill-Rowley, R. Cotta, A. Drlica-Wagner, S. Funk, J. Hewett, A. Ismail, T. Rizzo, and M. Wood. Complementarity and Searches for Dark Matter in the pMSSM. *arXiv:1305.6921 [astro-ph, physics:hep-ex, physics:hep-ph]*, May 2013. URL http://arxiv.org/abs/1305.6921. arXiv: 1305.6921.

[30] The ATLAS Collaboration. Search for dark matter candidates and large extra dimensions in events with a jet and missing transverse momentum with the ATLAS detector. *Journal of High Energy Physics*, 2013(4), April 2013. ISSN 1029-8479. doi: 10.1007/JHEP04(2013)075. URL http://arxiv.org/abs/1210.4491. arXiv: 1210.4491.

[31] Jessica Goodman, Masahiro Ibe, Arvind Rajaraman, William Shepherd, Tim M. P. Tait, and Hai-Bo Yu. Constraints on Dark Matter from Colliders. *Physical Review D*, 82(11), December 2010. ISSN 1550-7998, 1550-2368. doi: 10.1103/PhysRevD.82.116010. URL http://arxiv.org/abs/1008.1783. arXiv: 1008.1783.

[32] The IceCube Collaboration. Search for dark matter annihilations in the sun with the 79-string IceCube detector. *Phys. Rev. Lett.*, 110(13):131302, March 2013. doi: 10.1103/PhysRevLett.110.131302. URL http://link.aps.org/doi/10.1103/PhysRevLett.110.131302.

[33] T. Tanaka, K. Abe, Y. Hayato, T. Iida, J. Kameda, Y. Koshio, Y. Kouzuma, M. Miura, S. Moriyama, M. Nakahata, S. Nakayama, Y. Obayashi, H. Sekiya, M. Shiozawa, Y. Suzuki, A. Takeda, Y. Takenaga, K. Ueno, K. Ueshima, S. Yamada, T. Yokozawa, C. Ishihara, S. Hazama, H. Kaji, T. Kajita, K. Kaneyuki, T. McLachlan, K. Okumura, Y. Shimizu, N. Tanimoto, F. Dufour, E. Kearns, M. Litos, J. L. Raaf, J. L. Stone, L. R. Sulak, J. P. Cravens, K. Bays, W. R. Kropp, S. Mine, C. Regis, M. B. Smy, H. W. Sobel, K. S. Ganezer, J. Hill, W. E. Keig, J. S. Jang, J. Y. Kim, I. T. Lim, J. B. Albert, K. Scholberg, C. W. Walter, R. Wendell, T. Wongjirad, T. Ishizuka, S. Tasaka, J. G. Learned, S. Matsuno, S. Smith, K. Martens, M. Vagins, Y. Watanabe, T. Hasegawa, T. Ishida, T. Ishii, T. Kobayashi, T. Nakadaira, K. Nakamura, K. Nishikawa, H. Nishino, Y. Oyama, K. Sakashita, T. Sekiguchi, T. Tsukamoto, A. T. Suzuki, Y. Takeuchi, M. Ikeda, A. Minamino, T. Nakaya, L. Labarga, Y. Fukuda, Y. Itow, G. Mitsuka, C. K. Jung, C. McGrew, G. Lopez, C. Yanagisawa, N. Tamura, H. Ishino, A. Kibayashi,

M. Sakuda, Y. Kuno, M. Yoshida, S. B. Kim, B. S. Yang, H. Okazawa, Y. Choi, K. Nishijima, Y. Yokosawa, M. Koshiba, Y. Totsuka, M. Yokoyama, S. Chen, Y. Heng, Z. Yang, H. Zhang, D. Kielczewska, P. Mijakowski, K. Connolly, M. Dziomba, E. Thrane, R. J. Wilkes, and (The Super-Kamiokande Collaboration). An indirect search for weakly interacting massive particles in the sun using 3109.6 days of upward-going muons in super-kamiokande. *ApJ*, 742(2): 78, December 2011. ISSN 0004-637X. doi: 10.1088/0004-637X/742/2/78. URL http://iopscience.iop.org/0004-637X/742/2/78.

[34] Stefan Funk. Indirect Detection of Dark Matter with gamma rays. *arXiv:1310.2695 [astro-ph, physics:hep-ex]*, October 2013. URL http://arxiv.org/abs/1310.2695. arXiv: 1310.2695.

[35] Fermi-LAT Collaboration. Searching for Dark Matter Annihilation from Milky Way Dwarf Spheroidal Galaxies with Six Years of Fermi-LAT Data. *arXiv:1503.02641 [astro-ph, physics:hep-ex]*, March 2015. URL http://arxiv.org/abs/1503.02641. arXiv: 1503.02641.

[36] H. E. S. S. Collaboration. Search for a dark matter annihilation signal from the galactic center halo with h.e.s.s. *Physical Review Letters*, 106(16), April 2011. ISSN 0031-9007, 1079-7114. doi: 10.1103/PhysRevLett.106.161301. URL http://arxiv.org/abs/1103.3266. arXiv: 1103.3266.

[37] Christoph Weniger. A tentative gamma-ray line from dark matter annihilation at the fermi large area telescope. *Journal of Cosmology and Astroparticle Physics*, 2012(08):007–007, August 2012. ISSN 1475-7516. doi: 10.1088/1475-7516/2012/08/007. URL http://arxiv.org/abs/1204.2797. arXiv: 1204.2797.

[38] Fermi-LAT Collaboration. Search for Gamma-ray Spectral Lines with the Fermi Large Area Telescope and Dark Matter Implications. *arXiv:1305.5597 [astro-ph]*, May 2013. URL http://arxiv.org/abs/1305.5597. arXiv: 1305.5597.

[39] Kevork N. Abazajian, Nicolas Canac, Shunsaku Horiuchi, and Manoj Kaplinghat. Astrophysical and Dark Matter Interpretations of Extended Gamma-Ray Emission from the Galactic Center. *Physical Review D*, 90(2), July 2014. ISSN 1550-7998, 1550-2368. doi: 10.1103/PhysRevD.90.023526. URL http://arxiv.org/abs/1402.4090. arXiv: 1402.4090.

[40] J. Aleksić, S. Ansoldi, L. A. Antonelli, P. Antoranz, A. Babic, P. Bangale, U. Barres de Almeida, J. A. Barrio, J. Becerra González, W. Bednarek, K. Berger, E. Bernardini, A. Biland, O. Blanch, R. K. Bock, S. Bonnefoy, G. Bonnoli, F. Borracci, T. Bretz, E. Carmona, A. Carosi, D. Carreto Fidalgo, P. Colin,

E. Colombo, J. L. Contreras, J. Cortina, S. Covino, P. Da Vela, F. Dazzi, A. De Angelis, G. De Caneva, B. De Lotto, C. Delgado Mendez, M. Doert, A. Domínguez, D. Dominis Prester, D. Dorner, M. Doro, S. Einecke, D. Eisenacher, D. Elsaesser, E. Farina, D. Ferenc, M. V. Fonseca, L. Font, K. Frantzen, C. Fruck, R. J. García López, M. Garczarczyk, D. Garrido Terrats, M. Gaug, G. Giavitto, N. Godinović, A. González Muñoz, S. R. Gozzini, D. Hadasch, M. Hayashida, A. Herrero, D. Hildebrand, J. Hose, D. Hrupec, W. Idec, V. Kadenius, H. Kellermann, K. Kodani, Y. Konno, J. Krause, H. Kubo, J. Kushida, A. La Barbera, D. Lelas, N. Lewandowska, E. Lindfors, S. Lombardi, M. López, R. López-Coto, A. López-Oramas, E. Lorenz, I. Lozano, M. Makariev, K. Mallot, G. Maneva, N. Mankuzhiyil, K. Mannheim, L. Maraschi, B. Marcote, M. Mariotti, M. Martínez, D. Mazin, U. Menzel, M. Meucci, J. M. Miranda, R. Mirzoyan, A. Moralejo, P. Munar-Adrover, D. Nakajima, A. Niedzwiecki, K. Nilsson, K. Nishijima, N. Nowak, R. Orito, A. Overkemping, S. Paiano, M. Palatiello, D. Paneque, R. Paoletti, J. M. Paredes, X. Paredes-Fortuny, S. Partini, M. Persic, F. Prada, P. G. Prada Moroni, E. Prandini, S. Preziuso, I. Puljak, R. Reinthal, W. Rhode, M. Ribó, J. Rico, J. Rodriguez Garcia, S. Rügamer, A. Saggion, T. Saito, K. Saito, M. Salvati, K. Satalecka, V. Scalzotto, V. Scapin, C. Schultz, T. Schweizer, A. Sillanpää, J. Sitarek, I. Snidaric, D. Sobczynska, F. Spanier, V. Stamatescu, A. Stamerra, T. Steinbring, J. Storz, S. Sun, T. Surić, L. Takalo, H. Takami, F. Tavecchio, P. Temnikov, T. Terzić, D. Tescaro, M. Teshima, J. Thaele, O. Tibolla, D. F. Torres, T. Toyama, A. Treves, M. Uellenbeck, P. Vogler, R. M. Wagner, F. Zandanel, R. Zanin, and A. Ibarra. Optimized dark matter searches in deep observations of Segue 1 with MAGIC. *Journal of Cosmology and Astroparticle Physics*, 2014(02):008–008, February 2014. ISSN 1475-7516. doi: 10.1088/1475-7516/2014/02/008. URL http://arxiv.org/abs/1312.1535. arXiv: 1312.1535.

[41] David G. Cerdeno and Anne M. Green. Direct detection of WIMPs. *Nuclear Instruments and Methods in Physics Research Section B: Beam Interactions with Materials and Atoms*, 269(4):498–503, February 2011. ISSN 0168583X. doi: 10.1016/j.nimb.2010.12.064. URL http://arxiv.org/abs/1002.1912. arXiv: 1002.1912.

[42] J. D. Lewin and P. F. Smith. Review of mathematics, numerical factors, and corrections for dark matter experiments based on elastic nuclear recoil. *Astropart.Phys.*, 6:87–112, 1996. doi: 10.1016/S0927-6505(96)00047-3.

[43] Chris Savage, Katherine Freese, and Paolo Gondolo. Annual modulation of dark matter in the presence of streams. *Phys. Rev. D*, 74(4):043531, August 2006.

doi: 10.1103/PhysRevD.74.043531. URL http://link.aps.org/doi/10.1103/PhysRevD.74.043531.

[44] Jonathan L. Feng, Jason Kumar, Danny Marfatia, and David Sanford. Isospin-violating dark matter. *Physics Letters B*, 703(2):124–127, September 2011. ISSN 03702693. doi: 10.1016/j.physletb.2011.07.083. URL http://arxiv.org/abs/1102.4331. arXiv: 1102.4331.

[45] R. H. Helm. Inelastic and Elastic Scattering of 187-Mev Electrons from Selected Even-Even Nuclei. *Phys. Rev*, 104:1466–1475, 1956.

[46] J. Engel. Nuclear form-factors for the scattering of weakly interacting massive particles. *Phys. Lett*, B264:114–119, 1991.

[47] CDMS Collaboration. Silicon detector dark matter results from the final exposure of CDMS II. *arXiv:1304.4279 [astro-ph, physics:hep-ex, physics:physics]*, April 2013. URL http://arxiv.org/abs/1304.4279. arXiv: 1304.4279.

[48] XENON100 Collaboration. Dark matter results from 225 live days of XENON100 data. *Physical Review Letters*, 109(18), November 2012. ISSN 0031-9007, 1079-7114. doi: 10.1103/PhysRevLett.109.181301. URL http://arxiv.org/abs/1207.5988. arXiv: 1207.5988.

[49] LUX Collaboration. First results from the LUX dark matter experiment at the sanford underground research facility. *Physical Review Letters*, 112(9), March 2014. ISSN 0031-9007, 1079-7114. doi: 10.1103/PhysRevLett.112.091303. URL http://arxiv.org/abs/1310.8214. arXiv: 1310.8214.

[50] The PICASSO Collaboration. Constraints on low-mass WIMP interactions on 19f from PICASSO. *Physics Letters B*, 711(2):153–161, May 2012. ISSN 03702693. doi: 10.1016/j.physletb.2012.03.078. URL http://arxiv.org/abs/1202.1240. arXiv: 1202.1240.

[51] E. Behnke, J. Behnke, S. J. Brice, D. Broemmelsiek, J. I. Collar, A. Conner, P. S. Cooper, M. Crisler, C. E. Dahl, D. Fustin, E. Grace, J. Hall, M. Hu, I. Levine, W. H. Lippincott, T. Moan, T. Nania, E. Ramberg, A. E. Robinson, A. Sonnenschein, M. Szydagis, and E. Vázquez-Jáuregui. First dark matter search results from a 4-kg CF$_3$i bubble chamber operated in a deep underground site. *Physical Review D*, 86(5), September 2012. ISSN 1550-7998, 1550-2368. doi: 10.1103/PhysRevD.86.052001. URL http://arxiv.org/abs/1204.3094. arXiv: 1204.3094.

[52] XMASS collaboration. Light WIMP search in XMASS. *Physics Letters B*, 719 (1-3):78–82, February 2013. ISSN 03702693. doi: 10.1016/j.physletb.2013.01.001. URL http://arxiv.org/abs/1211.5404. arXiv: 1211.5404.

[53] Darkside Collaboration. Light yield in DarkSide-10: a prototype two-phase liquid argon TPC for dark matter searches. *arXiv:1204.6218 [astro-ph, physics:hep-ex]*, April 2012. URL http://arxiv.org/abs/1204.6218. arXiv: 1204.6218.

[54] CRESST Collaboration. Results on low mass WIMPs using an upgraded CRESST-II detector. *arXiv:1407.3146 [astro-ph, physics:physics]*, July 2014. URL http://arxiv.org/abs/1407.3146. arXiv: 1407.3146.

[55] C. E. Aalseth, P. S. Barbeau, J. Colaresi, J. I. Collar, J. Diaz Leon, J. E. Fast, N. E. Fields, T. W. Hossbach, A. Knecht, M. S. Kos, M. G. Marino, H. S. Miley, M. L. Miller, J. L. Orrell, and K. M. Yocum. Search for an annual modulation in three years of CoGeNT dark matter detector data. *arXiv:1401.3295 [astro-ph, physics:hep-ex, physics:hep-ph]*, January 2014. URL http://arxiv.org/abs/1401.3295. arXiv: 1401.3295.

[56] M. Felizardo, T. A. Girard, T. Morlat, A. C. Fernandes, A. R. Ramos, J. G. Marques, A. Kling, J. Puibasset, M. Auguste, D. Boyer, A. Cavaillou, J. Poupeney, C. Sudre, F. P. Carvalho, M. I. Prudencio, and R. Marques. The SIMPLE phase II dark matter search. *arXiv:1404.4309 [hep-ph, physics:physics]*, April 2014. URL http://arxiv.org/abs/1404.4309. arXiv: 1404.4309.

[57] C. Amole, M. Ardid, D. M. Asner, D. Baxter, E. Behnke, P. Bhattacharjee, H. Borsodi, M. Bou-Cabo, S. J. Brice, D. Broemmelsiek, K. Clark, J. I. Collar, P. S. Cooper, M. Crisler, C. E. Dahl, S. Daley, M. Das, F. Debris, N. Dhungana, J. Farine, I. Felis, R. Filgas, M. Fines-Neuschild, F. Girard, G. Giroux, M. Hai, J. Hall, O. Harris, C. M. Jackson, M. Jin, C. B. Krauss, M. Lafrenière, M. Laurin, I. Lawson, I. Levine, W. H. Lippincott, E. Mann, J. P. Martin, D. Maurya, P. Mitra, R. Neilson, A. J. Noble, A. Plante, R. B. Podviianiuk, S. Priya, A. E. Robinson, M. Ruschman, O. Scallon, S. Seth, A. Sonnenschein, N. Starinski, I. Štekl, E. Vàzquez-Jaùregui, J. Wells, U. Wichoski, V. Zacek, and J. Zhang. Dark Matter Search Results from the PICO-2l C$_3$F$_8$ Bubble Chamber. *arXiv:1503.00008 [astro-ph, physics:physics]*, February 2015. URL http://arxiv.org/abs/1503.00008. arXiv: 1503.00008.

[58] R. Bernabei, P. Belli, F. Cappella, V. Caracciolo, S. Castellano, R. Cerulli, C. J. Dai, A. d'Angelo, S. d'Angelo, A. Di Marco, H. L. He, A. Incicchitti, H. H. Kuang, X. H. Ma, F. Montecchia, D. Prosperi, X. D. Sheng, R. G. Wang, and Z. P. Ye.

Final model independent result of DAMA/LIBRA-phase1. *arXiv:1308.5109 [astro-ph, physics:hep-ex]*, August 2013. URL http://arxiv.org/abs/1308.5109. arXiv: 1308.5109.

[59] H. S. Lee, H. Bhang, J. H. Choi, S. Choi, I. S. Hahn, E. J. Jeon, H. W. Joo, W. G. Kang, B. H. Kim, G. B. Kim, H. J. Kim, J. H. Kim, K. W. Kim, S. C. Kim, S. K. Kim, Y. D. Kim, Y. H. Kim, J. H. Lee, J. K. Lee, S. J. Lee, D. S. Leonard, J. Li, J. Li, Y. J. Li, X. R. Li, S. S. Myung, S. L. Olsen, J. W. Park, I. S. Seong, J. H. So, and Q. Yue. A search for low-mass dark matter with CsI(tl) crystal detectors. *arXiv:1404.3443 [astro-ph, physics:hep-ex, physics:physics]*, April 2014. URL http://arxiv.org/abs/1404.3443. arXiv: 1404.3443.

[60] G. Gerbier M. Drees. 24. dark matter. 010001(September 2013):1–21, 2014.

[61] R. Agnese, Z. Ahmed, A. J. Anderson, S. Arrenberg, D. Balakishiyeva, R. Basu Thakur, D. A. Bauer, J. Billard, A. Borgland, D. Brandt, P. L. Brink, T. Bruch, R. Bunker, B. Cabrera, D. O. Caldwell, D. G. Cerdeno, H. Chagani, J. Cooley, B. Cornell, C. H. Crewdson, P. Cushman, M. Daal, F. Dejongh, E. do Couto e Silva, T. Doughty, L. Esteban, S. Fallows, E. Figueroa-Feliciano, J. Filippini, J. Fox, M. Fritts, G. L. Godfrey, S. R. Golwala, J. Hall, R. H. Harris, S. A. Hertel, T. Hofer, D. Holmgren, L. Hsu, M. E. Huber, A. Jastram, O. Kamaev, B. Kara, M. H. Kelsey, A. Kennedy, P. Kim, M. Kiveni, K. Koch, M. Kos, S. W. Leman, B. Loer, E. Lopez Asamar, R. Mahapatra, V. Mandic, C. Martinez, K. A. McCarthy, N. Mirabolfathi, R. A. Moffatt, D. C. Moore, P. Nadeau, R. H. Nelson, K. Page, R. Partridge, M. Pepin, A. Phipps, K. Prasad, M. Pyle, H. Qiu, W. Rau, P. Redl, A. Reisetter, Y. Ricci, T. Saab, B. Sadoulet, J. Sander, K. Schneck, R. W. Schnee, S. Scorza, B. Serfass, B. Shank, D. Speller, K. M. Sundqvist, A. N. Villano, B. Welliver, D. H. Wright, S. Yellin, J. J. Yen, J. Yoo, B. A. Young, and J. Zhang. Silicon Detector Dark Matter Results from the Final Exposure of CDMS II. *Phys. Rev. Lett.*, 111(25):251301, December 2013. doi: 10.1103/PhysRevLett.111.251301. URL http://link.aps.org/doi/10.1103/PhysRevLett.111.251301.

[62] R. Agnese, A. J. Anderson, M. Asai, D. Balakishiyeva, R. Basu Thakur, D. A. Bauer, J. Beaty, J. Billard, A. Borgland, M. A. Bowles, D. Brandt, P. L. Brink, R. Bunker, B. Cabrera, D. O. Caldwell, D. G. Cerdeno, H. Chagani, Y. Chen, M. Cherry, J. Cooley, B. Cornell, C. H. Crewdson, P. Cushman, M. Daal, D. DeVaney, P. C. F. Di Stefano, E. Do Couto E. Silva, T. Doughty, L. Esteban, S. Fallows, E. Figueroa-Feliciano, G. L. Godfrey, S. R. Golwala, J. Hall, S. Hansen, H. R. Harris, S. A. Hertel, B. A. Hines, T. Hofer, D. Holmgren, L. Hsu, M. E. Huber, A. Jastram, O. Kamaev, B. Kara, M. H. Kelsey, S. Kenany, A. Kennedy, M. Kiveni,

K. Koch, A. Leder, B. Loer, E. Lopez Asamar, R. Mahapatra, V. Mandic, C. Martinez, K. A. McCarthy, N. Mirabolfathi, R. A. Moffatt, R. H. Nelson, L. Novak, K. Page, R. Partridge, M. Pepin, A. Phipps, M. Platt, K. Prasad, M. Pyle, H. Qiu, W. Rau, P. Redl, A. Reisetter, R. W. Resch, Y. Ricci, M. Ruschman, T. Saab, B. Sadoulet, J. Sander, R. L. Schmitt, K. Schneck, R. W. Schnee, S. Scorza, D. N. Seitz, B. Serfass, B. Shank, D. Speller, A. Tomada, S. Upadhyayula, A. N. Villano, B. Welliver, D. H. Wright, S. Yellin, J. J. Yen, B. A. Young, and J. Zhang. Search for Low-Mass WIMPs with SuperCDMS. *Physical Review Letters*, 112(24), June 2014. ISSN 0031-9007, 1079-7114. doi: 10.1103/PhysRevLett.112.241302. URL http://arxiv.org/abs/1402.7137. arXiv: 1402.7137.

[63] The EDELWEISS collaboration. Search for low-mass WIMPs with EDELWEISS-II heat-and-ionization detectors. *Phys. Rev. D*, 86:051701, September 2012. doi: 10.1103/PhysRevD.86.051701. URL http://link.aps.org/doi/10.1103/PhysRevD.86.051701.

[64] CRESST Collaboration, G. Angloher, A. Bento, C. Bucci, L. Canonica, A. Erb, F. v Feilitzsch, N. Ferreiro Iachellini, P. Gorla, A. Gütlein, D. Hauff, P. Huff, J. Jochum, M. Kiefer, C. Kister, H. Kluck, H. Kraus, J.-C. Lanfranchi, J. Loebell, A. Münster, F. Petricca, W. Potzel, F. Pröbst, F. Reindl, S. Roth, K. Rottler, C. Sailer, K. Schäffner, J. Schieck, J. Schmaler, S. Scholl, S. Schönert, W. Seidel, M. v Sivers, L. Stodolsky, C. Strandhagen, R. Strauss, A. Tanzke, M. Uffinger, A. Ulrich, I. Usherov, S. Wawoczny, M. Willers, M. Wüstrich, and A. Zöller. Results on low mass WIMPs using an upgraded CRESST-II detector. *The European Physical Journal C*, 74(12), December 2014. ISSN 1434-6044, 1434-6052. doi: 10.1140/epjc/s10052-014-3184-9. URL http://arxiv.org/abs/1407.3146. arXiv: 1407.3146.

[65] Kathryn M. Zurek. Asymmetric Dark Matter: Theories, Signatures, and Constraints. *arXiv:1308.0338 [astro-ph, physics:hep-ph]*, 2013. URL http://arxiv.org/abs/1308.0338. arXiv: 1308.0338.

[66] A. Gütlein, G. Angloher, A. Bento, C. Bucci, L. Canonica, A. Erb, F. v Feilitzsch, N. Ferreiro Iachellini, P. Gorla, D. Hauff, J. Jochum, M. Kiefer, H. Kluck, H. Kraus, J.-C. Lanfranchi, J. Loebell, A. Münster, F. Petricca, W. Potzel, F. Pröbst, F. Reindl, S. Roth, K. Rottler, C. Sailer, K. Schäffner, J. Schieck, S. Schönert, W. Seidel, M. v Sivers, L. Stodolsky, C. Strandhagen, R. Strauss, A. Tanzke, M. Uffinger, A. Ulrich, I. Usherov, S. Wawoczny, M. Willers, M. Wüstrich, and A. Zöller. Impact of Coherent Neutrino Nucleus Scattering on Direct Dark Matter Searches based on CaWO$_4$ Crystals. *Astroparticle Physics*, 69:44–49,

September 2015. ISSN 09276505. doi: 10.1016/j.astropartphys.2015.03.010. URL http://arxiv.org/abs/1408.2357. arXiv: 1408.2357.

[67] Marc Schumann. Dark Matter 2014. *arXiv:1501.01200 [astro-ph, physics:hep-ph, physics:physics]*, January 2015. URL http://arxiv.org/abs/1501.01200. arXiv: 1501.01200.

[68] Holger Martin Kluck. *Measurement of the cosmic-induced neutron yield at the Modane underground laboratory*. PhD thesis, 2013.

[69] The EDELWEISS collaboration. Muon-induced background in the EDELWEISS dark matter search. *Astroparticle Physics*, 44:28–39, April 2013. ISSN 0927-6505. doi: 10.1016/j.astropartphys.2013.01.014. URL http://www.sciencedirect.com/science/article/pii/S0927650513000248.

[70] The EDELWEISS collaboration. Background discrimination capabilities of a heat and ionization germanium cryogenic detector. *Astroparticle Physics*, 14(4):329–337, January 2001. ISSN 09276505. doi: 10.1016/S0927-6505(00)00127-4. URL http://arxiv.org/abs/astro-ph/0004308. arXiv: astro-ph/0004308.

[71] The EDELWEISS collaboration. First results of the EDELWEISS-II WIMP search using Ge cryogenic detectors with interleaved electrodes. *Physics Letters B*, 687(4–5):294–298, April 2010. ISSN 0370-2693. doi: 10.1016/j.physletb.2010.03.057. URL http://www.sciencedirect.com/science/article/pii/S0370269310003783.

[72] M. Laubenstein, M. Hult, J. Gasparro, D. Arnold, S. Neumaier, G. Heusser, M. Köhler, P. Povinec, J.-L. Reyss, M. Schwaiger, and P. Theodórsson. Underground measurements of radioactivity. *Appl Radiat Isot*, 61(2-3):167–172, September 2004. ISSN 0969-8043. doi: 10.1016/j.apradiso.2004.03.039.

[73] B. Censier; et al. Edelweiss read-out electronics and future prospects. *Journal of Low Temperature Physics*, 2012.

[74] The EDELWEISS collaboration. Axion searches with the EDELWEISS-II experiment. *J. Cosmol. Astropart. Phys.*, 2013(11):067, November 2013. ISSN 1475-7516. doi: 10.1088/1475-7516/2013/11/067. URL http://iopscience.iop.org/1475-7516/2013/11/067.

[75] C. A. Baker, D. D. Doyle, P. Geltenbort, K. Green, M. G. D. van der Grinten, P. G. Harris, P. Iaydjiev, S. N. Ivanov, D. J. R. May, J. M. Pendlebury, J. D. Richardson, D. Shiers, and K. F. Smith. Improved Experimental Limit on the Electric Dipole Moment of the Neutron. *Phys. Rev. Lett.*,

97(13):131801, September 2006. doi: 10.1103/PhysRevLett.97.131801. URL http://link.aps.org/doi/10.1103/PhysRevLett.97.131801.

[76] R. D. Peccei and Helen R. Quinn. Constraints imposed by cp conservation in the presence of instantons. *Phys. Rev. D*, 16(1791), 1977.

[77] S. Weinberg. A new light boson? *Phys. Rev. Lett*, 40(223), 1978.

[78] F. Wilczek. Problem of strong p and t invariance in the presence of instantons. *Phys. Rev. Lett*, 40(279), 1978.

[79] J. Beringer et al. (Particle Data Group). *Phys. Rev D*, 86(010001), 2012.

[80] J. E. Kim. Weak interaction singlet and strong cp invariance. *Phys. Lett.*, 43(103), 1979.

[81] M. A. Shifman et al. Can confinement ensure natural cp invariance of strong interactions? *Nucl. Phys. B*, 166(493), 1980.

[82] A. R. Zhitniskiy. On possible suppression of the axion hadron interactions. *Yad. Fiz*, 31(497), 1980.

[83] M. Dine et al. A simple solution to the strong cp problem with a harmless axion. *Phtys. Lett. B*, 104(199), 1981.

[84] D. B. Kaplan. Opening the axion window. *Nucl. Phys. B*, 260(215), 1985.

[85] M. Srednicki. Axion couplings to matter. 1. cp conserving parts. *Nucl. Phys B*, 260(689), 1985.

[86] Svrcek and Witten. Axions in string theory. *JHEP*, 0606(051), 2006.

[87] V. Mateu and A. Pich. V(us) determination from hyperon semileptonic decays. *J. High Energy Phys*, 10(041), 2005.

[88] D. Adams et al. (Spin Muon Collaboration). Spin structure of the proton from polarized inclusive deep inelastic muon - proton scattering. *Phys. Rev. D*, 56(no. 9):5330–5358, 1997.

[89] G. Altarelli et al. Determination of the bjorken sum and strong coupling from polarized structure functions. *Nucl. Phys. B*, 496(337), 1997.

[90] S. Andriamonje et al. (CAST collaboration). An improved limit on the axion-photon coupling from the cast experiment. *JCAP*, 04(010), 2007.

[91] L. Di Lella et al. Search for solar kaluza-klein axions in theories of low-scale quantum gravity. *Phys. Rev. D*, 62(125011), 2000.

[92] A. Serenelli et al. New solar composition: The problem with solar models revisited. *Astrophys. J*, 705(L123), 2009.

[93] S. Moriyama. A proposal to search for a monochromatic component of solar axions using fe-57. *Phys. Rev. Lett*, 75(no. 18 3222), 1995.

[94] W. C. Haxton and K. Y. Lee. Red giant evolution, metallicity and new bounds on hadronic axions. *Phys. Rev. Lett*, 66(no. 20 2557), 1991.

[95] F. T. Avignone. Search for axions from the 1115-kev transition of cu-65. *Phys. Rev. D*, 37(618), 1988.

[96] S. Andriamonje et al. (CAST collaboration). Search for 14.4-kev solar axions emitted in the m1-transition of fe-57 nuclei with cast. *JCAP*, 12(002), 2009.

[97] John N. Bahcall, Sarbani Basu, and M. H. Pinsonneault. How uncertain are solar neutrino predictions? *Physics Letters B*, 433(1–2):1–8, August 1998. ISSN 0370-2693. doi: 10.1016/S0370-2693(98)00657-1. URL http://www.sciencedirect.com/science/article/pii/S0370269398006571.

[98] K. Barth et al. Cast constraints on the axion-electron coupling. *JCAP*, 05(010), 2013.

[99] M. Pospelov et al. Bosonic super-wimps as kev-scale dark matter. *Phys. Rev D*, 78(115012), 2008.

[100] R. J. Creswick et al. Theory for the direct detection of solar axions by coherent primakoff conversion in germanium detectors. *Phys. Lett*, B 427(235), 1998.

[101] A. Derevianko et al. Axio-electric effect. *Phys. Rev*, D 82(065006), 2010.

[102] F. Alessandria et al. Search for 14.4 kev solar axions from m1 transition of fe-57 with cuore crystals. *JCAP*, 05(007), 2013.

[103] URL http://physics.nist.gov/PhysRefData/Xcom/html/xcom1.html.

[104] Wm. J. Veigele. Photon cross sections from 0.1 keV to 1 MeV for elements Z = 1 to Z = 94. *Atomic Data and Nuclear Data Tables*, 5(1):51–111, 1973. ISSN 0092-640X. doi: 10.1016/S0092-640X(73)80015-4. URL http://www.sciencedirect.com/science/article/pii/S0092640X73800154.

[105] S. Cebrian et al. Prospects of solar axion searches with crystal detectors. *Astrop. Phys*, 10(397), 1999.

[106] Z. Ahmed et al. (CDMS Collaboration). Search for axions with the cdms experiment. *Phys. Rev. Lett*, 103(141802), 2009.

[107] R. Bernabei et al. Search for solar axions by primakoff effect in nai crystals. *Phys.Lett B*, 515(6), 2001.

[108] A. Morales et al. Particle dark matter and solar axion searches with a small germanium detector at the canfranc underground laboratory. *Astropart. Phys*, 16 (325), 2002.

[109] Neil W. Ashcroft and N. David Mermin. *Solid State Physics*. Brooks/Cole, New York, January 1976. ISBN 9780030839931.

[110] W. Buchmüller and F. Hoogeveen. Coherent production of light scalar or pseudoscalar particles in Bragg scattering. *Physics Letters B*, 237(2):278–283, March 1990. ISSN 0370-2693. doi: 10.1016/0370-2693(90)91444-G. URL http://www.sciencedirect.com/science/article/pii/037026939091444G.

[111] E. Arik et al. (CAST Collab.). Cast search for sub-ev mass solar axions with 3he buffer gas. *Phys. Rev. Lett*, 107(261302), 2011.

[112] F. T. Avignone III et al. Experimental search for solar axions via coherent primakoff conversion in a germanium spectrometer. *Phys. Rev. Lett.*, 81(5068), 1998.

[113] G. G. Raffelt. *Stars as Laboratories for Fundamental Physics*. University of Chicago Press, Chicago, 1996.

[114] A. V. Derbin. Search for solar axions produced by compton process and bremsstrahlung using axioelectric effect. *JETP Lett*, 95(379), 2012.

[115] K. Abe, K. Hieda, K. Hiraide, S. Hirano, Y. Kishimoto, K. Kobayashi, S. Moriyama, and K. Nakagawa et al. Search for solar axions in xmass, a large liquid-xenon detector. arXiv: 1212.6153v2.

[116] P. Gondolo and G. G. Raffelt. Solar neutrino limit on axions and kev-mass bosons. *Phys. Rev. D*, 79(107301), 2009.

[117] The XENON100 Collaboration. First Axion Results from the XENON100 Experiment. *Physical Review D*, 90(6), September 2014. ISSN 1550-7998, 1550-2368. doi: 10.1103/PhysRevD.90.062009. URL http://arxiv.org/abs/1404.1455. arXiv: 1404.1455.

[118] G. G. Raffelt. Astrophysical axion bounds. *Lect. Notes Phys*, 741(51), 2008.

[119] C. E. Aalseth et al. (CoGeNT Collaboration). Experimental constraints on a dark matter origin for the dama annual modulation effect. *Phys. Rev. Lett*, 101((2008) 251301 [Erratum-ibid.102 109903]), 2009.

[120] Dan Hooper and Tim Linden. Origin of the gamma rays from the Galactic Center. *Phys. Rev. D*, 84(12):123005, December 2011. doi: 10.1103/PhysRevD.84.123005. URL http://link.aps.org/doi/10.1103/PhysRevD.84.123005.

[121] D. V. Poda, E. Armengaud, Q. Arnaud, C. Augier, A. Benoît, A. Benoît, L. Bergé, R. S. Boiko, T. Bergmann, J. Blümer, A. Broniatowski, V. Brudanin, P. Camus, A. Cazes, B. Censier, M. Chapellier, F. Charlieux, D. M. Chernyak, N. Coron, P. Coulter, G. A. Cox, F. A. Danevich, T. de Boissière, R. Decourt, M. De Jesus, L. Devoyon, A.-A. Drillien, L. Dumoulin, K. Eitel, C. Enss, D. Filosofov, A. Fleischmann, N. Fourches, J. Gascon, L. Gastaldo, G. Gerbier, A. Giuliani, M. Gros, L. Hehn, S. Henry, S. Hervé, G. Heuermann, V. Humbert, I. M. Ivanov, A. Juillard, C. Kéfélian, M. Kleifges, H. Kluck, V. V. Kobychev, F. Koskas, V. Kozlov, H. Kraus, V. A. Kudryavtsev, H. Le Sueur, M. Loidl, P. Magnier, E. P. Makarov, M. Mancuso, P. de Marcillac, S. Marnieros, C. Marrache-Kikuchi, A. Menshikov, S. G. Nasonov, X.-F. Navick, C. Nones, E. Olivieri, P. Pari, B. Paul, Y. Penichot, G. Pessina, M. C. Piro, O. Plantevin, T. Redon, M. Robinson, M. Rodrigues, S. Rozov, V. Sanglard, B. Schmidt, V. N. Shlegel, B. Siebenborn, O. Strazzer, D. Tcherniakhovski, M. Tenconi, L. Torres, V. I. Tretyak, L. Vagneron, Ya V. Vasiliev, M. Velazquez, O. Viraphong, R. J. Walker, M. Weber, E. Yakushev, X. Zhang, and V. N. Zhdankov. Scintillating bolometers based on ZnMoO$_4$ and Zn^{100}MoO$_4$ crystals to search for 0ν2β decay of ^{100}Mo (LUMINEU project): first tests at the Modane Underground Laboratory. *arXiv:1502.01161 [nucl-ex, physics:physics]*, February 2015. URL http://arxiv.org/abs/1502.01161. arXiv: 1502.01161.

[122] The EDELWEISS collaboration. Measurement of the response of heat-and-ionization germanium detectors to nuclear recoils. *Nuclear Instruments and Methods in Physics Research Section A: Accelerators, Spectrometers, Detectors and Associated Equipment*, 577(3):558–568, July 2007. ISSN 01689002. doi: 10.1016/j.nima.2007.04.118. URL http://arxiv.org/abs/astro-ph/0607502. arXiv: astro-ph/0607502.

[123] John N. Bahcall. Exchange and Overlap Effects in Electron Capture and in Related Phenomena. *Phys. Rev.*, 132(1):362–367, October 1963. doi: 10.1103/PhysRev.132.362. URL http://link.aps.org/doi/10.1103/PhysRev.132.362.

[124] A.J. Anderson. *A Search for Light Weakly-Interacting Massive Particles with SuperCDMS and Applications to Neutrino Physics*. PhD thesis, 2015.

[125] Particle Data Group. Statistics. *Phys. Rev. D*, 86(Part 1), 2012.

[126] G. J. Feldman and R. D. Cousins. A unified approach to the classicalstatistical analysis of small signals. *Phys.Rev. D*, 57(3873), 1998.

[127] R. Cousins. Why isn't every physicist a Bayesian. *American Journal of Physics*, 63(398), 1995.

[128] K. Crammer G. Cowan, E. Gross, and O. Vitells. Asymptotic formulae for likelihood-based tests of new physics. *Eur. Phys. J. C*, 71(1554), 2011.

[129] N. Reid. Likelihood inference in the presence of nuisance parameters. In *Proceedings of PHYSTAT2003*. L. Lyons, R. Mount, and R. Reitmeyer, eds, eConf C030908, 2003.

[130] W. A. Rolke, A. M. Lopez, and J. Conrad. *Nucl. Instrum. Methods A*, 551(493), 2005.